Higher order corrections to Semileptonic and Nonleptonic B-meson Decays

Zur Erlangung des akademischen Grades eines

Dᴏᴋᴛᴏʀs ᴅᴇʀ Nᴀᴛᴜʀᴡɪssᴇɴsᴄʜᴀғᴛᴇɴ (Dr. rer. nat.)

von der KIT-Fakultät für Physik
des Karlsruher Instituts für Technologie (KIT)

genehmigte

Dissertation

von

M.Sc. Manuel Egner,
geboren am 02.11.1996 in Karlsruhe.

Tag der mündlichen Prüfung: 14. Februar 2025
Erstgutachter: Prof. Dr. Matthias Steinhauser
Zweitgutachter: Prof. Dr. Ulrich Nierste

Ich versichere wahrheitsgemäß, die Arbeit selbstständig angefertigt, alle benutzten Hilfsmittel vollständig und genau angegeben und alles kenntlich gemacht zu haben, was aus Arbeiten anderer unverändert oder mit Änderungen entnommen wurde.

Karlsruhe, 08.01.2025

. . . .

(Manuel Egner)

als Doktorarbeit anerkannt,

Karlsruhe, 08.01.2025

. . . .

(Prof. Dr. Matthias Steinhauser)

Abstract

B mesons are bound states of a bottom antiquark and a light up, down or strange quark. These bound states decay via the weak interaction into lighter mesons. The leading contribution to such decays can be described by the free decay of the mesons bottom antiquark. Lifetimes of weakly decaying B mesons are measured with an accuracy of the order of the per mille level. However, the theoretical predictions can not match this precision since only next-to-leading order QCD corrections to the free quark decay are known which lead to a theoretical uncertainty that is much larger than the experimental uncertainty.

In this thesis, the next-to-next-to-leading order QCD corrections to the semileptonic and nonleptonic bottom quark decays with full charm quark mass dependence are calculated, which constitute the dominant decay channels in Standard Model predictions for B-meson lifetimes within the Heavy Quark Expansion. These contributions will reduce the dependence on the renormalization scale and therefore the theoretical uncertainty on the decay width prediction.

The calculation of the next-to-next-to-leading order corrections requires the correct treatment of γ_5 in $d \neq 4$ dimensions and the corresponding adoption of the evanescent operators in the effective theory. Furthermore, the calculation of the master integrals is non-trivial and is done using state-of-the-art techniques.

The obtained next-to-next-to-leading order result is then analyzed for different renormalization schemes for the quark masses and included in the theoretical prediction of the total decay width of B mesons.

Zusammenfassung

B Mesonen sind gebundene Zustände, die aus einem bottom Antiquark und einem leichten up, down oder strange Quark bestehen. Sie können über die schwache Wechselwirkung in leichtere Mesonen zerfallen. In führender Ordnung kann der Zerfall der B Mesonen mit dem Zerfall eines freien bottom Antiquarks beschrieben werden. Die Lebensdauer von B Mesonen kann mit einer Genauigkeit im Promill-Bereich gemessen werden. Das gilt jedoch nicht für die theoretischen Vorhersagen, da für diese lediglich nächst-zu-führende Ordnung QCD Korrekturen bekannt sind deren theoretische Unsicherheit größer als die experimentelle ist.

In dieser Arbeit werden die nächst-zu-nächst-zu-führende Ordnung QCD Korrekturen zu den semileptonischen und nichtleptonischen Zerfällen mit voller Charm-Massen- abhängigkeit berechnet, welche den dominanten Beitrag der Standard Modell Vorhersage in der Heavy Quark Expansion bilden. Diese Beiträge werden die Abhängigkeit von der Renormierungsskala und damit verbunden die theoretische Unsicherheit der Zerfallsrate reduzieren.

Die Berechnung der nächst-zu-nächst-zu-führende Ordnung Korrekturen setzen das ko- rrekte Behandeln von γ_5 in $d \neq 4$ Dimensionen und das entsprechende Anpassen der evaneszenten Operatoren in der effektiven Theorie voraus. Des weiteren werden für die nicht-triviale Berechnung der Master-Integrale aktuelle Techniken angewendet.

Das berechnete Ergebnis wird zudem auf sein Verhalten unter unterschiedlichen Massen- renormierungsschemen untersucht sowie in die theoretische Vorhersage für die totale Zerfallsbreite der B Mesonen eingearbeitet.

Contents

1. Introduction

The goal of particle physics is to study the smallest building blocks of matter and its interactions. These smallest building blocks are described by the Standard Model of particle physics (SM) which includes leptons, quarks, gauge bosons, gluons and the Higgs boson. The quarks are colour-charged and can never be found as free particles, they form bound states. This phenomenon is known as confinement. Common bound states of quarks are the hadrons that consist of three quarks, for example the proton and neutron with the quark content (uud) and (udd), and the mesons that consist of a quark-antiquark pair. Most bound states of quarks are not stable and decay, for example via the weak interaction.

In this thesis, we discuss the weak decays of one class of such bound states, the B mesons. The B mesons consist of one bottom antiquark and one light quark. The three B mesons B^+, B_d and B_s have the quark content $(\bar{b}u)$, $(\bar{b}d)$ and $(\bar{b}s)$ respectively. The lifetime of these mesons have been measured very precisely with an accuracy of the order of per mille [1]:

$$
\begin{aligned}
\tau(B^+) &= (1.638 \pm 0.004)\,\mathrm{ps}\,, \\
\tau(B_d) &= (1.517 \pm 0.004)\,\mathrm{ps}\,, \\
\tau(B_s) &= (1.520 \pm 0.005)\,\mathrm{ps}\,.
\end{aligned} \tag{1.1}
$$

The theoretical description of such decays is carried out in the framework of the heavy quark expansion (HQE). In this prescription, the decay width, the inverse of the lifetime, of the mesons is described as a series of operators in $\Lambda_{\mathrm{QCD}}/m_b$ and in the strong coupling constant α_s. The leading term of this expansion describes the weak decay of a free bottom quark and is numerically the largest contribution to the total decay width. The free bottom quark decays via the weak interaction either to an up-type quark and a lepton-neutrino pair or an up-type quark and an additional quark-antiquark pair. These two decay modes are called semileptonic and nonleptonic respectively. Sample Feynman diagrams for such decays are shown in Figure 1.1.

For the semileptonic decay of the bottom quark, calculations at NLO [2] and NNLO [3, 4, 5] in QCD are known for nearly 20 years. More recently, even N^{3}LO became available [6, 7, 8]. This is however not the case for the nonleptonic decay modes, where only the NLO corrections were known completely before 2024 [9, 10, 11, 12, 13]. In Ref. [14], rough approximations of the NNLO nonleptonic contributions were made, however they can not be used for phenomenological analysis. Since the bottom quark decay is the numerically largest contribution to the decay width of the meson, the missing knowledge of the higher order corrections for the nonleptonic decays remains an issue.

The theoretical uncertainty is more than one order of magnitude larger than the experimental precision. Considering the total decay width of the B mesons taking into account all
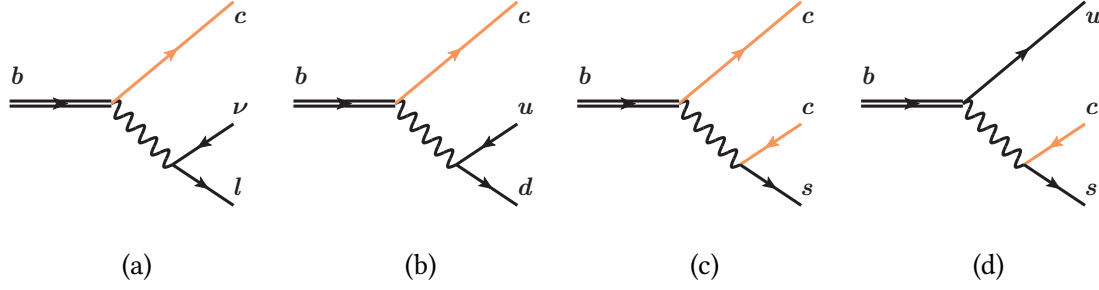
Figure 1.1.: Sample Feynman diagrams for the semileptonic (a) and nonleptonic (b), (c) and (d) decays of bottom quarks. Bottom quarks, charm quarks and massless particles are drawn as double black, orange and single black lines respectively.

known contributions yields theoretical predictions with uncertainties of around 20% [15]:

$$\Gamma(B^+) = \left(0.576^{+0.107}_{-0.067}\right) \text{ ps}^{-1},$$
$$\Gamma(B_d) = \left(0.627^{+0.110}_{-0.070}\right) \text{ ps}^{-1},$$
$$\Gamma(B_s) = \left(0.625^{+0.110}_{-0.071}\right) \text{ ps}^{-1}. \tag{1.2}$$

The uncertainty on the total decay width is mainly dominated by the uncertainty due to missing higher orders and is expected to be reduced once higher-order QCD corrections are included, in particular to the free b-quark decay.

Besides the total decay rate also the lifetime ratios of B meson decays are interesting and important observables. These ratios has the advantage that the prefactor of the total decay width,

$$\Gamma_0 = \frac{G_F^2 m_b^5 |V_{cb}|^2}{192\pi^3}, \tag{1.3}$$

cancels out, which would otherwise introduce a strong dependence on the heavy quark mass, m_b^5. In addition to this, since the main contribution to the decay width induced by the bottom quark decay contributes equally to every B meson, the lifetime ratios are more sensitive to subleading HQE corrections.

In recent publications, the theoretical analyses mainly focused on these lifetime ratios and very good agreement between experimental data [1]

$$\left.\frac{\tau(B^+)}{\tau(B_d)}\right|_{\text{exp}} = 1.076(4),$$
$$\left.\frac{\tau(B_s)}{\tau(B_d)}\right|_{\text{exp}} = 1.0032(32), \tag{1.4}$$

and theoretical prediction via the HQE [15, 17] [1]

$$\left.\frac{\tau(B^+)}{\tau(B_d)}\right|_{\text{HQE}} = 1.086(22),$$

---

[1]The numerical values obtained for the lifetime ratios strongly depend on the non-perturbative input parameters, for example the operator matrix element of the Darwin operator. The two scenarios A and B show the results for two different sets of input parameters, see Ref. [15] for more details.

$$\left.\frac{\tau(B_s)}{\tau(B_d)}\right|_{\text{HQE}} = \begin{cases} 1.028(11) & \text{Scenario A} \\ 1.003(6) & \text{Scenario B} \end{cases} \tag{1.5}$$

is observed. The theoretical predictions for the lifetime ratios are characterized by the higher order operator contributions in the HQE and a theoretical uncertainty of the order of per-cent is obtained.

The next step in the analyses of B mesons is the calculation of the NNLO QCD corrections to the nonleptonic bottom quark decays, which will reduce the theoretical uncertainty on the total decay width significantly . This is the main goal of this thesis.

In our calculation, we take into account finite bottom and charm quark masses. We consider contributions from the effective $\Delta B = 1$ current-current operators. Calculating the NNLO corrections to the nonleptonic decays introduces physical final states with up to five particles of which up to four can be massive. Processes like these are most conveniently calculated using the optical theorem that translates the complicated phase space integrals into diagrams of two point functions with, in the case of these NNLO corrections, up to four loops. The calculation of these four loop diagrams itself introduces several subtleties that have to be addressed. In order to be consistent with operator bases used in previous calculations, we have to use Fierz identities and adjust the evanescent operators appearing in multiloop calculations. Furthermore, the calculation of the four loop integrals appearing in the calculation of the Feynman diagrams is highly non-trivial and requires the usage of modern techniques.

The structure of this thesis is as follows: First we introduce in Chapter 2 the framework used for the calculation of the B meson decay width. In particular, we introduce in detail two possible operator bases. In Chapter 3, the methods used for the calculation of master integrals are described in detail. Afterwards, the calculation of the semileptonic bottom quark decay is discussed in Chapter 4 and the results are compared to the literature. This calculation serves as a benchmark and cross check for our calculation setup. Chapter 5 constitutes the main part of this thesis, where the nonleptonic bottom quark decays are calculated. The calculations performed in this part are more involved than the for semileptonic decays. In particular, we have to determine a consistent basis of the evanescent operators and the corresponding renormalization constants. Further details about the renormalization constants are also given in Appendix C. In Chapter 6, several renormalization schemes for the charm and bottom quark masses are introduced and the behaviour of the NNLO predictions is investigated. Finally, in Chapter 7 the new QCD corrections are used to update the theoretical prediction of B meson observables.

2. Heavy Quark Expansion

The decays of bottom quarks inside B mesons via the weak interaction link two energy scales: The scale $\mu = O(M_W)$ where the weak interaction takes place and the scale $\mu \leq O(\text{GeV})$ of the strong interactions that bind the meson together. The description of such weak decay processes are conveniently carried out in an effective theory framework, in which we perform an Operator Produkt Expansion (OPE) [18, 19, 20, 21]. This effective theory is matched to the Standard Model at the scale of the weak decay and is used to do the calculation at the scale of the hadronic energy scale. The OPE splits the full physical problem into two separated parts, the long-distance contributions described by the operator matrix element and the short-distance contributions described by the Wilson coefficients.

The first step towards the effective theory is to consider the decay of a quark, in this case a bottom quark, via the weak interaction into three other quarks. As an example, the decay into the three quarks c, $\overline{u}$ and d is considered in the following. In the Standard Model, such a process is described by the amplitude

$$A = -\frac{G_F}{\sqrt{2}} V_{cb}^* V_{ud} \left(\overline{c}\gamma^{\mu_1} P_L b\right) \frac{\left(g_{\mu_1\mu_2} - \frac{p_{\mu_1}p_{\mu_2}}{M_W^2}\right)}{p^2 - M_W^2} \left(\overline{d}\gamma^{\mu_2} P_L u\right), \tag{2.1}$$

where $P_L = (1 - \gamma_5)/2$ is the left-handed projector, M_W denotes the mass of the W-boson, p its momentum and $\overline{c}, b, \overline{d}, u$ the spinors of the four different quarks. Since the momentum transfer via the W-boson is small compared to its mass, this process can be approximately described by expanding in p^2/M_W^2 yielding

$$A = \frac{G_F}{\sqrt{2}} V_{cb}^* V_{ud} \left(\overline{c}\gamma^{\mu_1} P_L b\right) \left(\overline{d}\gamma_{\mu_1} P_L u\right) + O\left(\frac{p^2}{M_W^2}\right). \tag{2.2}$$

The same expression can also be obtained by considering the effective Hamiltonian

$$\mathcal{H}_{\text{eff}} = \frac{G_F}{\sqrt{2}} V_{cb}^* V_{ud} (\overline{c}\gamma^{\mu_1} P_L b)(\overline{d}\gamma_{\mu_1} P_L u) + \text{higher order operators}. \tag{2.3}$$

where the higher order operators correspond to the terms in $O\left(p^2/M_W^2\right)$. In this effective theory, the W boson is not a physical degree of freedom anymore. Taking into account QCD effects as illustrated in Figure 2.1, this effective Hamiltonian has to be modified to be

$$\mathcal{H}_{\text{eff}} = \frac{G_F}{\sqrt{2}} V_{cb}^* V_{ud} \left[C_1(\mu)O_1 + C_2(\mu)O_2\right] + \text{higher order operators}, \tag{2.4}$$

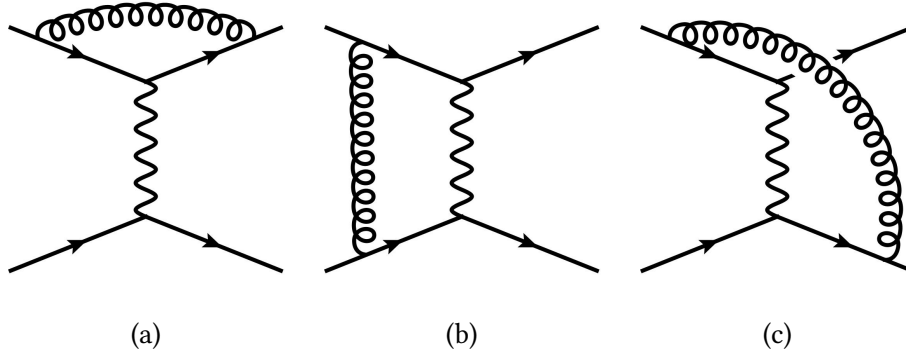(a)   (b)   (c)

Figure 2.1.: Feynman diagrams with gluon corrections that lead to the two different effective operators.

where

$$O_1 = (\bar{c}^\alpha \gamma^{\mu_1} P_L b^\beta)(\bar{d}^\beta \gamma_{\mu_1} P_L u^\alpha) , \tag{2.5}$$

$$O_2 = (\bar{c}^\alpha \gamma^{\mu_1} P_L b^\alpha)(\bar{d}^\beta \gamma_{\mu_1} P_L u^\beta) . \tag{2.6}$$

While for the diagram in Figure 2.1 (a), the colour structure is the same as for the operator in Equation (2.3), in diagram (b) and (c) where the gluons connect both fermion lines, both operators are needed to account for the complete colour structure. The functions $C_1(\mu)$ and $C_2(\mu)$ are the Wilson coefficients of the four-quark operators. The Wilson coefficients are determined by requiring that the effective theory with the Hamiltonian given above and the full theory with a physical W boson produce the same result for physical amplitudes at a certain scale, in this case at $\mu = M_W$. This so-called matching of effective and full theory allows us to determine the matching coefficients as perturbative expansions in α_s by considering the same amplitude in the effective and full theory to the same order in QCD.

2.1. Evanescent operators

As described in Ref. [22], it is necessary to include so-called evanescent operators in loop calculations that are performed in such an effective operator setup. The existence of these evanescent operators stems from the fact that we work in $d \neq 4$ dimensions and therefore the Dirac matrices are no four dimensional but d dimensional objects. In $d = 4$ dimensions, it is always possible to reduce every combination of Dirac matrices to a linear combination of 16 bilinear covariants

$$\{ 1, \gamma^\mu, \gamma_5, \sigma^{\mu\nu}, \gamma_5 \gamma^\nu \} . \tag{2.7}$$

However, this can not be done when working in an arbitrary dimension d. Consider for example the insertion of the operator O_2 given in Equation (2.6) into a four point function as shown in Figure 2.2 (a). This Feynman diagram consists of two separate spin lines, of which both carry one γ^μ from the operator insertion. Going to higher loop orders of this

diagram, meaning adding gluons as shown in Figure 2.2 (b), increases the number of Dirac matrices on each fermion line. For example at one loop order, one obtains

$$(\overline{c}^\alpha \gamma^{\mu_1} \gamma^{\mu_2} \gamma^{\mu_3} P_L b^\alpha)(\overline{d}^\beta \gamma_{\mu_1} \gamma_{\mu_2} \gamma_{\mu_3} P_L u^\beta) \,. \tag{2.8}$$

Considering this expression in $d = 4$ dimensions, it would be possible to reduce the number of Dirac matrices to one on each spin line and the structure given above could be mapped to the effective operator O_2. However, this is not possible for arbitrary dimension d. In d dimensions, the structure in Equation (2.8) is independent of O_2 and has to be treated as part of an independent operator. This independent operator reads

$$E_2 = (\overline{c}^\alpha \gamma^{\mu_1} \gamma^{\mu_2} \gamma^{\mu_3} P_L b^\alpha)(\overline{d}^\beta \gamma_{\mu_1} \gamma_{\mu_2} \gamma_{\mu_3} P_L u^\beta) - 16(\overline{c}^\alpha \gamma^{\mu_1} P_L b^\alpha)(\overline{d}^\beta \gamma_{\mu_1} P_L u^\beta) \,, \tag{2.9}$$

where the second term in its definition ensures that $\langle E_2 \rangle = 0$ in the limit $d \to 4$. This property of the operator E_2 is needed in order to avoid redundancy in the operator basis in the limit of four dimensions. Operators that are introduced in the same way as E_2 operator are called evanescent operators.

The condition of vanishing matrix elements of evanescent operators in four dimensions implies that the matrix elements of such operators are of the order of ϵ^1 or higher:

$$\langle E_2 \rangle = O(\epsilon) \,. \tag{2.10}$$

It is important to note that the definition of E_2 in Equation (2.9) is not unique. This means that we are free to add arbitrary terms that do not violate the condition in Equation (2.10), for example

$$\begin{aligned} E_2 = &(\overline{c}^\alpha \gamma^{\mu_1} \gamma^{\mu_2} \gamma^{\mu_3} P_L b^\alpha)(\overline{d}^\beta \gamma_{\mu_1} \gamma_{\mu_2} \gamma_{\mu_3} P_L u^\beta) - 16(\overline{c}^\alpha \gamma^{\mu_1} P_L b^\alpha)(\overline{d}^\beta \gamma_{\mu_1} P_L u^\beta) \\ &+ \sum_{n>0} A_n \epsilon^n (\overline{c}^\alpha \gamma^{\mu_1} P_L b^\alpha)(\overline{d}^\beta \gamma_{\mu_1} P_L u^\beta) \,, \end{aligned} \tag{2.11}$$

with arbitrary coefficients A_n. As mentioned above, the need for evanescent operators stems from the growing number of Dirac matrices that appear in higher-order loop calculations. This also implies that the number of evanescent operators has to grow with the number of loops.

2.2. Operator basis

The decay of B mesons are conveniently described in the framework of the HQE. The two dominating decay modes of the meson can be classified as the semileptonic (SL) and nonleptonic (NL) modes. Therefore the effective Hamiltonian we have to consider reads [23]

$$\mathcal{H}_{\text{eff}} = \mathcal{H}_{\text{eff}}^{\text{NL}} + \mathcal{H}_{\text{eff}}^{\text{SL}} + \mathcal{H}_{\text{eff}}^{\text{rare}} \,. \tag{2.12}$$
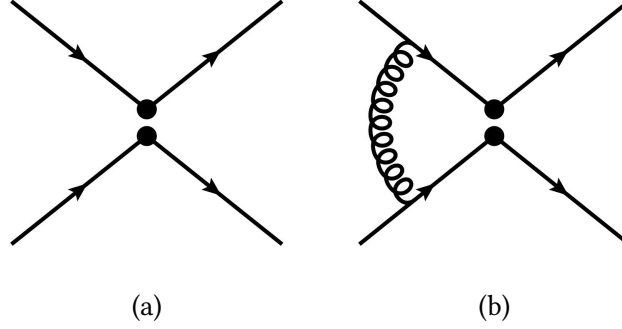
(a)   (b)

Figure 2.2.: Sample diagrams for four-quark operator insertions at LO (a) and NLO (b). The number of Dirac matrices γ^μ on each spin line increases with the number of loops.

The effective Hamiltonian for the semileptonic decay mode only consists of one four-fermion $\Delta B = 1$ operator structure that is given by

$$\mathcal{H}^{\mathrm{SL}}_{\mathrm{eff}} = \sum_{q_1=u,c} \sum_{l=e,\mu,\tau} O^{q_1 l}_{\mathrm{SL}} + \mathrm{h.c.} \tag{2.13}$$

with

$$O^{q_1 l}_{\mathrm{SL}} = (\bar{q}_1 \gamma^\mu P_L b)(\bar{l}\gamma_\mu P_L \nu). \tag{2.14}$$

For the nonleptonic decays, the effective Hamiltonian reads

$$\mathcal{H}^{\mathrm{NL}}_{\mathrm{eff}} = \frac{4G_F}{\sqrt{2}} \left[\sum_{q_{1,3}=u,c} \sum_{q_2=d,s} \lambda_{q_1 q_2 q_3} \left(C_1(\mu_b) O^{q_1 q_2 q_3}_1 + C_2(\mu_b) O^{q_1 q_2 q_3}_2 \right) \right.$$

$$\left. - \sum_{q_1=d,s} \sum_{i=3,4,5,6,8} \lambda_{q_1} C_i(\mu_b) O^{q_1}_i \right] + \mathrm{h.c.}, \tag{2.15}$$

where the effective four-fermion $\Delta B = 1$ operators $O^{q_1 q_2 q_3}_i$ with $i \in \{1, 2\}$ describe the interaction of the four quarks $\{b, q_1, q_2, q_3\}$. The $\lambda_{q_1 q_2 q_3} = V^*_{q_1 b} V_{q_2 q_3}$ and $\lambda_{q_1} = V^*_{tb} V_{tq_1}$ denote the corresponding CKM factor. Since the quark content of these two so-called current-current operators are always given by these four quarks, we omit the label $q_1 q_2 q_3$ in the definition of the operators in the following chapters and refer to them as O_1 and O_2 instead. The operators O_i with $i \in \{3, 4, 5, 6\}$ denote the penguin operators that couple the b-q_1 quark line to an arbitrary quark-antiquark pair. Note that the definition of the operators in the effective Hamiltonian shown in Equation (2.15) is not unique but depends on the choice of basis. The two most common operator bases are the `CMM` and the `historical` operator basis which will be discussed in the following sections.

2.2.1. Historical basis

Throughout most parts of this thesis, the so-called historical basis for the four-quark operators is used. The two current-current operators O_1 and O_2 in this basis read [22, 23,

24, 25]

$$O_1^{q_1q_2q_3} = (\overline{q}_1^{\alpha}\gamma^{\mu}P_L b^{\beta})(\overline{q}_2^{\beta}\gamma_{\mu}P_L q_3^{\alpha}),$$
$$O_2^{q_1q_2q_3} = (\overline{q}_1^{\alpha}\gamma^{\mu}P_L b^{\alpha})(\overline{q}_2^{\beta}\gamma_{\mu}P_L q_3^{\beta}),$$

(2.16)

while the penguin operators O_3 to O_6 and the chromomagnetic operator O_8 are given by

$$O_3^{q_1} = (\overline{q}_1^{\alpha}\gamma^{\mu}P_L b^{\alpha}) \sum_q (\overline{q}^{\beta}\gamma_{\mu}P_L q^{\beta}),$$

$$O_4^{q_1} = (\overline{q}_1^{\alpha}\gamma^{\mu}P_L b^{\beta}) \sum_q (\overline{q}^{\beta}\gamma_{\mu}P_L q^{\alpha}),$$

$$O_5^{q_1} = (\overline{q}_1^{\alpha}\gamma^{\mu_1}P_L b^{\alpha}) \sum_q (\overline{q}^{\beta}\gamma_{\mu_1}P_R q^{\beta}),$$

$$O_6^{q_1} = (\overline{q}_1^{\alpha}\gamma^{\mu_1}P_L b^{\beta}) \sum_q (\overline{q}^{\beta}\gamma_{\mu_1}P_R q^{\alpha}),$$

$$O_8 = \frac{g_s}{16\pi^2} m_b \overline{s}^{\alpha}\sigma^{\mu\nu}P_R T_{\alpha\beta}^a b^{\beta} G_{\mu\nu}^a,$$

(2.17)

where α and β denote $SU(3)$ colour indices, $\sigma^{\mu\nu} = i[\gamma^{\mu},\gamma^{\nu}]/2$. The QCD filed strength tensor is defined by [26]

$$G_{\mu\nu}^a = \partial_{\mu}G_{\nu}^a - \partial_{\nu}G_{\mu}^a + g_s f^{abc}G_{\mu}^a G_{\nu}^b,$$

(2.18)

with the strong coupling constant g_s and the structure constants f^{abc}. The sum over q in the definition of the penguin operators $O_{3,\ldots,6}$ in Equation (2.17) runs over all quark flavours. The evanescent operators of the current-current operators at first and second order are given by

$$E_1^{(1)\,q_1q_2q_3} = (\overline{q}_1^{\alpha}\gamma^{\mu_1\mu_2\mu_3}P_L b^{\beta})(\overline{q}_2^{\beta}\gamma_{\mu_1\mu_2\mu_3}P_L q_3^{\alpha}) - (16-4\epsilon)O_1^{q_1q_2q_3},$$
$$E_2^{(1)\,q_1q_2q_3} = (\overline{q}_1^{\alpha}\gamma^{\mu_1\mu_2\mu_3}P_L b^{\alpha})(\overline{q}_2^{\beta}\gamma_{\mu_1\mu_2\mu_3}P_L q_3^{\beta}) - (16-4\epsilon)O_2^{q_1q_2q_3},$$
$$E_1^{(2)\,q_1q_2q_3} = (\overline{q}_1^{\alpha}\gamma^{\mu_1\ldots\mu_5}P_L b^{\beta})(\overline{q}_2^{\beta}\gamma_{\mu_1\ldots\mu_5}P_L q_3^{\alpha}) - (256-224\epsilon)O_1^{q_1q_2q_3},$$
$$E_2^{(2)\,q_1q_2q_3} = (\overline{q}_1^{\alpha}\gamma^{\mu_1\ldots\mu_5}P_L b^{\alpha})(\overline{q}_2^{\beta}\gamma_{\mu_1\ldots\mu_5}P_L q_3^{\beta}) - (256-224\epsilon)O_2^{q_1q_2q_3}.$$

(2.19)

Where $\gamma^{\mu_1\ldots\mu_5} = \gamma^{\mu_1\mu_2\mu_3\mu_4\mu_5} = \gamma^{\mu_1}\gamma^{\mu_2}\gamma^{\mu_3}\gamma^{\mu_4}\gamma^{\mu_5}$ is used to render the expressions more compact. It is important to note the structure of the evanescent operators. They are built out of higher order Dirac structures and the physical operator with the corresponding colour structure multiplied by a linear combination of powers of ϵ. The term of the order ϵ^0 multiplied with the physical operator ensures that the evanescent operator vanishes in $d = 4$ dimensions, as motivated above. Its value is fixed by this requirement and can therefore not be changed. The remaining terms with higher powers in ϵ are needed to ensure special symmetry relations. The coefficients at $O(\epsilon)$ are known in the literature. However, it is in principle possible (and necessary at NNLO) to add terms of the physical operators multiplied with higher powers of ϵ. They are introduced as free parameters in the definition of the evanescent operators at a later stage of this work and determined in a

way to ensure Fierz symmetry up to NNLO. For a detailed description see Chapter 5.1.3.
For the penguin operators, the first and second order evanescent operators read

$$E_3^{(1)\,q_1} = (\overline{q}_1^\alpha \gamma^{\mu_1\mu_2\mu_3} P_L b^\alpha) \sum_q (\overline{q}^\beta \gamma_{\mu_1\mu_2\mu_3} P_L q^\beta) - (16 - 4\epsilon)\, O_3^{q_1}\,,$$

$$E_4^{(1)\,q_1} = (\overline{q}_1^\alpha \gamma^{\mu_1\mu_2\mu_3} P_L b^\beta) \sum_q (\overline{q}^\beta \gamma_{\mu_1\mu_2\mu_3} P_L q^\alpha) - (16 - 4\epsilon)\, O_4^{q_1}\,,$$

$$E_5^{(1)\,q_1} = (\overline{q}_1^\alpha \gamma^{\mu_1\mu_2\mu_3} P_L b^\alpha) \sum_q (\overline{q}^\beta \gamma_{\mu_1\mu_2\mu_3} P_R q^\beta) - (4 + 4\epsilon)\, O_5^{q_1}\,,$$

$$E_6^{(1)\,q_1} = (\overline{q}_1^\alpha \gamma^{\mu_1\mu_2\mu_3} P_L b^\beta) \sum_q (\overline{q}^\beta \gamma_{\mu_1\mu_2\mu_3} P_R q^\alpha) - (4 + 4\epsilon)\, O_6^{q_1}\,,$$

$$E_3^{(2)\,q_1} = (\overline{q}_1^\alpha \gamma^{\mu_1\dots\mu_5} P_L b^\alpha) \sum_q (\overline{q}^\beta \gamma_{\mu_1\dots\mu_5} P_L q^\beta) - (256 - 224\epsilon)\, O_3^{q_1}\,,$$

$$E_4^{(2)\,q_1} = (\overline{q}_1^\alpha \gamma^{\mu_1\dots\mu_5} P_L b^\beta) \sum_q (\overline{q}^\beta \gamma_{\mu_1\dots\mu_5} P_L q^\alpha) - (256 - 224\epsilon)\, O_4^{q_1}\,,$$

$$E_5^{(2)\,q_1} = (\overline{q}_1^\alpha \gamma^{\mu_1\dots\mu_7} P_L b^\alpha) \sum_q (\overline{q}^\beta \gamma_{\mu_1\dots\mu_7} P_R q^\beta) - (16 + 128\epsilon)\, O_5^{q_1}\,,$$

$$E_6^{(2)\,q_1} = (\overline{q}_1^\alpha \gamma^{\mu_1\dots\mu_7} P_L b^\beta) \sum_q (\overline{q}^\beta \gamma_{\mu_1\dots\mu_7} P_R q^\alpha) - (16 + 128\epsilon)\, O_6^{q_1}\,. \tag{2.20}$$

In later stages of this thesis, also the third and fourth order evanescent operators of the
current-current operators are needed. They are given by

$$E_1^{(3)\,q_1q_2q_3} = (\overline{q}_1^\alpha \gamma^{\mu_1\dots\mu_7} P_L b^\beta)(\overline{q}_2^\alpha \gamma_{\mu_1\dots\mu_7} P_L q_3^\beta) - (4096 - 7680\epsilon) O_1^{q_1q_2q_3}\,,$$

$$E_2^{(3)\,q_1q_2q_3} = (\overline{q}_1^\alpha \gamma^{\mu_1\dots\mu_7} P_L b^\alpha)(\overline{q}_2^\beta \gamma_{\mu_1\dots\mu_7} P_L q_3^\beta) - (4096 - 7680\epsilon) O_2^{q_1q_2q_3}\,,$$

$$E_1^{(4)\,q_1q_2q_3} = (\overline{q}_1^\alpha \gamma^{\mu_1\dots\mu_9} P_L b^\beta)(\overline{q}_2^\alpha \gamma_{\mu_1\dots\mu_9} P_L q_3^\beta) - (65536 - 176128\epsilon) O_1^{q_1q_2q_3}\,,$$

$$E_2^{(4)\,q_1q_2q_3} = (\overline{q}_1^\alpha \gamma^{\mu_1\dots\mu_9} P_L b^\alpha)(\overline{q}_2^\beta \gamma_{\mu_1\dots\mu_9} P_L q_3^\beta) - (65536 - 176128\epsilon) O_2^{q_1q_2q_3}\,. \tag{2.21}$$

2.2.2. CMM basis

The CMM basis is constructed in a way to use anti-commuting γ_5 consistently at any loop
order [27]. This is, however, not possible for all physical problems. In order to keep the
notation for operators and bases unambiguous, we denote all operators in the historical
basis as O_i and $E_i^{(j)}$ and all operators in the CMM basis as O_i' and $E_i'^{(j)}$. The current-current
operators in the CMM basis read

$$O_1'^{\,q_1q_2q_3} = (\overline{q}_1^\alpha T_{\alpha\beta}^a \gamma^\mu P_L b^\beta)(\overline{q}_2^\gamma T_{\gamma\delta}^a \gamma_\mu P_L q_3^\delta)$$
$$= (\overline{q}_1 T^a \gamma^\mu P_L b)(\overline{q}_2 T^a \gamma_\mu P_L q_3)\,,$$
$$O_2'^{\,q_1q_2q_3} = (\overline{q}_1^\alpha \gamma^\mu P_L b^\alpha)(\overline{q}_2^\beta \gamma_\mu P_L q_3^\beta)$$
$$= (\overline{q}_1 \gamma^\mu P_L b)(\overline{q}_2 \gamma_\mu P_L q_3)\,. \tag{2.22}$$

In the following, the colour indices of the quarks are not shown explicitly for the CMM
operators. One observes that the operator O_2' corresponds exactly to the operator O_2 given

in Equation (2.16), whereas the operator O_1' now contains two generators of the SU(3), T^a. In fact, the two bases are related via linear transformations which are discussed in detail in the following Section 2.2.3.

The penguin operators in the CMM basis are given by

$$O_3'^{q_1} = (\overline{q}_1 \gamma^\mu P_L b) \sum_q (\overline{q} \gamma_\mu q) \,,$$

$$O_4'^{q_1} = (\overline{q}_1 \gamma^\mu T^a P_L b) \sum_q (\overline{q} \gamma_\mu T^a q) \,,$$

$$O_5'^{q_1} = (\overline{q}_1 \gamma^{\mu_1 \mu_2 \mu_3} P_L b) \sum_q (\overline{q} \gamma_{\mu_1 \mu_2 \mu_3} q) \,,$$

$$O_6'^{q_1} = (\overline{q}_1 \gamma^{\mu_1 \mu_2 \mu_3} T^a P_L b) \sum_q (\overline{q} \gamma_{\mu_1 \mu_2 \mu_3} T^a q) \,,$$

$$O_8 = \frac{g_s}{16\pi^2} m_b \overline{s} \sigma^{\mu\nu} P_R T^a b G_{\mu\nu}^a \,, \tag{2.23}$$

where the sum runs over all possible quark flavours q. Note that the definition of the operator O_8 is the same in both bases. The first and second order evanescent operators for the current-current operators are given by

$$E_1'^{(1)\, q_1 q_2 q_3} = (\overline{q}_1 \gamma^{\mu_1 \mu_2 \mu_3} T^a P_L b) (\overline{q}_2 \gamma_{\mu_1 \mu_2 \mu_3} T^a P_L q_3) - 16 O_1'^{q_1 q_2 q_3} \,,$$

$$E_2'^{(1)\, q_1 q_2 q_3} = (\overline{q}_1 \gamma^{\mu_1 \mu_2 \mu_3} P_L b) (\overline{q}_2 \gamma_{\mu_1 \mu_2 \mu_3} P_L q_3) - 16 O_2'^{q_1 q_2 q_3} \,,$$

$$E_1'^{(2)\, q_1 q_2 q_3} = (\overline{q}_1 \gamma^{\mu_1 \dots \mu_5} T^a P_L b) (\overline{q}_2 \gamma_{\mu_1 \dots \mu_5} T^a P_L q_3) - 256 O_1'^{q_1 q_2 q_3} - 20 E_1'^{(1)\, q_1 q_2 q_3} \,,$$

$$E_2'^{(2)\, q_1 q_2 q_3} = (\overline{q}_1 \gamma^{\mu_1 \dots \mu_5} P_L b) (\overline{q}_2 \gamma_{\mu_1 \dots \mu_5} P_L q_3) - 256 O_2'^{q_1 q_2 q_3} - 20 E_2'^{(1)\, q_1 q_2 q_3} \,. \tag{2.24}$$

The evanescent operators of first and second order for the penguin operators in Equation (2.23) read

$$E_3'^{(1)\, q_1} = (\overline{q}_1 \gamma^{\mu_1 \dots \mu_5} P_L b) \sum_q (\overline{q} \gamma_{\mu_1 \dots \mu_5} q) + 64 O_3'^{q_1} - 20 O_5'^{q_1} \,,$$

$$E_4'^{(1)\, q_1} = (\overline{q}_1 \gamma^{\mu_1 \dots \mu_5} T^a P_L b) \sum_q (\overline{q} \gamma_{\mu_1 \dots \mu_5} T^a q) + 64 O_4'^{q_1} - 20 O_6'^{q_1} \,,$$

$$E_3'^{(2)\, q_1} = (\overline{q}_1 \gamma^{\mu_1 \dots \mu_7} P_L b) \sum_q (\overline{q} \gamma_{\mu_1 \dots \mu_7} q) + 1280 O_3'^{q_1} - 336 O_5'^{q_1} \,,$$

$$E_4'^{(2)\, q_1} = (\overline{q}_1 \gamma^{\mu_1 \dots \mu_7} T^a P_L b) \sum_q (\overline{q} \gamma_{\mu_1 \dots \mu_7} T^a q) + 1280 O_4'^{q_1} - 336 O_6'^{q_1} \,. \tag{2.25}$$

For the calculations performed in this thesis, the historical basis is used. However, the CMM basis definition are used to determine the anomalous dimension matrix of the historical basis by transforming its CMM counterpart from one basis to the other. For the calculation of the two loop renormalization constants in the CMM basis and for their transformation the the historical basis, also the evanescent operators of the current-current operators O_1' and O_2' at third and fourth order are needed

$$E_1'^{(3)\, q_1 q_2 q_3} = (\overline{q}_1 \gamma^{\mu_1 \dots \mu_7} T^a P_L b)(\overline{q}_2 \gamma_{\mu_1 \dots \mu_7} T^a P_L q_3) - 4096 O_1'^{q_1 q_2 q_3} - 336 E_1'^{(1)\, q_1 q_2 q_3} \,,$$

$$E_2'^{(3)\,q_1q_2q_3} = (\bar{q}_1\gamma^{\mu_1...\mu_7}P_Lb)(\bar{q}_2\gamma_{\mu_1...\mu_7}P_Lq_3) - 4096O_2'^{q_1q_2q_3} - 336E_2'^{(1)\,q_1q_2q_3},$$

$$E_1'^{(4)\,q_1q_2q_3} = (\bar{q}_1\gamma^{\mu_1...\mu_9}T^aP_Lb)(\bar{q}_2\gamma_{\mu_1...\mu_9}T^aP_Lq_3) - 65536O_1'^{q_1q_2q_3} - 5440E_1'^{(1)\,q_1q_2q_3},$$

$$E_2'^{(4)\,q_1q_2q_3} = (\bar{q}_1\gamma^{\mu_1...\mu_9}P_Lb)(\bar{q}_2\gamma_{\mu_1...\mu_9}P_Lq_3) - 65536O_2'^{q_1q_2q_3} - 5440E_2'^{(1)\,q_1q_2q_3}. \qquad (2.26)$$

The two bases introduced in the last two Section are connected via linear transformations. This procedure is described in the next section.

2.2.3. Basis change

The operator definition in the historical and the CMM basis is linked by the property of the Gell-Mann matrices

$$T^a_{\alpha\beta}T^a_{\gamma\delta} = \frac{1}{2}\left(\delta_{\alpha\delta}\delta_{\gamma\beta} - \frac{1}{n_c}\delta_{\alpha\beta}\delta_{\gamma\delta}\right). \qquad (2.27)$$

Inserting this relation into Eq (2.22), we obtain

$$
\begin{aligned}
O_1' &= (\bar{q}_1T^a\gamma^\mu P_Lb)(\bar{q}_2T^a\gamma_\mu P_Lq_3) = (\bar{q}_1^\alpha T^a_{\alpha\beta}\gamma^\mu P_Lb^\beta)(\bar{q}_2^\gamma T^a_{\gamma\delta}\gamma_\mu P_Lq_3^\delta) \\
&= \frac{1}{2}(\bar{q}_1^\alpha\gamma^\mu P_Lb^\beta)(\bar{q}_2^\gamma\gamma_\mu P_Lq_3^\delta)\delta_{\alpha\delta}\delta_{\gamma\beta} - \frac{1}{2n_c}(\bar{q}_1^\alpha\gamma^\mu P_Lb^\beta)(\bar{q}_2^\gamma\gamma_\mu P_Lq_3^\delta)\delta_{\alpha\beta}\delta_{\gamma\delta} \\
&= \frac{1}{2}(\bar{q}_1^\alpha\gamma^\mu P_Lb^\beta)(\bar{q}_2^\beta\gamma_\mu P_Lq_3^\alpha) - \frac{1}{2n_c}(\bar{q}_1^\alpha\gamma^\mu P_Lb^\alpha)(\bar{q}_2^\delta\gamma_\mu P_Lq_3^\delta) \\
&= \frac{1}{2}O_1 - \frac{1}{2n_c}O_2 = \frac{1}{2}O_1 - \frac{1}{6}O_2.
\end{aligned} \qquad (2.28)
$$

Since $O_2' = O_2$ we can write down the linear transformation

$$\begin{pmatrix} O_1' \\ O_2' \end{pmatrix} = \begin{pmatrix} \frac{1}{2} & -\frac{1}{2n_c} \\ 0 & 1 \end{pmatrix} \cdot \begin{pmatrix} O_1 \\ O_2 \end{pmatrix} = R^{-1} \cdot \begin{pmatrix} O_1 \\ O_2 \end{pmatrix}, \qquad (2.29)$$

where the transformation matrix is introduced as R^{-1} to be consistent with [27, 28, 29]. Inverting this relation to find the transformation from the CMM to the traditional basis then yields

$$\begin{pmatrix} O_1 \\ O_2 \end{pmatrix} = R \cdot \begin{pmatrix} O_1' \\ O_2' \end{pmatrix} = \begin{pmatrix} 2 & \frac{1}{3} \\ 0 & 1 \end{pmatrix} \cdot \begin{pmatrix} O_1' \\ O_2' \end{pmatrix}, \qquad (2.30)$$

where $n_c = 3$ is set. For the two current-current operators, the relations between the two bases are quite simple. To obtain the full transformation for all operators defined above, we follow the general procedure outlined in Ref. [27] which consists of several steps. Let us first consider a basis of physical operators o_i and evanescent operators $e_i^{(n)}$ (lowercase letters are used to distinguish these toy operators from the operator definitions above). In a first step, the physical operators are modified by adding linear combinations of evanescent operators:

$$o_i' = o_i + \sum_k W_{ik}e_k^{(n)}, \qquad\qquad e_k'^{(n)} = e_k^{(n)}. \qquad (2.31)$$

In a second step, terms of physical operators multiplied with powers of ϵ are added to the evanescent operators. In this case, these additional terms contain up to quadratic powers in ϵ:

$$o_i'' = o_i' \qquad e_k''^{(n)} = e_k'^{(n)} + \epsilon \sum_j U_{kj} o_j' + \epsilon^2 \sum_j V_{kj} o_j' \,. \tag{2.32}$$

In principle, the ϵ-power of the additional terms that are added to the evanescent operators in Equation (2.32) can be arbitrary high. Since our calculations go up to NNLO, we have to include terms with power of 2.

In a last step, the double primed operators are rotated to

$$o_i''' = R_{ij} \left(o_j + \sum_k W_{jk} e_k^{(n)} \right), \qquad e_k'''^{(n)} = M_{kl} \left(e_l'^{(n)} + \epsilon \sum_j U_{lj} o_j' + \epsilon^2 \sum_j V_{lj} o_j' \right). \tag{2.33}$$

Following this transformation scheme, the matrices R, M, W, U and V for the transformation from CMM to the historical basis can be obtained. In this case, the CMM operators in Equations (2.22), (2.23) and (2.24) take the role of the operators o_i and $e_k^{(n)}$ while the historical basis operators in Equations (2.16), (2.17), (2.19) correspond to the triple primed operators in the scheme above:

$$\vec{O} = R \left(\vec{O}' + W \vec{E}' \right),$$
$$\vec{E} = M \left(\left(\epsilon U \vec{O} + \epsilon^2 V \right) \vec{O} + \left(1 + \epsilon U W + \epsilon^2 V W \right) \vec{E}' \right). \tag{2.34}$$

In the calculations outlined in the following chapters, we focus on the current-current operators. Since the penguin operators are absent in most part of the calculation (if not mentioned explicitly), it is useful to consider only the subset of current-current operators, including evanescent operators of first, second and third order. This means, we consider in the CMM basis the two current-current operators and the six corresponding evanescent operators up to third order

$$\vec{O}' = \{O_1', O_2'\},$$
$$\vec{E}' = \{E_1'^{(1)}, E_2'^{(1)}, E_1'^{(2)}, E_2'^{(2)}, E_1'^{(3)}, E_2'^{(3)}\}, \tag{2.35}$$

and transform to the historical basis with the operators

$$\vec{O} = \{O_1, O_2\},$$
$$\vec{E} = \{E_1^{(1)}, E_2^{(1)}, E_1^{(2)}, E_2^{(2)}, E_1^{(3)}, E_2^{(3)}\}. \tag{2.36}$$

The corresponding set of the transformation matrices R, M and U that link the operator definitions given in Equations (2.22), (2.24), (2.26), (2.16), (2.19) and (2.21) are all obtained by the application of Equation (2.27). They read:

$$R = \begin{pmatrix} 2 & \frac{1}{3} \\ 0 & 1 \end{pmatrix}, \qquad U = \begin{pmatrix} 4 & 0 \\ 0 & 4 \\ 144 & 0 \\ 0 & 144 \\ 6336 & 0 \\ 0 & 6336 \end{pmatrix},$$

$$
M = \begin{pmatrix}
2 & \frac{1}{3} & 0 & 0 & 0 & 0 \\
0 & 1 & 0 & 0 & 0 & 0 \\
40 & \frac{20}{3} & 2 & \frac{1}{3} & 0 & 0 \\
0 & 20 & 0 & 1 & 0 & 0 \\
672 & 112 & 0 & 0 & 2 & \frac{1}{3} \\
0 & 336 & 0 & 0 & 0 & 1
\end{pmatrix} .
\tag{2.37}
$$

Note that for the operators considered in this subset, all entries of W are zero. Also the values of the matrix V are all zero here since the evanescent operators in Equations (2.24), (2.26), (2.19) and (2.21) only include terms proportional to ϵ^1. However, the matrix V will be relevant for the calculation of NNLO corrections where the definitions of the evanescent operators have to be redefined. The details of this calculation is outlined in Section 5.1.3. The entries of the matrix W will remain zero for the calculations including only current-current operators. However, we will encounter non-vanishing entries of W once the penguin operators are included in the transformation, see Appendix C.4.

2.3. Decay width of B mesons

In the previous sections, the effective Hamiltonian $\mathcal{H}_{\text{eff}}$ of the HQE was outlined and described. Using this effective Hamiltonian, the decay width of a B meson can be obtained by integrating the squared transition amplitude over the phase space

$$
\Gamma(B) = \frac{1}{2m_B} \sum_X \int \mathrm{dPS} \, (2\pi)^4 \, \delta^{(4)} \left(p_B - p_X \right) \left| \langle X(p_x) | \mathcal{H}_{\text{eff}} | B(p_B) \rangle \right|^2 ,
\tag{2.38}
$$

where m_B and p_B denote mass and four-momentum of the B meson and X all possible final states into which the meson can decay. The calculation of the decay width using Equation (2.38) includes the explicit calculation of the final states phase space. At NNLO, considering massive charm quarks, this means that phase space integrals over up to five particles, of which up to four can be massive, have to be computed. This phase space integration can be avoided by using the optical theorem, relating the decay width to the discontinuity of the forward scattering matrix element with the time ordered double insertion of the effective Hamiltonian:

$$
\Gamma(B) = \frac{1}{m_B} \mathrm{Im} \left[\langle B | \int \mathrm{d}^4 x \, T \left\{ \mathcal{H}_{\text{eff}}(x), \mathcal{H}_{\text{eff}}(0) \right\} | B \rangle \right]
$$
$$
= \frac{1}{m_B} \mathrm{Im} \left[\mathcal{M}(B \to B) \right] .
\tag{2.39}
$$

Since the bottom quark is relatively heavy compared to the typical hadronic scale, $m_b \gg \Lambda_{\text{QCD}}$, this expression of the decay width can be rewritten in the HQE. In a first step, the momentum of the bottom quark is parametrised via

$$
p_b^\mu = m_b v^\mu + k^\mu,
\tag{2.40}
$$

where $v^\mu = p_B^\mu / m_B$ denotes the four-velocity of the meson. The remaining part of the momentum $k^\mu \propto \Lambda_{\text{QCD}}$ includes non-perturbative interactions of the bottom quark with

the light particles inside the meson. By splitting the momentum of the bottom quarks, the quark field can be reparametrised by

$$b(x) = \exp\left(-im_b v \cdot x\right) b_v(x), \tag{2.41}$$

where the main contribution of the momentum is factored out, leaving a slowly oscillating field $b_v(x)$. Considering the covariant derivative of the bottom quark field using the reparametrisation above, one obtains one large term proportional to the bottom mass m_b and an additional term proportional to k and therefore proportional to Λ_{QCD}:

$$D_\mu b(x) = \exp\left(-im_b v \cdot x\right)\left(-im_b v_\mu + D_\mu\right) b_v(x). \tag{2.42}$$

Using this ansatz, the expression for the decay width in Equation (2.39) can be written as

$$\Gamma(B) = \Gamma_3 + \Gamma_5 \frac{\langle O_5 \rangle}{m_b^2} + \Gamma_6 \frac{\langle O_6 \rangle}{m_b^3} + \cdots + 16\pi^2 \left(\tilde{\Gamma}_6 \frac{\langle \tilde{O}_6 \rangle}{m_b^3} + \tilde{\Gamma}_7 \frac{\langle \tilde{O}_7 \rangle}{m_b^4} \right), \tag{2.43}$$

where $\langle O_i \rangle = \langle B|O_i|B\rangle/(2m_B)$. The Γ_i denote the short distance functions and are computed perturbatively:

$$\Gamma_i = \Gamma_i^{(0)} + \frac{\alpha_s}{4\pi}\Gamma_i^{(1)} + \left(\frac{\alpha_s}{4\pi}\right)^2 \Gamma_i^{(2)} + O\left(\alpha_s^3\right). \tag{2.44}$$

The $\langle O_i \rangle$ and $\langle \tilde{O}_i \rangle$ in Equation (2.43) denote the matrix elements of the effective $\Delta B = 0$ operators where the two quark operators are denoted with O_i and the four-quark operators are given by $\tilde{O}_i$. Since the four-quark operators $\tilde{O}_i$ are induced by loop-enhanced diagrams, it has become convention to introduce them with an additional factor of $16\pi^2$. In Figure 2.3 (adapted from Ref. [15]), a visualization of the decay width given above is shown.

In the following, the different contributions to Equation (2.43) are discussed in detail. An overview over the current status of the calculation of the short distance effects can be found in Table 2.1.

- Γ_3:

   As can be seen in the left-most diagram in Figure 2.3, Γ_3 only describes the decay of the B mesons bottom quark and in contrast to the other operators, it does not include interactions between the bottom and the spectator quark. Therefore, in order to compute only Γ_3, Equation (2.39) can be modified to

$$\Gamma_3 = \Gamma(b) = \frac{1}{m_b}\text{Im}\left[\mathcal{M}\left(b \rightarrow b\right)\right], \tag{2.45}$$

   which corresponds to the calculation of the imaginary part of two-point functions with insertion of two four-quark operators. Γ_3 has no suppression of Λ_{QCD}/m_b and is therefore the numerically dominant contribution to the total decay width $\Gamma(B)$. For the semileptonic contributions to Γ_3, NLO [2], NNLO [3, 4, 5] and even N³LO [6, 8] corrections are known.
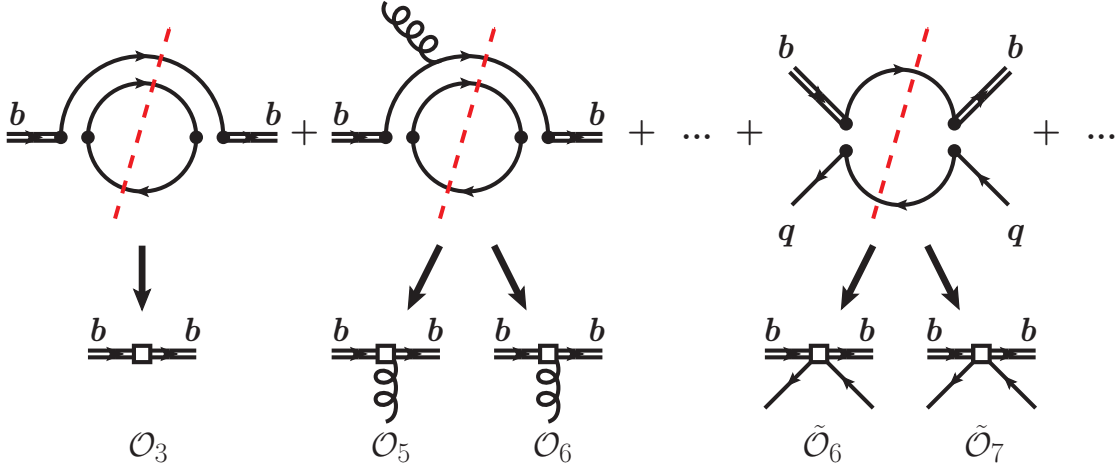
Figure 2.3.: Diagrammatic visualization of the total decay width of a B meson in the HQE. The dots denote the insertion of the $\Delta B = 1$ operators of the effective Hamiltonian given in Equation (2.15). The squares denote the $\Delta B = 0$ operators O_i and $\tilde{O}_i$ in Equation (2.43). Bottom quarks are drawn as double black lines. The first diagram on the left corresponds to the first term Γ_3 induced by O_3. The second diagram gives rise to O_5 and O_6. The right-most diagram produces the four-quark operators $\tilde{O}_6$ and $\tilde{O}_7$. In the case of O_3, O_5 and O_6 the spectator quarks are not shown.

For nonleptonic decays, considering the decay of the bottom quark into three arbitrary quarks, $b \to q_1 \bar{q}_2 q_3$, we obtain from Equation (2.45)

$$\Gamma_3^{q_1 q_2 q_3}(\rho) = \frac{1}{m_b} \sum_{i,j=1,2} \left(\frac{4 G_F |\lambda_{q_1 q_2 q_3}|}{\sqrt{2}} \right)^2$$

$$C_i^\dagger(\mu_b) C_j(\mu_b) \, \mathrm{Im} \left[i \int \mathrm{d}^4 x e^{iqx} \langle b | T \left\{ O_i^{\dagger \, q_1 q_2 q_3}(x) O_j^{q_1 q_2 q_3}(0) \right\} | b \rangle \bigg|_{q^2 = m_b^2} \right],$$

$$(2.46)$$

where only the insertion of the current-current operators O_1 and O_2 are considered. In principle we also have to include the penguin operators O_3 to O_6 in addition to the current-current operators. The decay width can then be written as

$$\Gamma_3^{\mathrm{NL}} = \Gamma_3^{\mathrm{NL},\, C-C} + \Gamma_3^{\mathrm{NL},\, C-P} + \Gamma_3^{\mathrm{NL}\, P-P}. \qquad (2.47)$$

However, since the Wilson coefficients of the penguin operators are small compared to the Wilson coefficients of O_1 and O_2, they are often considered as higher order corrections in the literature, meaning each insertion of a penguin operator enters the α_s power counting with an extra order [30, 31]. This means that $\Gamma_3^{\mathrm{NL},\, C-P}$ with no additional gluon attached would be treated as $O(\alpha_s)$ and $\Gamma_3^{\mathrm{NL},\, P-P}$ as order $O(\alpha_s^2)$. In this work, we do not want to apply this counting but work with a consistent

power counting in α_s. However, due to the smallness of the penguin operator Wilson coefficients and the fact that they do not contribute to all nonleptonic decays but only to the ones where two quarks of the same flavour are produced in the final state such as $b \to c\bar{c}s$ and $b \to u\bar{u}d$, we focus on the current-current operators. In the following, if not mentioned explicitly, the penguin operators are not considered and we assume $\Gamma_3^{\mathrm{NL}} = \Gamma_3^{\mathrm{NL}, C-C}$.

The NLO corrections to Γ_3^{NL} have been obtained in Refs. [32, 9, 11, 33, 12, 13, 30, 31]. While the accuracy for the semileptonic case already reaches N³LO, for the nonleptonic contributions only partial results at NNLO have been determined in Ref. [14]. They are carried out in full QCD without using the effective Hamiltonian and assuming massless quarks in the final state. Because of this, the precision of the nonleptonic decay modes are limited by the NLO contributions [9, 10, 11, 12, 13]. The main goal of this thesis is the calculation of the NNLO corrections to the nonleptonic decays, $\Gamma_3^{\mathrm{NL}\,(2)}$ [34].

- Γ_5:
  The two-quark operator contribution at order $1/m_b^2$ can be divided into two parts

$$\Gamma_5 \frac{\langle O_5 \rangle}{m_b^2} = \Gamma_0 \left[c_\pi \frac{\langle O_\pi \rangle}{m_b^2} + c_G \frac{\langle O_G \rangle}{m_b^2} \right], \tag{2.48}$$

where O_π denotes the kinetic operator

$$\langle O_\pi \rangle = \langle B | \bar{b}_v \left(iD_\mu \right)^2 \left(iD^\mu \right) b_v | B \rangle = -2m_B \mu_\pi^2(B), \tag{2.49}$$

and O_G the chromomagnetic operator

$$\langle O_G \rangle = \langle B | \bar{b}_v \left(iD_\mu \right) \left(iD_\nu \right) \left(-i\sigma^{\mu\nu} \right) b_v | B \rangle = 2m_B \mu_G^2(B). \tag{2.50}$$

The field b_v corresponds to the field in the reparametrisation of the bottom quark field in Equation (2.41). The coefficient c_π of the kinetic operator is related to the coefficient Γ_3, $c_\pi^{(i)} = -\Gamma_3^{(i)}/2$. The coefficients of the chromomagnetic operator c_G for the nonleptonic decay channels are known at LO [35, 36, 37] and also NLO are known partially [38], however the NLO contribution for the final state including two charm quarks is not known yet. For the semileptonic decays, the LO [39, 40] as well as the NLO [41, 42, 43] results for these coefficients are known.

- Γ_6:
  At order $1/m_b^3$, the operator O_6 contains the Darwin operator whose matrix element is defined in the following way:

$$\langle O_6 \rangle = \langle B | \bar{b}_v \left(iD_\mu \right) \left(iv \cdot D \right) \left(iD^\mu \right) b_v | B \rangle = 2m_B \rho_D^3(B). \tag{2.51}$$

For the Darwin operator, the situation is similar to the $1/m_b^2$ operators: For the semileptonic decay width, the QCD corrections are known at LO [44] and NLO [45, 46], while for the nonleptonic decay only LO coefficients have been calculated [47, 48, 49]. It is interesting to note, that the coefficients of the Darwin operator are about one order larger than the coefficients of the $1/m_b^2$ operators, due to an accidental suppression of the latter [47, 15].
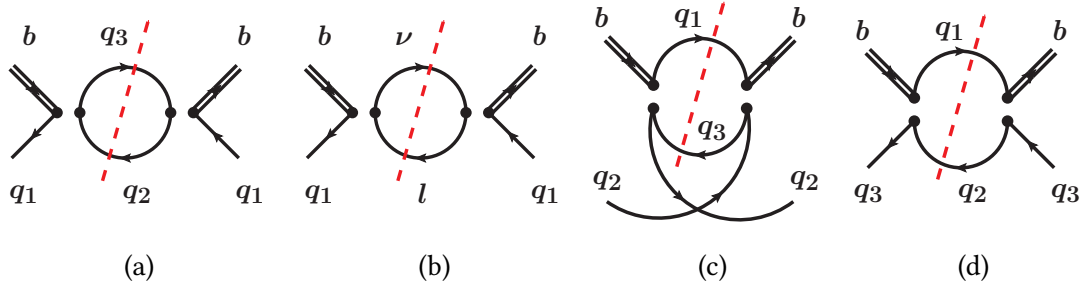
Figure 2.4.: Diagrams showing the three different topologies for the discontinuity: The weak annihilation (a) and (b), the Pauli interference (c) and the weak-exchange (d). The corresponding contributions in Equations (2.52) and (2.53) are labeled by WA, PI and WE respectively.

- $\tilde{\Gamma}_6$ and $\tilde{\Gamma}_7$:

  The four-quark operator contributions denoted by $\tilde{\Gamma}_6$ and $\tilde{\Gamma}_7$ are not considered in detail in this thesis, however we list them here for completeness. The corresponding diagram that shows how to obtain these four-quark operators can be found in Figure 2.3. The contributions to $\tilde{\Gamma}_6$ can be written in the following form

$$16\pi^2\tilde{\Gamma}_6 \frac{\langle \tilde{O}_6 \rangle}{m_b^3} = \Gamma_0 \sum_{i=1}^{4} \left[A_{i,q_1q_2}^{\mathrm{WE}} \frac{\langle \tilde{O}_i^{q_3} \rangle}{m_b^3} + A_{i,q_1q_3}^{\mathrm{PI}} \frac{\langle \tilde{O}_i^{q_2} \rangle}{m_b^3} + A_{i,q_2q_3}^{\mathrm{WA}} \frac{\langle \tilde{O}_i^{q_1} \rangle}{m_b^3} + A_{i,q_1l}^{\mathrm{WA}} \frac{\langle \tilde{O}_i^{q_1} \rangle}{m_b^3} \right],$$

(2.52)

where $A_{i,q_1q_2}^{\mathrm{WE}}$ and $A_{i,q_1q_3}^{\mathrm{PI}}$ denote the different topologies for weak exchange (WE) and Pauli interference (PI) while A_{i,q_1l}^{WA} and $A_{i,q_2q_3}^{\mathrm{WA}}$ represent the weak annihilation (WA). The corresponding Feynman diagrams can be found in Figure 2.4. The coefficients A are known up to NLO for nonleptonic and semileptonic decays [50, 51]. Note that these four-quark operator contributions are the first where the short distance coefficients depend on the spectator quark of the meson and therefore vary for different mesons B_q.

At order $1/m_b^4$, the $\tilde{\Gamma}_7$ contribution can be written as

$$16\pi^2\tilde{\Gamma}_7 \frac{\langle \tilde{O}_7 \rangle}{m_b^4} = \Gamma_0 \sum_{i=1}^{1} 8 \left[B_{i,q_1q_2}^{\mathrm{WE}} \frac{\langle \tilde{P}_i^{q_3} \rangle}{m_b^4} + B_{i,q_1q_3}^{\mathrm{PI}} \frac{\langle \tilde{P}_i^{q_2} \rangle}{m_b^4} + B_{i,q_2q_3}^{\mathrm{WA}} \frac{\langle \tilde{P}_i^{q_1} \rangle}{m_b^4} + B_{i,q_1l}^{\mathrm{WA}} \frac{\langle \tilde{P}_i^{q_1} \rangle}{m_b^4} \right].$$

(2.53)

The four-quark operators at this order can be found for example in [15]. For this contribution, only the LO coefficients are known [52, 53, 51].

For the calculation of the contributions to the decay width starting from order $1/m_b^2$, in addition to the perturbative quantities Γ_i and $\tilde{\Gamma}_i$, non-perturbative input is needed for the matrix elements $\langle O_i \rangle$ and $\langle \tilde{O}_i \rangle$. These matrix elements account for the hadronic effects. For example, for the matrix elements involving two-quark operators the kinetic and chromomagnetic terms, the values for these matrix elements can be extracted from global

$\Gamma_3^{\mathrm{SL},(1)}$	[2]	$\Gamma_3^{\mathrm{NL},(1)}$	[32, 9, 11, 33, 12, 13, 30, 31]
$\Gamma_3^{\mathrm{SL},(2)}$	[3, 4, 5]	$\Gamma_3^{\mathrm{NL},(2)}$	incomplete [14]
$\Gamma_3^{\mathrm{SL},(3)}$	[6, 7, 8]	$\Gamma_3^{\mathrm{NL},(3)}$	-
$\Gamma_5^{\mathrm{SL},(0)}$	[39, 40]	$\Gamma_5^{\mathrm{NL},(0)}$	[35, 36, 37]
$\Gamma_5^{\mathrm{SL},(1)}$	[41, 42, 43]	$\Gamma_5^{\mathrm{NL},(1)}$	$b \to c\bar{u}d$ [38], $b \to c\bar{c}s$ missing
$\Gamma_6^{\mathrm{SL},(0)}$	[44]	$\Gamma_6^{\mathrm{NL},(0)}$	[47, 48, 49]
$\Gamma_6^{\mathrm{SL},(1)}$	[45, 46]	$\Gamma_6^{\mathrm{NL},(1)}$	-
$\tilde{\Gamma}_6^{\mathrm{SL},(0)}$	[61]	$\tilde{\Gamma}_6^{\mathrm{NL},(0)}$	[62]
$\tilde{\Gamma}_6^{\mathrm{SL},(1)}$	[51]	$\tilde{\Gamma}_6^{\mathrm{NL},(1)}$	[63]
$\Gamma_7^{\mathrm{SL},(0)}$	[52, 53, 51]	$\Gamma_7^{\mathrm{NL},(0)}$	-
$\Gamma_8^{\mathrm{SL},(0)}$	[64]	$\Gamma_8^{\mathrm{NL},(0)}$	-

Table 2.1.: Literature overview of the short distance contributions to semileptonic and nonleptonic B meson decays.

fits of the $B \to X_c l \bar{\nu}_l$ decays [54, 55]. For the numerical values of the four-quark operator matrix elements, calculations performed on the lattice [56, 57] or estimates exploiting HQET sum rules [58, 59, 60] are used.

In the following chapters, the calculation of Γ_3 for both, semileptonic and nonleptonic decays, up to NNLO is described. The starting point for these calculations is the optical theorem given in Equation (2.45) which translates the phase space integration to loop integrals. The methods that are used to calculate these loop integrals are described in the next chapter.

3. Calculation of loop integrals

The Feynman diagrams that have to be calculated in calculations outlined in this thesis include integrals over several loop momenta, starting from two loop integrals at LO up to four loops at NNLO. The number of loops is related to the fact that we use the optical theorem in Equation (2.39). This means that the LO calculation is already a two loop calculation. However, only the imaginary part of the corresponding loop integrals is needed.

The occurring integrals are functions of two arguments, ϵ, the parameter of dimensional regularization, and the two quark masses m_c and m_b. However, by dimensional analysis, we can factor out an overall factor of m_b^n and only use the mass ratio $\rho = m_c/m_b$, which reduces the number of arguments to two. Two different methods for the integral calculation are used here, both will be described in detail in this chapter. In the first approach which is outlined in Section 3.1, exact analytic results for the master integrals in terms of iterated integrals are computed using the differential equation of the master integrals. This solution provides the opportunity to evaluate the result numerically at every arbitrary value of ρ. In this ansatz, there are two possible bottlenecks: Finding the solutions of the master integrals via the differential equation and computing the boundary conditions. In the calculations outlined here, the boundary conditions are the critical point. As it will be shown in Section 3.2, the most simplest boundary from a computational point of view is the limit $\rho = 1$, which implies neglecting several physical final states at NNLO. In cases like this, the second approach, known as `expand and match` [65, 66, 67], turns out to be very useful. In this method, analytic expansions of the integrals with highly precise numerical coefficients are obtained by solving the differential equation and matching to numerical boundary conditions. The application of the `expand and match` method is possible for all problems discussed in this thesis, while we were only able to find a fully analytic solution in LO and NLO calculations and the NNLO semileptonic decays.

Both approaches rely on the differential equation of the master integrals. These equations are obtained by using IBP relations, in this work the program `Kira` is used for this. Since the integrals, except for ϵ, only depend on one variable, the mass ratio $\rho = m_c/m_b$, it is a natural choice to set up the differential equation in this variable. The derivative of an integral with at a charm propagator with respect to ρ, raises the index of the charm propagator by one. Consider for example a loop integral with exactly one charm propagator:

$$
\begin{aligned}
\frac{\mathrm{d}}{\mathrm{d}\rho} I\left(\vec{n}\right) &= \frac{\mathrm{d}}{\mathrm{d}\rho} \int \frac{\mathrm{d}k_1 \mathrm{d}k_2 \dots}{\dots \left(\rho^2 - k_1^2\right)^{n_i} \dots} \\
&= -2\rho n_i \int \frac{\mathrm{d}k_1 \mathrm{d}k_2 \dots}{\dots \left(\rho^2 - k_1^2\right)^{n_i+1} \dots} = -2\rho n_i I\left(\dots, n_i+1, \dots\right),
\end{aligned}
\tag{3.1}
$$

where we have set $m_b = 1$. In general, the integral on the right-hand side with the raised index $n_i + 1$ is not a master integral but can be reduced to the set of original master integrals by applying IBP relations. For a system of N master integrals in a vector $\vec{I}$, we apply the derivative $d/d\rho$ to $\vec{I}$ and subsequently use IBP relations to ensure that on the right-hand-side only elements of $\vec{I}$ appear. Then we arrive at a closed set of differential equations of the form

$$\frac{\mathrm{d}\vec{I}}{\mathrm{d}\rho} = A\left(\epsilon, \rho\right) \cdot \vec{I}, \tag{3.2}$$

where $A(\epsilon, \rho)$ is a $N \times N$ matrix. This set of differential equations serves as starting point for the calculation of the integrals in both approaches mentioned above.

3.1. Analytic solutions with differential equations

In this section the calculation of an exact analytic solution of the master integrals is described. The starting point is the differential equation in equation (3.2). In this equation, the matrix $A(\epsilon, \rho)$ has no specific form and can include numerators and denominators with polynomials of arbitrary power in ϵ and ρ. In a first step, the basis of master integrals is chosen in a way that the denominators in the differential equation factorize in ϵ and ρ. This can be done using the Mathematica package ImproveMasters [68], see Appendix A.3. In the following, we will refer to a basis of integrals that fulfil this requirement as a good basis. After a good basis is found, it is convenient to transform the differential equation to a special form, the so-called canonical or ϵ-form [69, 70, 71]. Finding such a transformation is not always possible and strongly depends on the structure of the differential equation and the letters of the iterated integrals that solve these equations. For a more detailed description on the algorithm to obtain the ϵ-form, see Appendix B.2. Assuming a transformation to ϵ-form can be found, the integrals $\vec{I}$ are transformed by

$$\vec{I} = T \cdot \vec{J}, \tag{3.3}$$

in a way that the differential equation takes the form

$$\frac{\mathrm{d}\vec{J}}{\mathrm{d}\rho} = \epsilon \cdot \tilde{A}\left(\rho\right) \cdot \vec{J}. \tag{3.4}$$

In the basis $\vec{J}$, the differential equation now has a form where the matrix $\tilde{A}$ only depends on the mass ratio ρ and ϵ only appears as a global prefactor. This special form of the differential equation is called ϵ-form or canonical form. We can further rewrite Equation (3.4) in the form

$$\frac{\mathrm{d}\vec{J}}{\mathrm{d}\rho} = \epsilon \cdot \sum_{l=1}^{N_l} \tilde{A}_l \frac{1}{L_l(\rho)} \cdot \vec{J}. \tag{3.5}$$

The functions $L_l(\rho)$ are called letters of the differential equation and define the class of iterated integrals that solve the differential equation, see also Appendix B.4. To find the

transformation to ϵ-form we use the `Mathematica` packages `Libra` [72] and `Canonica` [73] together. In a first step, we bring the differential equation matrix to a lower block triangular form

$$
A = \begin{pmatrix}
A_{11} & 0 & \cdots & 0 \\
A_{21} & A_{22} & \cdots & 0 \\
\vdots & \vdots & \ddots & \vdots \\
A_{n1} & A_{n2} & \cdots & A_{nn}
\end{pmatrix},
\tag{3.6}
$$

using `Libra` and its build-in functions. The A_{ii} in Equation (3.6) are quadratic matrices. Finding the transformation to ϵ-form with `Libra` gets very tedious with growing numbers of master integrals. Instead of `Libra` we use `Canonica` for this step and transform the matrix given in Equation 3.6 block by block starting from the top left in the order A_{11}, A_{22}, A_{21}, A_{33}, ..., A_{nn}.

After the system of differential equations is brought to ϵ-form, it can now be solved for the integrals $\vec{J}$ by inserting a series ansatz in ϵ for the integrals:

$$
\vec{J} = \frac{\vec{j}_{-4}}{\epsilon^4} + \frac{\vec{j}_{-3}}{\epsilon^3} + \frac{\vec{j}_{-2}}{\epsilon^2} + \frac{\vec{j}_{-1}}{\epsilon} + \vec{j}_0 + \vec{j}_1 \epsilon + \vec{j}_2 \epsilon^2 + O\left(\epsilon^3\right),
\tag{3.7}
$$

where $\vec{j}_i$ are functions of ρ. For our applications, the master integrals have at n-loop at most ϵ^{-n} poles. The integrals now have to be determined by calculating the coefficients $\vec{j}_i$. Inserting the ansatz into the differential equation in canonical form and considering every occurring order in ϵ separately, the following equations are obtained:

$$
\frac{d\vec{j}_{-4}}{d\rho} = 0,
$$

$$
\frac{d\vec{j}_{-3}}{d\rho} = \tilde{A}(\rho) \cdot \vec{j}_{-4},
$$

$$
\frac{d\vec{j}_{-2}}{d\rho} = \tilde{A}(\rho) \cdot \vec{j}_{-3}, \dots
\tag{3.8}
$$

These differential equations can now be solved one after the other starting with the lowest index, in this case -4. The equation for $\vec{j}_{-4}$ is solved trivially by a constant vector $\vec{c}_{-4}$. Because of the factor ϵ in Equation (3.4), the derivative of $\vec{j}_{-3}$ is proportional to $\vec{j}_{-4} = \vec{c}_{-4}$ and therefore the solution for $\vec{j}_{-3}$ is obtained by the integral over $\tilde{A} \cdot \vec{c}_{-4}$ plus an integration constant $\vec{c}_{-3}$. In the same manner, all the following $\vec{j}_i$ can be expressed as integrals over $\vec{j}_{i-1}$ and by inserting all the previously obtained results for the lower case j's, the solutions are given in terms of iterated integrals over constants and the matrix $\tilde{A}$:

$$
\vec{j}_{-4} = \vec{c}_{-4},
$$

$$
\vec{j}_{-3} = \vec{c}_{-3} + \int^{\rho} d\rho' \tilde{A}(\rho') \cdot \vec{c}_{-4},
$$

$$
\vec{j}_{-2} = \vec{c}_{-2} + \int^{\rho} d\rho' \tilde{A}(\rho') \cdot \vec{c}_{-3} + \int^{\rho} d\rho' \tilde{A}(\rho') \cdot \int^{\rho'} d\rho'' \tilde{A}(\rho'') \cdot \vec{c}_{-4}, \dots
\tag{3.9}
$$

The iterated integrals that appear in such solutions can often be expressed in terms of special functions like Harmonic Polylogarithms [74], see Appendix B for more details. The last step is the calculation of the integration constants. This is done by considering a limit in which the values of the integrals are known or can be calculated. In the problems considered in this work, the limit $\rho = m_c/m_b \to 1$ turns out to be a suitable point for the calculation of asymptotic expansions of the master integrals. This procedure is outlined in detail in the next Section 3.2. The values of the integrals in the boundary limits are then matched to the expressions calculated above:

$$\vec{I}(\rho = 1) = \lim_{\rho \to 1} \left(T \cdot \vec{J}(\vec{c}_i) \right) . \tag{3.10}$$

These relations lead to a system of equations which can be solved for $\vec{c}_i$.

As an alternative approach to the ϵ-form, we decouple the coupled system of differential equations and then solve the higher order differential equations separately [75]. This is done in practice using the `Mathematica` package `OreSys` [76] that depends on `Sigma.m` [77]. The starting point of this approach is the untransformed differential equation (3.2). We insert an expansion in ϵ for the master integrals $\vec{I}$, similar to Equation (3.7):

$$\vec{I} = \frac{\vec{i}_{-4}}{\epsilon^4} + \frac{\vec{i}_{-3}}{\epsilon^3} + \frac{\vec{i}_{-2}}{\epsilon^2} + \frac{\vec{i}_{-1}}{\epsilon} + \vec{i}_0 + \vec{i}_1 \epsilon + \vec{i}_2 \epsilon^2 + O\left(\epsilon^3\right) , \tag{3.11}$$

where all $\vec{i}_n$ are functions of ρ. After inserting the ansatz, we consider every ϵ order of the differential equation separately. Starting from the lowest ϵ order, we decouple the differential equation for the components of $\vec{i}_n$ using `OreSys`. Decoupling a m-dimensional set of first order differential equations leads to a set of uncoupled differential equations, which can also be of higher order than one, and a set of linear equations for the m components of $\vec{i}_n$. Using the decoupled equations, we find the solution of $\vec{i}_n$ as a functions of the iterated integrals with the help of `HarmonicSums` [78]. These solutions include undetermined coefficients that can be calculated by matching to boundary conditions of the integrals, similar to the determination of the integration constants in the previous approach. An explicit example of this procedure is shown in Appendix B.3.

3.2. Analytic boundary conditions

In the previous section it is described how the analytic solution to a differential equation of master integrals can be found. After this procedure, the obtained result consists of iterated integrals and undetermined integration constants. In the calculation presented in this work, asymptotic expansions [79] of the master integrals are calculated which serve as boundary condition to fix these integration constants. This is described in the following. The asymptotic expansions are calculated in the limit of heavy charm masses $\rho = m_c/m_b \to 1$. In this limit, the method of regions [79, 80] leads to two possible scalings of the loop momenta k^μ, which we name hard (h) and ultrasoft (us):

- (h): $|k^\mu| \sim m_b$,

- (us): $|k^\mu| \sim \delta m_b$,

where $\delta = 1 - m_c^2/m_b^2$. Since we are dealing with two, three and four loop momenta integrals at LO, NLO and NNLO, there are four, eight and sixteen different momentum regions which can contribute to the asymptotic expansion. The full result of the expansion is obtained by summing the results of all regions. In principle, it would also be possible to perform the expansion around $\rho = 0$. However, in this limit, significantly more regions contribute. Furthermore, more complicated integrals have to be considered, see for example Ref. [3, 4], where this approach has been applied to the NNLO corrections of the semileptonic decay rate.

In our calculation, we use the `Mathematica` package `asy.m` [81, 82]. It can be used to find the momentum regions of an integral which have non-zero contributions (non-zero in this case can also mean zero imaginary part and non-zero real part) and the scalings of the propagators in this regions. However, it does not show the regions nor the corresponding momentum routings.

`asy.m` is used to discard regions that are zero before expansion of regions is applied. To use it accordingly, a proper momentum routing has to be found in a first step. This means, that the scalings of the propagators should be unique to one of the possible regions. The steps to achieve this are outlined in the following:

1. In a first step, one wants to ensure that all propagators with masses also include the external momentum q. If this is not yet the case, the corresponding loop momentum k_i is shifted by q:

$$\frac{1}{\left(m_q^2 - k_1^2\right)} \xrightarrow{k_1 \to k_1 + q} \frac{1}{\left(m_q^2 - (k_1 + q)^2\right)} , \qquad (3.12)$$

where m_q can be either $\{m_b, m_c\}$. If this shift of the loop momentum is not done, the propagator would scale like $1/\delta^0$ for both, hard and ultrasoft k_1, since $m_b \sim \delta^0$ would be dominating. Since `asy.m` shows only the leading scaling of the propagators, this would mean that such a propagator would scale always with $1/\delta^0$ no matter the scaling of the momentum. After the momentum shift the propagators can be expressed by

$$\frac{1}{\left(m_b^2 - (k_1 + q)\right)} = \frac{1}{\left(-k_1^2 - 2k_1.q\right)} , \qquad (3.13)$$

$$\frac{1}{\left(m_c^2 - (k_1 + q)\right)} = \frac{1}{\left(-\delta - k_1^2 - 2k_1.q\right)} , \qquad (3.14)$$

for the two different masses. This leads to scalings $\sim 1/\delta^0$ (hard k_1) and $\sim 1/\delta^1$ (ultrasoft k_1) for both mass cases.

2. The momentum routing should be unique. Therefore the case that one loop momentum only occurs in propagators where also other loop momenta are present should be avoided. This means that there should be a propagator characterizing the

scaling of one loop momentum. Consider for example an integrand with the loop momentum k_1 flowing through only two propagators

$$\frac{1}{\left(-(k_1 + k_2)^2\right)\left(m_b^2 - (k_1 + k_3 + q)^2\right)} \, . \tag{3.15}$$

Assuming the loop momenta k_2 and k_3 to be hard in the following, the scalings of these two propagators are $\sim 1/\delta^0$ and $\sim 1/\delta^0$ regardless of the scaling of k_1. By shifting $k_1 \to k_1 - k_3$, these two propagators transform to

$$\frac{1}{\left(-(k_1 + k_2)^2\right)\left(m_b^2 - (k_1 + k_3 + q)^2\right)}$$

$$\xrightarrow{k_1 \to k_1 - k_3} \frac{1}{\left(-(k_1 + k_2 - k_3)^2\right)\left(m_b^2 - (k_1 + q)^2\right)} \, . \tag{3.16}$$

Now we observe the scalings $\sim 1/\delta^0$ and $\sim 1/\delta^0$ for hard k_1 and $\sim 1/\delta^0$ and $\sim 1/\delta^1$ for ultrasoft k_1 in the same scenario as described above are obtained.

3. The propagators should be kept as simple as possible, so we try to find possible replacements like

$$\frac{1}{\left(-(k_1 - k_2 + k_3)^2\right)\left(m_c^2 - (k_1 - k_2 + q)^2\right)\left(-k_1^2\right)}$$

$$\xrightarrow{k_1 \to k_1 + k_2} \frac{1}{\left(-(k_1 - k_3)^2\right)\left(m_c^2 - (k_1 + q)^2\right)\left(-(k_1 + k_2)^2\right)} \, . \tag{3.17}$$

After a suitable momentum routing is found, `asy.m` is applied to every master integral separately. As an input it needs the propagators appearing in the integral and the scaling of the masses and external momentum. As an output it provides the scaling of the propagators in the regions which are not zero.

For illustration, we consider the easiest integral that appears in our calculations, a two loop sunset integral with one massive charm line, as an example:

$$I = \int \int \frac{\mathrm{d}k_1 \, \mathrm{d}k_2}{\left(-k_1^2\right)\left(-k_2^2\right)\left(m_c^2 - (k_1 - k_2 + q)^2\right)} \, . \tag{3.18}$$

This integral is one of the two LO integrals of the semileptonic as well as the $b \to c\bar{u}d$ decay. Giving `asy.m` the information about the propagators, the scaling of the masses $m_b \sim \delta^0$, $m_c \sim \delta^1$ and the on-shell condition $q^2 = m_b^2$, we obtain the output

$$\{\{0, 0, 0\}, \{0, 0, 1\}\} \, , \tag{3.19}$$

which tells us that two regions are non-zero and their corresponding scaling. Considering the four possible regions of the integral given in Equation (3.18), we find the scalings shown in Table 3.1. Comparing these results to the `asy.m` result in Equation (3.19), we

k_1	k_2	propagator scaling
(h)	(h)	$\{0, 0, 0\}$
(us)	(h)	$\{-2, 0, 0\}$
(h)	(us)	$\{0, -2, 0\}$
(us)	(us)	$\{-2, -2, -1\}$

Table 3.1.: Scalings for hard and ultrasoft loop momenta. The list in the third row shows the scaling of the propagators of the sample LO integral in the same ordering as in Equation (3.18).

find that the regions $\{h, h\}$ and $\{us, us\}$ are non-zero. Out of these two regions, only the double ultrasoft region will produce a non-vanishing imaginary part.

In the calculation of the semileptonic decay to N^{3}LO [6], asy.m was only used as a cross check to make sure that all contributing regions were found. Here it is used to discard regions which are zero before the expansion is carried out. Since asy.m is applied at the level of the master integrals, it is manageable to apply this procedure to every separate integral.

Expanding propagators and calculating expanded integrals

After the non-vanishing regions are found, the momenta are rescaled and the integrand is expanded in the remaining regions. This expansion leads to new propagators and scalar products of loop momenta and/or the external momentum in the numerator, which now have to be calculated. The power of these denominators and numerators depend on the expansion depth. They are raised by one in every expansion step, for example:

$$\frac{1}{(-\delta - k_1^2 - 2q.k_1)} = \frac{1}{-\delta - 2q.k_1}\left(1 + \frac{k_1^2}{-\delta - k_1^2 - 2q.k_1}\right), \tag{3.20}$$

where k_1 is an ultrasoft loop momentum. The expansion is done separately for each integral in its (according to asy.m) non-vanishing regions.

After naively expanding the propagators, new integrals remain that have to be calculated. In order to do this, an IBP reduction to a set of master integrals is performed. This is done with the following steps:

- First, every region $((h, h, us, us), (h, us, us, us), (us, us, us, us))$ is considered separately. Not all possible regions contribute here. For example, the loop momentum of the lepton neutrino loop has to be ultrasoft since the Feynman diagram would have no imaginary part in case of a hard momentum which would correspond to on-shell integrals with no cut. For every expanded master integral, a new integral family is defined which contains the propagators encountered in the expanded integral. As a result of the expansion of the propagators, we also obtain scalar products of loop momenta and the external momentum in the numerator. They are included in the newly defined integral families as additional numerators. The integral families for the different regions are then compared and, if possible, mapped to each other in order to reduce the number of families that have to be considered in the next steps.

- Up to this point, only the occurring propagators and numerators have been included in the integral family definitions. In a next step, massless propagators with linear combination of loop and external momenta are added to complete the basis of propagators.

- After completing the basis with additional massless propagators, it can happen that these sets of propagators contain linear dependent ones. Using partial fraction decomposition, the family definitions can be adjusted such that only linear independent propagators appear in each family. For this step, the code `LIMIT` [83] has been used. This code is based on `LiteRed` [84, 85]. After the partial fractioning mappings between different families are found using the code `minimizefam.nb` which is also part of `LIMIT`.

- After the procedure described above, a minimal set of integral families is found. Each integral which contributes to the amplitude is part of one of these families. In a last step, an IBP reduction to master integrals is performed using `kira`. All integrals can be computed in terms of Γ-functions using the following relations ($q^2 = m_b^2$):

$$
I_1(n_1, n_2) = \int \frac{\mathrm{d}^d k_1}{\left(-k_1^2\right)^{n_1} \left(-(k_1 + q)^2\right)^{n_2}}
$$
$$
= i\pi^{d/2} \frac{\Gamma(n_1 + n_2 - 2 + \epsilon)\,\Gamma(2 - n_2 - \epsilon)\,\Gamma(2 - n_1 - \epsilon)}{\Gamma(n_1)\,\Gamma(n_2)\,\Gamma(4 - n_1 - n_2 - 2\epsilon)} \left(-q^2\right)^{2 - \epsilon + n_1 + n_2},
$$
$$
I_2(n_1, n_2) = \int \frac{\mathrm{d}^d k_1}{\left(-k_1^2\right)^{n_1} \left(m_b^2 - (k_1 + q)^2\right)^{n_2}}
$$
$$
= i\pi^{d/2} \frac{\Gamma(n_1 + n_2 - 2\epsilon)\,\Gamma(4 - n_2 - 2n_1 - 2\epsilon)}{\Gamma(n_2)\,\Gamma(4 - n_1 - n_2 - 2\epsilon)},
$$
$$
I_3(n_1, n_2, n_3) = \int \frac{\mathrm{d}^d k_1}{\left(-k_1^2\right)^{n_1} \left(-2q.k_1\right)^{n_2} \left(-\delta - 2q.k_1\right)^{n_3}}
$$
$$
= i\pi^{d/2} \left(-\delta\right)^{4 - 2\epsilon - 2n_1 - n_2 - n_3}
$$
$$
\frac{\Gamma(4 - 2\epsilon - 2n_1 - n_2)\,\Gamma(2 - \epsilon - n_1)\,\Gamma(2n_1 + n_2 + n_3 - 4 + 2\epsilon)}{\Gamma(n_1)\,\Gamma(n_3)\,\Gamma(4 - 2\epsilon - 2n_1)},
$$
$$
I_4(1, 1, 1) = \int \frac{\mathrm{d}^d k_1 \mathrm{d}^d k_2}{\left(m_b^2 - (k_1 + k_2)^2\right) \left(m_b^2 - k_1^2\right) \left(m_b^2 - (k_2 + q)^2\right)}
$$
$$
= \left(i\pi^{d/2}\right)^2 m_1^2 \left(\frac{\mu^2}{m_1^2}\right)^{2\epsilon} \frac{1}{2\pi i} \int_{-i\infty}^{i\infty} \mathrm{d}z
$$
$$
\frac{\Gamma(\epsilon + z)\,\Gamma^2(1 - \epsilon - z)\,\Gamma(-z)\,\Gamma(-1 + 2\epsilon + z)\,\Gamma(3 - 4\epsilon - 2z)}{\Gamma(2 - 2\epsilon - 2z)\,\Gamma(3 - 3\epsilon - z)}.
$$

$$(3.21)$$

The relations given here for integrals $I_1(n_1, n_2)$, $I_2(n_1, n_2)$ and $I_3(n_1, n_2, n_3)$ can be obtained using Feynman parameters, see Appendix B.5. For integral $I_4(1, 1, 1)$ which

corresponds to the sunset diagram with three massive lines, the result is calculated using Mellin-Barnes techniques. The integration is performed along the imaginary axis. To calculate this integral, the integration path can be closed in the complex plain and the value of the integral is obtained by picking up the enclosed poles, for the explicit calculation, see Appendix B.6. The result as an expansion in ϵ is given by

$$
I_4(1,1,1) = \left(i\pi^{d/2}\right)^2 \left[-\frac{1}{\epsilon^2} - \frac{2}{\epsilon} + \left(\frac{1}{2} - \frac{11\pi^2}{12}\right) + \left(\frac{85}{4} - \frac{17\pi^2}{24} - \frac{3\pi^2 \log 2}{2} - \frac{181\zeta(3)}{12}\right)\epsilon \right.
$$
$$
+ \left(\frac{907}{8} + \frac{373\pi^2}{48} - \frac{167\pi^4}{72} - \frac{3\pi^2 \ln 2}{4} - 3\pi^2 \log^2 2 + \frac{3\log^4 2}{2} + 36\mathrm{Li}_4(1/2)\right.
$$
$$
\left. \left. - \frac{157\zeta(3)}{24}\right)\epsilon^2 + O\left(\epsilon^3\right) \right]. \tag{3.22}
$$

After the calculation of the boundary conditions, the undetermined coefficients in the analytic solution in Equation (3.9) can be determined. To do this, the iterated integrals are expanded in the limit $\rho \to 1$ and the obtained expansion is matched to the asymptotic expansions. The expansion of the iterated integrals can be done in a convenient way using the `Mathematica` package `HarmonicSums` [78].

The exact analytic calculation, especially the calculation of the boundary conditions, can be very complicated and tedious. In this work, the boundary conditions are only calculated analytically in the limit $\rho \to 1$, since the expansion around the limit $\rho \to 0$ is much more involved. Since the calculation is also restricted to the imaginary part of the integrals, this limits the solution to the contribution of only one charm quark in the final state. This contribution is by far the dominating one in the physical region and therefore provides a very good approximation for the total decay width in the semileptonic decay channel. For a more detailed discussion about the separation and the calculation of the different contributions, see, for example, Section 4.1. For the complete contribution including all possible final states and in particular for the nonleptonic decay channels, another approach is used. In principle, it would be possible to do the calculation with the analytic approach outlined before, however we would have to calculate also the real part of the master integrals that will contribute to the imaginary part once we cross physical thresholds, see Section 3.3 for more details. A method that is capable of doing this is described in the next section.

3.3. Semianalytic results with Expand and Match

The exact analytic calculation of the master integrals as described in the previous section highly depends on the possibility to find an ϵ-form. Finding this transformation simplifies the equations a lot. As an alternative to the transformation to ϵ-form, it is also possible to decouple the system of differential equations using packages like `OreSys`, as also described above. In our case, the limiting factor of the fully analytic approach is the analytic calculation of the boundary conditions, as described in the first part of this chapter.

In this section we describe a method to compute precise analytic expansions with numerical coefficients [65, 66, 67]. This method, called `expand and match` is used for the calculation of the master integrals in the nonleptonic decay channels. As a preparation we also apply it to the semileptonic decay channel where it allows us to obtain results valid for $\rho \in [0, 1]$. Starting point for the calculation is again Equation (3.2). In contrast to the procedures described in the previous section, the differential equation does not have to be transformed to a special form. The only requirement the differential equation has to fulfil is the absence of $1/\epsilon$ poles on the diagonal. Nevertheless, let us stress that a suitable choice of the integral basis and therefore the form of $A(\epsilon, \rho)$ is very useful, especially the choice of an integral basis where ϵ and the mass ratio ρ factorize in the denominator. This leads to a simpler set of linear equations and therefore reduces the needed computational resources.

Procedure

The goal is to use the differential equation to obtain precise expansions for the master integral around properly chosen points in phase space. In a first step, an expansion point for the integrals and a suitable ansatz corresponding to this point has to be chosen. As a first example, consider a regular point of the differential equation where the integrals can be approximated by a Taylor expansion. The corresponding ansatz for integral i then reads

$$I_i(\rho, \epsilon, \rho_0) = \sum_{j=\epsilon_{\min}}^{\epsilon_{\max}} \sum_{n=0}^{n_{\max}} c_{i,j,n} \epsilon^j (\rho - \rho_0)^n \ . \tag{3.23}$$

The value inserted for $\epsilon_{\min}$ is problem depended. For all the integrals that have to be calculated in the following, it is sufficient to set $\epsilon_{\min} = -4$, since in the case of the NNLO b-decays there are at most ϵ^{-4} for the individual integrals. In case $\epsilon_{\min} > -4$ is chosen, the calculation will fail since inconsistent equations are generated in intermediate steps, see the discussion below.

The values for $n_{\max}$ and $\epsilon_{\max}$ are in principle arbitrary and depend on the needed expansion depth, where $\epsilon_{\max}$ is determined by the highest pole of the coefficient of integral i and the ϵ-poles appearing in the matrix $A(\epsilon, \rho)$. The value of $n_{\max}$ constrains the accuracy of the expansion and is set to $n_{\max} = 50$ for all calculations performed in this work.

Inserting the ansatz given in Equation (3.23) into the differential equation (3.2) leads to a system of linear equations that connect the coefficients $c_{i,j,n}$. Consider for example the differential equation for the two master integrals which appear at LO in the decay channel

with one charm quark in the final state:

$$\frac{\mathrm{d}}{\mathrm{d}\rho}\begin{pmatrix} I_1 \\ I_2 \end{pmatrix} = \begin{pmatrix} 0 & 2\rho \\ \frac{2(2-7\epsilon+6\epsilon^2)}{\rho-\rho^3} & -\frac{2(\epsilon+2\rho^2-5\epsilon\rho^2)}{\rho-\rho^3} \end{pmatrix} \cdot \begin{pmatrix} I_1 \\ I_2 \end{pmatrix}. \tag{3.24}$$

After inserting the ansatz (3.23) into Equation (3.24), we shift ρ to $\rho' = \rho + \rho_0$ and consider the coefficients of each power of ϵ and ρ' which leads to

$$c_{1,-2,1} - 2\rho_0 c_{2,-2,0} = 0,$$
$$2c_{1,-2,2} - 2c_{2,-2,0} - 2\rho_0 c_{2,-2,1} = 0,$$
$$3c_{1,-2,3} - 2c_{2,-2,1} - 2\rho_0 c_{2,-2,-2} = 0,$$
$$\dots \tag{3.25}$$

for the first row of the differential equation. Analogue equations are obtained for the second. This set of linear equations can then be solved for a small set of $c_{i,j,n}$ which have to be determined by a dedicated numerical evaluation. In our case we evaluate a neighbouring expansion and evaluate both expansions at one dedicated point. In the following this is denoted by matching. As a result, an expansion for the integrals in the form of Equation (3.23) around the expansion point ρ_0 is obtained. Every expansion has a limited radius of convergence that is determined by the singular points of the differential equation. The procedure to construct expansions that cover the whole phase space $\rho \in [0, 1]$ is the following:

1. As a starting point, a Taylor expansion ansatz around a regular point of the differential equation $\rho_0 = \rho_1$ is set up.

2. The expansion of step 1 is inserted in the differential equation, the resulting linear equations for the $c_{i,j,n}$ are solved.

3. The remaining set of coefficients $c_{i,j,n}$ are determined by matching the expansion to a numerical evaluation of the master integrals at ρ_1. This is done using the program AMFlow and is discussed in detail in Section 3.4. After this step, an expansion around ρ_1 with a radius of convergence R_1 is obtained that can be used to evaluate the master integrals in the phase space region $\rho \in [\rho_1 - R_1, \rho_1 + R_1]$.

4. Steps 1 and 2 are repeated for an expansion point $\rho_0 = \rho_2$, where $\rho_1 \neq \rho_2$.

5. The remaining set of coefficients $c_{i,j,n}$ for the expansion around ρ_2 are now determined by matching the expansion around ρ_2 to the numerical evaluation of the expansion around ρ_1 obtained in step 3 evaluated at some point ρ_3, where ρ_3 is in between ρ_1 and ρ_2. It is convenient to choose

$$\rho_3 = \frac{|\rho_1 - \rho_2|}{2}$$

6. Steps 4 and 5 are repeated until the whole phase space is covered.

Up to this point, only Taylor expansions (3.23) are discussed. When constructing expansions around singular points of the differential equation, this ansatz is however not enough. The problem of choosing the correct ansatz is addressed in the following subsection.

Different ansätze

For the singular points of the differential equation a Taylor expansion is not appropriate and a more general ansatz including logarithms and square roots has to be chosen. It has the form

$$
I_i(\rho, \epsilon, \rho_0) = \sum_{j=\epsilon_{\min}}^{\epsilon_{\max}} \sum_{m=0}^{j+|\epsilon_{\min}|} \sum_{n=n_{\min}}^{n_{\max}} c_{i,j,m,n} \, \epsilon^j \, (\rho - \rho_0)^{\frac{n}{2}} \log^m (\rho - \rho_0) \; .
\tag{3.26}
$$

There are two subtleties that should be noticed in this ansatz:

- The upper limit of the index m which sets the power of the logarithms, depends on the ϵ order j.

- The sum over n, the power of the square roots, starts at $n_{\min}$ which is usually chosen to be $n_{\min} < 0$.

Note that square roots are usually needed for expansions around thresholds. In Ref. [86] it was found that the production of n_q massive particles with mass m_q around threshold behaves like

$$
\left(s - \left(n_q m_q \right)^2 \right)^{\frac{3n_q - 5}{2}} \; ,
\tag{3.27}
$$

where s denotes the energy of the system. Therefore the expansion around the thresholds of two and four charm quarks will lead to square roots whereas for the expansion around the three charm threshold only even n terms contribute and the ansatz can be modified to

$$
I_i(\rho, \epsilon, \rho_0) = \sum_{j=-4}^{\epsilon_{\max}} \sum_{m=0}^{j+4} \sum_{n=0}^{n_{\max}} c_{i,j,m,n} \, \epsilon^j \, (\rho - \rho_0)^n \log^m (\rho - \rho_0) \; .
\tag{3.28}
$$

This simplification is in principle not necessary. The solution of the ansatz including the square roots will produce coefficients $c_{i,j,m,n}$ that are zero for uneven n and therefore automatically reproduce the ansatz in Equation (3.28). From a computational point of view it is advisable to directly use ansatz (3.28) to reduce the number of coefficients and linear equations and therefore reduce the computing time.

In addition to physical thresholds with more than one massive quark in the final state, all the differential equations considered in this work have singular points at $\rho = 0$ and $\rho = 1$. For the expansion around $\rho_0 = 0$, the ansatz in Equation (3.28) with ρ_0 can be adopted

$$
I_i(\rho, \epsilon, \rho_0 = 0) = \sum_{j=-4}^{\epsilon_{\max}} \sum_{m=0}^{j+4} \sum_{n=0}^{n_{\max}} c_{i,j,m,n} \, \epsilon^j \, \rho^n \log^m (\rho) \; ,
\tag{3.29}
$$

while for the expansion around $\rho = 1$, the sign of the argument of the logarithm is flipped to keep the logarithm real for values $\rho < 1$:

$$
I_i(\rho, \epsilon, \rho_0 = 1) = \sum_{j=-4}^{\epsilon_{\max}} \sum_{m=0}^{j+4} \sum_{n=0}^{n_{\max}} c_{i,j,m,n} \, \epsilon^j \, (1 - \rho)^n \log^m (1 - \rho) \; .
\tag{3.30}
$$

Implementation

The generation of the linear equation for the coefficients $c_{i,j,m,n}$ is done using `Mathematica` code. For the NNLO calculations, the system of equations gets very large ($> 10^6$ equations) and a solution with `Mathematica` can not be obtained in a reasonable time. Instead the usage of `kira` [87, 88] together with `firefly` [89, 90] turns out to be very convenient. In the following, a few technical remarks about the implementation are given.

- Solving the linear equations with `kira` requires to transform the `Mathematica` output to `kira` notation. This means that the coefficients $c_{i,j,m,n}$ are translated into numbers that encode the indices i, j, m, n. The linear equations are arranged in a way that a sum of the $c_{i,j,m,n}$ with corresponding prefactors equal 0. As an example, the `kira` notation for the equations given in the example above for $\rho_0 = 1/2$ are shown:

$$c_{1,-2,0,1} - c_{2,-2,0,0} = 0$$
$$\begin{aligned} 10010300001 * (1) \\ 10000300002 * (-1) \end{aligned}$$

$$2c_{1,-2,0,2} - 2c_{2,-2,0,0} - c_{2,-2,0,1} = 0 \quad \rightarrow \quad \begin{aligned} 10020300001 * (2) \\ 10000300002 * (-2) \\ 10010300002 * (-1) \end{aligned}$$

$$3c_{1,-2,0,3} - 2c_{2,-2,0,1} - c_{2,-2,0,2} = 0 \quad \begin{aligned} 10030300001 * (3) \\ 10010300002 * (-2) \\ 10020300002 * (-1) \end{aligned}$$

  Every term of a sum corresponds to one line in the `kira` notation. Equations are separated by an empty line. The encoding of the coefficients works as follows:
  The first three digits after the leading 1 denote the index n corresponding to the power of $(\rho - \rho_0)$. The next two digits represent the ϵ power j, where the index j is shifted by 4, meaning $j = -4$ would correspond to 00 and $j = 1$ to 05. The next index represents the power m of the logarithm (in this example this is always zero, corresponding to 00) and the last three digits give the integral number i.
  The encoding of the coefficients may look arbitrary, but it turns out that a definition as described here is very useful. When solving a set of linear equations, `kira` prefers smaller numbers as masters. In the encoding used here, this means that the coefficients with $n = 0$ are favoured to be chosen as masters, which is useful when matching the expansions to a numerical evaluation of the master integrals.

- In case the ansatz is not sufficient to describe the behaviour of the integrals, for example if a Taylor expansion is used at a physical threshold, the system of linear equations is inconsistent and can not be solved. In this case `kira` fails and does not produce result files. In addition to choosing the wrong ansatz, this behaviour is also observed when choosing the wrong $n_{\min}$ for the ansatz with square roots around a 2-particle or 4-particle threshold, for example not allowing for negative n.

- The accuracy of the `expand and match` approach is limited by several factors. Of course, the accuracy of the numerical results of the master integrals that are used to

determine the coefficients of the first/starting Taylor expansion gives a limit for the numerical coefficients of the expansion and the accuracy at the expansion point ρ_0. The accuracy is furthermore limited by the number of terms included in the ansatz, meaning the value of $n_{\max}$. The effect of these two limitations can be reduced by investing more computation power.

- The radius of convergence of different expansions is limited by the distance of the expansion point to the next singular point of the differential equation. This can impose numerical instabilities when the matching of a Taylor expansion close to a threshold is matched to the expansion around this threshold. It is observed that the convergence behaviour of the Taylor expansion can be improved by using Möbius transformations [91, 67]. The procedure is as follows:
  Let ρ_0 be the expansion point. The radius of convergence of this expansion is limited by the distance to the closer of the two neighbouring singular points of the differential equation ρ_{-1} and ρ_1, where $\rho_{-1} < \rho_0 < \rho_1$. By switching from the variable ρ to

$$
y = \frac{(\rho - \rho_0)\,(\rho_1 - \rho_{-1})}{(\rho - \rho_1)\,(\rho_{-1} - \rho_0) + (\rho - \rho_{-1})\,(\rho_1 - \rho_0)}\,, \tag{3.31}
$$

the points $\{\rho_{-1}, \rho_0, \rho_1\}$ are mapped to $\{-1, 0, 1\}$. By applying this variable transformation, the radius of convergence is expanded into the direction of the farther singular point. This can improve the numerical stability near the closer singular point.

- For the `expand and match` method it is important that the diagonal entries of the matrix A do not have poles in ϵ. Such poles do not allow us to solve the differential equation by an expansion in ϵ. To avoid these poles, we modify the basis of master integrals in the affected sector be replacing the problematic master integral I_1 with an integral I_1' that is related to I_1 via an IBP relation of the form

$$
I_1' = \epsilon \cdot I_1 + \dots \tag{3.32}
$$

Exchanging I_1 by I_1' in the set of basis integrals can remove the problematic pole in the differential equation. Defining the transformation matrix B that transforms the original set of master integrals $\vec{I}$ to the new set of master integrals $\vec{I}'$ using equations of the form of Equation (3.32)

$$
\vec{I}' = B \cdot \vec{I}, \tag{3.33}
$$

we obtain for the differential equation of the new set of masters

$$
\frac{d\vec{I}'}{d\rho} = \left[B \cdot A \cdot B^{-1} - \left(B \frac{dB^{-1}}{d\rho} \right) \right] \cdot \vec{I}' = \tilde{A} \cdot \vec{I}', \tag{3.34}
$$

where A is the differential equation matrix for the integrals $\vec{I}$ as defined in Equation (3.2). Since not all relations of the form of Equation (3.32) can remove the

problematic poles on the diagonal, we iteratively scan the reduction tables for such relations, calculate the corresponding $\tilde{A}$ and, in case there are still poles on the diagonal, repeat the procedure for the next possible master integral candidate until we find a suitable replacement.

Crossing thresholds

The crossing of physical thresholds is the most challenging part of the `expand and match` approach. The expansion around a physical threshold has the form given in Equation (3.26) or (3.28), depending of the number of massive particles in the final state. These ansätze include logarithms and square roots that are real valued for positive arguments but produce a non-vanishing imaginary part when their argument is smaller than zero.

This is illustrated by the example of the three charm quark threshold at $\rho_0 = 1/3$ that appears in the calculation of the semileptonic and the nonleptonic $b \to c\bar{u}d$ and $b \to u\bar{c}s$ decay channels. These decay channels have final states at NNLO that include one or three massive (charm) quarks which manifest in the differential equation as singular points at $\{0, 1/3, 1\}$. Let us assume the starting point of the calculation is at $\rho = 1/2$ where numerical results for the master integrals have been calculated numerically, see Section 3.4. The next step is to construct a Taylor expansion around this point with the ansatz

$$I_i(\rho, \epsilon, \rho_0 = 1/2) = \sum_{j=\epsilon_{\min}}^{\epsilon_{\max}} \sum_{n=0}^{n_{\max}} c_{i,j,n} \, \epsilon^j \left(\rho - \frac{1}{2} \right)^n, \tag{3.35}$$

and determine the coefficients $c_{i,j,n}$ as described above. At this expansion point, it is physically possible to produce one charm quark in the final state but not three of them. Therefore the one-charm contribution of the integrals have both, real and imaginary part, while the three-charm contribution is only real-valued at this point. Since the differential equations are purely real, the imaginary and real parts of the master integrals completely decouple in the region where they can be described with Taylor expansions.

The next step would be the expansion around the threshold at $\rho = 1/3$, where the ansatz

$$I_i(\rho, \epsilon, \rho_0 = 1/3) = \sum_{j=-4}^{\epsilon_{\max}} \sum_{m=0}^{j+4} \sum_{n=0}^{n_{\max}} c_{i,j,m,n} \epsilon^j \left(\rho - \frac{1}{3} \right)^n \log^m \left(\rho - \frac{1}{3} \right), \tag{3.36}$$

is needed. At this point, it is interesting to observe how this ansatz gives rise to the three-charm contribution. The matching to the Taylor expansion around $\rho = 1/2$ is done at some point $\rho_{\text{match}} \in (1/3, 1/2)$. At ρ_{match}, the argument of the logarithm is positive. When crossing the threshold with this expansion, the argument of the logarithm becomes negative and produces an additional imaginary part for the master integrals via

$$\log(x) = \log(|x|) - i\pi \quad \text{for } x < 0. \tag{3.37}$$

The sign of the imaginary part is defined by the direction from which the branch cut of the logarithm is approached and therefore determined by the definition of the mass in the propagator in the Feynman prescription. This additional imaginary part originating from the logarithms correspond to the contribution of three-charm final states that can be produced in the phase space where $\rho < 1/3$. At $\rho = 1/3$ these contributions are exactly zero because there is no phase space available.

3.4. Numerical boundary conditions

To fix the boundary constants for the `expand and match` approach, we use `AMFlow` [92] to obtain numerical values for the master integrals at dedicated values of ρ with 80 digits precision. These numerical values are then matched to Taylor expansions around regular points obtained with the procedure described above. The numerical evaluation is done at a regular point since `AMFlow` can not reproduce the power-log behaviour around thresholds but only calculates the hard contribution of integrals.

In principle, it would be possible to use `AMFlow` throughout this whole thesis to calculate all master integrals directly at the physical point. However, this would lead to a loss of flexibility in the calculation, meaning that the masses can not be varied and especially no changes of the mass renormalization schemes can be applied to the final result. Also it would not be possible to reproduce the square root or log behaviour of the integrals around thresholds. Therefore, `AMFlow` is only used as input for the procedure outlined above.

In contrast to the analytic calculation, we have more freedom in choosing the kinematic point of our boundary conditions. Two thing should be considered when choosing this point:

- We want to choose the starting point in the physical interesting region, which means $\rho \in [0.2, 0.3]$. This means that we can use the Taylor expansion that is matched to the starting point for all or most of the phenomenological analysis. Since every matching to a new expansion and or crossing thresholds can reduce the precision of the expansions, the first expansion is the one with, in principle, the highest precision.

- The starting point should not be close to a physical threshold. This would reduce the radius of convergence of the first expansion and therefore unnecessarily increase the number of needed expansions.

Taking these considerations into account, we choose as a starting point for our expansions $\rho_0 = 1/4$ for the decay channel $b \to c\bar{u}d$. For the decay $b \to c\bar{c}s$, where $\rho = 1/4$ corresponds to a physical threshold with four massive charm quarks, we choose $\rho_0 = 1/5$ and $\rho_0 = 1/3$ as independent starting points, see also discussion in Section 5.2.2. In addition to the starting point of the `expand and match` method, we also compute the master integrals numerically with `AMFlow` at various points in the interval $\rho \in (0, 1)$. These values are used to check the convergence of the expansions of the master integrals. We usually choose a precision of 40 digits for these control calculations.

4. Semileptonic b decays

In this chapter, the calculation of the semileptonic decay channel $b \to cl\bar{\nu}$ is outlined. This decay was investigated at NLO first in Ref. [2] where an analytic expression for the decay width is obtained.

In Ref. [3, 4] and Ref. [5], NNLO results were calculated. These calculations were not done in an exact analytical way but carried out in expansions around different limits of the charm quark mass. In Ref. [5] an expansion around $m_c \approx m_b$ was performed while the results in Ref. [3, 4] are obtained with an expansion around $m_c \approx 0$. The latter approach is much more involved since the asymptotic expansion around the zero mass limit includes way more kinematic regions that have to be taken into account. For phenomenological analysis, both approximations lead to good results since both expansions show a good convergence for the physical charm and bottom quark mass.

Note however that the expansion around $m_c \approx m_b$ does not describe correctly the contribution of three charm quarks in the final state. This process is not possible at NLO, where only one additional gluon can appear in the final state as real emission. At NNLO, this gluon can produce a $c\bar{c}$ pair leading to three massive quarks in the physical final state. It turns out that this contribution is numerically small for physical charm mass which leads to good agreement of both expansions. We will elaborate on this special contribution in detail in the following chapter. At N³LO, the expansion around $m_c \approx m_b$ is done [6, 7, 8], while no expansions for the massless limit are available.

This chapter has two purposes: We will show the calculation of the fully analytic result for the NNLO one-charm corrections of the semileptonic decay. Furthermore we will provide semianalytic expansions that allow us to cover the whole kinematic phase space between $m_c = 0$ and $m_c = 1$ including the one and three charm final states. This calculation will also serve as a cross check for our setup which we will use for the nonleptonic decay channels.

4.1. Calculation

For the implementation of this calculation, the general setup as described in Appendix A is used. We generate all Feynman diagrams with `qgraf`, find integral families with `tapir`, map to these families with `exp`. The actual computation is done with `FORM`. Finally we reduce the amplitude to scalar master integrals with `kira`. Furthermore, we apply `ImproveMasters` to obtain basis master integrals such that the ϵ and ρ dependence in the denominators of the IBP relations factorize.

However, since the semileptonic decay channel is a special subclass of the nonleptonic decays, it is possible to simplify the calculation in a few points that are outlined in the following:
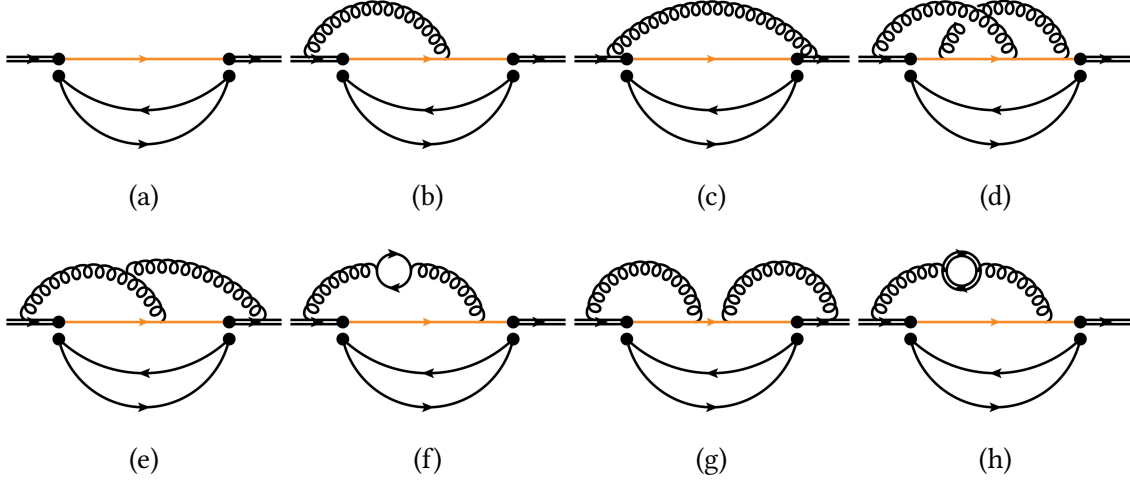
Figure 4.1.: Sample Feynman diagrams for the semileptonic decay channel at LO (a), NLO (b), (c) and NNLO (d), (e), (f), (g), (h). Black double lines denote bottom quarks, orange lines charm quarks and single black lines massless particles like lepton, neutrino, up, down or strange quarks. The insertion of operator 4.1 is with two black dots.

- Since lepton and neutrino do not carry any colour charge, there is only one effective operator that has to be considered:

$$O = (\bar{q}_1^\alpha \gamma^\mu P_L b^\alpha)(\bar{l}\gamma_\mu P_L \nu), \tag{4.1}$$

which corresponds to O_2 in Equation (2.16) when replacing q_2, q_3 with l, ν.

- The lepton-neutrino loop does not couple to gluons. Therefore it would be possible to integrate out this loop separately, reducing the number of loops in the remaining integrals by one. This is done for example in the calculation of the N^{3}LO calculation to reduce the number of loops from five to four [6]. However, in this work, this simplification is not exploited since we want to keep the calculation as close as possible to the nonleptonic decay channels, where such a separate integration of the closed loop is not possible.

- The separated lepton neutrino loop can be used to simplify the IBP reduction with kira. Since only one lepton and one neutrino propagator appear in the definition of each integral family, it is clear that both of them have to be cut in order to create a physical final state. This information can be passed to kira using the option cut_propagators[]. This information can be helpful to reduce the complexity of the reduction.

After assembling the bare amplitude for the semileptonic decays, there are poles up to the power of ϵ^{-1} and ϵ^{-2} left at NLO and NNLO. To cancel these poles, the bare parameters in the amplitude and the bottom quark wave function have to be renormalized. We

renormalize the strong coupling constant α_s in the $\overline{\text{MS}}$ scheme:

$$\alpha_s^{\text{bare}}(\mu) = \alpha_s^{\text{ren}}(\mu)\left(1 + \frac{\alpha_s^{\text{ren}}(\mu)}{\pi}\left(-\frac{11C_A}{12} + \frac{n_f T_F}{3}\right) + O\left(\alpha_s^2\right)\right). \tag{4.2}$$

The quark masses m_b and m_c and the bottom quark wave function are renormalized in the on-shell scheme. The renormalization constants Z_m^{OS} and Z_2^{OS} up to order α_s^2 are taken from Ref. [93].

The decay width of the semileptonic decay channel can be written in the form

$$\Gamma_3^{clv} = \Gamma_0\left[X_0 + C_F\left(\frac{\alpha_s}{\pi}X_1 + \left(\frac{\alpha_s}{\pi}\right)^2 X_2\right)\right] + O\left(\alpha_s^3\right), \tag{4.3}$$

where

$$\Gamma_0 = \frac{A_{\text{ew}}G_F^2\,|V_{cb}|^2\,m_b^5}{192\pi^3}. \tag{4.4}$$

The strong coupling constant is defined with five active flavours in this case $\alpha_s = \alpha_s^{(5)}(\mu)$. The leading electroweak correction is included in the prefactor $A_{\text{ew}} = 1.014$ [94]. In the following discussion, we divide the NNLO contribution X_2 into two parts

$$X_2 = X_2^{1c}(\rho) + X_2^{3c}(\rho) \tag{4.5}$$

denoting the contribution from one and three charm quarks in the physical final state. Sample diagrams that have this three charm cut are shown in figure 4.2. The physical origin of the three charm contribution $X_2^{3c}(\rho)$ imposes an interesting problem in the calculation of the master integrals. For fixing the integration constants that remain after solving the differential equation, boundary conditions of the master integrals have to be computed, which is conveniently done by computing asymptotic expansions around $\rho = 1$, see Section 3.2 for details. The boundary conditions are only calculated for the imaginary part since the real part of the integrals is much more involved. In this limit, the three-charm cut has no physical phase space and therefore zero imaginary part. The integrals that contribute to $X_2^{3c}(\rho)$ generate an imaginary part only after crossing the threshold at $\rho = 1/3$. As a consequence, we neglect the $X_2^{3c}(\rho)$ contribution in the analytic approach. An alternative would be to fix the boundaries at $\rho = 0$, where both contributions are physical. This would require a much more involved analytic expansion of the master integrals, see for example Ref. [3]. This is not done in this thesis, instead we apply the expand and match method described in Section 3.3 as a second approach to correctly describe the $X_2^{1c}(\rho)$ as well as the $X_2^{3c}(\rho)$ contribution.

The master integral calculation is structured as follows:

- For $X_2^{1c}(\rho)$ we manage to solve the differential equation analytically by fixing the boundary conditions at $\rho = 1$, see Section 3.1. As discussed in the following Section 4.3, this contribution is by far the dominating one in the phase space region of the physical charm mass.
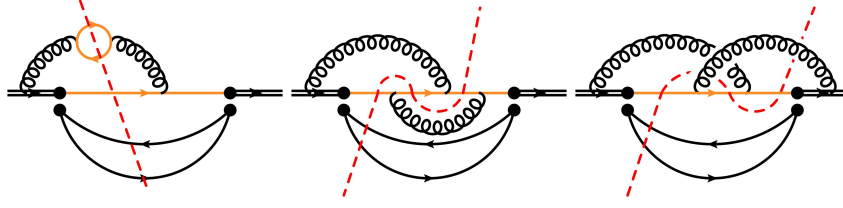
Figure 4.2.: Sample diagrams for the semileptonic decays that have cuts with three charm quarks in the final state. The same colour coding as in Figure 4.1 is used. The physical cut through three charm quarks is shown by the dashed red line. Note that in the nonplanar diagram, the gluon lines are not cut.

- In a second calculation, the `expand and match` ansatz described in Section 3.3 is used to compute all of the master integrals including both, real and imaginary part. This allows us to cover the whole phase space for both, $X_2^{1c}(\rho)$ and $X_2^{3c}(\rho)$ contributions. These results can be used as a check of the $X_2^{1c}(\rho)$ for $\rho \geq 1/3$ and to obtain the full decay width for $\rho \leq 1/3$. Also this calculation provides a check of our setup for the calculation of the nonleptonic decay channels in Chapter 5.2.

4.2. LO and NLO

At LO, only one Feynman diagram contributes, it is shown in Figure 4.1a. After IBP reduction, two master integrals are found. We calculate them analytically by transforming their corresponding differential equation into ϵ-form and solving them order by order in ϵ. This procedure is described in detail in Section 3.1 and partly shown in the example in Appendix B.2. We obtain the well known analytic result for the decay width [2]

$$X_0 = 1 - 8\rho^2 + 8\rho^6 - \rho^8 - 24\rho^4 \log(\rho).$$ (4.6)

For the NLO contribution, four diagrams have to be considered which lead to 10 master integrals. As for the LO calculation, the differential equation is set up in the mass ratio $\rho = m_c/m_b$ and can be solved analytically after transforming to ϵ-form. The boundary conditions are obtained by calculating asymptotic expansions of the master integrals around $\rho = 1$ and matching them to the analytic solutions of the differential equation. The semileptonic NLO amplitude is renormalized by including counterterms coming from the wave function renormalization of the bottom quark and the renormalization of the charm quark mass. Both renormalizations are carried out in the on-shell scheme. The following analytic expression for the renormalized NLO amplitude is obtained:

$$X_1 = \frac{25}{8} - \frac{\pi^2}{2} - \frac{239}{6}\rho^2 + 16\pi^2\rho^3 - 8\pi^2\rho^4 + 16\pi^2\rho^5 + \frac{239}{6}\rho^6 + \left(-\frac{25}{8} - \frac{\pi^2}{2}\right)\rho^8$$

$$+ \left(-72\rho^4 - 2\rho^8\right)(H_0(\rho))^2 + \left(-\frac{17}{6} + \frac{32}{3}\rho^2 - \frac{32}{3}\rho^6 + \frac{17}{6}\rho^8\right)H_{-1}(\rho)$$

$$+ \left(-2 + 24\rho^4 - 2\rho^8\right)H_0(\rho)H_{-1}(\rho) + \left(\frac{17}{6} - \frac{32}{3}\rho^2 + \frac{32}{3}\rho^6 - \frac{17}{6}\rho^8\right)H_1(\rho)$$

$$+ \left(-20\rho^2 - 90\rho^4 + \frac{4}{3}\rho^6 - \frac{17}{3}\rho^8\right) H_0(\rho) + \left(6 + 64\rho^3 + 96\rho^4 + 64\rho^5 + 6\rho^8\right) H_{-1,0}(\rho)$$

$$+ \left(-4 + 64\rho^3 - 120\rho^4 + 64\rho^5 - 4\rho^8\right) H_1(\rho) H_0(\rho)$$

$$+ \left(6 - 64\rho^3 + 96\rho^4 - 64\rho^5 + 6\rho^8\right) H_{0,1}(\rho), \tag{4.7}$$

which agrees with the results known from the literature [2]. The functions H denote the Harmonic Polylogarithms [95], for a detailed description of this set of functions, see Appendix B.4.1. The expansions of X_1 around $\rho = 0$ and $\rho = 1$ yield

$$X_1\Big|_{\rho \to 0} = \frac{25}{8} - \frac{\pi^2}{2} + \left(-34 - 24 l_\rho\right) \rho^2 + 16\pi^2 \rho^3 + \left(-\frac{273}{2} - 8\pi^2 + 36 l_\rho - 72 l_\rho^2\right) \rho^4$$

$$+ 16\pi^2 \rho^5 + \left(-\frac{526}{9} + \frac{152 l_\rho}{3}\right) \rho^6 + \left(-\frac{8857}{3600} - \frac{\pi^2}{2} + \frac{8 l_\rho}{5} - 2 l_\rho^2\right) \rho^8 + O\left(\rho^9\right), \quad (4.8)$$

and

$$X_1\Big|_{\delta \to 0} = -\frac{48}{5}\delta^5 + \frac{72}{5}\delta^6 + \left(-\frac{158152}{11025} + \frac{512}{105} l_\delta\right) \delta^7 + \left(\frac{79496}{11025} - \frac{256}{105} l_\delta\right) \delta^8$$

$$+ \left(-\frac{125299}{99225} + \frac{128}{315} l_\delta\right) \delta^9 + \left(-\frac{44659}{198450} + \frac{64}{315} l_\delta\right) \delta^{10} + O\left(\delta^{11}\right), \quad (4.9)$$

where $l_\rho = \log \rho$ and $l_\delta = \log 2\delta$ with $\delta = 1 - \rho$. The expansions of the analytic result in Equation (4.7) are carried out using the Mathematica package HarmonicSums [78].

4.3. Decay width $b \to c l \bar{\nu}$ at NNLO

At NNLO, 129 master integrals remain in eight families after IBP reduction. As described above, the NNLO contribution originates from two sorts of physical final states that differ in the number of charm quarks. For the dominant contribution with one charm quark in the final state, X_2^{1c}, an exact analytic calculation is performed. Out of the 129 master integrals, only 95 contribute to X_2^{1c}. This can be seen by checking the behaviour in the limit $\rho \to 1$: If the imaginary part of an integral is zero in this limit, the integral does not have a physical cut through one charm line. This check can be done when calculating the boundary conditions. Since the goal is to obtain a fully analytic result here, the boundary conditions of the integrals are calculated as an asymptotic expansion as outlined in Section 3.2. Already at the stage of using asy.m it is possible to separate the integrals with non-vanishing imaginary part from the purely real ones, since in order to produce an imaginary part, at least one region with at least two ultrasoft momenta has to be present. Another way would be to calculate the master integrals numerically with AMFlow at some point $\rho \in (1/3, 1)$ and check whether the imaginary part is different from zero.

For the 95 integrals, the differential equation is set up in ρ. However, a transformation to canonical form of the differential equation in this variable can not be found, since square root letters appear and therefore a variable transformation is needed. It turns out that the transformation

$$\rho = \frac{1 - t^2}{1 + t^2},$$

$$t = \frac{\sqrt{1-\rho}}{\sqrt{1+\rho}}, \tag{4.10}$$

rationalizes all the square root letters. After transformation to the variable t, the differential equation for a subset of 91 master integrals can be brought to ϵ-form. The remaining four integrals are in top-level sectors and can be decomposed into one 3×3 subblock and one uncoupled integral. These four integrals can then be solved as described in Section 3.1. We decouple the differential equations with OreSys and find solutions in terms of iterated integrals using HarmonicSums. An example for this procedure can be found in Appendix B.3.

The solution of the master integrals can be expressed in terms of iterated integrals with the alphabet

$$\left\{ \frac{1}{1+t}, \frac{1}{t}, \frac{1}{1-t}, \frac{t}{1+t^2}, \frac{t^3}{1+t^4} \right\}. \tag{4.11}$$

The analytic results for X_2^{1c} are not shown here explicitly but can be found in electronic form in [96]. The expression contains 313 different iterated integrals up to weight five. For numerical evaluation of these function, the program ginac [97, 98] can be used. The analytic solution can be expanded around different limits using HarmonicSums [78]. Expanding around $\delta = 1 - \rho = 0$ yields

$$
\begin{aligned}
X_2^{1c}(\delta)\Big|_{\delta \to 0} =\; & C_F \left[\left(-\frac{46}{5} + \frac{32\pi^2}{5} - \frac{32\pi^2 l_2}{5} + \frac{48\zeta_3}{5} \right) \delta^5 + \left(\frac{69}{5} - \frac{48\pi^2}{5} + \frac{48\pi^2 l_2}{5} - \frac{72\zeta_3}{5} \right) \delta^6 \right. \\
& \left. + \left(\frac{39329}{3675} + \frac{3044\pi^2}{945} - \frac{496\pi^2 l_2}{105} - \frac{352 l_\delta}{105} + \frac{248\zeta_3}{35} \right) \delta^7 \right] \\
& + C_A \left[\left(-\frac{286}{15} - \frac{8\pi^2}{5} + \frac{16\pi^2 l_2}{5} - \frac{24\zeta_3}{5} \right) \delta^5 + \left(\frac{99}{5} + \frac{12\pi^2}{5} - \frac{24\pi^2 l_2}{5} + \frac{36\zeta_3}{5} \right) \delta^6 \right. \\
& + \left(-\frac{99547507}{1157625} + \frac{62206\pi^2}{33075} + \frac{248\pi^2 l_2}{105} + \frac{1333376 l_\delta}{33075} - \frac{256\pi^2 l_\delta}{315} \right. \\
& \left. \left. - \frac{1408 l_\delta^2}{315} + \frac{132\zeta_3}{35} \right) \delta^7 \right] \\
& + T_F n_l \left[\frac{56}{15} \delta^5 - \frac{12}{5} \delta^6 + \left(\frac{25577548}{1157625} - \frac{512\pi^2}{945} - \frac{417664 l_\delta}{33075} + \frac{512 l_\delta^2}{315} \right) \delta^7 \right] \\
& + T_F n_h \left[\left(\frac{184}{3} - \frac{32\pi^2}{5} \right) \delta^5 + \left(-12 + \frac{8\pi^2}{5} \right) \delta^6 + \left(\frac{107444}{2835} - \frac{3848\pi^2}{945} \right) \delta^7 \right] \\
& + T_F n_c \left[\left(\frac{184}{3} - \frac{32\pi^2}{5} \right) \delta^5 + \left(-\frac{828}{5} + \frac{88\pi^2}{5} \right) \delta^6 \right. \\
& \left. + \left(\frac{108580}{567} - \frac{18968\pi^2}{945} \right) \delta^7 \right] + O\left(\delta^8 \right),
\end{aligned}
\tag{4.12}
$$

for the X_2^{1c} contribution. Since there is no phase space for the three charm quark final state in this limit, the corresponding quantity X_2^{3c} is trivially zero

$$X_2^{3c}(\delta)\Big|_{\delta \to 0} = 0. \tag{4.13}$$

In addition to the expansion around $\rho = 1$, also the expansion around $\rho = 0$ of X_2^{1c} can be computed:

$$
\begin{aligned}
X_2^{1c}(\rho)\Big|_{\rho \to 0} =C_F &\left[\frac{25775}{5184} - \frac{13339\pi^2}{2592} + \frac{17\pi^4}{120} + \frac{17\pi^2 l_2}{3} + \frac{13 l_\rho}{8} - \frac{\pi^2 l_\rho}{4} - \frac{101\zeta_3}{72} + l_\rho \zeta(3) \right. \\
&- \frac{5\pi^2}{3}\rho + \left(-\frac{45323}{162} + \frac{403\pi^2}{54} + \frac{991\pi^4}{540} - \frac{20\pi^2 l_2}{3} - \frac{6631 l_\rho}{54} + \frac{52\pi^2 l_\rho}{9} - \frac{290 l_\rho^2}{9} \right. \\
&\left. + \frac{4\pi^2 l_\rho^2}{3} - \frac{14 l_\rho^3}{3} - \frac{2 l_\rho^4}{3} + \frac{599\zeta_3}{3} + 60 l_\rho \zeta_3 \right) \rho^2 + \left(\frac{359\pi^2}{9} - \frac{56\pi^3}{3} + \frac{124\pi^2 l_\rho}{3} \right) \rho^3 \Bigg] \\
+ C_A &\left[\frac{75623}{5184} - \frac{101\pi^2}{5184} + \frac{11\pi^4}{240} - \frac{17\pi^2 l_2}{6} - \frac{13 l_\rho}{16} + \frac{\pi^2 l_\rho}{8} - \frac{1111\zeta_3}{144} - \frac{l_\rho \zeta_3}{2} \right. \\
&+ \frac{5\pi^2}{6}\rho + \left(-\frac{56207}{648} - \frac{745\pi^2}{108} - \frac{331\pi^4}{1080} + \frac{10\pi^2 l_2}{3} - \frac{5699 l_\rho}{108} - \frac{26\pi^2 l_\rho}{9} + \frac{181 l_\rho^2}{9} \right. \\
&\left. - \frac{2\pi^2 l_\rho^2}{3} + \frac{7 l_\rho^3}{3} + \frac{l_\rho^4}{3} - \frac{599\zeta_3}{6} - 30 l_\rho \zeta_3 \right) \rho^2 \\
&+ \left(\frac{1243\pi^2}{6} + \frac{28\pi^3}{3} - \frac{1136\pi^2 l_2}{3} - 62\pi^2 l_\rho \right) \rho^3 \Bigg] \\
+ T_f n_c &\left[\frac{20063}{5184} + \frac{61\pi^2}{216} + \frac{415 l_\rho}{72} - \frac{\pi^2 l_\rho}{9} + \frac{5 l_\rho^2}{3} + \frac{2 l_\rho^3}{9} + \frac{4\zeta_3}{3} - \frac{13\pi^2}{8}\rho \right. \\
&+ \left(-\frac{1475}{162} + \frac{106\pi^2}{27} - \frac{184 l_\rho}{9} - \frac{44 l_\rho^2}{3} \right) \rho^2 + \left(\frac{929\pi^2}{72} + 16\pi^2 l_\rho \right) \rho^3 \Bigg] \\
+ T_f n_h &\left[\frac{16987}{576} - \frac{85\pi^2}{216} - \frac{64\zeta_3}{3} + \left(-\frac{1198}{45} + \frac{8\pi^2}{3} \right) \rho^2 \right] \\
+ T_f n_l &\left[\frac{1009}{288} + \frac{77\pi^2}{216} + \frac{8\zeta_3}{3} + \left(\frac{118}{3} - \frac{4\pi^2}{3} + \frac{52 l_\rho}{3} - 8 l_\rho^2 \right) \rho^2 \right. \\
&\left. + \left(-\frac{112\pi^2}{9} + \frac{64\pi^2 l_2}{3} + \frac{32\pi^2 l_\rho}{3} \right) \rho^3 \right] + O\left(\rho^4 \right) .
\end{aligned}
\tag{4.14}
$$

As described above, this expression is only one part of the NNLO contribution and therefore does not agree with what is obtained in Refs. [3, 4]. Even more, the expansion of $X_2^{1c}(\rho)$ diverges logarithmically in the limit $\rho \to 0$ for the colour factors C_F, C_A and $T_F n_c$. Since the calculation in Ref. [3, 4] provides the sum of both contributions $X_2^{1c}(\rho)$ and $X_2^{3c}(\rho)$, it is possible to extract the expansion of the three charm contribution $X_2^{3c}(\rho)$ around $\rho = 0$ by taking the difference of the expressions given in Refs. [3, 4] and $X_2^{1c}(\rho)$. We obtain

$$
\begin{aligned}
X_2^{3c}(\rho)\Big|_{\rho \to 0} =C_F &\left[-\frac{409}{576} - \frac{349\pi^2}{288} - \frac{7\pi^4}{144} + \frac{19\pi^2 l_2}{6} - \frac{13 l_\rho}{8} + \frac{1\pi^2 l_\rho}{4} - \frac{115\zeta_3}{24} - l_\rho \zeta_3 \right. \\
&+ \frac{5\pi^2}{3}\rho + \left(\frac{12083}{648} - \frac{103\pi^2}{36} - \frac{29\pi^4}{18} - \frac{4\pi^2 l_2}{3} + \frac{961 l_\rho}{54} - \frac{52\pi^2 l_\rho}{9} \right.
\end{aligned}
$$

$$
\left.-\frac{34l_\rho^2}{9}-\frac{4\pi^2 l_\rho^2}{3}+\frac{14l_\rho^3}{3}+\frac{2l_\rho^4}{3}-\frac{341\zeta_3}{3}-60l_\rho\zeta_3\right)\rho^2
$$

$$
\left.+\left(\frac{131\pi^2}{3}-\frac{56\pi^3}{3}-\frac{124\pi^2 l_\rho}{3}\right)\rho^3\right]
$$

$$
+C_A\left[\frac{409}{1152}+\frac{349\pi^2}{576}+\frac{7\pi^4}{288}-\frac{19\pi^2 l_2}{12}+\frac{13l_\rho}{16}-\frac{\pi^2 l_\rho}{8}+\frac{115\zeta_3}{48}+\frac{l_\rho\zeta_3}{2}\right.
$$

$$
-\frac{5\pi^2}{6}\rho+\left(-\frac{12083}{1296}+\frac{103\pi^2}{72}+\frac{29\pi^4}{36}+\frac{2\pi^2 l_2}{3}-\frac{961l_\rho}{108}+\frac{26\pi^2 l_\rho}{9}\right.
$$

$$
\left.+\frac{17l_\rho^2}{9}+\frac{2\pi^2 l_\rho^2}{3}-\frac{7l_\rho^3}{3}-\frac{l_\rho^4}{3}+\frac{341\zeta_3}{6}+30l_\rho\zeta_3\right)\rho^2
$$

$$
\left.+\left(-\frac{131\pi^2}{6}+\frac{28\pi^3}{3}+\frac{62\pi^2 l_\rho}{3}\right)\rho^3\right]
$$

$$
+n_cT_f\left[-\frac{38225}{5184}+\frac{2\pi^2}{27}-\frac{415l_\rho}{72}+\frac{\pi^2 l_\rho}{9}-\frac{5l_\rho^2}{3}-\frac{2l_\rho^3}{9}+\frac{4\zeta_3}{3}+\frac{3\pi^2}{8}\rho\right.
$$

$$
\left.+\left(\frac{9305}{162}+\frac{38\pi^2}{27}+\frac{340l_\rho}{9}+\frac{20l_\rho^2}{3}\right)\rho^2+\left(\frac{209\pi^2}{72}+\frac{16\pi^2 l_\rho}{3}\right)\rho^3\right]+O\left(\rho^4\right).
$$

$$(4.15)$$

The two different contributions as well as their sum are shown in Figure 4.3. We observe that $X_2^{3c}(\rho)$ is non-negligible only close to $\rho=0$ where it develops a logarithmic singularity, which can be also seen from the expansion given in Equation (4.15). This singularity cancels the singular behaviour of $X_2^{1c}(\rho)$ in the limit $\rho\to 0$ which renders the total decay width finite at $\rho=0$.

As a cross check of our result as well as a preparation for the nonleptonic decay channel, the calculation of the master integrals are repeated using the semianalytic method described in Section 3.3. In this approach, the differential equation including all the 129 master integrals is considered. The singular points of the differential equation are

$$
\rho_{\text{sing}}=\{0,1/3,1\}.
$$

The ansätze needed for expansions around these points are already introduced in the previous chapter and can be found in Equation (3.29) for $\rho_0=0$, in Equation (3.28) for $\rho_0=1/3$ and in Equation (3.30) for $\rho_0=1$. In between these singular expansion points, additional Taylor expansions are calculate to transport the expansions over the whole phase space $\rho\in[0,1]$ with a suitable precision. Altogether the following points are chosen for expansions of the integrals:

$$
\rho_0=\{0,1/12,1/6,1/4,1/3,1/2,1\}.
$$

$$(4.16)$$

Note that the convergence of the expansions is always limited by the distance to the next singular point. Because of this, it is sufficient to choose only one point $\rho_0=1/2$ between $\rho_0=1/3$ and $\rho_0=1$, but more expansions are needed to cover the region between $\rho_0=1/3$
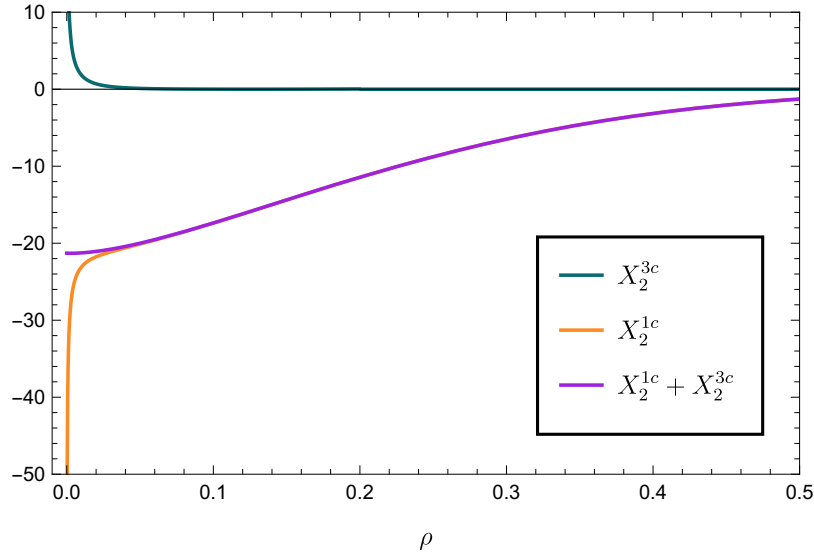
Figure 4.3.: The NNLO contributions for the semileptonic decay channel as a function of $\rho = m_c/m_b$. The orange line shows the contribution $X_2^{1c}(\rho)$ that is calculated analytically in this thesis. The green line shows the contribution $X_2^{3c}(\rho)$ that is obtained by comparing to Refs. [3, 4]. The purple line gives the complete decay width, the sum of $X_2^{1c}(\rho)$ and $X_2^{3c}(\rho)$.

and $\rho_0 = 0$.

As a starting point, the integrals are calculated at $\rho_0 = 1/2$ numerically with AMFlow and matched to the Taylor expansion. From a precision point of view, this is not the most obvious choice. The physical point of $\rho = m_c/m_b$ is in the region $\rho \in [0.2, 0.3]$ and therefore on the other side of the three charm threshold. To obtain an expansion that describes the physically interesting region, one thus has to cross the three-charm threshold which implies a loss of precision, as it will be shown in the following paragraphs. However, this calculation serves as an proof of concept and shows that, with suitable choices of expansion points and expansion depths, the whole phase space can be covered using only one numerical calculation as starting point.

For the expansion around $\rho_0 = 1$, instead of matching to the expansion around $\rho_0 = 1/2$, we use the analytic boundary conditions obtained from the asymptotic expansion to fix the expansion coefficients.

In order to estimate the precision of the expand and match expansions of the master integrals, the cancellation of the poles in the renormalized amplitude provides a suitable check. The counterterms obtained from the LO and NLO calculations are known analytically and are therefore exact. The cancellation of the pole at order ϵ^n between the analytical counterterms and the numerical poles of the NNLO bare amplitude

$$\delta(X_2|_\epsilon^n) = \left| \frac{X_2^{\text{bare}}|_{\epsilon^n} + X_2^{\text{CT}}|_{\epsilon^n}}{X_2^{\text{CT}}|_{\epsilon^n}} \right| \tag{4.17}$$

gives a good estimate on the precision of the ϵ-finite result. We plot the results in Figure 4.4. We observe that the cancellation around $\rho_0 = 1/2$ is of the order of the precision of the
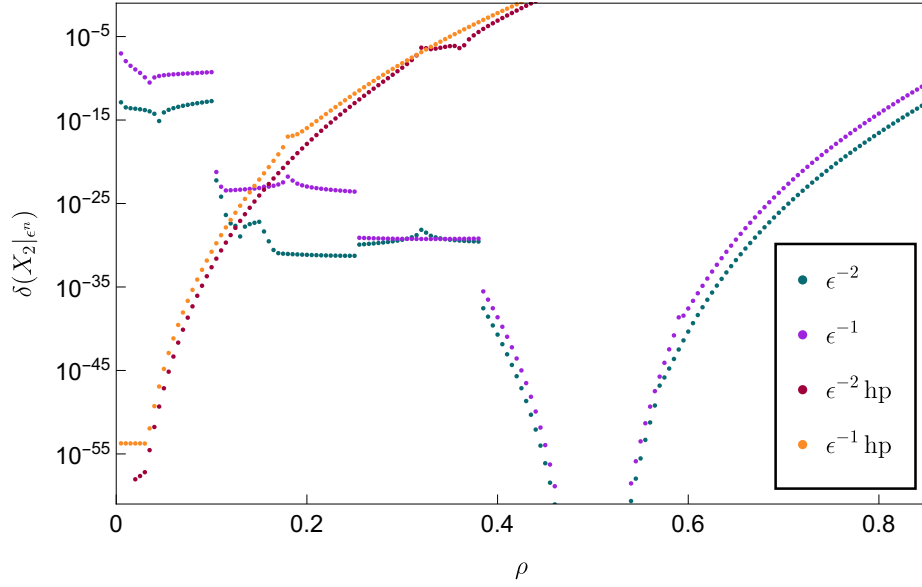
Figure 4.4.: Relative cancellation of poles between analytic counterterms and the bare NNLO amplitude obtained with `expand and match` according to Equation (4.17). The green and purple dots show the cancellation using the `expand and match` results where the boundary conditions are fixed at $\rho_0 = 1/2$. The red and orange dots show the cancellation for the high precision expansion around $\rho = 0$ that is matched to numerical results at $\rho = 1/100$.

numerical boundary condition. When matching to the threshold expansion, the following Taylor expansions and finally to the power log expansion around $\rho_0 = 0$ we loose further precision and observe a relative pole cancellation of the order of $\sim 10^{-10}$ at ϵ^{-1} and $\sim 10^{-15}$ at ϵ^{-2}. As mentioned above, this calculation serves as a showcase for the `expand and match` procedure and the choice of the point where the numerical boundary conditions are computed is not optimal for phenomenological analysis of the results in the region $\rho \in [0, 0.3]$, since we loose precision by the several matching steps. One way to improve our precision in this case would be to compute numerical boundary conditions on the other side of the threshold. As an example on how the choice of the boundary conditions can lead to higher precision, Figure 4.4 also shows the pole cancellation for a set of master integral expansions where we matched the expansion around $\rho_0 = 0$ to `AMFlow` results obtained at $\rho = 1/100$. We labelled the corresponding datapoints with „hp" for „high precision". We observe that this leads to significantly better pole cancellations compared to previous approach.

Since the `expand and match` approach covers both X_2^{1c} and X_2^{3c}, we can compare the numerical expansion of the renormalized amplitude with the analytic expansion obtained in Refs. [3, 4] term by term. Using our expansion around ρ_0, we can reproduce the all terms with at least eight digits precision. Using the „high precision" expansion, we find even 50 digits agreement between our numerical and the analytic expansion terms.

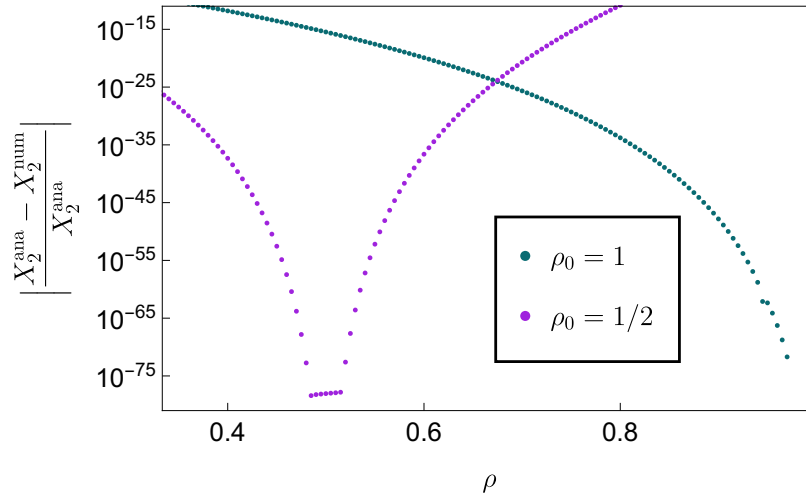Another cross check for our result is the relative difference between the `expand and match`

Figure 4.5.: The relative difference between analytic result and expansion results according to Equation (4.18). The plot is shown for the region $\rho > 1/3$, where $X_2^{3c} = 0$ and therefore both approaches should produce the same numbers.

result and the analytic expression obtained for X_2^{1c}

$$\left| \frac{X_2^{\text{ana}} - X_2^{\text{num}}}{X_2^{\text{ana}}} \right| . \tag{4.18}$$

In Figure 4.5, we consider the relative difference of the analytic result and the expansion around $\rho_0 = 1/2$ and $\rho_0 = 1$ in the region $\rho > 1/3$. In this region, the three charm contribution is zero and therefore both results should agree. We observe that we can reproduce the fully analytic results by using the expansions with a precision of ≥ 20 digits.

4.4. Decay width $b \to ul\bar{\nu}$ at NNLO

The CKM suppressed decay channel $b \to ul\bar{\nu}$ can be obtained from the $\rho \to 0$ limit of the $b \to cl\bar{\nu}$ result. This limit yields the complete result up to NLO, however at NNLO the contribution with two massive charm quarks are not covered and a dedicated calculation is necessary. We denote the additional contribution by X_2^C and write the decay rate as

$$\Gamma_3^{ul\nu} = \Gamma_3^{cl\nu}\bigg|_{\rho \to 0} + \Gamma_0 \left[\left(\frac{\alpha_s}{\pi} \right)^2 C_F T_F X_2^C \right] + O\left(\alpha_s^3 \right) . \tag{4.19}$$

In total, there are four Feynman diagrams contributing to X_2^C, corresponding to the semileptonic NLO diagrams with the insertion of a charm loop in the gluon propagator. They are shown in Figure 4.6. After integration-by-parts reduction, we find 16 master integrals which are computed with the expand and match approach as described before in Chap. 3. In contrast to $b \to cl\bar{\nu}$, the physical cuts are no longer located at $\rho = 1$ and $\rho = 1/3$
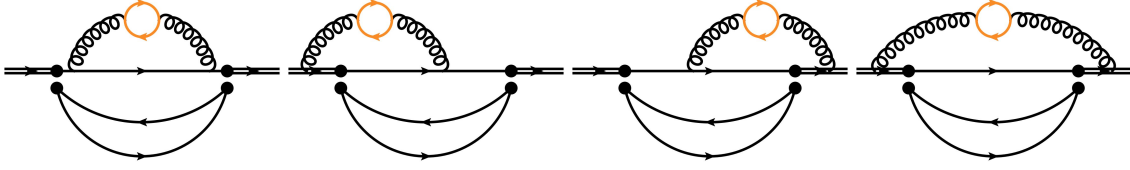
Figure 4.6.: The four Feynman diagrams contributing to the NNLO correction to $b \to u l \bar{v}$ with two charm quarks in the final state. Double black lines, orange lines and single black lines denote bottom quarks, charm quarks and massless particles respetively.

but at $\rho = 1/2$ which can also be observed in the singular points of the corresponding differential equation:

$$\rho_{\text{sing}} \in \{0, 1/2\} \,. \tag{4.20}$$

Because of the singular point induced by the two charm cut, the situation for the calculation of the master integrals is comparable to the $b \to c l \bar{v}$ case and an analytic solution with boundary conditions around $\rho \approx 1$ is not suitable in this case, which is why `expand` and `match` is used again for this decay. For the expansion around $\rho_0 = 0$ the ansatz in Equation (3.29) can be used. For the second singular point $\rho_0 = 1/2$, which corresponds to the two charm threshold, the solution of the differential equation includes square roots and therefore the ansatz given in Equation (3.26) is chosen.

This ansatz allows also for negative powers of the square roots, however the solution of the differential equation yields $n \geq 0$. For all other points it is safe to use the Taylor ansatz given in Equation (3.23). As a boundary condition, an `AMFlow` calculation t $\rho = 0.95$ is performed and matched to a Taylor expansion around the same point. Starting from there, the whole phase space between $\rho \in [0, 1]$ is covered using appropriate expansions. The expansion around the two charm threshold at $\rho_0 = 1/2$ is the most complicated and expensive expansion in this case and also the expansion where most precision is lost in the matching.

The counterterms that are needed to renormalize the X_2^C contribution are obtained by renormalization of the strong coupling constants α_s in the NLO $b \to u l \bar{v}$ diagrams. The strong coupling constant is renormalized in the $\overline{\text{MS}}$ scheme as given in Equation (4.2). After renormalization, the finite result can be compared to Ref. [3], where the expansion terms up to ρ^7 for an expansion around the massless limit are calculated analytically. The expansion coefficients given there can be compared separately for every power in ρ to the coefficients of the semianalytic expansion around $\rho_0 = 0$ that is obtained as the last `expand` and `match` step. The semianalytic expansion reads

$$
\begin{aligned}
X_2^C = {} & 3.220344021 - 12.33700550\rho + 47.31894507\rho^2 + \left(119.8984347 + 105.2757797 l_\rho\right)\rho^3 \\
& + \left(-104.9523986 + 120.0509597 l_\rho - 8.000000000 l_\rho^2\right)\rho^4 - 73.69304592\rho^5 \\
& + \left(34.95609932 + 1.600000001 l_\rho - 7.111111113 l_\rho^2\right)\rho^6 - 33.83864354\rho^7
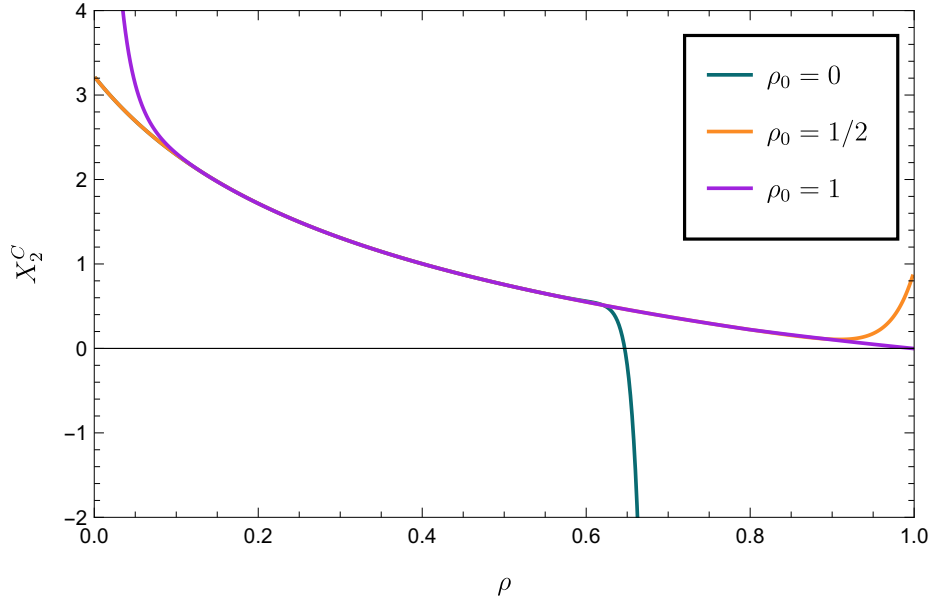\end{aligned}
$$

Figure 4.7.: The X_2^C contribution for the decay channel $b \rightarrow u l \overline{v}$ as a function of the mass ratio ρ. The green, orange and purple lines show the result using the master integral expansions around $\rho_0 = 0$, $\rho_0 = 1/2$ and $\rho_0 = 1$.

$$+ \left(8.629463297 - 18.07979000 l_\rho - 1.90000001 l_\rho^2 + 1.333333334 l_\rho^3 \right) \rho^8 + (\rho^9) , \quad (4.21)$$

where $l_\rho = \log \rho$. The agreement with the results given in Ref. [3] is of the order of at least 9 significant digits, which confirms that the crossing of the two charm threshold with ansatz (3.26) is correct.

Other cross checks for the X_2^C term can be obtained by taking different limits for ρ. The limit $\rho \rightarrow 1$ of $\Gamma \left(B \rightarrow X_u l \overline{v} \right)$ reproduces to the n_h part of the $\Gamma \left(B \rightarrow X_c l \overline{v} \right)$ result in the limit $\rho \rightarrow 0$, while the limit $\rho \rightarrow 0$ of $\Gamma \left(B \rightarrow X_u l \overline{v} \right)$ corresponds to the n_l part of the $\Gamma \left(B \rightarrow X_c l \overline{v} \right)$ result in the limit $\rho \rightarrow 0$. Figure 4.8 shows these cross checks schematically. For the cross check in the $\rho \rightarrow 1$ limit, the agreement is of the order of 30 digits, while at $\rho \rightarrow 0$ the first 9 digits agree. This can be explained by the fact that the expansion around $\rho = 1$ is close to the AMFlow starting point of the expand and match method while for the expansion around zero, several expansions have to be matched and the two charm threshold has to be crossed, which leads to a loss of accuracy. However, the accuracy could be improved by adding more intermediate steps, increasing the expansion depth or moving the AMFlow point. The finite result for X_2^C as a function of ρ is shown in Fig. 4.7. When setting $\mu = m_b$ we obtain for the decay width

$$\Gamma_3^{ulv} = \Gamma_0 \left[1 + \frac{\alpha_s}{\pi} C_F \left(\frac{25}{8} - \frac{\pi^2}{2} \right) + \left(\frac{\alpha_s}{\pi} \right)^2 \left(C_F^2 \left(\frac{11047}{2592} - \frac{515\pi^2}{81} + \frac{67\pi^4}{720} + \frac{53\pi^2 l_2}{6} - \frac{223\zeta_3}{36} \right) \right. \right.$$

$$+ C_A C_F \left(\frac{154927}{10368} + \frac{95\pi^2}{162} + \frac{101\pi^4}{1440} - \frac{53\pi^2 l_2}{12} - \frac{383\zeta_3}{72} \right)$$

$$+ C_F T_F n_l \left(-\frac{1009}{288} + \frac{77\pi^2}{216} + \frac{8\zeta_3}{3} \right) + C_F T_F n_h \left(\frac{16987}{576} - \frac{85\pi^2}{216} - \frac{64\zeta_3}{3} \right)$$
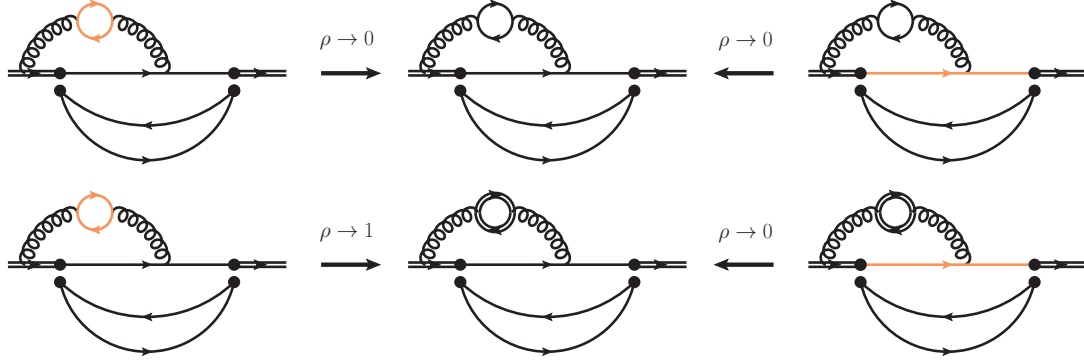
49

Figure 4.8.: Possible cross checks for the contribution X_2^C. On the left hand side, the X_2^C contribution is shown, on the right hand side the corresponding diagram of the contribution X_2^{1C} of the $b \to c l \bar{\nu}$ decay channel is shown. Double black lines, orange lines and single black lines denote bottom quarks, charm quarks and massless quarks, leptons and neutrinos respectively.

$$+ C_F T_F n_c \left(-\frac{1009}{288} + \frac{77\pi^2}{216} + \frac{8\zeta_3}{3} + X_2^C \right) \Big) \Big],$$ (4.22)

where $l_2 = \log 2$. The first expansion terms of the expression for X_2^C is given in Equation (4.21). The prefactor Γ_0 is similar to Equation (4.4) $\Gamma_0 = A_{\mathrm{ew}} G_F^2 |V_{ub}|^2 m_b^5 / 192 / \pi^3$. For the on-shell values $m_b^{\mathrm{OS}} = 4.7\mathrm{GeV}$ and $m_c^{\mathrm{OS}} = 1.3\mathrm{GeV}$, we obtain

$$\Gamma_3^{ul\nu} = \Gamma_0 \left[1 - 2.413 \frac{\alpha_s}{\pi} + \left(-21.295 + 0.929_{X_2^C} \right) \left(\frac{\alpha_s}{\pi} \right)^2 \right].$$ (4.23)

The NNLO correction from secondary charm production is labelled with the subscript X_2^C, it contributes to around $\sim 5\%$ of the NNLO contribution.

5. Nonleptonic b decays in the on-shell mass scheme

In this chapter, we consider nonleptonic decays of B mesons. In contrast to the semileptonic decay, we now face various channels with different numbers of massive quarks in the final state. We can group them into three classes:

- Two charm quarks in the final state: $b \to c\bar{c}s$, $b \to c\bar{c}d$

- One charm quark in the final state: $b \to c\bar{u}d$, $b \to c\bar{u}s$, $b \to u\bar{c}d$, $b \to u\bar{c}s$

- No charm quark in the final state: $b \to u\bar{u}d$, $b \to u\bar{u}s$

At NNLO we can have two additional charm quarks from the splitting of a gluon into a $c\bar{c}$ pair which leads to two, three and four charms in the physical final state. This is in analogy to the semileptonic decay rate discussed in Chapter 4. In Figure 5.1 NNLO Feynman diagrams for the different decay channels are shown.
In the following, we will focus on the four channels $b \to c\bar{u}d$, $b \to c\bar{c}s$, $b \to u\bar{c}s$ and $b \to u\bar{u}d$. The results for all the other channels listed above can be obtained from these four channels by adapting the CKM matrix elements in the prefactor accordingly.
In comparison to the semileptonic decays, we find more Feynman diagrams since the quark pair produced by the W-boson can couple to gluons, which is not the case for the lepton neutrino pair that is produced in the semileptonic decay. The semileptonic diagrams form a subset of the nonleptonic diagrams and we check explicitly that our nonleptonic calculation correctly reproduces this contribution by comparing to the results in Chapter 4.
The calculation is structured in a similar way as the calculation of the semileptonic decay and follows the general setup described in Appendix A and Chapter 3. However, it involves additional subtleties in the treatment of γ_5 and the renormalization of the four-quark operators introduced in Chapter 2. The γ_5 problem is addressed using Fierz identities as discussed in detail in the following Section 5.1. The calculation of the corresponding operator renormalization constants is presented in Appendix C.
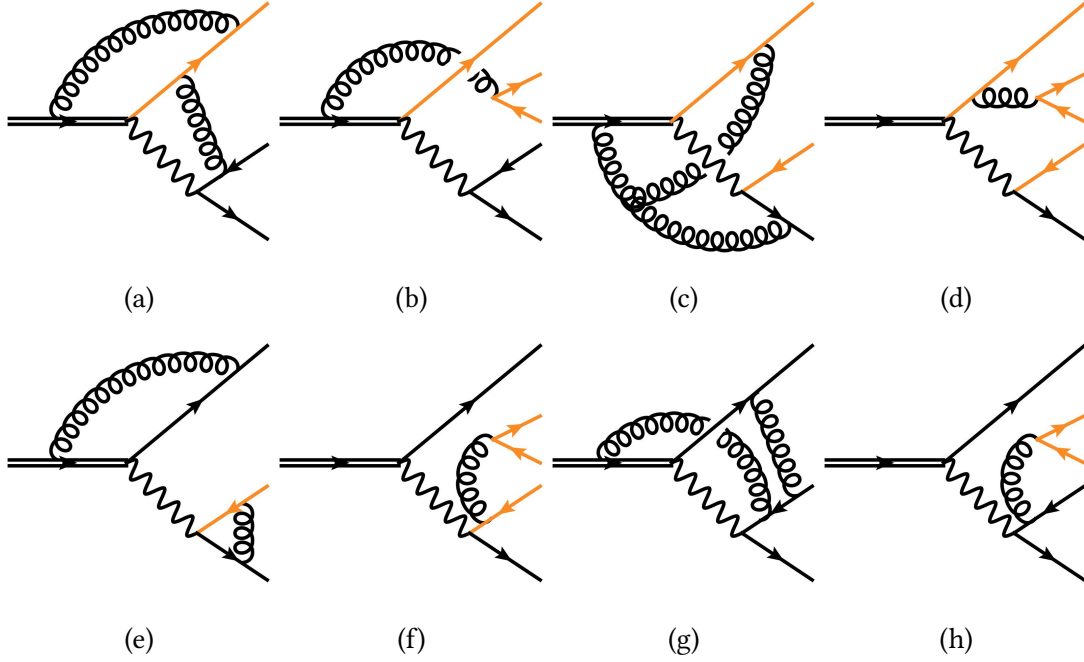
Figure 5.1.: Sample diagrams for the nonleptonic decay modes with zero (g), one (a), (e), two (c), (h), three (b), (f) and four (d) massive charm quarks in the final state at NNLO. Double black, orange and single black lines denote bottom, charm and massless quarks respectively.

5.1. Fierz identites and evanescent operators

In the calculation of the nonleptonic decay channels, problems with the treatment of γ_5 arise starting from NLO. This chapter will explain how these problems can be solved and how the calculation of quantities including traces of γ_5 can be carried out consistently in d dimensions using Fierz identities.

5.1.1. γ_5 in $d = 4 - 2\epsilon$ dimensions

The effective operators defined in Chapter 2 include chirality projectors P_L that consist of terms with γ_5. The matrix γ_5 is defined in four dimensions as

$$\gamma_5 = i\gamma_0\gamma_1\gamma_2\gamma_3, \tag{5.1}$$

and has three basic properties: the anti-commutativity with other Dirac matrices γ^μ, the cyclicity of traces and the non-vanishing trace of γ_5 multiplied by four different Dirac matrices

$$\{\gamma_5, \gamma^\mu\} = 0, \tag{5.2}$$

$$\text{Tr}\left[\gamma_5\gamma^\mu\gamma^\nu\gamma^\rho\gamma^\sigma\right] = \text{Tr}\left[\gamma^\mu\gamma^\nu\gamma^\rho\gamma^\sigma\gamma_5\right], \tag{5.3}$$

$$\text{Tr}\left[\gamma_5\gamma^\mu\gamma^\nu\gamma^\rho\gamma^\sigma\right] = -4i\epsilon^{\mu\nu\rho\sigma}. \tag{5.4}$$

(a)   (b)
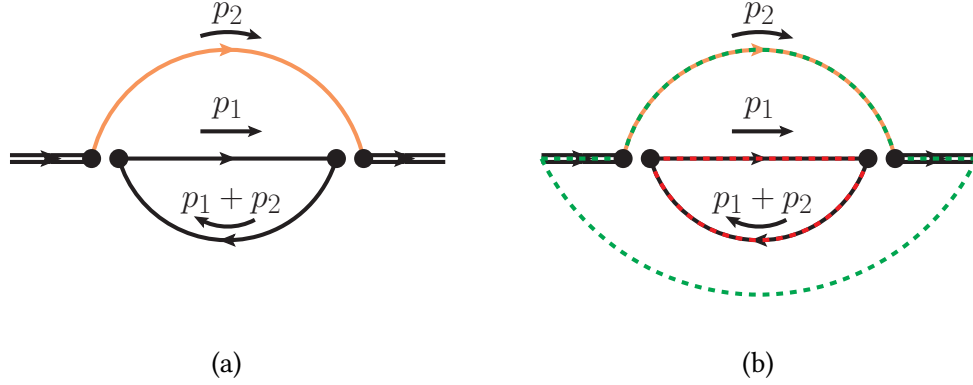
Figure 5.2.: The LO diagram for the decay $b \to c\bar{u}d$ with explicit momentum flow is shown in (a). Double black, orange and single black lines denote bottom, charm and massless quarks respectively. The two fermion traces for this diagram are shown in (b) with the same colour coding as in Equation (5.6).

Furthermore, γ_5 fulfils the equations

$$\mathrm{Tr}[\gamma_5] = 0,$$
$$\mathrm{Tr}[\gamma^\mu \gamma^\nu \gamma_5] = 0. \tag{5.5}$$

However, γ_5 is by definition a four-dimensional quantity, which makes its treatment in multiloop calculations with dimensional regularization tricky. There are different schemes that address this problem. One of them is the scheme used in this thesis, the naive dimensional regularization scheme (NDR) with anti-commuting γ_5. This scheme is also used for the calculation of the anomalous dimension and the operator renormalization constants [22, 28] and to be consistent with these calculations, it is also chosen here. Working in NDR means that we only use the anti-commutativity of γ_5 given in Equation (5.2) in our calculation and never exploit Equation (5.3) and (5.4).

To see the consequence of this, the structure of the Feynman diagrams has to be investigated in detail. In a first step, the LO diagram shown in Figure 5.2 is considered. After inserting an arbitrary combination of effective operators, the fermion line flow in the diagram looks as shown in Figure 5.2. This structure of one external fermion line and one separated loop is the same for every diagram and does not depend on the operators since these only affect the colour flow through the diagram.

From a calculation point of view, by multiplying a projector $(\slashed{q} + m_b)$ where q is the external momentum of the bottom quark and taking the trace, two separate traces over Dirac matrices have to be calculated

$$\mathrm{Tr}\left[(\slashed{q} + m_b)(\gamma_\nu P_L)(\slashed{p}_2 + m_c)(\gamma_\mu P_L)\right] \cdot \mathrm{Tr}\left[\slashed{p}_1(\gamma^\nu P_L)(\slashed{p}_2 + \slashed{p}_1)(\gamma^\mu P_L)\right], \tag{5.6}$$

where the momentum labelling of Figure 5.2 (b) is adapted. The two traces are shown with the same colour coding as in Equation (5.6). In both traces, the left handed projector in the effective operator produces the factor $(1 - \gamma_5)$ twice, leading to terms with zero, one and two appearances of γ_5 in each trace. Using anti-commutativity of γ_5, two γ_5 in one
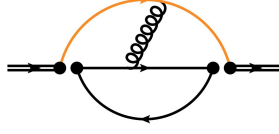
Figure 5.3.: Sample diagram that develops a problematic trace over Driac matrices.

trace can be reduced to zero, which leads to an expression with at most one γ_5 per trace. The traces with no γ_5 can be calculated without any problems in d dimensions. For the traces with one γ_5, we focus on the internal loop that corresponds to the trace

$$\text{Tr}\left[\left(\slashed{p}_2 + \slashed{p}_1\right)\gamma_\mu\slashed{p}_1\gamma_\nu\gamma_5\right] = \left(p_2^\alpha + p_1^\alpha\right)p_1^\beta\text{Tr}\left[\gamma_\alpha\gamma_\mu\gamma_\beta\gamma_\nu\gamma_5\right], \tag{5.7}$$

with loop momentum p_1 and momentum p_2 which is a linear combination of the external momentum q and other loop momenta. In principle this trace has four open indices, two of them contracted with the two momenta p_1 and p_2. However, since the whole diagram itself only has one external momentum, tensor reduction will reduce this to a prefactor proportional to $g^{\alpha\beta}q^2$ or $q^\alpha q^\beta$ which will reduce the trace given above to

$$\text{Tr}\left[\gamma_\mu\gamma_\nu\gamma_5\right], \tag{5.8}$$

which vanishes in any dimension. For the semileptonic decay channel, the argument described above always holds since lepton and neutrino do not couple to gluons and the trace given in Equation (5.7) appears in every diagram. Therefore, applying NDR with anti-commuting γ_5 does not lead to any problems in this decay channel at all orders in α_s since all traces with one remaining γ_5 can be discarded.

However, the situation changes when the nonleptonic decay channels are considered. At LO, the situation is the same as for the semileptonic case, but starting from NLO, traces over Dirac matrices that are ill-defined in d dimensions arise from diagrams where the two fermion lines are connected by gluons. A sample Feynman diagram for this case is shown in Figure 5.3. Here, the Trace over the massless loop reads

$$\text{Tr}\left[\gamma_{\mu_1}P_L\slashed{p}_1\gamma_{\mu_2}P_L\slashed{p}_2\gamma_\nu\slashed{p}_3\right], \tag{5.9}$$

where the Lorentz indices of the four fermion operators are denoted with μ_1, μ_2 and the coupling to the gluon with the index ν. Even after applying the argument above that reduces the number of open indices in the trace by two, we are left with traces like

$$\text{Tr}\left[\gamma_{\mu_1}\gamma_5\gamma_{\mu_2}\gamma_\nu\gamma_\alpha\right]. \tag{5.10}$$

A possible way out of this problem, as already introduced in the NLO calculations in Ref. [11], is the use of Fierz identities. For a detailed overview over such identities, see Appendix B.7.

5.1.2. Fierz identities for nonleptonic b decays

The application of Fierz identities in the calculation of the nonleptonic decay channels allows us to employ NDR scheme for γ_5. The decay width can be written as

$$\Gamma^{q_1 q_2 q_3}(\rho) = \frac{1}{m_b} \sum_{i,j=1,2} \left(\frac{4 G_F |\lambda_{q_1 q_2 q_3}|}{\sqrt{2}} \right)^2$$

$$C_i^\dagger(\mu_b) C_j(\mu_b) \operatorname{Im} \left[i \int \mathrm{d}^4 x e^{iqx} \langle b | T \left\{ O_i^{\dagger \, q_1 q_2 q_3}(x) O_j^{q_1 q_2 q_3}(0) \right\} | b \rangle \Bigg|_{q^2 = m_b^2} \right], \quad (5.11)$$

which leads to two fermion traces and therefore introduces the problems with γ_5 that are outlined above. Following Ref. [11], instead of $\Gamma^{q_1 q_2 q_3}(\rho)$ in Equation (5.11), we consider the same expression where one of the operators is replaced by its fierzed counterpart. For the operators O_1 and O_2

$$O_1^{q_1 q_2 q_3} = (\overline{q}_1^\alpha \gamma^\mu P_L b^\beta)(\overline{q}_2^\beta \gamma_\mu P_L q_3^\alpha),$$
$$O_2^{q_1 q_2 q_3} = (\overline{q}_1^\alpha \gamma^\mu P_L b^\alpha)(\overline{q}_2^\beta \gamma_\mu P_L q_3^\beta), \quad (5.12)$$

the fierzed counterparts, denoted by a tilde, read

$$\tilde{O}_1^{q_2 q_1 q_3} = (\overline{q}_2^\beta \gamma^\mu P_L b^\beta)(\overline{q}_1^\alpha \gamma_\mu P_L q_3^\alpha),$$
$$\tilde{O}_2^{q_2 q_1 q_3} = (\overline{q}_2^\beta \gamma^\mu P_L b^\alpha)(\overline{q}_1^\alpha \gamma_\mu P_L q_3^\beta). \quad (5.13)$$

We find that the colour structures are flipped between fierzed and unfierzed operators. Comparing the operator definitions in Equations (5.12) and (5.13), we find:

$$\begin{pmatrix} \tilde{O}_1^{q_2 q_1 q_3} \\ \tilde{O}_2^{q_2 q_1 q_3} \end{pmatrix} = \begin{pmatrix} 0 & 1 \\ 1 & 0 \end{pmatrix} \cdot \begin{pmatrix} O_1^{q_1 q_2 q_3} \\ O_2^{q_1 q_2 q_3} \end{pmatrix} = \begin{pmatrix} O_2^{q_1 q_2 q_3} \\ O_1^{q_1 q_2 q_3} \end{pmatrix}. \quad (5.14)$$

We want to use this symmetry of the current-current operators to replace one operator in Equation (5.11) by its fierzed counterpart. In Ref. [22], it is shown that this is achieved by choosing a specific form of the anomalous dimension matrix.

To do such a replacement, we have to ensure that the Wilson coefficients of the unfierzed and fierzed operators are the same. For this, we require the initial condition and the running of the operators to be the same [22]. It turns out that it is sufficient to fix the running given by the anomalous dimension. We demand:

$$\tilde{\gamma}(\tilde{O}_1, \tilde{O}_2) \stackrel{!}{=} \gamma(O_1, O_2) = \begin{pmatrix} \gamma_{11} & \gamma_{12} \\ \gamma_{21} & \gamma_{22} \end{pmatrix}, \quad (5.15)$$

with the ADM $\tilde{\gamma}$ of the fierzed operators $\tilde{O}_1$ and $\tilde{O}_2$ and the ADM γ of the operators O_1 and O_2. Using the relation between fierzed and unfierzed operators given in Equation (5.14), we find the following equation that relates γ and $\tilde{\gamma}$:

$$\tilde{\gamma}(\tilde{O}_1, \tilde{O}_2) = \begin{pmatrix} \tilde{\gamma}_{11} & \tilde{\gamma}_{12} \\ \tilde{\gamma}_{12} & \tilde{\gamma}_{22} \end{pmatrix} = \begin{pmatrix} 0 & 1 \\ 1 & 0 \end{pmatrix} \cdot \begin{pmatrix} \gamma_{11} & \gamma_{12} \\ \gamma_{21} & \gamma_{22} \end{pmatrix} \cdot \begin{pmatrix} 0 & 1 \\ 1 & 0 \end{pmatrix} = \begin{pmatrix} \gamma_{22} & \gamma_{21} \\ \gamma_{12} & \gamma_{11} \end{pmatrix}. \quad (5.16)$$

Combining Equation (5.16) and (5.15), we find that the anomalous dimension has to be of the form

$$\gamma = \begin{pmatrix} \gamma_{11} & \gamma_{12} \\ \gamma_{12} & \gamma_{11} \end{pmatrix}. \tag{5.17}$$

Note that an ADM of this form becomes diagonal when going to the basis $O_\pm = O_1 \pm O_2$ and therefore in this case the two operators O_+ and O_- do not mix under renormalization. The anomalous dimension can be written as expansion in α_s

$$\gamma = \gamma^{(0)} + \frac{\alpha_s}{\pi}\gamma^{(1)} + \left(\frac{\alpha_s}{\pi}\right)^2 \gamma^{(2)} + O\left(\alpha_s^3\right), \tag{5.18}$$

and the requirement in Equation (5.17) holds for every $\gamma^{(i)}$. The $\gamma^{(i)}$ for $i \geq 1$ depends on the choice of the evanescent operators. We can construct an ADM that fulfils Equation (5.17) by an appropriate choice of evanescent operators. This is discussed in detail in Section 5.1.3. After defining such a set of physical and evanescent operators that leads to an ADM in the required form, we are allowed to replace $O_i^{\dagger\,q_1q_2q_3}$ in Equation (5.11) by its fierzed counterpart and obtain

$$\tilde{\Gamma}^{q_1q_2q_3}(\rho) = \frac{1}{m_b} \sum_{i,j=1,2} \left(\frac{4G_F|\lambda_{q_1q_2q_3}|}{\sqrt{2}}\right)^2$$

$$\tilde{C}_i^\dagger(\mu_b)C_j(\mu_b) \, \text{Im} \left[i \int \mathrm{d}^4x \, e^{iqx} \langle b|T\left\{\tilde{O}_i^{\dagger\,q_2q_1q_3}(x)O_j^{q_1q_2q_3}(0)\right\}|b\rangle \bigg|_{q^2=m_b^2} \right]. \tag{5.19}$$

Note that the different ordering of the quarks in $\tilde{O}_i^\dagger$ compared to Equation (5.11). The quantity $\tilde{\Gamma}^{q_1q_2q_3}(\rho)$ leads to only one fermion trace involving γ_5 as illustrated in Figure 5.4. Instead of the two traces in Equation (5.6), we obtain only one trace

$$\text{Tr}\left[(\not{q}+m_b)(\gamma_\nu P_L)(\not{p}_2+m_c)(\gamma_\mu P_L)\not{p}_1(\gamma^\nu P_L)\left(\not{p}_2+\not{p}_1\right)(\gamma^\mu P_L)\right]. \tag{5.20}$$

Here it is possible to use anti-commuting γ_5 to obtain traces with no or one γ_5. The latter can be discarded since the decay width is a parity even quantity. Note that this argument can not be applied at the level of two remaining traces in Equation (5.6) since the product of two parity odd traces can produce a parity even contribution that should not be discarded. In a final step we obtain $\Gamma^{q_1q_2q_3}(\rho)$ from $\tilde{\Gamma}^{q_1q_2q_3}(\rho)$ via

$$\Gamma^{q_1q_2q_3}(\rho) = \tilde{\Gamma}^{q_1q_2q_3}(\rho)\bigg|_{\tilde{C}_1\to C_2,\tilde{C}_2\to C_1}. \tag{5.21}$$

The considerations above suggest the following procedure to avoid problems with γ_5: We replace in each diagram the second operator by its fierzed counterpart, meaning we go from $\Gamma^{q_1q_2q_3}$ to $\tilde{\Gamma}^{q_1q_2q_3}$. After this, all diagrams only have one fermion line and therefore only one trace that has to be evaluated. This allows us to use anti-commuting γ_5. $\tilde{\Gamma}^{q_2q_1q_3}$ is related to $\Gamma^{q_1q_2q_3}$ via Equation (5.21). Note that the evanescent operators have to be modified to preserve the symmetry in Equation (5.21) and Equation (5.17) up to order $O(\alpha_s^2)$. This is described in the next section.
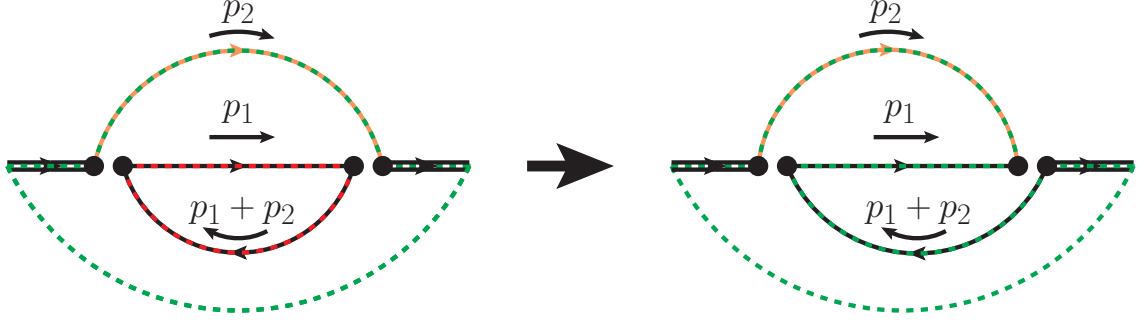
Figure 5.4.: The LO diagram for the decay $b \rightarrow c\bar{u}d$ before and after the application of Fierz identities. The left diagram corresponds to $\Gamma^{q_1 q_2 q_3}(\rho)$ in Equation (5.11) and leads to two traces that are visualized by red and green dots. On the right-hand side, the same diagram with the insertion of one fierzed and one un-fierzed operator is shown. This diagram corresponds to $\tilde{\Gamma}^{q_1 q_2 q_3}$ given in Equation (5.19) and only leads to one trace, shown by the green dots. Double black, orange and single black lines denote bottom, charm and massless quarks respectively.

5.1.3. Evanescent operators

The feasibility of the calculation of the nonleptonic decay rate depends on whether or not we can use Fierz transformations. Since Fierz identities are four-dimensional relations (for a more detailed description of Fierz identities, see Appendix B.7), the two quantities in Equation (5.21) only agree at leading ϵ order. However, the Fierz symmetry can be restored order by order in α_s by adjusting the evanescent operators in a way that the anomalous dimension is of the form given in Equation (5.17) [22]. In this section, we outline how the evanescent operators enter the definition of the ADM and how they can be determined in order to meet the requirement of Equation (5.17).

As a starting point, we have to obtain the ADM for the current-current operators in the historical basis and the corresponding evanescent operators with general coefficients of higher order ϵ terms. Since our calculation is done up to NNLO, we also need the anomalous dimension up to and including $\gamma^{(2)}$. Calculating this quantity directly would mean to calculate three loop renormalization constants in the historical basis, which can be avoided. In Chapter 2, the transformation from CMM to the historical basis and vice versa is introduced. With the same transformation matrices, it is possible to also transform the anomalous dimensions from the CMM (where all orders up to $\gamma^{(2)}$ are known from Ref. [28]) to the historical basis. The transformation rules only include the ADM in the CMM basis, the QCD beta function and renormalization constants up to order α_s^2 [27, 28]

$$\gamma^{(0)} = R\gamma'^{(0)}R^{-1},$$

$$\gamma^{(1)} = R\gamma'^{(1)}R^{-1} - \left[Z_{QQ}^{(1,0)}, \gamma^{(0)}\right] - 2\beta_0 Z_{QQ}^{(1,0)},$$

$$\gamma^{(2)} = R\gamma'^{(2)}R^{-1} - \left[Z_{QQ}^{(2,0)}, \gamma^{(0)}\right] - \left[Z_{QQ}^{(1,0)}, \gamma^{(1)}\right] + \left[Z_{QQ}^{(1,0)}, \gamma^{(0)}\right]Z_{QQ}^{(1,0)}$$

$$- 4\beta_0 Z_{QQ}^{(2,0)} - 2\beta_1 Z_{QQ}^{(1,0)} + 2\beta_0 (Z_{QQ}^{(1,0)})^2 . \tag{5.22}$$

The anomalous dimension $\gamma'^{(i)}$ in the CMM basis is denoted by a prime as introduced in Chapter 2. The matrix R gives the rotation of the physical operators from CMM to the historical basis and is defined in Equation (2.37). The matrices $Z_{QQ}^{(1,0)}$ and $Z_{QQ}^{(2,0)}$ result from the basis transformation of the renormalization constants. After their transformation from CMM to historical basis, a non-vanishing finite part remains which has to be removed in order to obtain $\overline{MS}$ renormalization constants in the historical basis. The sub block of this scheme change including the physical operators defines the two matrices $Z_{QQ}^{(1,0)}$ and $Z_{QQ}^{(2,0)}$. They are obtained by [28]

$$Z_{QQ}^{(1,0)} = -R Z_{QE}^{'(1,1)} U R^{-1} \,,$$
$$Z_{QQ}^{(2,0)} = R\Big[-Z_{QE}^{'(2,1)} U - Z_{QE}^{'(2,2)} V + Z_{QE}^{'(1,1)} V Z_{QQ}^{'(1,1)} \Big] R^{-1} \,, \qquad (5.23)$$

where U and V are the transformation matrices of the evanescent operators as introduced in Chapter 2. For a detailed derivation of $Z_{QQ}^{(1,0)}$ and $Z_{QQ}^{(2,0)}$, see Appendix C. Via these two matrices, the entries of U and V enter the anomalous dimension in the historical basis in our approach.

To demonstrate the procedure of calculating the evanescent operators, we first consider the calculation at NLO, where the first order evanescent operators are needed. They are given by

$$E_1^{(1),q_1 q_2 q_3} = (\bar{q}_1^\alpha \gamma^{\mu_1 \mu_2 \mu_3} P_L b^\beta)(\bar{q}_2^\beta \gamma_{\mu_1 \mu_2 \mu_3} P_L q_3^\alpha) - (16 - 4\epsilon) O_1^{q_1 q_2 q_3} \,,$$
$$E_2^{(1),q_1 q_2 q_3} = (\bar{q}_1^\alpha \gamma^{\mu_1 \mu_2 \mu_3} P_L b^\alpha)(\bar{q}_2^\beta \gamma_{\mu_1 \mu_2 \mu_3} P_L q_3^\beta) - (16 - 4\epsilon) O_2^{q_1 q_2 q_3} \,, \qquad (5.24)$$

where the terms $4\epsilon O_i^{q_1 q_2 q_3}$ are defined in a way that they exactly restore the Fierz symmetry at order $O(\alpha_s)$. This is the usual definition of the first order evanescent operators which can be found in the literature [22, 23, 24].

However, to demonstrate the procedure shown above, let us be agnostic about the ϵ^1-terms of the evanescent operators and introduce them as two undetermined coefficients a_1, a_2:

$$E_1^{(1),q_1 q_2 q_3} = (\bar{q}_1^\alpha \gamma^{\mu_1 \mu_2 \mu_3} P_L b^\beta)(\bar{q}_2^\beta \gamma_{\mu_1 \mu_2 \mu_3} P_L q_3^\alpha) - (16 + a_1 \epsilon) O_1^{q_1 q_2 q_3} \,,$$
$$E_2^{(1),q_1 q_2 q_3} = (\bar{q}_1^\alpha \gamma^{\mu_1 \mu_2 \mu_3} P_L b^\alpha)(\bar{q}_2^\beta \gamma_{\mu_1 \mu_2 \mu_3} P_L q_3^\beta) - (16 + a_2 \epsilon) O_2^{q_1 q_2 q_3} \,. \qquad (5.25)$$

Note that the 16 $O_i^{q_1 q_2 q_3}$ are fixed in order to ensure the vanishing matrix element of the evanescent operators in four dimensions, see Equation (2.10). The transformation for the evanescent operators from CMM to the traditional basis, considering only the first order evanescent operators, is in this case given by

$$\vec{E} = \begin{pmatrix} E_1^{(1),q_1 q_2 q_3} \\ E_2^{(1),q_1 q_2 q_3} \end{pmatrix} = M\left[\begin{pmatrix} E_1'^{(1),q_1 q_2 q_3} \\ E_2'^{(1),q_1 q_2 q_3} \end{pmatrix} + \epsilon U \begin{pmatrix} O_1'^{q_1 q_2 q_3} \\ O_2'^{q_1 q_2 q_3} \end{pmatrix} \right] = M\left[\vec{E}' + \epsilon U \vec{O}' \right] \,, \qquad (5.26)$$

with

$$M = \begin{pmatrix} 2 & \frac{1}{n_c} \\ 0 & 1 \end{pmatrix}, \quad U = \begin{pmatrix} U_{11} & U_{12} \\ U_{21} & U_{22} \end{pmatrix} \,. \qquad (5.27)$$

The operator definitions of the current-current operators and their corresponding first order evanescent operators are given in Equation (2.16) and (2.19). In a first step, all elements of U are introduced as undetermined constants. The first constraint to impose is that $E_1^{(1),q_1q_2q_3}$ only includes higher order ϵ-terms proportional to operator $O_1^{q_1q_2q_3}$ and similar for $E_2^{(1),q_1q_2q_3}$ and $O_2^{q_1q_2q_3}$. This yields two equations which reduces the degrees of freedom in the matrix U from four to two:

$$U = \begin{pmatrix} U_{11} & \frac{U_{11}-U_{22}}{2n_c} \\ 0 & U_{22} \end{pmatrix}. \tag{5.28}$$

In a next step, the anomalous dimension $\gamma^{(1)}$ is considered in the historical basis. We use the transformation given in Equation (5.22) to transform the anomalous dimension in the CMM basis taken from Ref. [28]. For the transformation, we need the finite renormalization matrix $Z_{QQ}^{(1,0)}$ that is obtained by inserting Equation (5.28) into Equation (5.23):

$$Z_{QQ}^{(1,0)} = \begin{pmatrix} -\frac{67}{108}U_{11} + \frac{1}{27}U_{22} & \frac{67}{324}U_{11} - \frac{37}{81}U_{22} \\ -\frac{1}{2}U_{11} & \frac{1}{6}U_{11} \end{pmatrix}. \tag{5.29}$$

The ADM in the historical basis reads:

$$\gamma^{(1)} = \begin{pmatrix} -\frac{335}{6} + \frac{254}{27}U_{11} + \frac{52}{27}U_{22} & -\frac{73}{2} + \frac{14}{81}U_{11} + \frac{796}{81} \\ -\frac{45}{2} + \frac{113}{18}U_{11} + \frac{2}{9}U_{22} & -\frac{11}{6} + \frac{31}{54}U_{11} - \frac{74}{27}U_{22} \end{pmatrix}$$
$$+ n_f \begin{pmatrix} \frac{26}{9} - \frac{67}{81}U_{11} + \frac{4}{81}U_{22} & 2 + \frac{67}{243}U_{11} - \frac{148}{243}U_{22} \\ \frac{10}{3} - \frac{2}{3}U_{11} & -\frac{10}{9} + \frac{2}{9}U_{11} \end{pmatrix}. \tag{5.30}$$

Following Equation (5.17), we impose that the elements of $\gamma^{(1)}$ fulfil $\gamma_{11}^{(1)} = \gamma_{22}^{(1)}$ and $\gamma_{21}^{(1)} = \gamma_{12}^{(1)}$, which yields the unique solution $U_{11} = U_{22} = 4$ and therefore

$$U = \begin{pmatrix} 4 & 0 \\ 0 & 4 \end{pmatrix}. \tag{5.31}$$

With these entries of the matrix U, we find

$$\epsilon M U \vec{O}' = \epsilon \begin{pmatrix} 2 & \frac{1}{n_c} \\ 0 & 1 \end{pmatrix} \begin{pmatrix} 4 & 0 \\ 0 & 4 \end{pmatrix} \begin{pmatrix} O_1' \\ O_2' \end{pmatrix}$$
$$= 4\epsilon \begin{pmatrix} 2O_1' + \frac{1}{n_c}O_2' \\ O_2' \end{pmatrix} = 4\epsilon \begin{pmatrix} O_1 \\ O_2 \end{pmatrix} = 4\epsilon\vec{O}, \tag{5.32}$$

and therefore

$$a_1 = -4, \quad a_2 = -4. \tag{5.33}$$

The finite renormalization matrix is obtained by

$$Z_{QQ}^{(1,0)} = \begin{pmatrix} -\frac{7}{3} & -1 \\ -2 & \frac{2}{3} \end{pmatrix}. \tag{5.34}$$

Let us stress, that all quantities that are needed for the calculation of $\gamma^{(1)}$ are know with exact dependence on n_c and the calculation demonstrated above is carried out for arbitrary values of n_c. The result for U is however independent of n_c.

When going to NNLO, also the evanescent operators of second order have to be included. In addition, the prefactor of the physical operators in the definition of the evanescent operators are extended by additional terms proportional to ϵ^2. They are introduced with undetermined coefficients A_2, B_1, B_2:

$$
E_1^{(1),q_1q_2q_3} = (\bar{q}_1^\alpha \gamma^{\mu_1\mu_2\mu_3} P_L b^\beta)(\bar{q}_2^\beta \gamma_{\mu_1\mu_2\mu_3} P_L q_3^\alpha) - (16 - 4\epsilon + A_2\epsilon^2)O_1^{q_1q_2q_3},
$$
$$
E_2^{(1),q_1q_2q_3} = (\bar{q}_1^\alpha \gamma^{\mu_1\mu_2\mu_3} P_L b^\alpha)(\bar{q}_2^\beta \gamma_{\mu_1\mu_2\mu_3} P_L q_3^\beta) - (16 - 4\epsilon + A_2\epsilon^2)O_2^{q_1q_2q_3},
$$
$$
E_1^{(2),q_1q_2q_3} = (\bar{q}_1^\alpha \gamma^{\mu_1\mu_2\mu_3\mu_4\mu_5} P_L b^\beta)(\bar{q}_2^\beta \gamma_{\mu_1\mu_2\mu_3\mu_4\mu_5} P_L q_3^\alpha) - (256 - 224\epsilon + B_1\epsilon^2)O_1^{q_1q_2q_3},
$$
$$
E_2^{(2),q_1q_2q_3} = (\bar{q}_1^\alpha \gamma^{\mu_1\mu_2\mu_3\mu_4\mu_5} P_L b^\alpha)(\bar{q}_2^\beta \gamma_{\mu_1\mu_2\mu_3\mu_4\mu_5} P_L q_3^\beta) - (256 - 224\epsilon + B_2\epsilon^2)O_2^{q_1q_2q_3}. \quad (5.35)
$$

We choose a set of evanescent operators where the ϵ^2 term of $E_1^{(1),q_1q_2q_3}$ and $E_2^{(1),q_1q_2q_3}$ is the same (A_2). This is a particular choice that is not necessary. In principle we could also introduce two independent coefficients A_1 and A_2. However, since the set of equations to determine the ϵ^2 coefficients is underdetermined and therefore has infinitely many solutions, we do not loose generality by assuming $A_1 = A_2$.

With this definition of the operator, the order ϵ^1 terms are fixed, see the operator definitions in Equation (5.35), and therefore the matrix U reads

$$
U = \begin{pmatrix} 4 & 0 \\ 0 & 4 \\ 144 & 0 \\ 0 & 144 \\ 6336 & 0 \\ 0 & 6336 \end{pmatrix}, \quad (5.36)
$$

where we also included the third generation evanescent operators. The ϵ^2 terms are described by the matrix V that is introduced in this case with eight arbitrary parameters for the evanescent operators at first and second order

$$
V = \begin{pmatrix} V_{11} & V_{12} \\ V_{21} & V_{22} \\ V_{31} & V_{32} \\ V_{41} & V_{42} \\ -1344 & 0 \\ 0 & -1344 \end{pmatrix}. \quad (5.37)
$$

The corresponding matrices R and M are given in Equation (2.37). The procedure is the same as outlined above at NLO.

Four equations are obtained from imposing that only physical operators with the same colour structure as the operator structure with three or five Dirac matrices on each fermion line appear in the definition of the evanescent operators.

Therefore we are left with four coefficients V_{ij}. We rotate the anomalous dimension

according to Equation (5.22). Next, we require for the anomalous dimension $\gamma_{21}^{(2)} = \gamma_{12}^{(2)}$ and $\gamma_{11}^{(2)} = \gamma_{22}^{(2)}$, which provides two additional equations. The remaining solution space is two dimensional. We give the general solution parametrized by the constants entering the definition of the evanescent operators

$$B_1 = -\frac{4384}{115} - \frac{32}{5}n_f + A_2\left(\frac{10388}{115} - \frac{8}{5}n_f\right), \qquad (5.38)$$

$$B_2 = -\frac{38944}{115} - \frac{32}{5}n_f + A_2\left(\frac{19028}{115} - \frac{8}{5}n_f\right). \qquad (5.39)$$

If we require $B_1 = B_2$, we obtain

$$A_2 = 4, \quad B_1 = B_2 = \frac{1616}{5} - \frac{64}{5}n_f, \qquad (5.40)$$

and observe that B_1 and B_2 depend on the number of active flavours n_f. If we require that the coefficients A_2, B_1 and B_2 do not depend on n_f, we obtain to two additional equations since the assumptions $\gamma_{21}^{(2)} = \gamma_{12}^{(2)}$ and $\gamma_{11}^{(2)} = \gamma_{22}^{(2)}$ are now considered for the entries of $\gamma^{(2)}$ proportional to n_f^0 and n_f^1 separately. The coefficients obtained with this ansatz are

$$A_2 = -4, \quad B_1 = -\frac{45936}{115}, \quad B_2 = -\frac{115096}{115}. \qquad (5.41)$$

In the following, we will use the constants given in Equation (5.41) for the evanescent operators. The matrix V corresponding to the n_f-independent constants reads

$$V = \begin{pmatrix} V_{11} & V_{12} \\ 0 & V_{11} - 6V_{12} \\ V_{31} & V_{32} \\ 0 & V_{31} - 6V_{32} \\ -1344 & 0 \\ 0 & -1344 \end{pmatrix} = \begin{pmatrix} 4 & 0 \\ 0 & 4 \\ \frac{36763}{115} & -\frac{2304}{23} \\ 0 & \frac{105856}{115} \\ -1344 & 0 \\ 0 & -1344 \end{pmatrix} \qquad (5.42)$$

The relation between the entries of V and the constants A_2, B_1 and B_2 can be found from the transformation of the evanescent operators given in Equation (2.34)

$$\epsilon^2 \begin{pmatrix} -A_2 O_1 \\ -A_2 O_2 \\ -B_1 O_1 \\ -B_2 O_2 \\ \dots \\ \dots \end{pmatrix} = \epsilon^2 M V \vec{O}'$$

$$= \epsilon^2 \begin{pmatrix} 2V_{11}O_1' + \frac{V_{11}}{3}O_2' \\ (V_{11} - 6V_{12})O_2' \\ (40V_{11} + 2V_{31})O_1' + \left(\frac{20V_{11}}{3} + \frac{V_{31}}{3}\right)O_2' \\ (20V_{11} - 120V_{12} + V_{31} - 6V_{32})O_2' \\ \dots \\ \dots \end{pmatrix}$$

$$
= \epsilon^2 \begin{pmatrix}
V_{11} O_1 \\
(V_{11} - V_{12}) O_2 \\
(20 V_{11} + V_{31}) O_1 \\
(20 V_{11} - 120 V_{12} + V_{31} - 6 V_{32}) O_2 \\
\dots \\
\dots
\end{pmatrix},
\tag{5.43}
$$

which yields

$$
V_{11} = -A_2 , \qquad V_{12} = 0 , \qquad V_{31} = -B_1 + 20 A_2 , \qquad V_{32} = \frac{B_2 - B_1}{6} .
\tag{5.44}
$$

The numerical values given in Equation (5.41) are functions of n_c, and a n_c-independent solution for these ϵ^2 coefficients does not exist here, in contrast to the ϵ^1 terms given in Equation (5.33).

The finite renormalization constant at two loop order for the n_f-independent constants reads

$$
\begin{aligned}
Z_{QQ}^{(2,0)} &= \begin{pmatrix}
-\frac{200}{9} + \frac{45}{8} V_{11} - \frac{9}{2} V_{12} - \frac{67}{288} V_{31} & \frac{68}{3} + \frac{25}{8} V_{11} - \frac{33}{4} V_{12} - \frac{5}{96} V_{31} + \frac{5}{16} V_{32} \\
-\frac{7}{4} + \frac{23}{8} V_{11} + 3 - \frac{5}{48} V_{31} & \frac{397}{36} + \frac{3}{8} V_{11} + \frac{27}{4} V_{12} - \frac{11}{144} V_{31} + \frac{11}{24} V_{32}
\end{pmatrix} \\
&\quad + n_f \begin{pmatrix}
\frac{7}{54} - \frac{7}{36} V_{11} & \frac{1}{18} - \frac{1}{12} V_{11} + \frac{1}{2} V_{12} \\
\frac{1}{9} - \frac{1}{6} V_{11} & -\frac{1}{27} + \frac{1}{18} V_{11} - \frac{1}{3} V_{12}
\end{pmatrix} \\
&= \begin{pmatrix}
-\frac{200}{9} - \frac{185}{18} A_2 + \frac{67}{288} B_1 & \frac{68}{3} - \frac{25}{6} A_2 + \frac{5}{96} B_2 \\
-\frac{7}{4} - \frac{119}{24} A_2 + \frac{5}{48} B_1 & \frac{397}{36} - \frac{137}{72} A_2 + \frac{11}{144} B_2
\end{pmatrix} + n_f \begin{pmatrix}
\frac{7}{54} + \frac{7}{36} A_2 & \frac{1}{18} + \frac{1}{12} A_2 \\
\frac{1}{9} + \frac{1}{6} A_2 & -\frac{1}{27} - \frac{1}{18} A_2
\end{pmatrix} \\
&= \begin{pmatrix}
-\frac{153257}{2070} - \frac{35}{54} n_f & -\frac{1763}{138} - \frac{5}{18} n_f \\
-\frac{6493}{276} - \frac{5}{9} n_f & -\frac{239239}{4140} + \frac{5}{27} n_f
\end{pmatrix} .
\end{aligned}
\tag{5.45}
$$

As presented in this chapter, the definitions of the evanescent operators are not unique and there are infinitely many different solutions that will lead to different numerical values for the renormalized Feynman diagrams at NNLO, which may seem confusing at first glance. However, the renormalized diagrams are no physical quantities but have to be considered together with the matching coefficients of the four-quark operators. The definition of the operator basis, including physical and evanescent operators, enters the anomalous dimension and therefore the running of the matching coefficients. By considering the renormalized amplitude at renormalization scale μ_b, multiplied with the corresponding matching coefficients at the same scale, the dependence on A_2, B_1 and B_2 in in the definition of the evanescent operators cancel exactly and the total decay rate does not depend on the definition of any evanescent operators any more. This can be checked explicitly after the NNLO corrections are calculated and the running of the operators is implemented for general coefficients A_2, B_1 and B_2. These calculations are done in the next chapter and the cancellation of the evanescent operator coefficients is shown explicitly in Section 5.2.1.

5.2. Nonleptonic decay width

The decay width of the nonleptonic decay channels is obtained by insertion of two four-fermion operators and has the following structure:

$$
\Gamma_3^{q_1 q_2 q_3} = \frac{G_F^2 m_b^5 |\lambda_{q_1 q_2 q_3}|^2}{192\pi^3} \left[X_0(\rho) + \frac{\alpha_s}{\pi} X_1(\rho) + \left(\frac{\alpha_s}{\pi} \right)^2 X_2(\rho) \right] + O\left(\alpha_s^3\right)
$$

$$
= \Gamma_0 \left[C_1^2(\mu_s) G_{11}^{q_1 q_2 q_3} + C_1(\mu_s) C_2(\mu_s) G_{12}^{q_1 q_2 q_3} + C_2^2(\mu_s) G_{22}^{q_1 q_2 q_3} \right], \tag{5.46}
$$

with the normalization of the decay width $\Gamma_0 = G_F^2 m_b^5 |V_{q_1 b}|^2 |V_{q_2 q_3}|^2 / (192\pi^3)$. The functions G_{ij} denote the contribution of diagrams with the insertion of operator O_i and O_j. The G_{ij} depend on the mass ratio ρ and the renormalization scale μ_s and can be expressed as a perturbative expansion in α_s by

$$
G_{ij} = G_{ij}^{(0)}(\rho, \mu_s) + \frac{\alpha_s}{\pi} G_{ij}^{(1)}(\rho, \mu_s) + \left(\frac{\alpha_s}{\pi} \right)^2 G_{ij}^{(2)}(\rho, \mu_s) + O(\alpha_s^3), \tag{5.47}
$$

where $\alpha_s \equiv \alpha_s^{(5)}(\mu_s)$ is the strong coupling constant with $n_f = 5$ active quarks at the renormalization scale μ_s. Note that the matching coefficients C_i in Equation (5.46) are functions of the renormalization scale μ_s. At the matching scale of the effective theory μ_W, the matching coefficients in the traditional basis for anti-commuting γ_5 are given by [99, 28]

$$
C_1(\mu_W) = \frac{\alpha_s}{4\pi} \left(\frac{11}{2} + 3L \right) + \left(\frac{\alpha_s}{4\pi} \right)^2 \left[\frac{14565}{368} + \frac{9\pi^2}{2} + \frac{205}{4}L + \frac{27}{2}L^2 \right.
$$

$$
\left. - n_f \left(\frac{55}{12} + \frac{\pi^2}{3} + \frac{10}{3}L + L^2 \right) - \frac{1}{2}T\left(\frac{m_t^2}{M_W^2} \right) \right] + O(\alpha_s^3),
$$

$$
C_2(\mu_W) = 1 - \frac{\alpha_s}{4\pi} \left(\frac{11}{6} + L \right) + \left(\frac{\alpha_s}{4\pi} \right)^2 \left[-\frac{1409251}{16560} - \frac{\pi^2}{6} - \frac{85}{12}L - \frac{L^2}{2} \right.
$$

$$
\left. + n_f \left(\frac{55}{36} + \frac{\pi^2}{9} + \frac{10}{9}L + \frac{L^2}{3} \right) + \frac{1}{6}T\left(\frac{m_t^2}{M_W^2} \right) \right] + O(\alpha_s^3), \tag{5.48}
$$

where the function $T(m_t^2/M_W^2)$ includes the effects of the top quark mass and $L = \log(\mu_W^2/M_W^2)$. As given in Equation (5.46), the matching coefficients are needed at the scale μ_s. The running of the Wilson coefficients from the scale μ_W to the scale μ_s can be obtained from the renormalization group equation [100, 101]

$$
\mu \frac{d}{d\mu} \vec{C}(\mu) = \gamma^T(g) \vec{C}(\mu). \tag{5.49}
$$

To perform the running up to NNLO in QCD, the ADM γ is needed up to $\gamma^{(2)}$. It is important to note that the definitions of the evanescent operators in Equation (5.35) and the coefficients in (5.39) enter the ADM. For implementation of the running, we used two different methods that both yield the same results:

	O_1	O_2	O_3	O_4	O_5	O_6
$C_i^{(0)}$	-0.251	1.109	0.011	-0.026	0.007	-0.032
$C_i^{(1)}$	4.382	-2.016				
$C_i^{(2)}$	36.63	-82.19				

Table 5.1.: Numerical values for the matching coefficients $C_i(\mu_s)$ in the historical basis at LO, NLO and NNLO at the scale $\mu_s = 4.7\,\text{GeV}$. The matching scale is $\mu_W = M_W$. For completeness, we also show the coefficients of the penguin operators O_{3-6} at LO. They are numerically small compared to the current-current operators O_1 and O_2.

- In a first approach, we used already available code from Ref. [102] that performs the running of the Wilson coefficients in the CMM basis. The CMM Wilson coefficients at the scale μ_s are then transformed to the traditional basis according to Equation (C.29). The choice of the evanescent operator coefficients enters the finite renormalization constant $Z_{QQ}^{(2,0)}$ and therefore affects the numerical value of the matching coefficients at order α_s^2. The numerical values for $Z_{QQ}^{(1,0)}$ and $Z_{QQ}^{(2,0)}$ with the evanescent operators definition of Equation (5.41) are given in Equation (C.27).

- In a second approach, the running is implemented in the historical basis. To obtain the ADM in this basis, we transform the ADM in the CMM basis to the historical basis following Equation (C.30). Again the evanescent operator choice enters via $Z_{QQ}^{(2,0)}$. The ADM in the historical basis with the evanescent operators definition of Equation (5.41) is given in Equation (C.36). For a more detailed discussion of the basis transformation of renormalization constants and anomalous dimensions, see Appendix C.2.

We checked explicitly that both approaches yield the same results for the C_1 and C_2 at the scale $\mu_s \sim m_b$. In Table 5.1, we summarize their numerical values at the scale $\mu_s = 4.7\,\text{GeV}$. In the following sections, the calculation of the four different nonleptonic decay channels $b \to c\bar{u}d$, $b \to c\bar{c}s$, $b \to u\bar{c}s$ and $b \to u\bar{u}d$ up to NNLO in the on-shell mass scheme are discussed in detail.

5.2.1. $b \to c\bar{u}d$

The decay channel $b \to c\bar{u}d$ is the dominant one since it is proportional to the CKM-matrix elements V_{cb} and V_{ud}. At leading order, there are four contributing Feynman diagrams, which only differ by the insertion of the effective operators. Since the four-quark operators only change the colour structure of the diagrams, we can reduce the LO contributions to the same set of master integrals that appear in the semileptonic case. The LO contributions of the functions G_{ij} in Equation (5.46) are obtained by

$$G_{11}^{(0)} = G_{22}^{(0)} = \frac{3}{2}G_{12}^{(0)} = 3\left(1 - 8\rho^2 + 8\rho^6 - \rho^8 - 24\rho^4 H_0(\rho)\right), \qquad (5.50)$$

where we set $\mu_s = m_b$. Note that

$$G_{11}^{(0)} = G_{22}^{(0)} = 3X_0 \,, \tag{5.51}$$

with X_0 given in Equation (4.6) denoting the LO contribution of the semileptonic decay width $b \to c l \overline{\nu}$. The factor three accounts for the three possible colours of the colour singlet $q\bar{q}$ which only appear in the nonleptonic decay channel.

There are 12 possibilities to attach a gluon to the LO diagram. Multiplied by the factor four to account for all the possible combinations of current-current operators, there are 48 contributing NLO diagrams. These diagrams can be reduced to 18 master integrals. Out of these 18 integrals, 10 correspond to exactly the same master integrals of the semileptonic subset and have already been calculated in Chapter 4. The additional master integrals are introduced by diagrams where gluons couple to the massless quarks $\overline{u}$ and d. Also for this additional set of NLO integrals we find analytic solutions expressed in terms of harmonic polylogarithms. For the renormalization at NLO, the counterterms coming from the LO diagram with the insertion of one physical and one first order evanescent operator have to be taken into account. The corresponding renormalization constants that mix the evanescent and physical operators are given in Appendix C. In addition to the renormalization of the four-quark operators, at NLO we obtain counterterms from the renormalization of the charm quark mass and the bottom quark wave function renormalization. They are both renormalized in the on-shell scheme. Since all master integrals can be calculated analytically, the G_{ij} for this decay can be expressed in terms of Harmonic Polylogarithms:

$$G_{11}^{(1)} = \frac{31}{2} - \frac{554\rho^2}{3} + \frac{554\rho^6}{3} - \frac{31\rho^8}{2} + \pi^2 \left(-2 + 16\rho^2 + 48\rho^4 - \frac{16\rho^6}{3} + \frac{2\rho^8}{3} \right)$$
$$+ \left(-\frac{62}{3} + \frac{640\rho^2}{3} - \frac{640\rho^6}{3} + \frac{62\rho^8}{3} \right) H_{-1}(\rho) + \left(\frac{62}{3} - \frac{640\rho^2}{3} + \frac{640\rho^6}{3} - \frac{62\rho^8}{3} \right) H_1(\rho)$$
$$+ \left(-96\rho^2 - 120\rho^4 + 32\pi^2\rho^4 + \frac{992\rho^6}{3} - \frac{124\rho^8}{3} \right) H_0(\rho) - \left(288\rho^4 + 64\rho^6 - \right.$$
$$\left. 8\rho^8 \right) (H_0(\rho))^2 + \left(8 - 64\rho^2 - 576\rho^4 - 64\rho^6 + 8\rho^8 \right) \left[H_{0,1}(\rho) - H_{0,-1}(\rho) \right], \tag{5.52}$$

$$G_{22}^{(1)} = \frac{31}{2} - \frac{550\rho^2}{3} + \frac{550\rho^6}{3} - \frac{31\rho^8}{2} + \pi^2 \left(-2 + 64\rho^3 - 32\rho^4 + 64\rho^5 - 2\rho^8 \right)$$
$$+ \left(-288\rho^4 - 8\rho^8 \right) (H_0(\rho))^2 + \left(-\frac{34}{3} + \frac{128\rho^2}{3} - \frac{128\rho^6}{3} + \frac{34\rho^8}{3} \right) H_{-1}(\rho)$$
$$+ \left(\frac{34}{3} - \frac{128\rho^2}{3} + \frac{128\rho^6}{3} - \frac{34\rho^8}{3} \right) H_1(\rho) + \left(-80\rho^2 - 432\rho^4 + \frac{16\rho^6}{3} - \frac{68\rho^8}{3} \right) H_0(\rho)$$
$$+ \left(16 + 256\rho^3 + 480\rho^4 + 256\rho^5 + 16\rho^8 \right) H_0(\rho)H_{-1}(\rho) - \left(16 - 256\rho^3 + 480\rho^4 \right.$$
$$\left. - 256\rho^5 + 16\rho^8 \right) H_0(\rho)H_1(\rho) - \left(24 + 256\rho^3 + 384\rho^4 + 256\rho^5 + 24\rho^8 \right) H_{0,-1}(\rho)$$
$$+ \left(24 - 256\rho^3 + 384\rho^4 - 256\rho^5 + 24\rho^8 \right) H_{0,1}(\rho), \tag{5.53}$$

$$G_{12}^{(1)} = -17 + \frac{1828\rho^2}{9} - \frac{1828\rho^6}{9} + 17\rho^8 - \pi^2 \left(\frac{4}{3} + \frac{32\rho^2}{3} - \frac{128\rho^3}{3} + \frac{160\rho^4}{3} - \frac{128\rho^5}{3} + \frac{32\rho^6}{3} \right.$$

$$
\begin{aligned}
&+ \frac{4\rho^8}{3}\Big) - \Big(\frac{160\rho^2}{3} - 352\rho^4 + \frac{1504\rho^6}{9} + \frac{376\rho^8}{9}\Big) H_0(\rho) + \Big(\frac{116}{9} + \frac{1088\rho^2}{9} - \frac{1088\rho^6}{9} \\
&- \frac{116\rho^8}{9}\Big) H_1(\rho) + \Big(-\frac{116}{9} - \frac{1088\rho^2}{9} + \frac{1088\rho^6}{9} + \frac{116\rho^8}{9}\Big) H_{-1}(\rho) + \Big(\frac{32}{3} + \frac{512\rho^3}{3} \\
&+ 320\rho^4 + \frac{512\rho^5}{3} + \frac{32\rho^8}{3}\Big) H_0(\rho) H_{-1}(\rho) - \Big(192\rho^4 - 128\rho^6 + \frac{16\rho^8}{3}\Big) (H_0(\rho))^2 \\
&+ \Big(-\frac{32}{3} + \frac{512\rho^3}{3} - 320\rho^4 + \frac{512\rho^5}{3} - \frac{32\rho^8}{3}\Big) H_1(\rho) H_0(\rho) + \Big(-16 - 128\rho^2 - \frac{512\rho^3}{3} \\
&- 640\rho^4 - \frac{512\rho^5}{3} - 128\rho^6 - 16\rho^8\Big) H_{0,-1}(\rho) + \Big(16 + 128\rho^2 - \frac{512\rho^3}{3} + 640\rho^4 - \frac{512\rho^5}{3} \\
&+ 128\rho^6 + 16\rho^8\Big) H_{0,1}(\rho),
\end{aligned}
\tag{5.54}
$$

where $\rho = m_c/m_b$ and $H_{\dots}(\rho)$ denote the Harmonic Polylogarithms. These results can be compared to the literature, where we find agreement with Ref. [11].

At NNLO we find 1308 diagrams which can be reduced to a set of 385 master integrals. For this set of integrals, the `expand and match` ansatz described in Chapter 3 is used. The singular points of the differential equation are

$$
\rho_{\text{singular}} \in \{0, 1/3, 1\},
\tag{5.55}
$$

where $\rho_{\text{singular}} = 1/3$ corresponds to the physical three charm quark threshold. The expansion points that we choose for the master integrals of this decay channel are

$$
\rho_0 = \{0, 1/4, 1/3, 1/2, 7/10, 1\},
\tag{5.56}
$$

which allows us to cover the complete phase space $\rho \in [0, 1]$. For phenomenological applications, the expansion around $\rho = 1/4$ is the most convenient one, since it covers the physical interesting region $\rho \in [0.2, 0.3]$ and uses a Taylor ansatz which makes it easy to evaluate numerically.

For the renormalization of the NNLO bare amplitude, we have to include evanescent operators up to second order in the LO diagrams and evanescent operators of first order in the NLO diagrams. The four-quark operator renormalization constants at two-loop order depend on the choice of the evanescent operator definition and are calculated in order to preserve Fierz symmetry at NNLO, following the method outlined in Chapter 5.1. They are given explicitly in Appendix C.

The charm and bottom quark masses, the bottom quark wave function are renormalized in the on-shell scheme. The strong coupling constant is renormalized in the $\overline{\text{MS}}$ scheme, analogue to the semileptonic decay channel. The counterterms can be calculated in a fully analytic form from LO and NLO diagrams. Since the NNLO master integrals are calculated with the `expand and match` method, the bare NNLO amplitude is obtained as an expansion around the different points listed in Equation (5.56). For simplicity, only the result of the renormalized amplitude for the expansion around $\rho = 0$ is given here explicitly. The G_{ij} at two loop order read

$$
G_{11}^{(2)} = 13.4947 - 24.6740\rho + \Big(115.542 - 625.679 l_\rho + 8l_\rho^2\Big)\rho^2 + (-76.2198 + 210.552 l_\rho)\rho^3
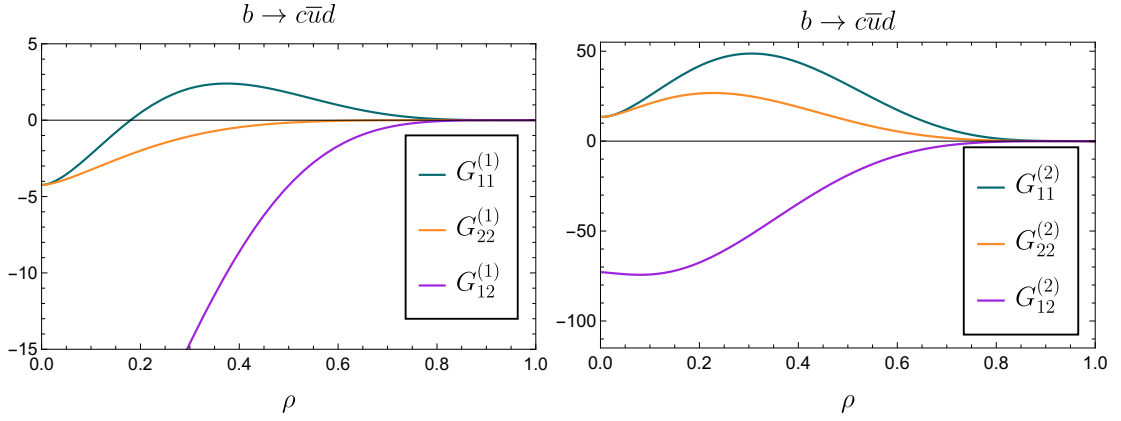$$

Figure 5.5.: The NLO and NNLO G_{ij} for the decay channel $b \to c\bar{u}d$ as functions of the mass ratio ρ.

$$+ \left(1829.82 + 2820.10 l_\rho - 1058.37 l_\rho^2 + 32 l_\rho^3\right) \rho^4 + (-74.0184 + 574.630 l_\rho)\rho^5$$

$$+ \left(-2197.51 - 12.1531 l_\rho + 892.933 l_\rho^2 - 257.185 l_\rho^3\right) \rho^6$$

$$+ (-371.871 + 433.678 l_\rho)\rho^7 + O(\rho^8), \tag{5.57}$$

$$G_{22}^{(2)} = 13.4947 - 24.6740\rho + \left(-2647.00 - 1257.33 l_\rho + 8 l_\rho^2\right) \rho^2 + (-2883.63 - 3842.57 l_\rho)\rho^3$$

$$+ \left(3403.78 - 4764.59 l_\rho - 777.272 l_\rho^2 + 32 l_\rho^3\right) \rho^4 + (-601.507 - 2397.66 l_\rho)\rho^5$$

$$+ \left(2833.10 - 559.776 l_\rho + 264.958 l_\rho^2 - 21.3333 l_\rho^3\right) \rho^6$$

$$+ (-440.110 + 57.8599 l_\rho)\rho^7 + O(\rho^8), \tag{5.58}$$

$$G_{12}^{(2)} = -72.8420 - 16.4493\rho + \left(-279.953 + 63.3413 l_\rho + 5.33333 l_\rho^2\right) \rho^2$$

$$+ (-3707.85 - 2702.08 l_\rho)\rho^3 + \left(2164.12 - 2197.00 l_\rho + 2041.82 l_\rho^2 + 21.3333 l_\rho^3\right) \rho^4$$

$$+ (-888.121 - 1177.33 l_\rho)\rho^5 + \left(1987.97 - 4886.67 l_\rho - 174.131 l_\rho^2 + 632.889 l_\rho^3\right) \rho^6$$

$$+ (846.185 - 66.7025 l_\rho)\rho^7 + O(\rho^8), \tag{5.59}$$

where $l_\rho = \log \rho$. We compute the expansion up to order ρ^{40} but only show the first expansion terms here. It should be stressed here again, that these expressions for G_{ij} are functions of the constants A_2, B_1 and B_2 that appear in the definition of the evanescent operators.

In Figure 5.5, the NLO and NNLO contributions $G_{ij}^{(1)}$ and $G_{ij}^{(2)}$ are shown as a function of the mass ratio ρ.

To get an estimate of the size of the perturbative corrections to the decay width, we evaluate our result for numerical values of the quark masses in the on-shell scheme $m_b^{\text{OS}} = 4.7\,\text{GeV}$,
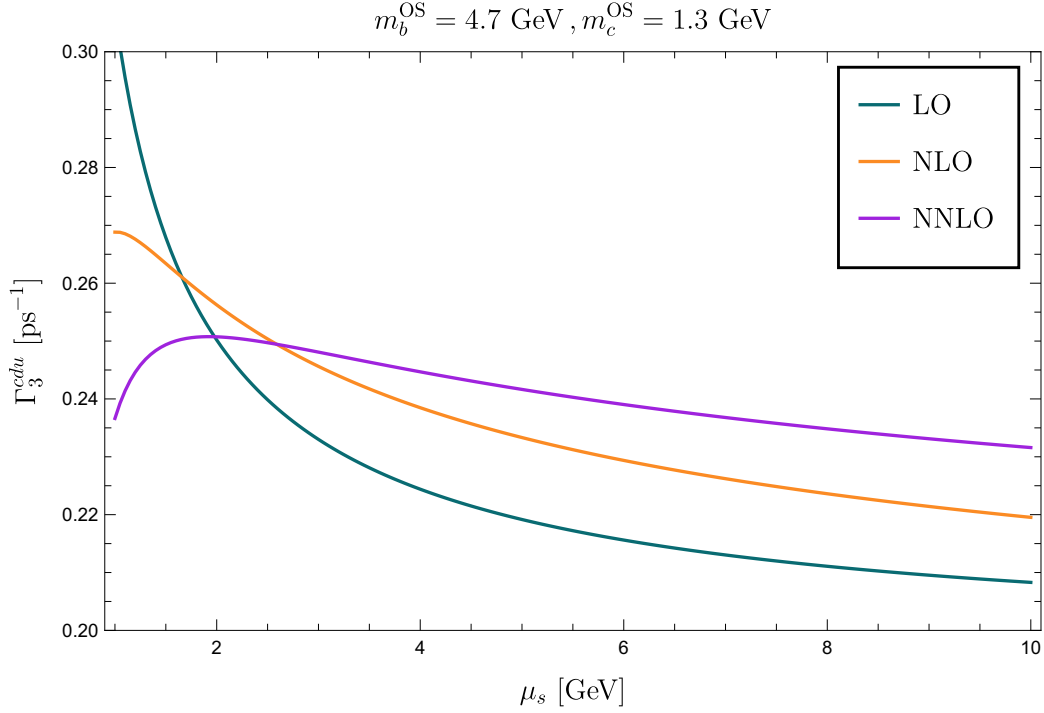
$$m_b^{\mathrm{OS}} = 4.7 \text{ GeV} \,, m_c^{\mathrm{OS}} = 1.3 \text{ GeV}$$

Figure 5.6.: The nonleptonic decay width Γ_3^{NL} for $b \rightarrow c\bar{u}d$ as a function of μ_s for the quark masses $m_b^{\mathrm{OS}} = 4.7$GeV, $m_c^{\mathrm{OS}} = 1.3$GeV in the on-shell scheme. The LO, NLO and NNLO results are shown in green, orange and purple respectively.

$m_c^{\mathrm{OS}} = 1.3 \,\text{GeV}$ and obtain

$$\Gamma_3^{cdu} = \Gamma_0 \left[1.89907 + 1.77538 \frac{\alpha_s}{\pi} + 14.1081 \left(\frac{\alpha_s}{\pi} \right)^2 \right], \tag{5.60}$$

with $\Gamma_0 = G_F^2 m_b^5 |V_{cb}|^2 |V_{ud}|^2 / (192\pi^3)$. In this result for the decay width, the dependence on the evanescent operator constants A_2, B_1 and B_2 drops out, which is demonstrated in the following:

For simplicity, we consider the same numerical values of the mass ratio ρ and the renormalization scale μ_s as in Equation (5.60). Note that the cancellation of the constants happens for arbitrary values of these parameters, we set them to numerical values only to keep the expressions compact. The constants A_2, B_1 and B_2 in the evanescent operators enter the $G_{ij}^{(2)}$. We replace B_1 and B_2 with A_2 using the relation given in Equation (5.39) and obtain

$$G_{11}^{(2)}(\rho = 1.3/4.7, \, \mu_s = 4.7 \,\text{GeV}) = 38.4337 - 2.43076 A_2 \,,$$
$$G_{22}^{(2)}(\rho = 1.3/4.7, \, \mu_s = 4.7 \,\text{GeV}) = 16.2384 - 2.43076 A_2 \,,$$
$$G_{12}^{(2)}(\rho = 1.3/4.7, \, \mu_s = 4.7 \,\text{GeV}) = -69.9077 - 3.31798 A_2 \,.$$

$$\tag{5.61}$$

This dependence should cancel against the A_2 terms that are introduced by the running of the matching coefficients. We perform the running of the matching coefficients in

the CMM basis and transform them via Equation (C.29) with the finite renormalization constants given in Equation (5.34) and (5.45) to the historical basis, where we again replace B_1 and B_2 with A_2 using Equation (5.39). At $\mu_s = 4.7\,\text{GeV}$ we then obtain the A_2-dependent matching coefficients

$$C_1(\mu_s = 4.7\,\text{GeV}) = -0.251101 + 1.09544\frac{\alpha_s}{\pi} + (2.90481 + 0.153875A_2)\left(\frac{\alpha_s}{\pi}\right)^2 + O(\alpha_s^3),$$

$$C_2(\mu_s = 4.7\,\text{GeV}) = 1.10867 - 0.503959\frac{\alpha_s}{\pi} + (-2.68677 + 0.61251A_2)\left(\frac{\alpha_s}{\pi}\right)^2 + O(\alpha_s^3).$$

$$(5.62)$$

The A_2 dependent terms that appear in the NNLO contributions in Equation (5.60) are introduced by the LO matching coefficients $C_i^{(0)}$ multiplied by the NNLO $G_{ij}^{(2)}$

$$\left(\frac{\alpha_s}{\pi}\right)^2 \left(C_1^{(0)\,2}G_{11}^{(2)} + C_1^{(0)}C_2^{(0)}G_{12}^{(2)} + C_2^{(0)\,2}G_{22}^{(2)}\right)$$

$$= \left(\frac{\alpha_s}{\pi}\right)^2 (\cdots - 3.875219915883491A_2),$$

$$(5.63)$$

and by the LO function $G_{ij}^{(0)}$ multiplied by NNLO matching coefficients $C_i^{(2)}$

$$\left(\frac{\alpha_s}{\pi}\right)^2 \left(C_1^{(2)}C_1^{(0)}G_{11}^{(0)} + (C_1^{(2)}C_2^{(0)} + C_1^{(0)}C_2^{(2)})G_{12}^{(0)} + C_2^{(2)}C_2^{(0)}G_{22}^{(0)}\right)$$

$$= \left(\frac{\alpha_s}{\pi}\right)^2 (\cdots + 3.875219915883492A_2).$$

$$(5.64)$$

Adding the two contributions in Equation (5.63) and Equation (5.64), we observe a cancellation of the A_2-terms with an accuracy of sixteen digits. The small remainder can be traced back to the precision of the semianalytic results that are used for the $G_{ij}^{(2)}$.

The result we obtain here for the decay width is expressed in terms of on-shell quark masses. The perturbative series of the on-shell mass shows a bad convergence behaviour and therefore the numerical value of the on-shell mass is not well-defined. Furthermore, the decay width is proportional to m_b^5, the results in the on-shell scheme has a large uncertainty induced by the quark masses m_c and m_b. A detailed discussion of more practical mass schemes and an analysis of the NNLO corrections in other mass schemes can be found in Chapter 6.

In Figure 5.6, the decay width as a function of the renormalization scale μ_s is shown for numerical values of the quark masses given above. The line colours denote the different orders of perturbation theory. Comparing the three lines shows a significant reduction of the scale uncertainty of the decay width. We estimate this uncertainty by dividing the difference between the minimal and maximal value in the interval $\{\mu_s/2, 2\mu_s\}$ around the central value $\mu_s = m_b = 4.7\,\text{GeV}$ by two. With this ansatz, we obtain a relative scale uncertainty of $\sim 7\%$ at LO, $\sim 6.5\%$ at NLO, and $\sim 3.5\%$ at NNLO compared to the central value at $\mu_s = m_b$. It is interesting to see that the NNLO corrections vanish at roughly $\mu_s \approx m_b/2$. In the region $\mu_s < 1.75\,\text{GeV}$, the breakdown of perturbation theory can be observed.

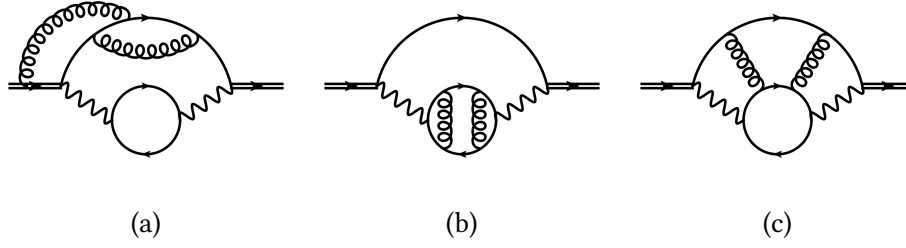(a)   (b)   (c)

Figure 5.7.: Sample Feynman diagrams for the three different diagram classes defined in Ref. [14]. The first class (a) denotes the semileptonic subset where gluons only couple to the external quark line. The second class (b) includes all diagrams where gluons are exchanged between internal quark lines. These contributions can be extracted from τ-lepton decays. The third class (c) includes all diagrams where the external and internal quark lines are connected by gluons.

Comparison to previous NNLO calculation of Ref. [14]

In Ref. [14], a first estimate of the nonleptonic decay width was made. The authors of Ref. [14] define three different sets of Feynman diagrams that contribute to the nonleptonic decay width:

- The semileptonic subset, shown in Figure 5.7 (a), where gluons are only attached to the bottom and charm quark propagators. This subset cancels in their result since they consider the ratio of nonleptonic and semileptonic decay width, so it is not given explicitly.

- The diagram subset where gluons are only exchanged inside the internal quark loop is shown in Figure 5.7 (b). This contribution corresponds to δ_1 in Equation (5.65). In Ref. [14] it is extracted directly from τ decays by using the R-ratio taken from Ref. [103]. Note that this is given as an expansion in α_s with three active flavours at the scale $\mu_s = m_\tau$.

- The third class includes all diagrams in which at least one gluon is exchanged between the internal quark loop and the external quark line. In the ansatz of Ref. [14], these diagrams only contribute starting from NNLO. Since they work with the Standard Model W-Boson, only the colour structure corresponding to the operator combination O_2-O_2 is present in their approach and therefore the corresponding NLO diagrams vanish by colour, which is not the case in our calculation.

The authors obtain a result for the decay width Γ^{cdu} which they give as a ratio to the semileptonic decay width Γ^{clv}:

$$\left. \frac{\Gamma_3^{cdu}}{3\Gamma_3^{clv}} \right|_{\rho \to 0} = 1 + \frac{\alpha_s}{\pi} + 4 \left(\log^2 \left(\frac{m_W}{m_b} \right) + \frac{15}{8} \log \left(\frac{m_W}{m_b} \right) + \delta_1 + \delta_2 \right) \left(\frac{\alpha_s}{\pi} \right)^2 + O\left(\alpha_s^3 \right), \quad (5.65)$$

where $\delta_1 \approx 1.3$ and $\delta_2 \approx 1.3$ [1]. δ_1 corresponds to the diagram class shown in Figure 5.7 (b), δ_2 gives the contribution of the diagram class in Figure 5.7 (c). The NNLO result is calculated under the assumption of massless quarks in the final state, meaning $\rho = 0$. It is interesting to see whether the calculation outlined in this thesis can reproduce these numbers.

As a first input, the semileptonic decay width is needed. Since the final state is considered to be massless, the semileptonic decay width is needed up to NNLO for $\rho = 0$, which can be extracted from our analytical results obtained in Chapter 4 or from any of the References [3, 4]. We obtain

$$\Gamma_3^{clv}\Big|_{\rho \to 0} = \Gamma_0 \left[1 + \frac{\alpha_s}{\pi} \left(\frac{25}{6} - \frac{2\pi^2}{3} \right) + \left(\frac{\alpha_s}{\pi} \right)^2 \left(\frac{226475}{2916} - \frac{24113\pi^2}{2916} + \frac{289\pi^4}{648} - \frac{53\pi^2}{27} l_2 \right. \right.$$

$$\left. \left. - \frac{6383}{162} \zeta(3) + \left(\frac{575}{72} - \frac{23\pi^2}{18} \right) \log \left(\frac{\mu_s^2}{m_b^2} \right) \right) \right] + O\left(\alpha_s^3\right) \tag{5.66}$$

$$= \Gamma_0 \left[-2.41307 \frac{\alpha_s}{\pi} + \left(-21.29552 - 4.62505 \log \left(\frac{\mu_s^2}{m_b^2} \right) \right) \left(\frac{\alpha_s}{\pi} \right)^2 \right] + O\left(\alpha_s^3\right) \tag{5.67}$$

For the nonleptonic decay width, which has the form

$$\Gamma_3^{cdu} = \Gamma_0 \left[C_1^2(\mu_s) G_{11} + C_1(\mu_s) C_2(\mu_s) G_{12} + C_2^2(\mu_s) G_{22} \right] , \tag{5.68}$$

the expression for the matching coefficients C_i and the G_{ij}, which are both functions of the renormalization scale μ_s, are given in Equations (5.48) and (5.57), (5.58), (5.59). The limit $\rho \to 0$ for the G_{ij} is obtained trivially from these expressions and reads

$$G_{11}\Big|_{\rho \to 0} = G_{22}\Big|_{\rho \to 0}$$

$$= 3 + \frac{\alpha_s}{\pi} \left(\frac{31}{2} - 2\pi^2 \right)$$

$$+ \left(\frac{\alpha_s}{\pi} \right)^2 \left(13.4947 + 14.1248 \log \left(\frac{\mu_s^2}{m_b^2} \right) + 3 \log^2 \left(\frac{\mu_s^2}{m_b^2} \right) \right) + O\left(\alpha_s^3\right) , \tag{5.69}$$

$$G_{12}\Big|_{\rho \to 0} = 2 + \frac{\alpha_s}{\pi} \left(-17 - \frac{4\pi^2}{3} \right)$$

$$+ \left(\frac{\alpha_s}{\pi} \right)^2 \left(-72.8419 - 61.2788 \log \left(\frac{\mu_s^2}{m_b^2} \right) - 9.66666 \log^2 \left(\frac{\mu_s^2}{m_b^2} \right) \right) + O\left(\alpha_s^3\right) . \tag{5.70}$$

With this information at hand, it is possible to reproduce the numbers in Equation (5.65). In order to reproduce the logarithms in Equation (5.65) one has to identify both the matching

---

[1] Note that there is an uncorrected typo in the arXiv version of Ref. [14] in the analytic expression for δ_2. In both, the arXiv and the published version, the numerical value of this contribution is given with $\delta_2 \approx 1.8$. However, evaluating the analytic expression for δ_2 in the published version yields $\delta_2 \approx 1.3$. One of the authors of Ref. [14] confirmed that this is the correct numerical value.

scale and the low scale with the bottom mass $\mu_w = \mu_s = m_b$. Identifying these scales means that the running of the Wilson coefficients is turned off which translates to ignoring the summation of large logarithms $\log(\mu_W/\mu_s)$ in our result. This ansatz yields for the ratio between the nonleptonic and semileptonic decay using our result for the nonleptonic decay width

$$
\left. \frac{\Gamma_3^{cdu}}{3\Gamma_3^{clv}} \right|_{\rho \to 0} = 1 + \frac{\alpha_s}{\pi} + 4 \left(\log^2 \left(\frac{m_W}{m_b} \right) + \frac{15}{8} \log \left(\frac{m_W}{m_b} \right) \right.
$$

$$
+ 2.87734 - 0.094796 n_c + 0.005895 n_h - 0.094796 n_l \right) \left(\frac{\alpha_s}{\pi} \right)^2 + O\left(\alpha_s^3 \right)
$$

$$
= 1 + \frac{\alpha_s}{\pi} + 4 \left(\log^2 \left(\frac{m_W}{m_b} \right) + \frac{15}{8} \log \left(\frac{m_W}{m_b} \right) + 2.50405 \right) \left(\frac{\alpha_s}{\pi} \right)^2 + O\left(\alpha_s^3 \right), \quad (5.71)
$$

which shows the same logarithmic behaviour as in Equation (5.65) and a non-logarithmic contribution which is close to $\delta_1 + \delta_2 \approx 2.6$. Since this previous calculation uses a different ansatz, the comparison of the final result is of limited use. However, it possible to cross-check different subsets of the calculation.

For cross-checks of Ref. [14], we consider the three diagram classes as defined before:

- The semileptonic subset, shown in Figure 5.7 (a):
  In our calculation ansatz, it is possible to extract this set of diagrams from the renormalized results and comparison to the literature [3, 5, 104] shows the expected agreement.

- The diagram subset where gluons are only exchanged inside the internal quark loop is shown in Figure 5.7 (b):
  In our approach, the separation of this diagram class is only possible for the operator combination O_2-O_2 at the level of the renormalized amplitude. For the other operator combinations, there are counterterms that contribute to both this class of diagrams and the third class. Therefore it is not possible to extract the renormalized expression for this set of diagrams in the ansatz presented in this work. However, a possible cross-check can be done using the τ decay R-ratio and the renormalized LO and NLO results. Using O_2-O_2 LO and NLO results given in Equations (5.50) and (5.53) and converting to the same scheme of active flavours as used in [103], we find agreement with our O_2-O_2 NNLO result.

- The third diagram class in which at least one gluon is exchanged between the internal quark loop and the external fermion line:
  Similar to the previous class of diagrams, it is not possible to extract the contribution of this class from the renormalized results because of the counterterms introduced by operator renormalization that contribute to both the second and third class.

Furthermore, we can compare the numerical values obtained in our calculation and Ref. [14]. We find

$$
\Gamma_{3\,\text{Ref. [14]}}^{cdu} = \Gamma_0 \left[3 - 4.2392 \frac{\alpha_s}{\pi} + \left(12L^2 + 22.5L + 12\delta_1 + 12\delta_2 - 71.12579 \right) \left(\frac{\alpha_s}{\pi} \right)^2 \right]
$$

$$= \Gamma_0 \left[3 - 4.2392 \frac{\alpha_s}{\pi} + 121.118 \left(\frac{\alpha_s}{\pi} \right)^2 \right] , \tag{5.72}$$

where $L = \log(m_W / m_b)$ and the values $m_b = 4.7$ GeV and $M_W = 81$ GeV have been used to obtain the numerical result in the second line. Since the authors of Ref. [14] assume massless charm quarks, these number should be compared to the massless limit of Γ_3^{cdu}, where we find

$$\Gamma_3^{cdu} \Big|_{\rho \to 0} = \Gamma_0 \left[3.31981 + 0.597456 \frac{\alpha_s}{\pi} - 25.645 \left(\frac{\alpha_s}{\pi} \right)^2 \right] , \tag{5.73}$$

We observe that the NNLO contributions of both approaches differ by about a factor five and have different signs. Also the NNLO contribution for finite charm mass in Equation (5.60) differs by a factor of ten from the corresponding term in Equation (5.65). This shows the importance of the resummation of the logs.

5.2.2. $b \to c\bar{c}s$

The calculation of the decay width $b \to c\bar{c}s$ is from a computational point of view the most challenging one of the nonleptonic decays since the two charm quarks in the final state lead to more massive propagators in the loop integrals. An additional subtlety in this decay channel is the occurrence of diagrams where a charm quark line is connected to the same four-quark operator twice. These *penguin-like topologies* appear via the insertion of current-current operators starting from NLO, see Figure 5.8 (c), (g) and (h) for sample Feynman diagrams. They form a finite gauge invariant subset which we will discuss separately in Section 5.3.2.

In this section we concentrate on the contribution where the charm quark lines of O_1 and O_2 do not form a closed loop. Sample Feynman diagrams for this contribution at NLO are shown in Figure 5.8 (a) and (b) and at NNLO in Figure 5.8 (d), (e) and (f). The $b \to c\bar{c}s$ decay channel always contains at least two massive charm quarks in the physical final state. Therefore, the phase space for this decay is zero for $\rho \geq 1/2$ in contrast to $b \to c\bar{u}d$. Furthermore, because of more massive propagators, the structure of the differential equations for the master integrals is way more complicated compared to the $b \to c\bar{u}d$ decay channel. For example, already at LO the solution of the differential equation for the master integrals contains square root letters which means that the solution cannot be expressed in terms of HPLs only. This makes the calculation of analytic solutions at LO and NLO more involved since we have to find a suitable variable transformation first in order to rationalize these letters. As outlined in Ref. [34], at LO and NLO level the variable transformation

$$\rho = \frac{x}{1 + x^2} \tag{5.74}$$

allows us to bring the differential equations of the master integrals into ϵ form. The analytic solution consists of iterated integrals over the alphabet

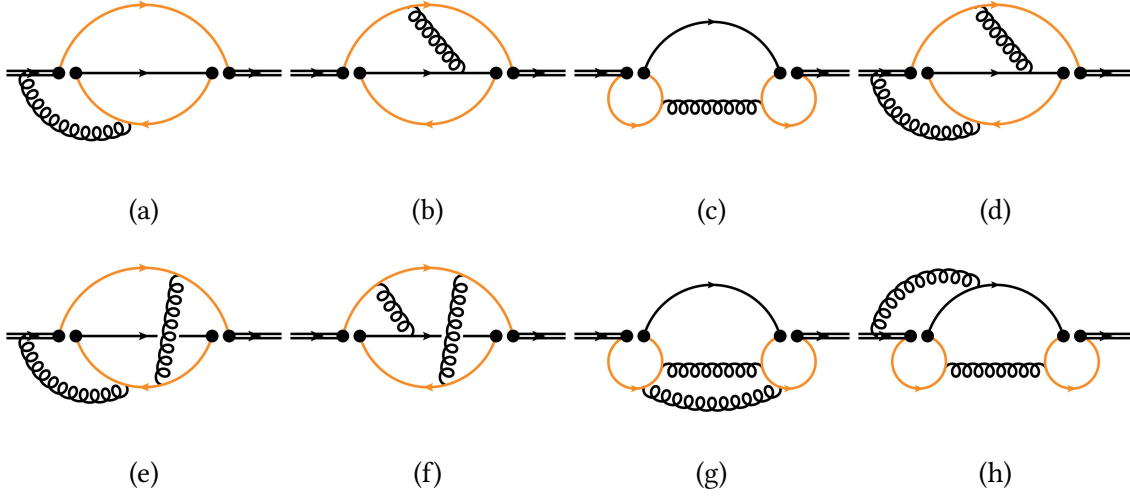$$\left\{ \frac{1}{x}, \frac{1}{1+x}, \frac{1}{1-x}, \frac{1}{1+x^2}, \frac{1}{1-x+x^2}, \frac{1}{1+x+x^2} \right\} , \tag{5.75}$$

Figure 5.8.: Sample Feynman diagrams for the decay channel $b \to c\bar{c}s$ at NLO (a), (b), (c) and NNLO (d), (e), (f), (g), (h). Examples for the penguin-like topologies are shown in (c), (g) and (h). Double black, orange and single black lines denote bottom, charm and massless quarks, respectively.

which correspond to cyclotomic harmonic polylogarithms [105], see Appendix B.4.2. In addition to the analytic solution of the LO and NLO master integrals, the `expand and match` ansatz is used for all master integrals at all orders in the $b \to c\bar{c}s$ decay channel. At LO and NLO, the singular points of the differential equation are

$$\rho_{\text{singular}} \in \{0, 1/2\} \,, \tag{5.76}$$

which correspond to the upper and lower bound of the considered values of ρ. As expansion points, we choose

$$\rho_0 = \{0, 1/5, 1/4, 1/3, 1/2\} \,, \tag{5.77}$$

where the expansion around $\rho_0 = 0$ has the structure of usual expansion ansatz around zero given in Equation (3.29) and the expansion around $\rho_0 = 1/2$ requires a square root ansatz given in Equation (3.26). For the other expansion points, a Taylor expansion is sufficient. We calculate the boundary conditions of the master integrals numerically with `AMFlow` at $\rho = 1/4$.

At LO, there are, similar to $b \to c\bar{u}d$, four diagrams which can be reduced to three master integrals and we obtain for the expansion around $\rho = 0$

$$G_{11}^{(0)} = G_{22}^{(0)} = \frac{3}{2}G_{12}^{(0)}$$
$$= 3\left(1 - 16\rho^2 + 24\rho^4 - 32\rho^6 + 2\rho^8 + 32\rho^{10} + \left(-48\rho^4 + 48\rho^8\right)l_\rho\right) + O\left(\rho^{12}\right) \,. \tag{5.78}$$

This result is obtained with the `expand and match` method. Nevertheless we give the expansion coefficients here as integers since the numerical precision is sufficiently high

(about 30 digits) to reconstruct the integer coefficients. This expression agrees with the results known in the literature [11, 106] and the limit $\rho \to 0$ agrees with the corresponding limit of the $b \to c\bar{u}d$ decay.

The analytic LO result reads:

$$
\begin{aligned}
G_{11}^{(0)} = G_{22}^{(0)} &= \frac{3}{2} G_{12}^{(0)} \\
&= \frac{3 \left(1 - x^2\right) \left(x^{12} - 8x^{10} - 43x^8 - 80x^6 - 43x^4 - 8x^2 + 1\right)}{\left(x^2 + 1\right)^7} \\
&\quad - \frac{144 \left(x^2 - x + 1\right) \left(x^2 + x + 1\right) \left(x^4 + 3x^2 + 1\right) x^4 \log(x)}{\left(x^2 + 1\right)^8} ,
\end{aligned}
\tag{5.79}
$$

which perfectly agrees with the `expand and match` result in Equation (5.78).

At NLO, we find 48 contributing diagrams that can be reduced to 26 master integrals. Note that the number of diagrams are the same as for the $b \to c\bar{u}d$ decay channel. However, the number of master integrals is larger which can be explained by the higher numbers of massive propagators appearing in the $b \to c\bar{c}s$ channel and the therefore more complex integral families, leading to more complicated IBP reductions and more master integrals. As mentioned above, the singular points of the differential equation do not change compared to LO and the same expansion points are chosen. The expansion around $\rho = 0$ yields

$$
\begin{aligned}
G_{11}^{(1)} =& - 4.23920 - \left(4.17265 + 192.000 l_\rho\right) \rho^2 + \left(355.654 + 967.654 l_\rho - 576.000 l_\rho^2\right) \rho^4 \\
& + \left(9.04556 - 1066.66 l_\rho - 128.000 l_\rho^2\right) \rho^6 \\
& - \left(723.224 + 602.321 l_\rho - 1264.00 l_\rho^2\right) \rho^8 + O\left(\rho^9\right) , \\
G_{22}^{(1)} =& - 4.23920 + \left(-162.0863 - 192.000 l_\rho\right) \rho^2 + 631.654 \rho^3 \\
& + \left(-478.086 + 843.827 l_\rho - 576.000 l_\rho^2\right) \rho^4 + \left(246.917 - 1770.66 l_\rho - 64.0000 l_\rho^2\right) \rho^6 \\
& - 631.654 \rho^7 + \left(-1207.13 + 190.227 l_\rho + 1440.00 l_\rho^2\right) \rho^8 + O\left(\rho^9\right) , \\
G_{12}^{(1)} =& - 30.1594 + \left(493.913 - 128.000 l_\rho\right) \rho^2 - 421.103 \rho^3 \\
& + \left(-328.000 + 1541.10 l_\rho - 384.000 l_\rho^2\right) \rho^4 + 842.206 \rho^5 \\
& + \left(646.319 - 406.880 l_\rho + 64.0000 l_\rho^2\right) \rho^6 - 1263.30 \rho^7 \\
& + \left(468.362 - 1468.92 l_\rho + 458.666 l_\rho^2\right) \rho^8 + O\left(\rho^9\right) ,
\end{aligned}
\tag{5.80}
$$

with $\mu_s = m_b$. Again, the limit $\rho \to 0$ agrees with the other decay channels. Furthermore, the result can be checked against Refs. [12, 11] where we find agreement. The analytic expressions are rather lengthy and therefore not shown here but can be found in computer readable form in the ancillary files of Ref. [34].

The NNLO contribution of the $b \to c\bar{c}s$ channel is the most complicated one concerning the IBP reduction and the calculation of the master integrals. For the 1308 diagrams,

we find 644 master integrals after IBP reduction. For the IBP reduction, `kira` together with `fermat` was used in a first approach. This attempt was however not successful for reducing all of the 49 integral families, especially some of the families with six massive propagators could not be reduced with `fermat`. Also a second approach where sectors with vanishing imaginary part were excluded from the reduction process was not successful. However, when using `kira` with `firefly` instead of `fermat`, the problematic families could be reduced within a couple of days.

At NNLO, in addition to the two massive particle cut at $\rho = 1/2$, there are physical final states with four charm quarks, see Figure 5.1 (d). This can be also observed when considering the singular points of the NNLO differential equation

$$\rho_{\text{singular}} \in \{0, 1/4, 1/2\} \,, \tag{5.81}$$

where the pole at at $\rho = 1/4$ stems from the four charm threshold. Since this threshold has an even number of massive particles, the master integral expansion around this point would require an expansion ansatz including square roots as given in Equation (3.26). Because of the relatively big number of master integrals and because we were not successful finding a good basis for these integrals, this expansion around the threshold would be a very expensive calculation requiring a large amount of computing resources. We try to avoid this by producing `AMFlow` results both above and below this threshold, at $\rho = 1/5$ and $\rho = 1/3$ and match them directly to Taylor expansions around these two expansion points independently. In addition, we compute the expansion around $\rho = 0$, which is also expensive but still cheap compared to the square root ansatz. In total, the expansion points are

$$\rho_0 = \{0, 1/5, 1/3\} \,. \tag{5.82}$$

The expansion around zero is then matched to the expansion around $\rho_0 = 1/5$. With these expansions at hand, it is not possible to describe the exact physical behaviour including square roots and logs around the threshold. However, the four charm contribution is expected to be relatively small and therefore the convergence of the Taylor expansions near the threshold should be quite good. To check this, we assemble the renormalized amplitude with the integrals expanded around $\rho_0 = 1/3$ and $\rho_0 = 1/5$ and take the difference of these results in the range $\rho \in [1/5, 1/3]$. In Figure 5.9, we show the renormalized NNLO amplitude for $b \to c\bar{c}s$ assembled with the master integral expansions around the expansion points $\rho_0 = 0$, $\rho_0 = 1/5$ and $\rho_0 = 1/3$. The relative differences of these three expansions are shown in Figure 5.9 in the lower plots. We observe that the relative difference of the Taylor expansions around $\rho_0 = 1/5$ and $\rho_0 = 1/3$ is of the order of $\leq 10^{-10}$ at the four particle threshold $\rho = 1/4$. Because of the good agreement there is no need for a threshold expansion around $\rho = 1/4$ and it is sufficient to use the expansion around $\rho = 1/3$ below and $\rho = 1/5$ above the threshold for phenomenological analyses.

For convenience we give the results for $G_{ij}^{(2)}$ around $\rho = 0$. They read:

$$\begin{aligned} G_{11}^{(2)} =& 13.4947 - 24.6740\rho + \left(-533.154 - 1251.35 l_\rho + 16.0000 l_\rho^2\right) \rho^2 \\ &+ \left(2998.33 + 210.551 l_\rho\right) \rho^3 + \left(116.662 + 10686.6 l_\rho - 628.278 l_\rho^2 + 64.0000 l_\rho^3\right) \rho^4 \end{aligned}$$
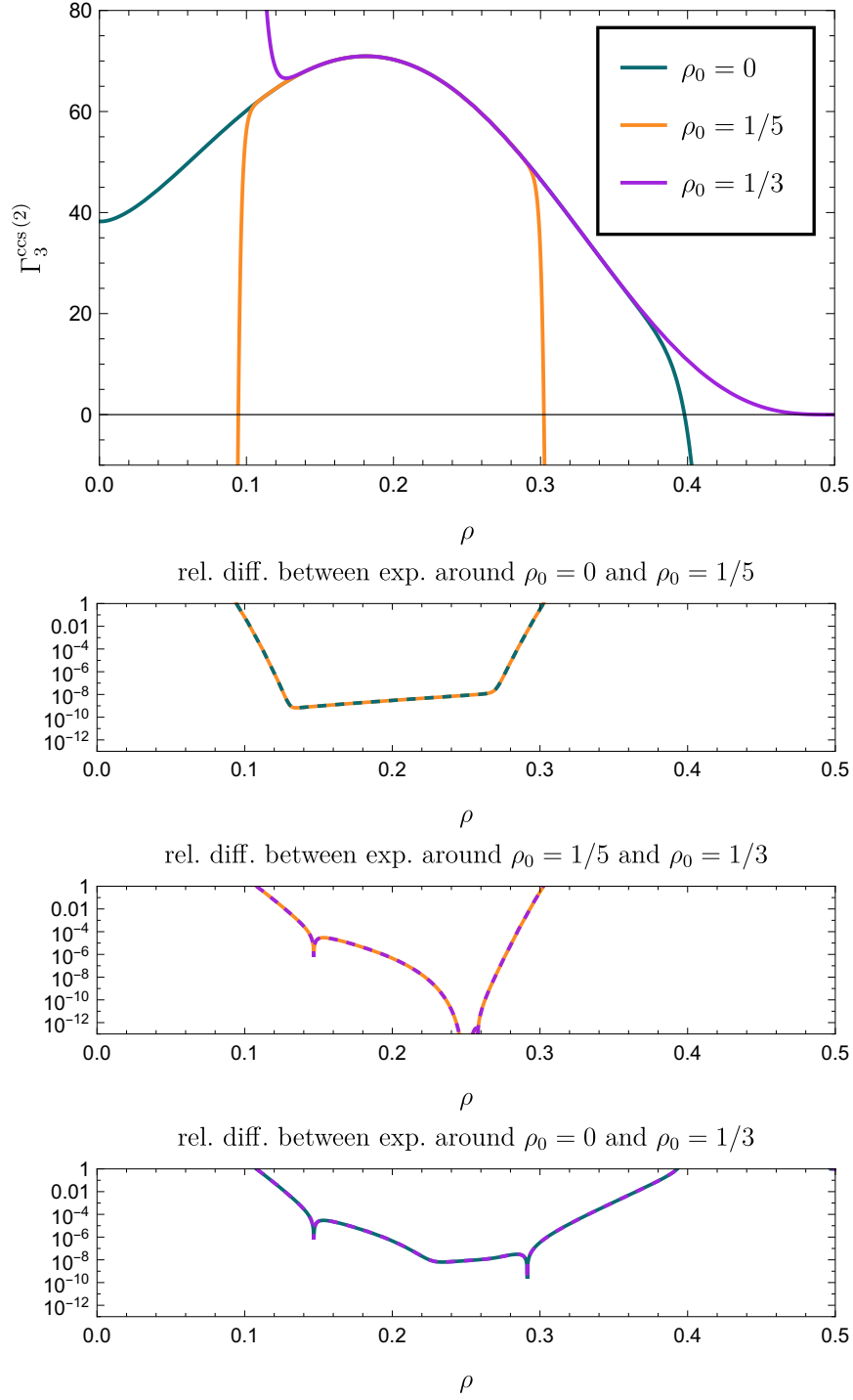
Figure 5.9.: The renormalized NNLO amplitude of the decay width $b \to c\bar{c}s$ using three different sets of master integral expansions shown in green, orange and purple in the top plot. The three lower panels show the relative difference between the three expressions obtained with the three different expansions. We observe good agreement in the physical interesting region around the four-charm threshold at $\rho = 1/4$.
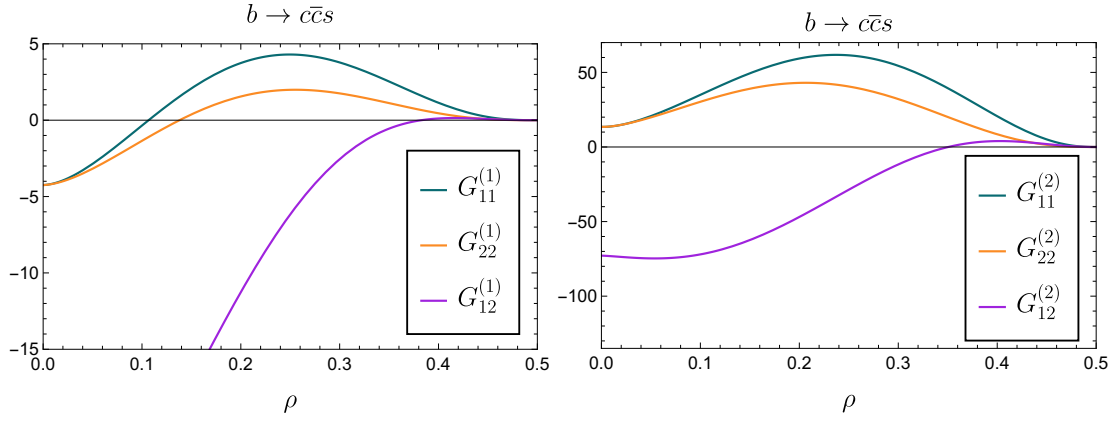
Figure 5.10.: The NLO and NNLO G_{ij} for the decay channel $b \to c\bar{c}s$ as functions of the mass ratio ρ.

$$+ \left(-2364.37 + 903.617 l_\rho\right) \rho^5 + \left(5409.89 - 6392.16 l_\rho - 5833.18 l_\rho^2 - 507.259 l_\rho^3\right) \rho^6$$

$$+ \left(-135.120 + 3582.30 l_\rho\right) \rho^7 + \left(-2320.40 - 15254.6 l_\rho + 6047.29 l_\rho^2 + 2654.91 l_\rho^3\right) \rho^8$$

$$+ O(\rho^9), \tag{5.83}$$

$$G_{22}^{(2)} = 13.4947 - 24.6740\rho + \left(-3295.69 - 1883.01 l_\rho + 16.0000 l_\rho^2\right) \rho^2$$

$$+ \left(190.918 - 3842.56 l_\rho\right) \rho^3 + \left(4770.24 + 5244.57 l_\rho - 347.178 l_\rho^2 + 64.0000 l_\rho^3\right) \rho^4$$

$$+ \left(1299.89 - 542.170 l_\rho\right) \rho^5 + \left(5832.60 - 7262.42 l_\rho - 10760.9 l_\rho^2 - 271.407 l_\rho^3\right) \rho^6$$

$$+ \left(1667.93 + 1806.31 l_\rho\right) \rho^7 + \left(-30465.4 - 19154.5 l_\rho + 9435.28 l_\rho^2 + 4491.90 l_\rho^3\right) \rho^8$$

$$+ O(\rho^9), \tag{5.84}$$

$$G_{12}^{(2)} = -72.8419 - 16.4493\rho + \left(3160.66 + 1152.54 l_\rho + 10.6666 l_\rho^2\right) \rho^2$$

$$+ \left(3980.72 + 2702.07 l_\rho\right) \rho^3 + \left(-5915.68 + 8133.91 l_\rho + 3393.24 l_\rho^2 + 42.6666 l_\rho^3\right) \rho^4$$

$$+ \left(-8194.22 + 5070.78 l_\rho\right) \rho^5 + \left(18013.7 + 3710.59 l_\rho + 1222.25 l_\rho^2 + 278.518 l_\rho^3\right) \rho^6$$

$$+ \left(184.414 + 7746.34 l_\rho\right) \rho^7 + \left(7997.58 + 2111.25 l_\rho - 9970.14 l_\rho^2 - 773.168 l_\rho^3\right) \rho^8$$

$$+ O(\rho^9). \tag{5.85}$$

In Figure 5.10, the NLO and NNLO corrections to different combinations of operator insertions are shown as functions of ρ. Note that we only plot the interval $\rho \in [0, 1/2]$ here since the phase space of this decay channel is zero for $\rho > 1/2$. Again, the limit $\rho \to 0$ is the same as for the other decay channels.

Evaluating the renormalized amplitude for the on-shell masses $m_c^{\mathrm{OS}} = 1.3\,\mathrm{GeV}$ and $m_b^{\mathrm{OS}} = 4.7\,\mathrm{GeV}$ at $\mu_s = m_b^{\mathrm{OS}}$, yields

$$\Gamma_3^{csc} = \Gamma_0 \left[0.86706 + 3.15768 \frac{\alpha_s}{\pi} + 37.3426 \left(\frac{\alpha_s}{\pi}\right)^2\right], \tag{5.86}$$
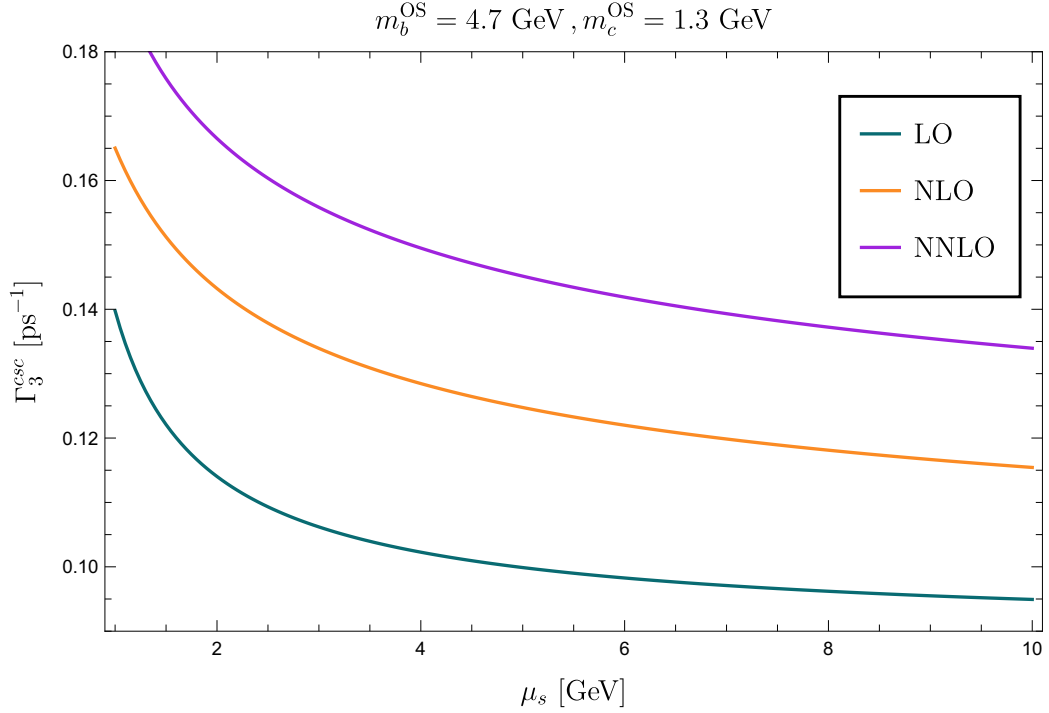
Figure 5.11.: The nonleptonic decay width Γ_3^{NL} for $b \to c\bar{c}s$ as a function of μ_s in the on-shell mass scheme. In this plot, neither contributions from penguin operators nor contributions from penguin-like topologies are included.

with $\Gamma_0 = G_F^2 m_b^5 |V_{cb}|^2 |V_{sc}|^2 / (192\pi^3)$ In Figure 5.11, the LO, NLO and NNLO contributions are shown as a function of the renormalization scale μ_s. As it was already observed in previous works [11, 13, 33], the NLO corrections in this decay channel are quite large, which is also true for the NNLO corrections. For $\mu_s = m_b$ the NLO and NNLO corrections are of the order of about 25% and 16% of the LO result, respectively.

5.2.3. $b \to u\bar{c}s$

The decay channel $b \to u\bar{c}s$ is very similar to $b \to c\bar{u}d$ since it has the same number of massive and massless quarks in the final state. In fact, it is possible to map the Feynman diagrams of the $b \to u\bar{c}s$ channel to the same scalar integral families that were defined for $b \to c\bar{u}d$, and we can reduce all occurring loop integrals to the same set of master integrals. From a practical point of view, the calculation of the bare amplitude of this decay channel therefore only requires a new IBP redcution of a integrals that did not appear in the $b \to c\bar{u}d$ amplitude. After IBP reduction, we insert the previously calculated analytic master integrals at LO and NLO and the `expand` and `match` expansions at NNLO for the master integrals.

At LO, the result is identical to the one of $b \to c\bar{u}d$ in Equation (5.50). Starting from NLO, the results differ from the $b \to c\bar{u}d$ case. We obtain

$$G_{11}^{(1)} = \frac{31}{2} - \frac{554}{3}\rho^2 + \frac{554}{3}\rho^6 - \frac{31}{2}\rho^8 + \pi^2 \left(-2 + 16\rho^2 + 48\rho^4 - \frac{16}{3}\rho^6 + \frac{2}{3}\rho^8 + 32\rho^4 H_0(\rho) \right)$$

$$
+ \left(-\frac{62}{3} + \frac{640}{3}\rho^2 - \frac{640}{3}\rho^6 + \frac{62}{3}\rho^8 \right) H_{-1}(\rho) + \left(-288\rho^4 - 64\rho^6 + 8\rho^8 \right) (H_0(\rho))^2
$$

$$
+ \left(-96\rho^2 - 120\rho^4 + \frac{992}{3}\rho^6 - \frac{124}{3}\rho^8 \right) H_0(\rho) + \left(\frac{62}{3} - \frac{640}{3}\rho^2 + \frac{640}{3}\rho^6 - \frac{62}{3}\rho^8 \right) H_1(\rho)
$$

$$
+ \left(8 - 64\rho^2 - 576\rho^4 - 64\rho^6 + 8\rho^8 \right) \left[H_{0,1}(\rho) - H_{0,-1}(\rho) \right], \tag{5.87}
$$

$$
G_{22}^{(1)} = G_{11}^{(1)}, \tag{5.88}
$$

$$
G_{12}^{(1)} = -17 + \frac{932}{9}\rho^2 - \frac{932}{9}\rho^6 + 17\rho^8 + \left(-\frac{224}{3}\rho^2 + \frac{2048}{3}\rho^4 + \frac{4384}{9}\rho^6 - \frac{344}{9}\rho^8 \right) H_0(\rho)
$$

$$
+ \pi^2 \left(-\frac{4}{3} + \frac{80}{3}\rho^2 - \frac{256}{3}\rho^3 + 96\rho^4 - \frac{256}{3}\rho^5 - \frac{16}{9}\rho^6 + \frac{20}{9}\rho^8 + \frac{128}{3}\rho^4 H_0(\rho) \right)
$$

$$
+ \left(-\frac{100}{9} + \frac{1952}{9}\rho^2 - \frac{1952}{9}\rho^6 + \frac{100}{9}\rho^8 + \left(-\frac{32}{3} - \frac{128}{3}\rho^2 - \frac{1024}{3}\rho^3 - 576\rho^4 \right. \right.
$$

$$
\left. \left. - \frac{1024}{3}\rho^5 - \frac{128}{3}\rho^6 - \frac{32}{3}\rho^8 \right) H_0(\rho) \right) H_{-1}(\rho) + \left(-192\rho^4 - 64\rho^6 + 16\rho^8 \right) (H_0(\rho))^2
$$

$$
+ \left(\frac{100}{9} - \frac{1952}{9}\rho^2 + \frac{1952}{9}\rho^6 - \frac{100}{9}\rho^8 + \left(\frac{32}{3} + \frac{128}{3}\rho^2 - \frac{1024}{3}\rho^3 + 576\rho^4 \right. \right.
$$

$$
\left. \left. - \frac{1024}{3}\rho^5 + \frac{128}{3}\rho^6 + \frac{32}{3}\rho^8 \right) H_0(\rho) \right) H_1(\rho)
$$

$$
+ \left(\frac{16}{3} + \frac{448}{3}\rho^2 + \frac{1024}{3}\rho^3 + 1152\rho^4 + \frac{1024}{3}\rho^5 + \frac{448}{3}\rho^6 + \frac{16}{3}\rho^8 \right) H_{0,-1}(\rho)
$$

$$
+ \left(-\frac{16}{3} - \frac{448}{3}\rho^2 + \frac{1024}{3}\rho^3 - 1152\rho^4 + \frac{1024}{3}\rho^5 - \frac{448}{3}\rho^6 - \frac{16}{3}\rho^8 \right) H_{0,1}(\rho). \tag{5.89}
$$

One observes that the coefficients $G_{22}^{(1)}$ and $G_{11}^{(1)}$ are the same in this decay channel.
At NNLO, we use the expansions for the master integrals obtained with the `expand and match` approach and obtain a piecewise defined solution. The renormalized NNLO result expanded around $\rho = 0$ up to order ρ^8 reads

$$
G_{11}^{(2)} = 13.4947 - 24.6740\rho + \left(-552.675 - 591.011 l_\rho - 8.00000 l_\rho^2 \right) \rho^2
$$

$$
+ \left(3314.34 + 210.551 l_\rho \right) \rho^3 + \left(-1000.88 + 5447.49 l_\rho - 505.906 l_\rho^2 - 64.0000 l_\rho^3 \right) \rho^4
$$

$$
+ \left(387.348 + 328.986 l_\rho \right) \rho^5 + \left(-2248.02 + 240.114 l_\rho + 1066.01 l_\rho^2 - 264.296 l_\rho^3 \right) \rho^6
$$

$$
+ \left(-159.907 + 306.177 l_\rho \right) \rho^7 + \left(306.693 - 508.164 l_\rho + 133.563 l_\rho^2 - 66.3703 l_\rho^3 \right) \rho^8
$$

$$
+ O(\rho^9), \tag{5.90}
$$

$$
G_{22}^{(2)} = G_{11}^{(2)}, \tag{5.91}
$$

$$
G_{12}^{(2)} = -72.8419 - 16.4493\rho + \left(3424.97 + 1112.31 l_\rho + 5.33333 l_\rho^2 + \right) \rho^2
$$

$$
+ \left(7782.51 + 5404.15 l_\rho \right) \rho^3 + \left(-72.4205 + 15986.63 l_\rho + 727.426 l_\rho^2 - 42.6666 l_\rho^3 \right) \rho^4
$$

$$
+ \left(-2108.79 + 9301.11 l_\rho \right) \rho^5 + \left(-8020.41 + 2479.56 l_\rho + 1176.61 l_\rho^2 - 311.703 l_\rho^3 \right) \rho^6
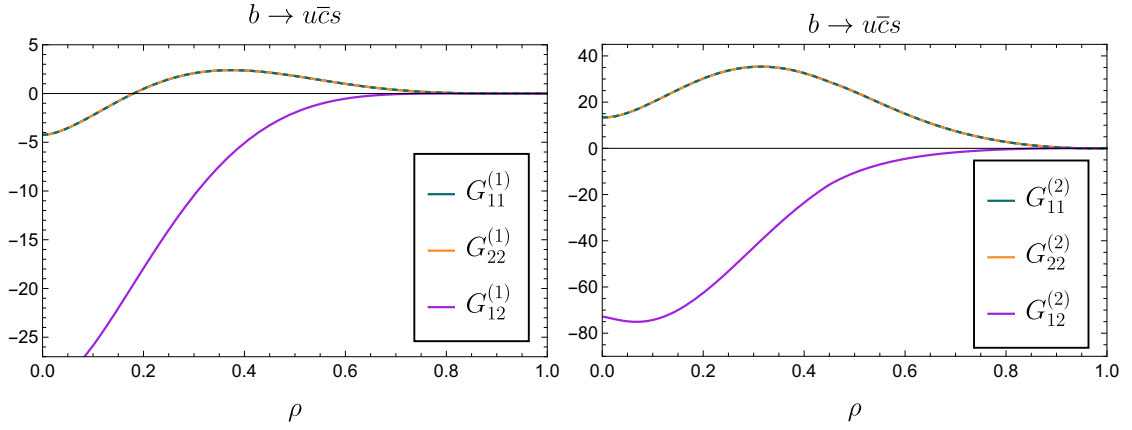$$

Figure 5.12.: The NLO and NNLO G_{ij} for the decay channel $b \to u\bar{c}s$ as functions of the mass ratio ρ. Since $G_{11}^{(n)}$ and $G_{22}^{(n)}$ have the same value in this decay channel, they are shown as dashed lines.

$$+ \left(629.490 + 1924.62 l_\rho \right) \rho^7 + \left(-1269.71 - 34.1428 l_\rho - 26.6329 l_\rho^2 + 81.3497 l_\rho^3 \right) \rho^8$$

$$+ O(\rho^9) . \tag{5.92}$$

Again we find agreement with the other decay channels in the massless limit $\rho \to 0$. In Figure 5.13, the LO, NLO and NNLO decay width for $b \to u\bar{c}s$ is shown as a function of the renormalization scale in the pole mass scheme. One observes a similar behaviour of the μ_s dependence compared to the $b \to c\bar{u}d$ decay. Note the scaling of the y-axis compared to the analogue plots of $b \to c\bar{u}d$ and $b \to c\bar{c}s$ in Figure 5.6 and 5.11. The absolute value of Γ_3^{usc} is much smaller than the previously discussed decay widths since its prefactor Γ_0 includes the CKM suppressed matrix element V_{ub} instead of V_{cb}. At the central scale $\mu_s = m_b$ we obtain for the decay rate

$$\Gamma_3^{usc} = \Gamma_0 \left[1.89907 + 4.39458 \frac{\alpha_s}{\pi} + 23.7335 \left(\frac{\alpha_s}{\pi} \right)^2 \right] , \tag{5.93}$$

with $\Gamma_0 = G_F^2 m_b^5 |V_{ub}|^2 |V_{cs}|^2 / (192\pi^3)$.

5.2.4. $b \to u\bar{u}d$

Note that, similar to $b \to u\bar{c}s$, also the $b \to u\bar{u}d$ decay channel comes with a CKM suppression compared to the dominant $b \to c\bar{u}d$ and $b \to c\bar{c}s$ decay channels and therefore only contributes to the total decay width of the B mesons at the order of 1% or less. At LO and NLO, all physical final states of the $b \to u\bar{u}d$ decay channel include only massless particles. At NNLO, there are contributions from secondary charm quark production, similar to $b \to ul\bar{\nu}$ discussed in Section 4.4. We proceed in a similar manner here. For the charm mass independent contribution of massless particle final states, we consider the limit $\rho \to 0$ limit of any of the three previously described decay modes. For

$$m_b^{\mathrm{OS}} = 4.7 \text{ GeV}, m_c^{\mathrm{OS}} = 1.3 \text{ GeV}$$
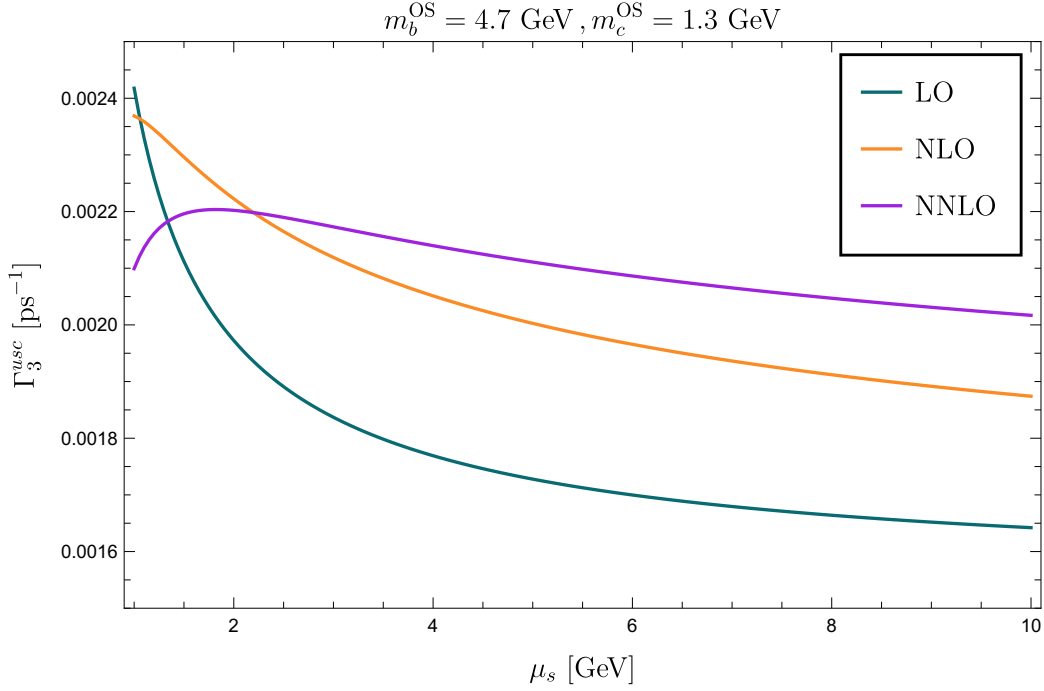
Figure 5.13.: The nonleptonic decay width Γ_3^{NL} for $b \rightarrow u\bar{c}s$ as a function of μ_s.

the charm quark mass dependent contribution at NNLO, an additional calculation has to be performed. We parametrize the decay width as follows:

$$\Gamma_3^{udu} = \frac{G_F^2 m_b^5 |V_{ub}|^2 |V_{ud}|^2}{192\pi^3} \left[X_0 + \frac{\alpha_s}{\pi} X_1 + \left(\frac{\alpha_s}{\pi} \right)^2 (X_2 + U_C(\rho)) \right] + \mathcal{O}\left(\alpha_s^3 \right). \tag{5.94}$$

The LO result, obtained by taking the limit $\rho \rightarrow 0$ of Equation (5.50) yields

$$G_{11}^{(0)} = G_{22}^{(0)} = \frac{3}{2} G_{12}^{(0)} = 3, \tag{5.95}$$

whereas at NLO, we obtain

$$G_{11}^{(1)} = G_{22}^{(1)} = \frac{31}{2} - 2\pi^2,$$
$$G_{12}^{(1)} = -17 - \frac{4}{3}\pi^2, \tag{5.96}$$

from Equations (5.52), (5.53), (5.54).

At NNLO, diagrams with cuts through five quarks including two massive charm quarks have to be considered, see Figure 5.14 (c). As given in Equation (5.94), the NNLO contributions split into a charm mass independent part and the contribution coming from these massive charms in the final state, which is labelled by U_C. The charm mass independent terms can be extracted from the decay width Γ_3^{cdu} by taking the limit $\rho \rightarrow 0$ and setting $n_h = 1$, $n_c = 0$, $n_l = 3$:

$$G_{11}^{(2)} = G_{22}^{(2)} = 8.19157, $$
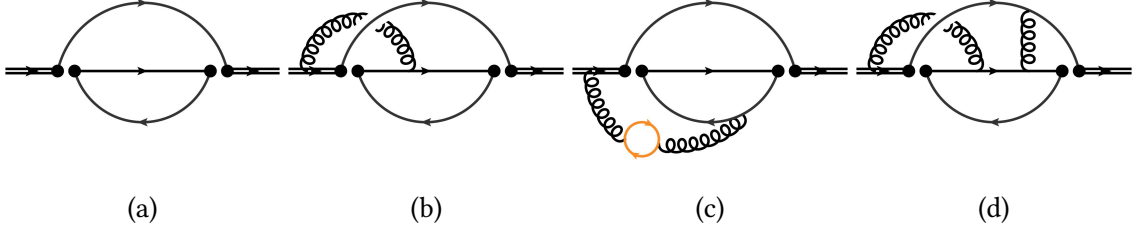
Figure 5.14.: Four sample Feynman diagrams for the $b \to u\bar{u}d$ decay channel at LO, NLO and NNLO. At NNLO, diagrams like (c) can produce final states with two charm quarks. Double black lines, orange lines and single black lines denote bottom quarks, charm quarks and massless quarks, respectively.

$$G_{12}^{(2)} = -85.6741 \,. \tag{5.97}$$

The U_C contribution is calculated separately. We find 48 contributing diagrams that can be reduced to 21 master integrals. The differential equation for these integrals has the singular points

$$\rho_{\text{singular}} \in \{0, 1/2\} \,, \tag{5.98}$$

where $\rho = 1/2$ corresponds to the physical two charm threshold. We solve this differential equation by using the expand and match approach. As an AMFlow starting point, we choose $\rho = 1/3$ and construct expansions around the points

$$\rho_0 = \{0, 1/3, 1/2, 7/10, 1\} \,. \tag{5.99}$$

For the expansion around $\rho_0 = 0$, we find for the U_C contribution the following expressions for the renormalized amplitude:

$$
\begin{aligned}
G_{11}^{(2)}\Big|_{U_C} &= 5.30314 - 24.6740\rho + 100.939\rho^2 + \left(239.797 + 210.552l_\rho\right)\rho^3 \\
&\quad + \left(-192.357 + 276.102l_\rho - 16l_\rho^2\right)\rho^4 - 147.386\rho^5 \\
&\quad + \left(72.5468 + 54.8845l_\rho - 14.2222l_\rho^3\right)\rho^6 - 67.773\rho^7 \\
&\quad + \left(-5.14049 - 10.9009l_\rho + 8.2l_\rho^2 - 2.66667l_\rho^3\right)\rho^8 + O\left(\rho^9\right) \,,
\end{aligned}
\tag{5.100}
$$

$$G_{22}^{(2)}\Big|_{U_C} = G_{11}^{(2)}\Big|_{U_C} \,, \tag{5.101}$$

$$
\begin{aligned}
G_{12}^{(2)}\Big|_{U_C} &= 12.8321 - 16.4493\rho - 12.3713\rho^2 + 93.9440\rho^3 + \left(75.3569 + 136.068l_\rho\right. \\
&\quad \left. -10.6667l_\rho^2\right)\rho^4 - 449.177\rho^5 + \left(-59.7255 - 440.577l_\rho + 40.2963l_\rho^2 + 42.6667l_\rho^3\right)\rho^6 \\
&\quad + 481.261\rho^7 + \left(4.80436 - 0.0700806l_\rho 3.33333l_\rho^2 + 12.4444l_\rho^3\right)\rho^8 + O\left(\rho^9\right) \,. \tag{5.102}
\end{aligned}
$$

Inserting the numerical values for the matching coefficients, setting the renormalization scale $\mu_s = m_b^{\text{OS}}$, the decay width is obtained to be

$$\Gamma_3^{udu} = \Gamma_0 \left[3.31981 + 0.597456\frac{\alpha_s}{\pi} + \left(-25.645 + 0.254978_{U_C}\right)\left(\frac{\alpha_s}{\pi}\right)^2\right] \,, \tag{5.103}$$

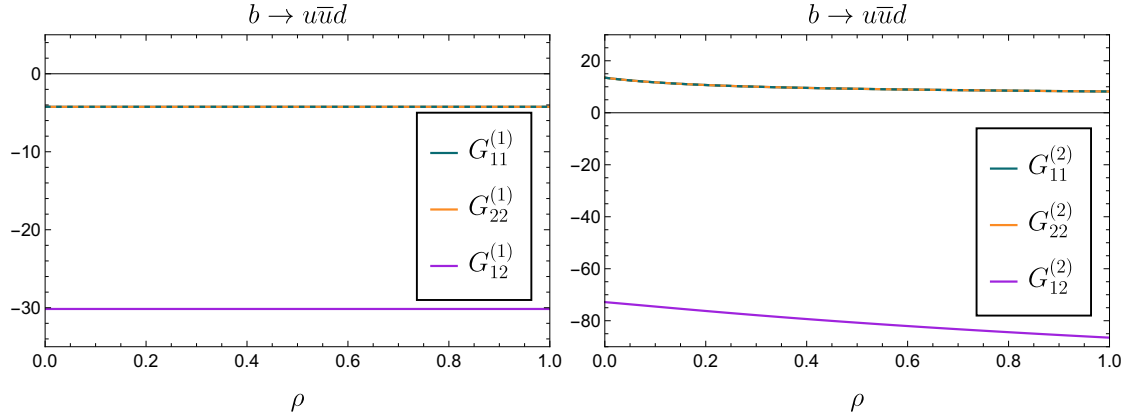Figure 5.15.: The NLO and NNLO G_{ij} for the decay channel $b \to u\bar{u}d$ as functions of the mass ratio ρ. Similar to the $b \to u\bar{c}s$ decay, we show $G_{ii}^{(n)}$ as dashed lines to make both of them visible. Note that the NLO functions are constant in ρ and charm quark mass effects only appear at NNLO.

for the numerical values $m_c^{\text{OS}} = 1.3\,\text{GeV}$ and $m_b^{\text{OS}} = 4.7\,\text{GeV}$ for the quark masses in the on-shell scheme, where $\Gamma_0 = G_F^2 m_b^5 |V_{ub}|^2 |V_{ud}|^2/(192\pi^3)$. The U_C contribution is flagged separately here and amounts to around 1% of the NNLO contribution. The nonleptonic decay width $b \to u\bar{u}d$ as a function of μ_s is shown in Figure 5.16. Note that this plot only includes the non-penguin contributions. One observes that the NNLO corrections are very small for large values of $\mu_s > 8\,\text{GeV}$ and negative for small values of μ_s. The dependence on μ_s is reduced significantly when going from LO to NLO and NNLO in the region $2\,\text{GeV} \leq \mu_s \leq 10\,\text{GeV}$.

Similar to the $b \to c\bar{c}s$ decay channel, the final states of the decay $b \to u\bar{u}d$ include two quarks of the same type and therefore obtain additional contributions from penguin operators and penguin-like topologies to the standard contributions. The calculation of such contributions are outlined in the next Section 5.3.
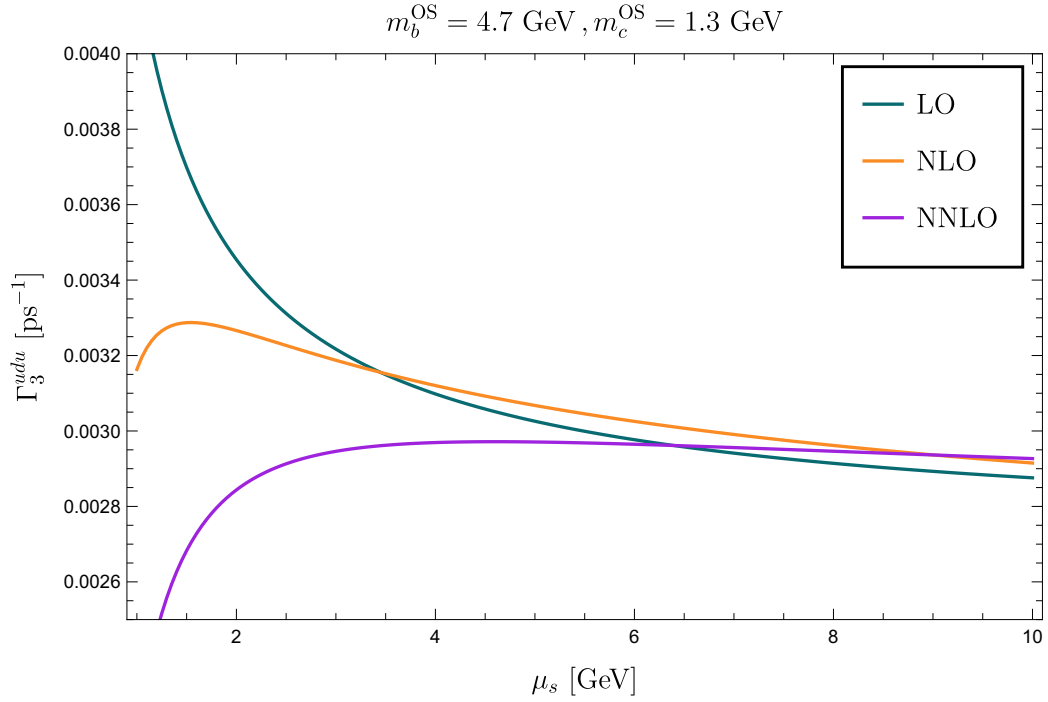
Figure 5.16.: The nonleptonic decay width for $b \rightarrow u\bar{u}d$ as a function of μ_s.

5.3. Penguin-like topology contributions

In this Section, the calculation of the penguin-like topologies with the insertion of current-current operators is outlined. This special class of topologies only contributes in decay channels with quark and antiquark of the same flavour in the final state, for example $b \rightarrow c\bar{c}s$ and $b \rightarrow u\bar{u}d$. Sample diagrams for the Penguin topologies at NLO and NNLO are shown in Figure 5.17.

In order to renormalize these topologies up to NNLO, we need counterterms from LO and NLO diagrams with the insertion of current-current operators O_1, O_2 the penguin operators O_3, O_4, O_5, O_6 and O_8, since these operators mix with the current-current operators under renormalization. For the counterterms introduced by the penguin operators O_{3-6} we need LO diagrams with up to two penguin operator insertions and NLO diagrams with one penguin and one current-current operator insertion. Sample diagrams for such counterterms are shown in Figure 5.18 (a) - (f).

In the calculations of diagrams with double insertions of current-current operators discussed in Chapter 5, a problem with closed fermion lines that lead to undefined traces over γ_5 was encountered. This problem was solved using Fierz identities which reduced the number of fermion lines from two to one. However, this procedure is not necessary when considering the insertion of one penguin and one current-current operator since such an operator combination leads to only on fermion trace in the non-penguin-like topologies, see for example Figure 5.18 (c) and (d). Therefore the usage of Fierz identities is not necessary here.

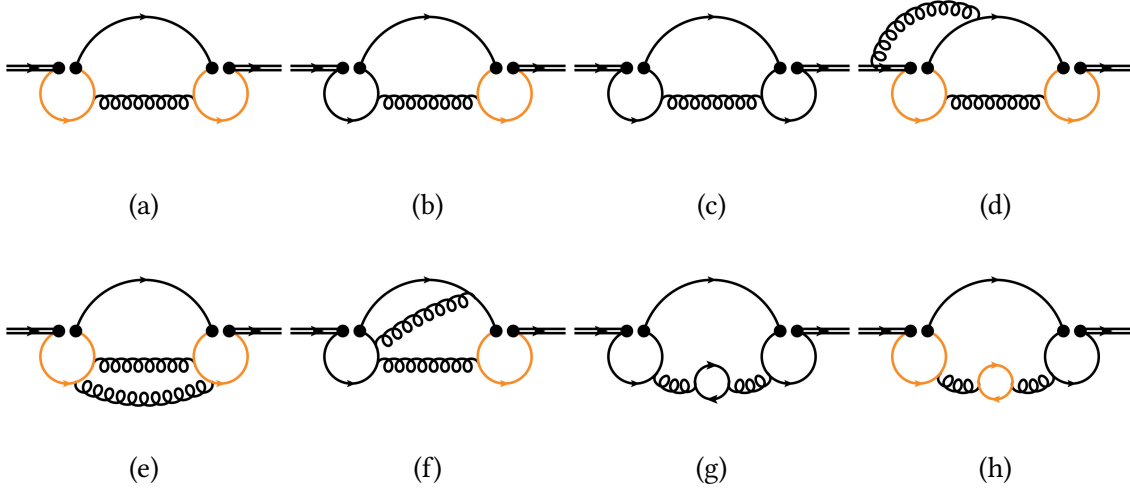Since the chromomagnetic operator O_8 is proportional to the strong coupling g_s, diagrams

Figure 5.17.: Sample diagrams for the penguin-like topologies with the insertion of two current-current operators at NLO and NNLO. The penguin-like topology diagrams contribute to the decay width $b \to c\bar{c}s$ and $b \to u\bar{u}d$. Double black, orange and single black lines denote bottom, charm and massless quarks respectively.

with the insertion of one operator O_8 are already of the order of α_s^1. Therefore, the only diagrams that we need for the counterterms including this operator is the order α_s^1 diagram with the insertion of one operator O_8 and one current-current operator.

We parametrize the nonleptonic decay width for decays $b \to q_1\bar{q}_3q_2$ that receive contributions from penguin-like topologies as follows:

$$
\begin{aligned}
\Gamma_3^{q_1q_2q_3} &= \frac{G_F^2 m_b^5 |\lambda_{q_1q_2q_3}|^2}{192\pi^3} \left[X_0(\rho) + X_0^{\text{PO}}(\rho) + \frac{\alpha_s}{\pi} \left(X_1(\rho) + X_1^{\text{PO}}(\rho) + X_1^{\text{PT}}(\rho) \right) \right. \\
&\quad \left. + \left(\frac{\alpha_s}{\pi} \right)^2 \left(X_2(\rho) + X_2^{\text{PT}}(\rho) \right) \right] + \mathcal{O}\left(\alpha_s^3 \right) \\
&= \Gamma_0 \left[C_1^2(\mu_s)G_{11} + C_1(\mu_s)C_2(\mu_s)G_{12} + C_2^2(\mu_s)G_{22} \right] \\
&\quad + \left[\frac{\alpha_s}{\pi} X_1^{\text{PT}}(\rho) + \left(\frac{\alpha_s}{\pi} \right)^2 X_2^{\text{PT}}(\rho) \right] + \left[X_0^{\text{PO}}(\rho) + \frac{\alpha_s}{\pi} X_1^{\text{PO}}(\rho) \right],
\end{aligned}
\tag{5.104}
$$

where the functions G_{11}, G_{12} and G_{22} are already calculated in the previous Sections 5.2.2 and 5.2.4. The contributions of penguin-like topology diagrams are denoted by X_i^{PT}. For completeness we also include the contributions with penguin operators (PO) that are needed for the renormalization of the penguin-like topologies. These contributions include operator insertions $O_{1-2} - O_{3-6}$ and $O_{3-6} - O_{3-6}$ at LO and $O_{1-2} - O_{3-6}$ at NLO.
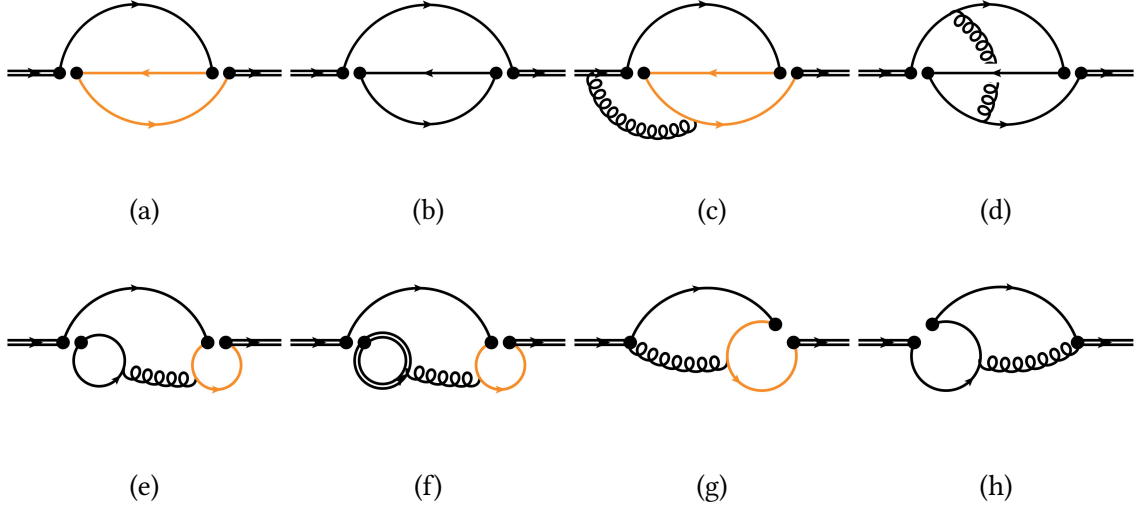
Figure 5.18.: Sample diagrams for the counterterms that are needed to renormalize the penguin-like topology diagrams shown in Figure 5.17. LO diagrams are needed with the insertion of one (a) or two (b) penguin operators O_{3-6}. At order α_s, diagrams with the insertion of one current-current operator and one penguin operator O_{3-6} (c), (d), (e), (f) or one operator O_8 (g), (h) are needed. Double black, orange and single black lines denote bottom, charm and massless quarks respectively.

5.3.1. Penguin operator insertions at LO

In a first step, we consider the contributions with the insertions of penguin operators X_i^{PO} at LO.

We perform the calculation for the decay width $b \to c\bar{c}s$ and obtain the corresponding $b \to u\bar{u}d$ contribution by taking the massless limit.

At order α_s^0, there is only the LO topology with 32 possible operator combinations contributing: The operator insertions $O_{3-6} - O_{3-6}$ yield $4 \times 4 = 16$ combinations while we obtain another $2 \times (2 \times 4) = 16$ combinations for the insertions $O_{1-2} - O_{3-6}$. The number of separated fermion lines in the diagrams differ, depending on the operator combination. Inserting two penguin operators leads to two separated fermion lines as shown in Figure 5.18 (b), while the insertion of one penguin and one current-current operator introduces only one fermion line, see Figure 5.18 (a).

The calculation of the LO diagrams is straightforward. The definition of the penguin operators in the historical basis are given in Equation (2.17). The LO diagrams can be reduced to the same set of three LO master integrals obtained in Section 5.2.2. We use the expansions calculated with the expand and match method and obtain a finite result

$$
\begin{aligned}
X_0^{\mathrm{PO}}(\rho)\Big|_{c\bar{c}s} = \Gamma_0 \Big[&-2\mathrm{Re}\big[V_{cb}V_{cs}^*V_{tb}V_{ts}^*\big]\,(3C_1C_3 + C_1C_4 + 3C_2C_4 + C_2C_3)\,G_{P,1}^{(0)}(\rho) \\
&-2\mathrm{Re}\big[V_{cb}V_{cs}^*V_{tb}V_{ts}^*\big]\,(3C_1C_5 + C_1C_6 + 3C_2C_6 + C_2C_5)\,G_{P,2}^{(0)}(\rho) \\
&+ |V_{tb}|^2\,|V_{ts}|^2\,\big(3C_3^2 + 3C_4^2 + 2C_3C_4 + 3C_5^2 + 2C_5C_6 + 3C_6^2\big)\,G_{P,1}^{(0)}(\rho)
\end{aligned}
$$

$$+2 |V_{tb}|^2 |V_{ts}|^2 (3C_3C_5 + C_3C_6 + 3C_4C_6 + C_4C_5) G_{P,2}^{(0)}(\rho) \Big] . \tag{5.105}$$

where $G_{P,1}^{(0)}(\rho)$ and $G_{P,2}^{(0)}(\rho)$ are functions of the mass ratio ρ and $\Gamma_0 = G_F^2 m_b^5/(192\pi^3)$. Their expansion around $\rho = 0$ reads

$$G_{P,1}^{(0)} = 1 - 16\rho^2 + 24\rho^4 - 32\rho^6 + 2\rho^8 - 48\rho^4 l_\rho + 48\rho^8 l_\rho + O\left(\rho^9\right) ,$$
$$G_{P,2}^{(0)} = 4\rho^2 + 12\rho^4 - 24\rho^6 - 32\rho^8 + 48\rho^4 l_\rho - 96\rho^6 l_\rho + 96\rho^8 l_\rho + O\left(\rho^9\right) . \tag{5.106}$$

The precision of the numerical expansion coefficients is high enough to reconstruct the integer coefficients in Equation (5.106).

The first two lines in Equation (5.105) are obtained by diagrams with one penguin operator and one current-current operator, the third and fourth line of Equation (5.105) show the results for the double insertion of penguin operators. We can compare Equation (5.105) to the analytic results given in Refs. [13, 23, 107] and find agreement.

The penguin operator contributions to the decay width $b \to u\bar{u}d$ at LO is obtained by taking the massless limit of $X_0^{\text{PO}}|_{c\bar{c}s}$ given in Equation (5.105). The massless limit of the phase space functions $G_{P,1}^{(0)}(\rho)$ and $G_{P,2}^{(0)}(\rho)$ yield

$$
\begin{aligned}
X_0^{\text{PO}}\Big|_{u\bar{u}d} &= \Gamma_0 \Big[-2\text{Re}[V_{ub}V_{ud}^* V_{tb}V_{td}^*] (3C_1C_3 + C_1C_4 + 3C_2C_4 + C_2C_3) G_{P,1}^{(0)}(\rho)\Big|_{\rho\to 0} \\
&\quad -2\text{Re}[V_{ub}V_{ud}^* V_{tb}V_{td}^*] (3C_1C_5 + C_1C_6 + 3C_2C_6 + C_2C_5) G_{P,2}^{(0)}(\rho)\Big|_{\rho\to 0} \\
&\quad + |V_{tb}|^2 |V_{td}|^2 \left(3C_3^2 + 3C_4^2 + 2C_3C_4 + 3C_5^2 + 2C_5C_6 + 3C_6^2\right) G_{P,1}^{(0)}(\rho)\Big|_{\rho\to 0} \\
&\quad +2 |V_{tb}|^2 |V_{td}|^2 (3C_3C_5 + C_3C_6 + 3C_4C_6 + C_4C_5) G_{P,2}^{(0)}(\rho)\Big|_{\rho\to 0} \Big] \\
&= \Gamma_0 \Big[-2\text{Re}[V_{ub}V_{ud}^* V_{tb}V_{td}^*] (3C_1C_3 + C_1C_4 + 3C_2C_4 + C_2C_3) \\
&\quad + |V_{tb}|^2 |V_{td}|^2 \left(3C_3^2 + 3C_4^2 + 2C_3C_4 + 3C_5^2 + 2C_5C_6 + 3C_6^2\right)\Big] . \tag{5.107}
\end{aligned}
$$

where we have used $G_{P,1}^{(0)}(\rho)|_{\rho\to 0} = 1$ and $G_{P,2}^{(0)}(\rho)|_{\rho\to 0} = 0$ and $\Gamma_0 = G_F^2 m_b^5/(192\pi^3)$.

5.3.2. Current-current operators in penguin-like topologies at NLO

With the LO contributions calculated in the previous section, we are able to renormalize the insertion of current-current operators into the penguin-like topologies at NLO.

At order α_s^1 there are four different non-vanishing diagrams with current-current operators in penguin-like topologies, sample diagrams are shown in Figure 5.17. They only differ by the flavour of the quarks that couple twice to the current-current operators. The diagrams with two charm quark loops and two massless quark loops shown in Figure 5.17 (a) and (c) contribute to the decay width of $b \to c\bar{c}s$ and $b \to u\bar{u}d$ respectively, while the diagram with one charm and one massless quark loop in in Figure 5.17 (b) contributes to both channels. This can be seen in Figure 5.19 (a) and (b), where the two three-quark cuts of the mixed NLO diagram are shown.
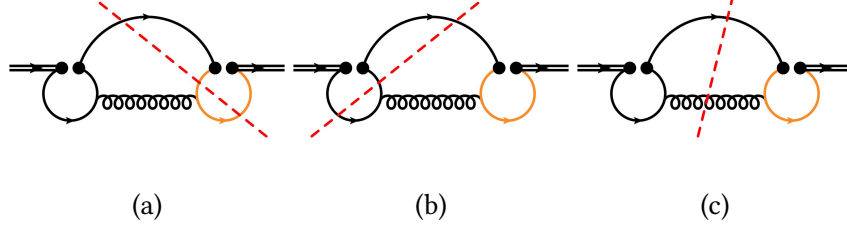
Figure 5.19.: The three different cuts through the penguin-like topologies at NLO. The diagrams (a) and (b) show the physical final states with three quarks. The cut shown in (a) contributes to the decay width $b \to c\bar{c}s$, the cut shown in (b) contributes to $b \to u\bar{u}d$. The cut through massless quark and gluon shown in (c) vanishes in these types of diagrams at NLO.

The penguin topology diagrams at NLO are only non-zero if both current-current operators are O_2 operators. All insertions of O_1 in these kind of diagrams vanish by colour. The operator definition of O_1 in the historical basis is given in Equation (2.16) and reads for the insertion of a penguin-like topology with a charm quark loop

$$O_1^{cq_2c} = (c^\alpha \gamma^\mu P_L b^\beta)(\bar{q}_2^\beta \gamma_\mu P_L c^\alpha) \,. \tag{5.108}$$

We observe that the colour structure of O_1 introduces the same colour index for both charm quark lines. Taking into account the coupling of the gluon to this charm quark line, we obtain the colour factor

$$T_{\alpha\alpha}^a = \text{Tr}\,[T^a] = 0 \,, \tag{5.109}$$

for the penguin-like topologies. However for the insertion of two operators O_2, the NLO diagram has the colour factor

$$T_{\alpha\beta}^a T_{\alpha'\beta'}^a \delta_{\alpha\alpha'} \delta_{\beta\beta'} = \text{Tr}\,[T^a T^a] \neq 0 \,, \tag{5.110}$$

and therefore the penguin-like topologies are non-zero for this operator combination.
In addition to the diagram in which the gluon connects the two quark loops, it is also possible to attach the gluon to only one of the quark bubbles. The insertion of the four-quark operator with a quark loop that does not couple to the gluon would then act as a flavour changing self-energy correction that transforms a bottom quark into a massless down-type quark. Two examples for such diagrams are shown in Figure 5.20. However, diagrams of this class are all zero individually since the flavour changing self-energy correction leads to a Dirac structure of the form

$$\gamma^\mu P_L \frac{\slashed{p} + m_c}{m_c^2 - p^2} \gamma_\mu P_L \,, \tag{5.111}$$

where the mass term in the numerator vanishes because of $P_L \gamma_\mu P_L = \gamma_\mu P_R P_L = 0$. The remaining term is proportional to $\slashed{p}$ and vanishes since the integral over the loop momentum p is odd and therefore zero. The vanishing of diagrams with flavour-changing self-energy
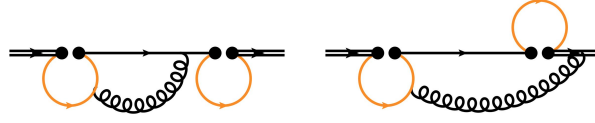
Figure 5.20.: Sample diagrams for the insertion of a four fermion operator into a quark line, acting as a flavour changing self-energy correction.

corrections is checked explicitly in our NLO calculation.

We can reduce the NLO penguin-like topology diagrams to eight master integrals with non-vanishing imaginary part. For the calculation of these master integrals, we use the expand and match method described in Chapter 3.3. In a first step, we set up the differential equation which has the singular points

$$\rho_{\text{singular}} \in \{0, 1/2\} . \tag{5.112}$$

These singularities are expected since the diagrams with a charm quark loop has a two charm threshold. As expansion points, we choose

$$\rho_0 \in \{0, 1/5, 1/3, 1/2\} . \tag{5.113}$$

As boundary conditions for the expansions, we evaluate the integrals with AMFlow at $\rho = 1/5$. When calculating the boundary conditions, we have to be careful to separate the possible cuts of the diagrams. In this calculation, we only want to include final states with three quarks as visualized in Figure 5.19 (a) and (b). In principle also the cut through a massless quark and a gluon is possible as shown in Figure 5.19 (c). However, at NLO, this additional cut turns out to be zero. This can be seen from the structure of the corresponding master integrals, they are shown in Figure 5.21. For all eight master integrals, there is no possible cut through two massless lines that would correspond to the cut through gluon and massless quark in Figure 5.19 (c). This observation is in agreement with Ref. [13], where the penguin-like topology contributions to the decay width $b \to c\bar{c}s$ are calculated. Furthermore, we want to distinguish the $c\bar{c}s$ and $u\bar{u}d$ final state to be able to compare with the literature. This means that we have to calculate the possible cuts shown in Figure 5.19 (a) and (b) separately. We separate the two cuts by calculating them individually with AMFlow using the option AMFlowInfo["Cut"].

For the renormalization of the NLO penguin-like topology diagrams, we need counterterms from LO diagrams with the insertion of one current-current operator and one penguin operator. These diagrams are calculated in Section 5.3.1. The renormalization constants for the four-quark operators including the penguin operators are obtained by transforming their counterparts from the CMM basis to the traditional basis, see Appendix C for more details and the exact expressions. Under renormalization, the penguin operators in the historical basis mix with O_2, see the one-loop renormalization constant given in Equation (C.44), and in this way, the LO diagrams with insertions of one current-current operator O_2 and one penguin operator generate counterterms for the penguin-like topology contributions with insertions of two O_2 operators at NLO.
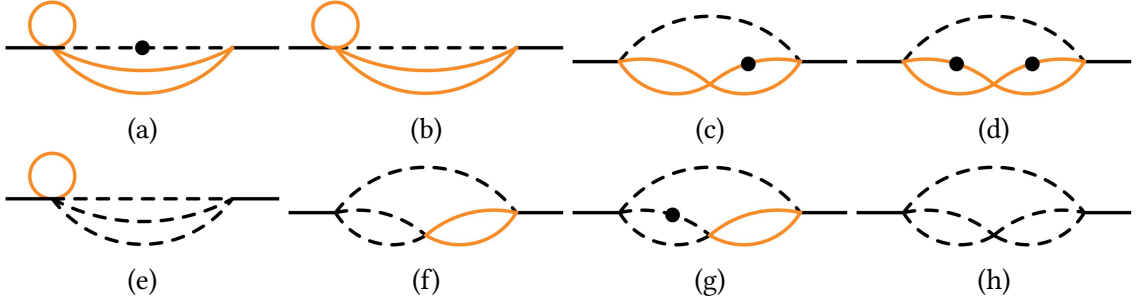
Figure 5.21.: The master integrals with non-vanishing imaginary part for the NLO penguin-like topologies. Black, orange and dashed lines denote bottom, charm and massless lines respectively. The integrals (a), (b), (c) and (d) contribute to the diagram with two charm quark bubbles in Figure 5.17 (a). All possible cuts in these integrals include two charm quark lines and one massless quark line. There are no cuts through two massless lines. The integrals shown in (e), (f), (g) and (h) contribute to the CKM suppressed diagrams with one or two up quark bubbles shown in Figure 5.17 (b) and (c). The integrals (f) and (g) appear in the calculation of both decay channels $b \to c\bar{c}s$ and $b \to u\bar{u}d$, while (e) and (h) only contribute to $b \to u\bar{u}d$.

We split the result in two parts according to their final states. We obtain for the expansion around $\rho = 0$ for the $b \to c\bar{c}s$ final state

$$
\begin{aligned}
X_1^{\text{PT}\,csc}(\rho) =& \frac{4}{3}\Gamma_0 C_2^2 |V_{cb}|^2 |V_{cs}|^2 \Big(-1.00000 + 8.00000\rho^2 + (-18.6667 - 32.0000)\,\rho^4 \\
& + \left(-14.4801 + 241.777 l_\rho\right)\rho^6 + \left(155.555 - 362.666 l_\rho + 128.000 l_\rho^2\right)\rho^8 \\
& + \left(-121.066 + 64.0000\right)\rho^{10}\Big) \\
& + \frac{4}{3}\Gamma_0 C_2^2 \text{Re}\left[V_{cb}V_{cs}V_{ub}^*V_{us}^*\right]\Big(-1.00000 + \left(-1.77777 - 10.6666 l_\rho\right)\rho^2 \\
& - 18.6667\rho^4 + \left(93.7589 - 42.6666 l_\rho^2\right)\rho^6 + \big(-126.637 + 16.0000 l_\rho \\
& + 64.0000 l_\rho^2\big)\rho^8 + 34.6666\rho^{10}\Big) + O(\rho^{11}) \,,
\end{aligned}
$$
(5.114)

with $\Gamma_0 = G_F^2 m_b^5/(192\pi^3)$. The contribution of the diagram with two charm bubbles is given in Ref. [13] in terms of two analytically calculated phase space functions. Expanding these functions around $m_c/m_b = 0$, we find agreement with our result in Equation (5.114). The CKM suppressed contribution for the $c\bar{c}s$ final state is a new result.
For the $b \to u\bar{u}d$ decay channel, we obtain the expansion

$$
\begin{aligned}
X_1^{\text{PT}\,udu}(\rho) =& \frac{4}{3}\Gamma_0 C_2^2 |V_{ub}|^2 |V_{ud}|^2 \Big(-1.00000\Big) \\
& + \frac{4}{3}\Gamma_0 C_2^2 \text{Re}\left[V_{cb}V_{cd}V_{ub}^*V_{ud}^*\right]\Big(-1.00000 + \left(9.77777 + 10.6666 l_\rho\right)\rho^2 \\
& - 32.0000 l_\rho\rho^4 + \left(-108.238 - 49.7777 l_\rho + 42.6666 l_\rho^2\right)\rho^6 + (187.469
\end{aligned}
$$

$$+26.6666 l_\rho - 64.0000 l_\rho^2 \Big) \rho^8 + \big(22.9333 - 64.0000 l_\rho\big) \rho^{10}\Big) + O(\rho^{11}) \,. \quad (5.115)$$

This expression is in agreement with the result obtained in Ref. [30] for the $u\bar{u}d$ final state. We also checked explicitly that the sum $X_1^{\mathrm{PT}\,csc}(\rho) + X_1^{\mathrm{PT}\,udu}(\rho)$ is equal to a calculation where we do not separate the different final states in the calculation of the master integrals.

5.3.3. Penguin operator insertions at NLO

In order to renormalize the NNLO penguin-like topology diagrams with two current-current operators, we need counterterms generated by the LO diagrams discussed in Section 5.3.1 and in addition counterterms that are generated by NLO diagrams with one current-current operator and one penguin operator. The calculation of these NLO diagrams is outlined in the following. Sample diagrams are shown in Figure 5.18 (c)-(f). In addition to these standard NLO topologies, we also obtain contributions with one current-current operator and one penguin operator in penguin-like topologies. Sample diagrams are shown in Figure 5.18 (e) and (f). For such diagrams we obtain two fermion lines. However, the internal fermion line carries at most four gamma matrices that can be reduced to two, see the discussion around Equation (5.7) in Section 5.1. Therefore these diagrams also do not require the usage of Fierz identities since

$$\mathrm{Tr}\,[\gamma_5] = \mathrm{Tr}\,[\gamma^\mu \gamma^\nu \gamma_5] = 0 \,. \quad (5.116)$$

We are therefore able to calculate all NLO diagrams with one penguin operator and one current-current operator using anti-commuting γ_5 without further problems.

In addition to the diagram classes described above, we find diagrams with insertions of penguin operators that act as flavour changing self-energy corrections, see Figure 5.22. For the insertion of current-current operators in diagrams of such topology, we observed that all such diagrams are zero individually, see discussion in Section 5.3.2. This can be seen from the Dirac structure of the flavour changing loop that reads in the case of a current-current operator insertions

$$\gamma^\mu P_L \frac{\slashed{p} + m}{m^2 - p^2} \gamma_\mu P_L \,. \quad (5.117)$$

Here the mass term vanishes because of $P_L \gamma_\mu P_L = 0$ and the remaining term including the $\slashed{p}$ is zero when integrating over the loop momentum p. The same Dirac structure as given in Equation (5.117) is obtained for an insertion of the penguin operators O_3 and O_4. However, for insertions of O_5 or O_6 into the diagrams shown in Figure 5.17, we find

$$\gamma^\mu P_L \frac{\slashed{p} + m}{m^2 - p^2} \gamma_\mu P_R \,. \quad (5.118)$$

The term proportional to $\slashed{p}$ still cancels due to the same argument as before, but for the mass term in the numerator we now obtain $\gamma^\mu P_L \gamma_\mu P_R \neq 0$ and therefore non-vanishing contributions from diagrams with massive loops of this kind. Since the flavour changing self-energy has to transform a strange quark to a bottom quark or vice versa, the only possible insertions of penguin operators are the ones with $q \in \{s, b\}$, where q is defined as
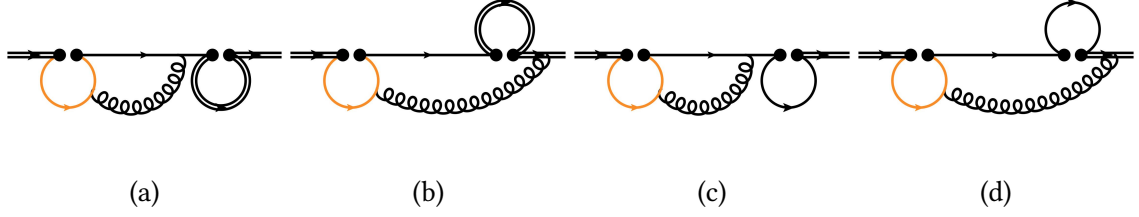
Figure 5.22.: Sample NLO diagrams for the insertion of a penguin operator that acts as flavour changing self-energy correction.

in Equation (2.17). Since the strange quark is massless, the only non-vanishing diagrams with these flavour changing self-energies are the diagrams shown in Figure 5.22 (a) and (b) with the penguin operator coupling three bottom quarks and one strange quark. It turns out that these two diagrams exactly cancel and therefore the sum over all flavour changing self-energy corrections with the insertion of penguin operators vanishes.

Some of the master integrals that appear in the calculations of the three loop diagrams have been already calculated in Section 5.2.2 and Section 5.3.2. The penguin-like topologies with penguin operators introduce 11 additional master integrals. They are calculated with the `expand and match` method around the same expansion points as given in Equation (5.113). In contrast to the NLO calculation for the current-current operators in penguin-like topologies, we now do not distinguish different final states anymore but sum over all occurring cuts.

The sum of all three-loop diagrams contributing to $X_1^{\text{PO}}(\rho)$ is divergent and has to be renormalized. Since we do not separate the different final states but sum over all cuts, we also include cuts that are not $c\bar{c}s$ or $u\bar{u}d$. One example is shown in Figure 5.23 (a) where we consider the insertion of one current-current operator and a penguin operator coupling to three strange quarks. This diagram obtains a non-vanishing contribution from the cut through $c\bar{c}s$ but also a contribution from the cut through $s\bar{s}s$.

The counterterms for the NLO diagrams are generated from LO diagrams with one or two penguin operator insertions. We renormalize the charm quark mass, the bottom quark wave function and take into account the operator mixing. We now also include insertions of the first order evanescent operators given in Equation (2.19) and (2.20). In addition to the LO diagrams calculated in Section 5.3.1, we also need counterterms generated by LO diagrams with two penguin operator insertions that have cuts through three quarks of the same flavour in order to renormalize diagrams like Figure 5.23 (a).

The renormalization constants are obtained by transforming their counterparts in the CMM basis to the historical basis and are given explicitly in Appendix C.

To keep the NLO result organized, we split it into different parts. We first consider the group of diagrams with a penguin operator O_{3-6} in a penguin-like topology that has a closed quark loop. We obtain six different topologies that differ by the quark-flavour of the penguin-like topology loop, up or charm, and the quark flavour of the closed quark loop induced by the penguin operator which can be bottom, charm or massless. Six sample diagrams for these classes are shown in Figure 5.24.
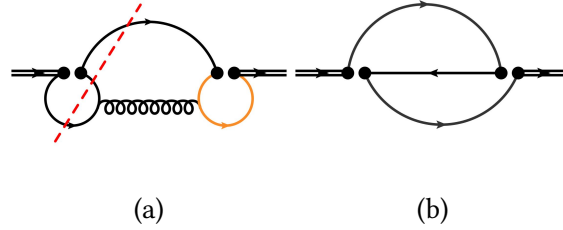
(a) (b)

Figure 5.23.: (a) shows a possible cut through three quarks of the same flavour in a NLO diagram with one penguin operator (left) and one current-current operator (right). The LO diagram with two penguin operator insertions and three strange quark propagators that yields the corresponding counterterm to renormalize the three-strange cut of the NLO diagram is shown in (b).
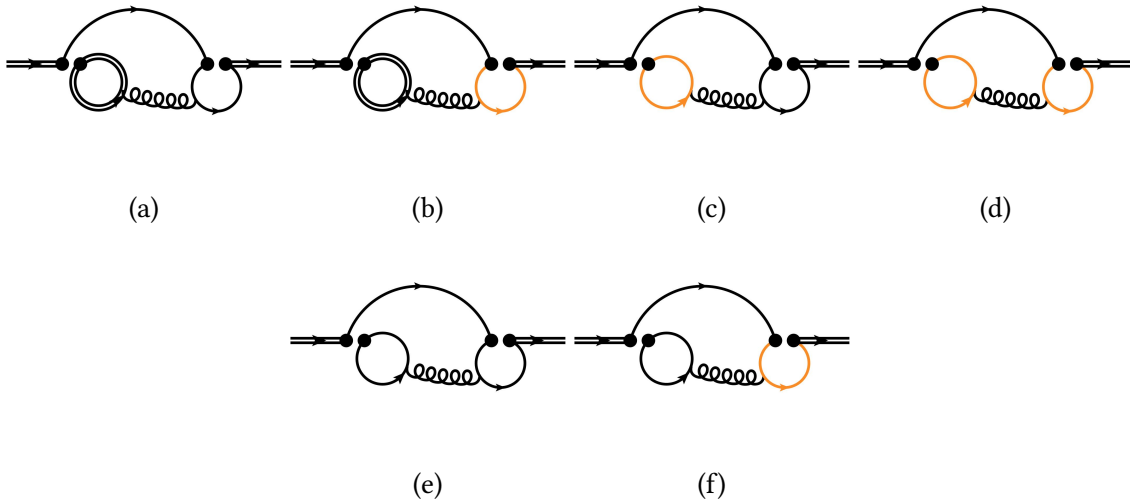

(a) (b) (c) (d)

(e) (f)

Figure 5.24.: The NLO diagrams with closed quark loops and insertions of one penguin (left) and one current-current (right) operator. Double black, orange and single black lines denote bottom, charm and massless quarks respectively.

We obtain for the renormalized result the expansion around $\rho = 0$

$$
\begin{aligned}
X_1^{\text{PO}, O_{3-6}}(\rho)\Big|_{n_f} = & \Gamma_0 C_2 (C_4 + C_6) n_c \Big[\text{Re}[V_{tb} V_{ts}^* V_{cb}^* V_{cs}] \Big(11.7777 - 113.7777 \rho^2 \\
& + \left(202.6666 + 64.0000 l_\rho \right) \rho^4 + \left(356.9496 - 810.6666 l_\rho + 170.6666 l_\rho^2 \right) \rho^6 \\
& + \left(-1462.6506 + 768.0000 l_\rho - 512.0000 l_\rho^2 \right) \rho^8 \Big) \\
& + \text{Re}[V_{tb} V_{ts}^* V_{ub}^* V_{us}] \Big(11.7777 - 59.5555 \rho^2 \\
& + \left(109.3333 + 32.0000 l_\rho \right) \rho^4 + \left(166.0303 - 234.6666 l_\rho + 85.3333 l_\rho^2 \right) \rho^6 \\
& + \left(-643.2678 + 10.6666 l_\rho - 128.0000 l_\rho^2 \right) \rho^8 \Big) \Big] \\
& + \Gamma_0 C_2 (C_4 + C_6) n_l \Big[\text{Re}[V_{tb} V_{ts}^* V_{cb}^* V_{cs}] \Big(11.7777 - 54.2222 \rho^2 \\
& + \left(93.3333 + 32.0000 l_\rho \right) \rho^4 + \left(190.9192 - 192.0000 l_\rho + 85.3333 l_\rho^2 \right) \rho^6 \\
& + \left(-629.9344 - 53.3333 l_\rho - 128.0000 l_\rho^2 \right) \rho^8 \Big) \\
& + \text{Re}[V_{tb} V_{ts}^* V_{ub}^* V_{us}] \Big(11.7777 \Big) \Big] \\
& + \Gamma_0 C_2 (C_4 + C_6) n_h \Big[\text{Re}[V_{tb} V_{ts}^* V_{cb}^* V_{cs}] \Big(4.2502 - 40.8888 \rho^2 \\
& + \left(58.9623 + 2.1333 l_\rho \right) \rho^4 + \left(205.8113 - 99.2507 l_\rho + 85.3333 l_\rho^2 \right) \rho^6 \\
& + \left(-568.2569 - 93.7650 l_\rho - 128.0000 l_\rho^2 \right) \rho^8 \Big) \\
& + \text{Re}[V_{tb} V_{ts}^* V_{ub}^* V_{us}] \Big(4.2502 \Big) \Big] + O(\rho^9),
\end{aligned}
\tag{5.119}
$$

where $\mu_s = m_b$ and $\Gamma_0 = G_F^2 m_b^5 / (192 \pi^3)$. The flags $n_h = 1$, $n_c = 1$, $n_l = 3$ denote the contributions from the diagrams with closed bottom quark, charm quark and massless quark loops, see Figure 5.24 (a) and (b), Figure 5.24 (c) and (d) and Figure 5.24 (e) and (f) respectively. The result in Equation (5.119) has no contributions from O_3, O_5. Diagrams with such operator insertions vanish by the same color-argument that can be applied for the insertion of O_1 in penguin-like topologies.

The next class of diagrams includes all NLO diagrams with one penguin operator O_{3-6} and one current-current operator that have no closed quark loops. We show sample diagrams for this group in Figure 5.25. This includes the standard topologies that also appeared in the calculation with two current-current operator insertions, see for example Figure 5.25 (a) and (b), but also penguin-like topologies as shown in Figure 5.25 (c) and (d).

We obtain for the expansion around $\rho = 0$:

$$
\begin{aligned}
X_1^{\text{PO}, O_{3-6}}(\rho)\Big|_{n_f=0} = & \Gamma_0 \text{Re}[V_{tb} V_{ts}^* V_{cb}^* V_{cs}] C_1 \Big[C_3 \Big(-8.4784 + \left(-8.3453 - 384.0000 l_\rho \right) \rho^2 \\
& + \left(711.3093 + 1935.3093 l_\rho - 1152.0000 l_\rho^2 \right) \rho^4 + \left(18.0911 - 2133.3333 l_\rho \right. \\
& \left. -256.0000 l_\rho^2 \right) \rho^6 + \left(-1446.4497 - 1204.6426 l_\rho + 2528.0000 l_\rho^2 \right) \rho^8 \Big)
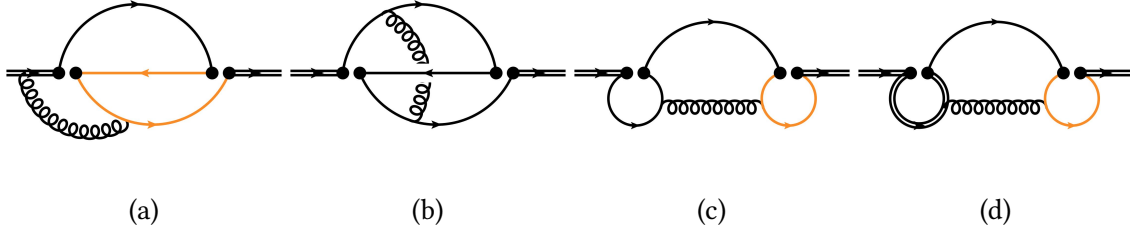\end{aligned}
$$

Figure 5.25.: Sample diagrams for the NLO contribution with one current-current and one penguin operator insertion that have no closed internal quark loop.

$$
+ C_4 \Big(-30.1594 + \big(493.9136 - 128.0000 l_\rho\big) \rho^2 - 421.1031 \rho^3
$$

$$
+ \Big(-328.0000 + 1541.1031 l_\rho - 384.0000 l_\rho^2 \Big) \rho^4 + 842.2062 \rho^5
$$

$$
+ \Big(646.3190 - 406.8808 l_\rho + 64.0000 l_\rho^2 \Big) \rho^6 - 1263.3093 \rho^7
$$

$$
+ \Big(468.3624 - 1468.9253 l_\rho + 458.6666 l_\rho^2 \Big) \rho^8 \Big)
$$

$$
+ C_5 \Big(\big(84.1726 + 96.0000 l_\rho \big) \rho^2 + \big(-1010.7913 + 80.6906 l_\rho
$$

$$
+ 1152.0000 l_\rho^2 \Big) \rho^4 + \Big(2554.4918 - 481.3812 l_\rho - 3072.0000 l_\rho^2 \Big) \rho^6
$$

$$
+ \Big(-1120.9187 - 3411.9520 l_\rho + 3584.0000 l_\rho^2 \Big) \rho^8 \Big)
$$

$$
+ C_6 \Big(\big(-3.9424 + 32.0000 l_\rho \big) \rho^2 + \Big(-432.9304 - 357.1031 l_\rho + 384.0000 l_\rho^2 \Big) \rho^4
$$

$$
+ \Big(1043.4972 + 607.5395 l_\rho - 1024.0000 l_\rho^2 \Big) \rho^6
$$

$$
+ \Big(-117.6395 - 1905.3173 l_\rho + 1194.6666 l_\rho^2 \Big) \rho^8 \Big) \Big]
$$

$$
+ \Gamma_0 \mathrm{Re}\big[V_{tb} V_{ts}^* V_{cb}^* V_{cs} \big] C_2 \Big[C_3 \Big(-26.8261 + \big(463.6914 - 128.000 l_\rho \big) \rho^2
$$

$$
- 421.1031 \rho^3 + \Big(-301.3333 + 1541.1031 l_\rho - 384. l_\rho^2 \Big) \rho^4 + 842.2062 \rho^5
$$

$$
+ \Big(897.4248 - 421.1031 l_\rho + 149.3333 l_\rho^2 \Big) \rho^6 - 1263.3093 \rho^7
$$

$$
+ \big(-60.7406 - 1671.5920 l_\rho + 330.6666 l_\rho \big) \rho^8 \Big)
$$

$$
+ C_4 \Big(-8.4784 + \big(324.1726 - 384.0000 l_\rho \big) \rho^2 + 1263.3093 \rho^3
$$

$$
+ \big(-956.1726 + 1687.6546 l_\rho - 1152.0000 l_\rho \big) \rho^4 + \big(493.8353
$$

$$
- 3541.3333 l_\rho - 128.0000 l_\rho 2 \big) \rho^6 - 1263.3093 \rho^7
$$

$$
+ \big(-2414.2776 + 380.4546 l_\rho + 2880.0000 l_\rho \big) \rho^8 \Big)
$$

$$
+ C_5 \Big(\big(-3.9424 + 32.0000 l_\rho \big) \rho^2 + \big(-432.9304 - 357.1031 l_\rho
$$

$$
+ 384.0000 l_\rho^2 \Big) \rho^4 + \Big(1043.4972 + 607.5395 l_\rho - 1024.0000 l_\rho^2 \Big) \rho^6
$$

$$+ \left(-117.6395 - 1905.3173 l_\rho + 1194.6666 l_\rho^2 \right) \rho^8 \Bigg)$$

$$+ C_6 \Bigg(\left(219.1294 \rho^2 + 96.0000 l_\rho \right) \rho^2 + \left(292.8632 + 2248.3453 l_\rho \right.$$

$$\left. + 1152.0000 l_\rho^2 \right) \rho^4 - 1263.3093 \rho^5 + \left(3161.0970 - 4128.0000 l_\rho \right.$$

$$\left. - 3744.0000 l_\rho^2 \right) \rho^6 - 2526.6187 \rho^7 + \left(-5611.1468 - 2294.0239 l_\rho \right.$$

$$\left. + 6336.0000 l_\rho^2 \right) \rho^8 \Bigg) \Bigg]$$

$$+ \Gamma_0 \mathrm{Re} [V_{tb} V_{ts}^* V_{ub}^* V_{us}] C_1 \Big[-8.4784 C_3 - 30.1594 C_4 \Big]$$

$$+ \Gamma_0 \mathrm{Re} [V_{tb} V_{ts}^* V_{ub}^* V_{us}] C_2 \Big[-26.8261 C_3 - 8.4784 C_4 \Big] + O(\rho^9) . \tag{5.120}$$

Note that this result includes all possible three-quark final states.

To complete the NLO contributions contributions with one penguin operator, we also consider the diagrams with the insertion of one current-current operator and one operator O_8. The two different diagrams for this contribution are shown in Figure 5.18 (g) and (h). For these diagrams, we find in total four master integrals that are not part of the NLO master integral basis calculated before since they are only two loop integrals. Three of them can be obtained from the LO master integrals calculated in Section 5.2.2, the fourth master integral (massless bubble multiplied by charm mass tadpole) can be calculated using Feynman parameters or can be obtained from Ref. [108].

For the expansion around $\rho = 0$ we obtain the result:

$$X_1^{\mathrm{PO}, O_8}(\rho) = \Gamma_0 \mathrm{Re} [V_{tb} V_{ts}^* V_{cb}^* V_{cs}] C_2 C_8 \Big[10.6666 - 192.0000 \rho^2 + \left(192.0000 - 768.0000 l_\rho \right) \rho^4$$

$$+ \left(-213.3333 + 512.0000 l_\rho \right) \rho^6 + 192.0000 \rho^8 + 128.0000 \rho^{10} \Big]$$

$$+ \Gamma_0 \mathrm{Re} [V_{tb} V_{ts}^* V_{ub}^* V_{us}] C_2 C_8 (10.6666) + O \left(\rho^{11} \right) , \tag{5.121}$$

with $\Gamma_0 = G_F^2 m_b^5 / (192 \pi^3)$. This result is in agreement with Ref. [13].

We finally obtain the NLO contribution with one penguin operator insertion by adding the three separately discussed parts:

$$X_1^{\mathrm{PO}} = X_1^{\mathrm{PO}, O_8}(\rho) + X_1^{\mathrm{PO}, O_{3-6}}(\rho) \Big|_{n_f} + X_1^{\mathrm{PO}, O_{3-6}}(\rho) \Big|_{n_f=0} . \tag{5.122}$$

5.3.4. Current-current operators in penguin-like topologies at NNLO

The next step would be the calculation of the NNLO diagrams with the insertion of two current-current operators in penguin-like topologies. The counterterms for such diagrams are generated by the diagrams that have been calculated in the previous subsections to obtain the three contributions X_1^{PT}, X_0^{PO} and X_1^{PO}.

We find 208 NNLO diagrams which can be reduced to 265 master integrals. We calculate the master integrals with `expand and match` for the expansion points

$$\rho_0 = \{ 0, 1/5, 1/3 \} , \tag{5.123}$$

and obtain the boundary conditions with `AMFlow` at $\rho = 1/5$. Again, we do not distinguish the different final states in the calculation of the master integrals but sum over all possible cuts.

The next step would be to fully assemble the renormalized NNLO amplitude . This calculation was not completed in this thesis.

6. Nonleptonic b-decays in the $\overline{\text{MS}}$ and kinetic mass scheme

The decay width has a strong dependence on the mass of the heavy quark, in the case of the B meson decays the bottom quark mass m_b. It is therefore necessary to choose an appropriate renormalization scheme for the quark mass. In the calculations carried out in the previous chapters, the on-shell or pole mass scheme was used for both charm and bottom quark mass. However, the pole mass scheme has the problem of renormalon ambiguities, which lead to a bad convergence behaviour of the perturbative series. Using the pole scheme is therefore a bad choice for a phenomenological analysis of our results. An alternative renormalization scheme is the (modified) minimal subtraction scheme, the $\overline{\text{MS}}$-scheme, which subtracts the divergent contributions of the quantum corrections to the quark two-point function. This mass scheme is especially appropriate for high-energy applications. For processes like the B meson decays, the so-called short-distance mass schemes that are free of renormalon ambiguities, like the kinetic mass scheme, are a good choice. The kinetic mass scheme relates the mass of the bottom quark directly to the mass of the B meson. In this chapter, we first introduce the $\overline{\text{MS}}$-scheme and investigate the behaviour of the NNLO results of the nonleptonic b-decay in this scheme. Afterwards the bottom quark mass is transformed into the kinetic mass scheme, where the best behaviour is expected.

Note that in this chapter, we focus on the nonleptonic decay width Γ_3^{NL} and therefore the numerical values and plots are not directly comparable to Ref. [109]. The plots in Ref. [109] show $\Gamma_3 = \Gamma_3^{\text{SL}} + \Gamma_3^{\text{NL}}$ where also the semileptonic decay is included.

6.1. Input parameters

In this chapter, the perturbative corrections are evaluated numerically. Before this is done, let us specify the numerical input values that will be used throughout the next sections.

Bottom and charm quark masses

In order to have consistent input values for the quark masses in the different schemes we use the $\overline{\text{MS}}$ mass for the charm quark and the kinetic mass for the bottom quark

$$\overline{m}_c(\mu_c = 2\,\text{GeV}) = 1.090 \pm 0.010\,\text{GeV}\,, \tag{6.1}$$

$$m_b^{\text{kin}}(\mu_{\text{kin}} = 1\,\text{GeV}) = 4.573 \pm 0.012\,\text{GeV}\,. \tag{6.2}$$

obtained in Ref. [55] as starting point for the mass values in other schemes. Note that precise values for the charm and bottom quark masses are also obtained from other methods, see e.g. Ref. [1, 110].

The value for the charm quark mass at $\mu_c = 2\,\text{GeV}$ given in Equation (6.1) is used to calculate the $\overline{\text{MS}}$ charm quark mass for arbitrary μ_c using the Mathematica package RunDec [111]. We find

$$\overline{m}_c(\mu_c = 3\,\text{GeV}) = 0.984 \pm 0.0090\,\text{GeV}\,,$$
$$\overline{m}_c(\mu_c = \overline{m}_b) = 0.918 \pm 0.008\,\text{GeV}\,,$$
$$\overline{m}_c(\mu_c = m_b^{\text{kin}}) = 0.904 \pm 0.008\,\text{GeV}\,. \tag{6.3}$$

The uncertainties on these numbers are obtained by using the upper and lower bounds of the charm mass at $\mu_c = 2\,\text{GeV}$ given in Equation (6.1) and recalculating the $\overline{MS}$ charm mass at $\mu_c \in \{3\,\text{GeV}, \overline{m}_b, \text{kin}\}$ with RunDec.

The bottom quark mass in Equation (6.2) is obtained for the Wilsonian cut-off $\mu_{\text{kin}} = 1\,\text{GeV}$. Using RunDec, the bottom mass in the $\overline{\text{MS}}$ scheme can be calculated from the bottom mass in the kinetic scheme, where we obtain

$$\overline{m}_b\,(\overline{m}_b) = 4.216^{+0.0126}_{-0.0126}\,\text{GeV}\,. \tag{6.4}$$

The uncertainties are obtained by variation of the bottom quark mass in the kinetic scheme according to the uncertainties in Equation (6.2) and recomputing the corresponding $\overline{\text{MS}}$ mass with RunDec.

For the calculation of the matching coefficients up to NNLO, the top quark mass is also needed. We take the numerical value of the pole mass from Ref. [1], see Table 6.1.

For the analysis in the on-shell mass scheme, we use the quark masses in the $\overline{\text{MS}}$ scheme in Equations (6.1) and Equation (6.4) and transform them to the on-shell scheme using RunDec. Since the perturbative expansion that relates the on-shell mass scheme and the $\overline{\text{MS}}$ mass scheme shows a bad convergence behaviour, the numerical value of the on-shell masses strongly depends on the used loop order. To demonstrate this issue, the conversion is first done using two loop relations between on-shell and $\overline{\text{MS}}$ masses, where we obtain

$$m_c^{\text{OS, 2loop}} = 1.553\,\text{GeV}\,,$$
$$m_b^{\text{OS, 2loop}} = 4.839\,\text{GeV}\,. \tag{6.5}$$

The four loop relation that is implemented in RunDec yields

$$m_c^{\text{OS, 4loop}} = 2.040\,\text{GeV}\,,$$
$$m_b^{\text{OS, 4loop}} = 5.091\,\text{GeV}\,, \tag{6.6}$$

which shows a big difference to the numbers obtained with the two loop relation. To account for this large difference, we assign the on-shell masses an uncertainty of $\pm 0.3\,\text{GeV}$ in the following analyses.

m_Z	m_W	$\alpha_s^{(5)}(m_Z)$	m_t
91.1880 GeV	80.3692 GeV	0.1180 ± 0.0010	172.57 GeV

Table 6.1.: Input parameters for Standard Model quantities, taken from Ref. [1]

Strong coupling constant

One of the input parameters is the strong coupling constant α_s with four active flavours, which has to be evaluated at different scales μ_s. This is done again using RunDec with the mass of the Z-Boson m_Z and the value of the strong coupling constant at the scale $\mu_s = m_Z$ as input parameters. Their numerical values are given in Table 6.1. The value of α_s at the scale μ_s is then obtained by running with five active flavours from $\mu = m_Z$ to $\mu = 2\overline{m}_b(\overline{m}_b)$, decoupling the bottom quark and then running with four active flavours from $\mu = 2\overline{m}_b(\overline{m}_b)$ to the scale $\mu = \mu_s$. With this procedure, we obtain

$$\alpha_s^{(4)}(m_b^{\text{kin}}) = 0.2183 . \tag{6.7}$$

Matching coefficients

The matching coefficients for the effective operators O_1 and O_2 are given in Equation (5.48) as an expansion in the strong coupling constant α_s with five active flavours. They include corrections from top quark masses. For these contributions, the numerical values for the top quark mass and the W boson mass given in Table 6.1 are used.

CKM matrix elements

For the CKM matrix elements we take the value of V_{cb} from the semileptonic fit [55]

$$|V_{cb}| = (41.97 \pm 0.48) \times 10^{-3} . \tag{6.8}$$

Furthermore, we use the results of the global CKM fit given in Ref. [112]:

$$|V_{us}| = 0.22498^{+0.00023}_{-0.00022} ,$$
$$\frac{|V_{ub}|}{|V_{cb}|} = 0.08887^{+0.00141}_{-0.00154} ,$$
$$\delta = \left(66.23^{+0.60}_{-1.43}\right)^{\circ} . \tag{6.9}$$

6.2. $\overline{\text{MS}}$-scheme

In this section we consider the $\overline{\text{MS}}$ mass scheme for both the charm and bottom mass. The relation between the on-shell and the $\overline{\text{MS}}$ mass is different for these two masses starting from order α_s^2. In the following, we derive the relations for the transformation of both the charm and bottom mass from the on-shell mass to the $\overline{\text{MS}}$ as an expansion in α_s with four active flavours.

Charm mass

The relation between the on-shell the $\overline{\text{MS}}$ mass as an expansion in α_s with four active flavours can be obtained from Ref. [93]

$$
m_c^{OS} = \overline{m}_c^{(5)}(\mu_c) \left[1 + \frac{\alpha_s^{(4)}(\mu_c)}{\pi} y_1 + \left(\frac{\alpha_s^{(4)}(\mu_c)}{\pi} \right)^2 \left(C_F^2 y_2^{FF} + C_F C_A y_2^{FA} \right. \right.
$$
$$
\left. \left. + C_F T_F \left(n_l \Delta_m \Big|_{x \to 0} + n_c \Delta_m \Big|_{x \to 1} + n_h \Delta_m \Big|_{x = \frac{\overline{m}_b}{\overline{m}_c}} \right) \right) \right] + O\left(\alpha_s^3 \right) , \qquad (6.10)
$$

with

$$
y_1 = C_F \left(1 + \frac{3}{4} l_m \right) ,
$$
$$
y_2^{FF} = \left(-\frac{71}{128} + \frac{3}{4} \zeta_3 + \frac{\pi^2 (5 - 8 l_2)}{16} - \frac{9}{32} l_m + \frac{9}{32} l_m^2 \right) ,
$$
$$
y_2^{FA} = \left(\frac{1111}{384} - \frac{3}{8} \zeta_3 + \frac{\pi^2 (3 l_2 - 1)}{12} + \frac{185}{96} l_m + \frac{11}{32} l_m^2 \right) ,
$$

$$(6.11)$$

where $l_m = \log(\mu_c^2 / \overline{m}_c^2)$ and $l_2 = \log 2$. There are three different fermionic contributions at order α_s^2 in Equation (6.10) that are labelled by n_l, n_c and n_h. They are expressed by the general function Δ_m for fermionic contributions that is taken from Ref. [114] and reads

$$
\Delta_m = \frac{1}{96} \left[48 x^4 \log^2 x + 48 x^2 \log x + 72 x^2 + 4 l_m (3 l_m + 13) \right.
$$
$$
+ 8 \pi^2 \left(x^4 - 3 x^3 - 3 x + 1 \right) + 71
$$
$$
- 48 (x + 1)^2 \left(x^2 - x + 1 \right) \left(\log x \log(1 + x) + \text{Li}_2(-x) \right)
$$
$$
\left. - 48 (x - 1)^2 \left(x^2 + x + 1 \right) \left(\log x \log(1 - x) + \text{Li}_2(x) \right) \right] , \qquad (6.12)
$$

with $l_m = \log(\mu_c^2 / \overline{m}_c^2)$ as defined above and the mass ratio $x = m_2 / m_1$ between internal and external quark with masses m_2 and m_1 respectively. Since we consider the relation for the charm quark mass, we set $m_1 = \overline{m}_c$ in this case. Therefore, $\Delta_m|_{x \to 1}$ is the contribution where a charm quark runs in the fermionic loop, while $\Delta_m|_{x = \overline{m}_b / \overline{m}_c}$ denotes the diagram where a bottom quark runs in the loop, as shown in Figure 6.1. The limits of this function needed in the $\overline{\text{MS}}$ mass relation read

$$
\Delta_m|_{x \to 0} = -\frac{71}{96} - \frac{\pi^2}{12} - \frac{13}{24} l_m - \frac{1}{8} l_m^2 ,
$$
$$
\Delta_m|_{x \to 1} = -\frac{143}{96} + \frac{\pi^2}{6} - \frac{13}{24} l_m - \frac{1}{8} l_m^2 . \qquad (6.13)
$$

Up, down and strange quarks are considered massless in our calculation and therefore we set $n_l = 3$. The corrections of top quarks are not considered since they are highly suppressed by the mass ratio.
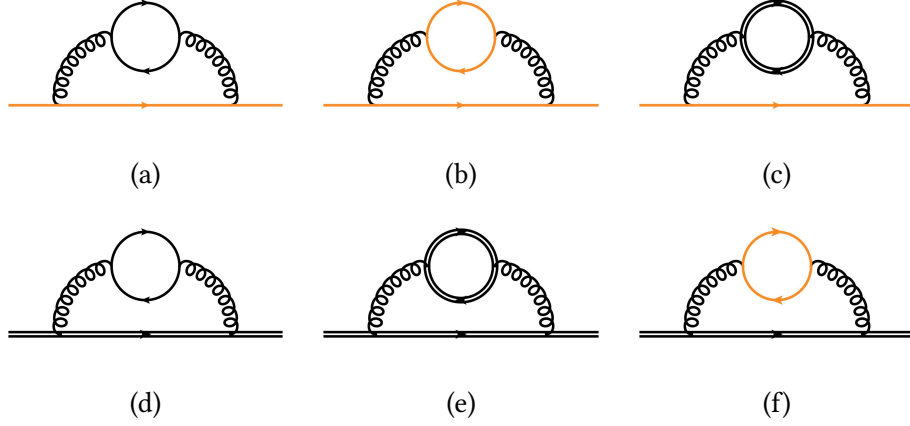
Figure 6.1.: The diagrams corresponding to (a) $\Delta_m|_{x\to0}$, (b) $\Delta_m|_{x\to1}$ and (c) $\Delta_m|_{x\to\overline{m}_b/\overline{m}_c}$ in the relation between charm quark on-shell and $\overline{\text{MS}}$ mass. The diagrams in (d), (e) and (f) show the corresponding diagrams for the analogous relation of the bottom quark. Double black, orange and single black lines denote bottom, charm and massless quarks respectively.

The expression in Equation (6.10) relates the on-shell mass to the $\overline{\text{MS}}$-mass at the scale $\mu_s = \mu_c$. To obtain an expansion in α_s at the scale $\mu_s \neq \mu_c$, the running of α_s has to be included using the one-loop relation

$$\alpha_s^{(4)}(\mu_c) = \alpha_s^{(4)}(\mu_s)\left[1 - \frac{\alpha_s^{(4)}(\mu_s)}{\pi}\beta_0 \log\left(\frac{\mu_c^2}{\mu_s^2}\right)\right] + O\left(\alpha_s^2\right) \tag{6.14}$$

with $\beta_0 = 11C_A/12 - T_F(n_l + n_c + n_h)/3$. In a last step, the $\overline{\text{MS}}$ mass defined with five active flavours has to be replaced by the $\overline{\text{MS}}$ mass with four active flavours [116]

$$\begin{aligned}\overline{m}_c^{(5)}(\mu_c) &= \zeta_m \overline{m}_c^{(4)}(\mu_c) \\ &= \left[1 + \left(\frac{\alpha_s^{(4)}}{\pi}\right)^2 \zeta_m^{(2)}\right]\overline{m}_c^{(4)}(\mu_c) + O\left(\alpha_s^3\right) \\ &= \left[1 + \left(\frac{\alpha_s^{(4)}}{\pi}\right)^2\left(-\frac{89}{432} + \frac{5}{36}\log\left(\frac{\mu_c^2}{m_b^2}\right) - \frac{1}{12}\log^2\left(\frac{\mu_c^2}{m_b^2}\right)\right)\right]\overline{m}_c^{(4)}(\mu_c) + O\left(\alpha_s^3\right).\end{aligned}$$

$$\tag{6.15}$$

The complete relation to transform the charm mass from on-shell to $\overline{\text{MS}}$ mass scheme with four active flavours therefore reads

$$\begin{aligned}m_c^{\text{OS}} = \overline{m}_c^{(4)}(\mu_c)\Bigg[&1 + \frac{\alpha_s^{(4)}(\mu_s)}{\pi}y_1 + \left(\frac{\alpha_s^{(4)}(\mu_s)}{\pi}\right)^2\left(C_F^2 y_2^{FF} + C_F C_A y_2^{FA}\right.\\ &\left.+ C_F T_F\left(n_l\Delta_m\Big|_{x\to0} + n_c\Delta_m\Big|_{x\to1} + n_h\Delta_m\Big|_{x=\frac{\overline{m}_b}{\overline{m}_c}}\right)\right)\Bigg]\end{aligned}$$

$$+ \left(\frac{\alpha_s^{(4)}(\mu_s)}{\pi} \right)^2 \left[-y_1 \beta_0 \log \left(\frac{\mu_c^2}{\mu_s^2} \right) + \zeta_m^{(2)} \right] + O\left(\alpha_s^3\right) . \tag{6.16}$$

Bottom mass

In an analogous way to the transformation of the charm mass, we can transform the bottom mass from on-shell into the $\overline{\text{MS}}$ scheme. However, there are some small differences. The starting point is the relation:

$$m_b^{\text{OS}} = \overline{m}_b^{(5)}(\mu_b) \left[1 + \frac{\alpha_s^{(4)}(\mu_b)}{\pi} y_1 + \left(\frac{\alpha_s^{(4)}(\mu_b)}{\pi} \right)^2 \left(C_F^2 y_2^{FF} + C_F C_A y_2^{FA} \right. \right.$$

$$\left. \left. + C_F T_F \left(n_l \Delta_m \Big|_{x \to 0} + n_c \Delta_m \Big|_{x = \frac{\overline{m}_c}{\overline{m}_b}} + n_h \Delta_m \Big|_{x \to 1} \right) \right) \right] + O\left(\alpha_s^3\right) . \tag{6.17}$$

Note that the terms introduced by closed massive fermion loops now have the inverted mass ratio compared to Equation 6.10. The corresponding Feynman diagrams are shown in Figure 6.1 (d), (e) and (f). When deriving the relation for the charm mass, the next step was to run the scale of the mass from μ_c to μ_s. This is not done for the bottom mass relation. Instead, the two scales μ_b and μ_s are identified with each other which yields $\log(\mu_b^2/\mu_s^2) = 0$. In contrast to the $\overline{\text{MS}}$ charm mass $\overline{m}_c$, the $\overline{\text{MS}}$ bottom mass $\overline{m}_b$ is considered with five active flavours and therefore there is no additional contribution similar to Equation (6.15).

6.3. Kinetic mass scheme

The kinetic mass scheme, introduced in Refs. [117, 118], is a short distance mass scheme that is expected to show good behaviour in applications like the B meson decay. This scheme relates the mass of the quark directly to the mass of the meson by

$$M_B = m_b + \overline{\Lambda} + \frac{\mu_\pi^2 + d_B \mu_G^2}{2m_b} + O\left(\Lambda_{\text{QCD}}\right) , \tag{6.18}$$

where $d_H = 3$ for a pseudoscalar and $d_B = -1$ for vector mesons. Note that $\overline{\Lambda}$ as well as μ_π are functions of the Wilsonian cutoff μ_{kin}, where $\Lambda_{QCD} \ll \mu_{\text{kin}} \ll M_B$. Equation (6.18) can be inverted to obtain an cutoff-dependent equation for the heavy quark mass as a function of the meson mass:

$$m_b(\mu_{\text{kin}}) = M_B - \overline{\Lambda}(\mu_{\text{kin}}) - \frac{\mu_\pi^2(\mu_{\text{kin}}) + d_H \mu_G^2(\mu_{\text{kin}})}{2m_b(\mu_{\text{kin}})} + O\left(\Lambda_{\text{QCD}}\right) . \tag{6.19}$$

Averaging over vector and pseudoscalar mesons B^* and B and taking into account that $d_B = 3$ and $d_B = -1$ respectively, the μ_G terms cancel and we obtain

$$m_b(\mu_{\text{kin}}) = M_{\overline{B}} - \overline{\Lambda}(\mu_{\text{kin}}) - \frac{\mu_\pi^2(\mu_{\text{kin}})}{2m_b(\mu_{\text{kin}})} + O\left(\Lambda_{\text{QCD}}\right) , \tag{6.20}$$

where

$$M_{\overline{B}} = \frac{M_B + 3M_{B^*}}{4} \, . \tag{6.21}$$

The relation between the quark mass in the kinetic and the on-shell scheme is then obtained with

$$m_Q^{\text{kin}}(\mu_{\text{kin}}) = m_Q^{\text{OS}} - \overline{\Lambda}(\mu_{\text{kin}})\Big|_{\text{pert}} - \frac{\mu_\pi^2(\mu_{\text{kin}})\Big|_{\text{pert}}}{2m_Q^{\text{kin}}(\mu_{\text{kin}})} + O\left(\Lambda_{\text{QCD}}\right) \, . \tag{6.22}$$

The advantage of this mass definition is the fact that the renormalon ambiguity present in m_Q^{OS} now cancels against the ones in $\overline{\Lambda}(\mu_{\text{kin}})|_{\text{pert}}$ and $\mu_\pi^2(\mu_{\text{kin}})|_{\text{pert}}$. The relation between the on-shell and kinetic mass up to two loop order is given by [119]

$$\begin{aligned}
\frac{m_b^{\text{OS}}}{m_b^{\text{kin}}} =& 1 - \frac{\alpha_s^{(3)}(\mu_s)}{\pi}\left[-\frac{4}{3}C_F\frac{\mu_{\text{kin}}}{m_b^{\text{kin}}} - \frac{1}{2}C_F\left(\frac{\mu_{\text{kin}}}{m_b^{\text{kin}}}\right)^2\right] \\
&- \left(\frac{\alpha_s^{(3)}(\mu_s)}{\pi}\right)^2\left[C_F\left(C_A\left(-\frac{215}{27} + \frac{2\pi^2}{9} + \frac{22}{9}L_\mu\right) + n_lT_F\left(\frac{64}{27} - \frac{8}{9}L_\mu\right)\right)\frac{\mu_{\text{kin}}}{m_b^{\text{kin}}} \right. \\
&\left. + C_F\left(C_A\left(-\frac{91}{36} + \frac{\pi^2}{12} + \frac{11}{12}L_\mu\right) + n_lT_F\left(\frac{13}{18} - \frac{1}{3}L_\mu\right)\right)\left(\frac{\mu_{\text{kin}}}{m_b^{\text{kin}}}\right)^2\right] + O\left(\alpha_s^3\right) \, , \tag{6.23}
\end{aligned}$$

where $n_l = 3$ and $L_\mu = \log(2\mu_{\text{kin}}/\mu_s)$ with the Wilsonian cutoff μ_{kin} and μ_s the renormalization scale of the strong coupling constant.

Since this relation is given as an expansion in α_s with three active flavours, the decoupling relation [115] has to be applied to couple the charm quark to the running of the strong coupling constant:

$$\alpha_s^{(3)}(\mu_s) = \alpha_s^{(4)}(\mu_s)\left(1 + \frac{\alpha_s^{(4)}(\mu_s)}{\pi}\frac{n_hT_F}{3}\log\left(\frac{\mu_s^2}{m_c^2}\right)\right) + O\left(\alpha_s^3\right) \, . \tag{6.24}$$

The relation between on-shell and kinetic bottom quark mass with four active flavours is then obtained by

$$\begin{aligned}
m_b^{\text{OS}} =& m_b^{\text{kin}}\left[1 - \frac{\alpha_s^{(4)}(\mu_s)}{\pi}\left(-\frac{4}{3}C_F\frac{\mu_{\text{kin}}}{m_b^{\text{kin}}} - \frac{1}{2}C_F\left(\frac{\mu_{\text{kin}}}{m_b^{\text{kin}}}\right)^2\right)\right. \\
&- \left(\frac{\alpha_s^{(4)}(\mu_s)}{\pi}\right)^2\left(C_F\left(C_A\left(-\frac{215}{27} + \frac{2\pi^2}{9} + \frac{22}{9}L_\mu\right) + n_lT_F\left(\frac{64}{27} - \frac{8}{9}L_\mu\right)\right)\frac{\mu_{\text{kin}}}{m_b^{\text{kin}}} \right. \\
&\left.+ C_F\left(C_A\left(-\frac{91}{36} + \frac{\pi^2}{12} + \frac{11}{12}L_\mu\right) + n_lT_F\left(\frac{13}{18} - \frac{1}{3}L_\mu\right)\right)\left(\frac{\mu_{\text{kin}}}{m_b^{\text{kin}}}\right)^2\right)
\end{aligned}$$

$$-\frac{n_h T_F}{3} \left(\frac{\alpha_s^{(4)}(\mu_s)}{\pi}\right)^2 \left(-\frac{4}{3} C_F \frac{\mu_{\text{kin}}}{m_b^{\text{kin}}} - \frac{1}{2} C_F \left(\frac{\mu_{\text{kin}}}{m_b^{\text{kin}}}\right)^2\right) \log\left(\frac{\mu_s^2}{m_c^2}\right)\right] + O\left(\alpha_s^3\right) . \qquad (6.25)$$

Furthermore, when switching to the kinetic mass scheme, the operators at higher orders in $1/m_b$ also have to be transformed according to

$$\mu_\pi^2(0) = \mu_\pi^2(\mu_{\text{kin}}) - \mu_\pi^2(\mu_{\text{kin}})\Big|_{\text{pert}} ,$$
$$\rho_D^3(0) = \rho_D^3(\mu_{\text{kin}}) - \rho_D^3(\mu_{\text{kin}})\Big|_{\text{pert}} . \qquad (6.26)$$

The perturbative contributions $\mu_\pi^2(\mu_{\text{kin}})|_{\text{pert}}$ and $\rho_D^3(\mu_{\text{kin}})|_{\text{pert}}$ are calculated up to N³LO in Ref. [113]. In our calculation, only the contributions up to NNLO are needed; they read

$$\mu_\pi^2(\mu_{\text{kin}})\Big|_{\text{pert}} = \frac{\alpha_s^{(3)}(\mu_s)}{\pi} C_F \mu_{\text{kin}}^2$$
$$\left[1 + \frac{\alpha_s^{(3)}(\mu_s)}{\pi} \left(\frac{C_A}{18} \left(91 - 3\pi^2 - 33 L_\mu\right) - \frac{n_l T_F}{9} \left(13 - 6 L_\mu\right)\right)\right] + O\left(\alpha_s^3\right) ,$$

$$\rho_D^3(\mu_{\text{kin}})\Big|_{\text{pert}} = \frac{\alpha_s^{(3)}(\mu_s)}{\pi} C_F \mu_{\text{kin}}^3$$
$$\left[\frac{2}{3} + \frac{\alpha_s^{(3)}(\mu_s)}{\pi} \left(\frac{C_A}{18} \left(57 - 2\pi^2 - 22 L_\mu\right) - \frac{4 n_l T_F}{9} \left(2 - L_\mu\right)\right)\right] + O\left(\alpha_s^3\right) ,$$
$$(6.27)$$

where $L_\mu = \log(2\mu_{\text{kin}}/\mu_s)$ with μ_s the scale of the strong coupling constant α_s with three active flavours and the Wilsonian cutoff μ_{kin}. These relations are given as expansions in α_s with three active flavours, so again the decoupling relation given in Equation (6.24) is applied to go to four active flavours. This yields an additional term for both $\mu_\pi^2(\mu_{\text{kin}})|_{\text{pert}}$ and $\rho_D^3(\mu_{\text{kin}})|_{\text{pert}}$, and we obtain

$$\mu_\pi^2(\mu_{\text{kin}})\Big|_{\text{pert}} = \frac{\alpha_s^{(4)}(\mu_s)}{\pi} C_F \mu_{\text{kin}}^2 \left[1 + \frac{\alpha_s^{(4)}(\mu_s)}{\pi} \left(\frac{C_A}{18} \left(91 - 3\pi^2 - 33 L_\mu\right) - \frac{n_l T_F}{9} \left(13 - 6 L_\mu\right)\right.\right.$$
$$\left.\left. - \frac{n_h T_F}{3} \log\left(\frac{\mu_s^2}{m_c^2}\right)\right)\right] + O\left(\alpha_s^3\right) ,$$

$$\rho_D^3(\mu_{\text{kin}})\Big|_{\text{pert}} = \frac{\alpha_s^{(4)}(\mu_s)}{\pi} C_F \mu_{\text{kin}}^3 \left[\frac{2}{3} + \frac{\alpha_s^{(4)}(\mu_s)}{\pi} \left(\frac{C_A}{18} \left(57 - 2\pi^2 - 22 L_\mu\right) - \frac{4 n_l T_F}{9} \left(2 - L_\mu\right)\right.\right.$$
$$\left.\left. - \frac{2 n_h T_F}{9} \log\left(\frac{\mu_s^2}{m_c^2}\right)\right)\right] + O\left(\alpha_s^3\right) . \qquad (6.28)$$

These perturbative terms $\mu_\pi^2(\mu_{\text{kin}})|_{\text{pert}}$ and $\rho_D^2(\mu_{\text{kin}})|_{\text{pert}}$ are taken into account as corrections to Γ_3 when doing the analysis in the kinetic mass scheme.

Decay width in the kinetic mass scheme

Let us consider the nonleptonic decay width of the B-meson including operators up to order $1/m_b^3$ is given in Equation (2.43). We write the decay width as a perturbative series in α_s, obtaining

$$
\begin{aligned}
\Gamma(B) = \frac{G_F^2 m_b^5 |\lambda_{q_1 q_2 q_3}|^2}{192 \pi^3} &\left[\left(1 - \frac{\mu_\pi^2}{2 m_b^2} \right) \sum_n \left(\frac{\alpha_s}{\pi} \right)^n X_n(\rho) \right. \\
&\left. + \frac{\mu_G^2}{m_b^2} \sum_n \left(\frac{\alpha_s}{\pi} \right)^n X_n^G(\rho) + \frac{\rho_D^3}{m_b^3} \sum_n \left(\frac{\alpha_s}{\pi} \right)^n X_n^D(\rho) \right] + O\left(\frac{1}{m_b^4} \right) \\
= \Gamma_0 &\left[\left(C_1^2 G_{11} + C_1 C_2 G_{12} + C_2^2 G_{22} \right) \left(1 - \frac{\mu_\pi^2(0)}{2 m_b^2} \right) \right. \\
&+ \left(3 C_1^2 G_{G,11} + 2 C_1 C_2 G_{G,12} + 3 C_2^2 G_{G,22} \right) \frac{\mu_G^2(0)}{m_b^2} \\
&\left. + \left(3 C_1^2 G_{D,11} + 2 C_1 C_2 G_{D,12} + 3 C_2^2 G_{D,22} \right) \frac{\rho_D(0)}{m_b^3} \right] + O\left(\frac{1}{m_b^4} \right) .
\end{aligned}
\tag{6.29}
$$

The functions G_{ij} which enter the computation of Γ_3 and the μ_π operator are calculated for the different decay channels in Chapter 5.2 and are known up to NNLO. The functions $G_{G,ij}$ and $G_{D,ij}$ are the corresponding coefficients for the chromo-magnetic operator μ_G and the Darwin operator ρ_D. These coefficients are known at LO [47]. Their explicit expressions for all four partonic decay channels can be found in Appendix D.

When going to the kinetic scheme, the operators $\mu_\pi^2(0)$ and $\rho_D^3(0)$ have to be replaced according to Equation (6.26) and the perturbative corrections are considered as corrections to the decay width Γ_3. In the following, these contributions will be labelled by δ_{μ_π} and δ_{ρ_D}, respectively. Note that the functions $G_{D,ij}$ are functions of the mass ratio and therefore also obtain corrections from the mass renormalization scheme conversion.

Note that the prefactors of μ_π are the same G_{ij} as for Γ_3 and are therefore known up to NNLO, while for the $G_{D,ij}$, only the LO contributions $G_{D,ij}^{(0)}$ are known. To be consistent with the order of $G_{D,ij}$, we consider the Wilson coefficients to the same order in these terms. This means that for the last line in Equation (6.29), we obtain

$$
\left(3 C_1^{(0)\,2} G_{D,11}^{(0)} + 2 C_1^{(0)} C_2^{(0)} G_{D,12}^{(0)} + 3 C_2^{2\,(0)} G_{D,22}^{(0)} \right) \frac{\rho_D(0)}{m_b^3} .
\tag{6.30}
$$

Furthermore, we set the $\log(\mu_0^2/m_b^2)$ terms that appear in the Darwin operator coefficients $G_{D,ij}$ to zero in our analysis of Γ_3. They will eventually cancel against the logarithms in the $\tilde{\Gamma}_6$ contribution once the complete decay width is considered. The same convention has been used in the phenomenological analysis discussed in Chapter 7.

6.4. Comparison of different quark mass renormalization schemes

In this Section, the decay width Γ_3 is analyzed and compared for different mass schemes. For this analysis, the numerical values listed in Section 6.1 are used. There are different mass schemes considered in the following:

- On-shell scheme for bottom and charm quark.

- $\overline{\text{MS}}$ scheme for bottom and charm quark.

- $\overline{\text{MS}}$ scheme for charm quark, kinetic mass scheme for bottom quark.

For all of these schemes, the decay width Γ_3 is considered as an expansion in α_s up to NNLO, and its behaviour as a function of the renormalization scale μ_s is investigated. The decay width is assembled by adding up the contributing channels $b \to c\bar{u}d$, $b \to c\bar{u}s$, $b \to c\bar{c}s$, $b \to c\bar{c}d$ and the CKM suppressed channels $b \to u\bar{c}s$, $b \to u\bar{c}d$, $b \to u\bar{u}d$ and $b \to u\bar{u}d$. Higher order operators in $1/m_b$ are not included here, for a more detailed analysis see Ref. [109].

For the uncertainty estimate of the numerical values obtained for the decay width, we vary the renormalization scale μ_s between $m_b/2 \le \mu_s \le 2m_b$. For the strong coupling constant we consider the uncertainty shown in Table 6.1 and for the quark masses the uncertainties given in Equation (6.1) and (6.2) are assumed.

On-shell scheme for bottom and charm quark

As a starting point we consider the on-shell mass scheme in which the calculation of the NNLO contributions in Chapter 5.2 is carried out. As already stated above, the on-shell scheme is not suitable for phenomenological analysis of the B decays; however, it serves as a reference point for the other schemes. Note that the calculation in the on-shell scheme performed in the previous chapters uses the strong coupling constant with five active flavours, see Chapter 5.2.

The decay width Γ_3 at the scale $\mu_s = m_b^{\text{OS}}$ as a sum over all possible nonleptonic final states reads

$$
\Gamma_3^{\text{NL}}\Big|_{m_c^{\text{OS, 2loop}}, m_b^{\text{OS, 2loop}}} = \left[\left(0.25450 + 0.25681 \frac{\alpha_s^{(4)}}{\pi} + 2.48539 \left(\frac{\alpha_s^{(4)}}{\pi} \right)^2 \right) \Bigg|_{b \to c\bar{u}x} \right.
$$
$$
+ \left(0.07752 + 0.34686 \frac{\alpha_s^{(4)}}{\pi} + 4.64997 \left(\frac{\alpha_s^{(4)}}{\pi} \right)^2 \right) \Bigg|_{b \to c\bar{c}x}
$$
$$
+ \left(0.00200 + 0.00549 \frac{\alpha_s^{(4)}}{\pi} + 0.03514 \left(\frac{\alpha_s^{(4)}}{\pi} \right)^2 \right) \Bigg|_{b \to u\bar{c}x}
$$
$$
\left. + \left(0.00424 + 0.00065 \frac{\alpha_s^{(4)}}{\pi} - 0.03307 \left(\frac{\alpha_s^{(4)}}{\pi} \right)^2 \right) \Bigg|_{b \to u\bar{u}x} \right] \text{ps}^{-1}
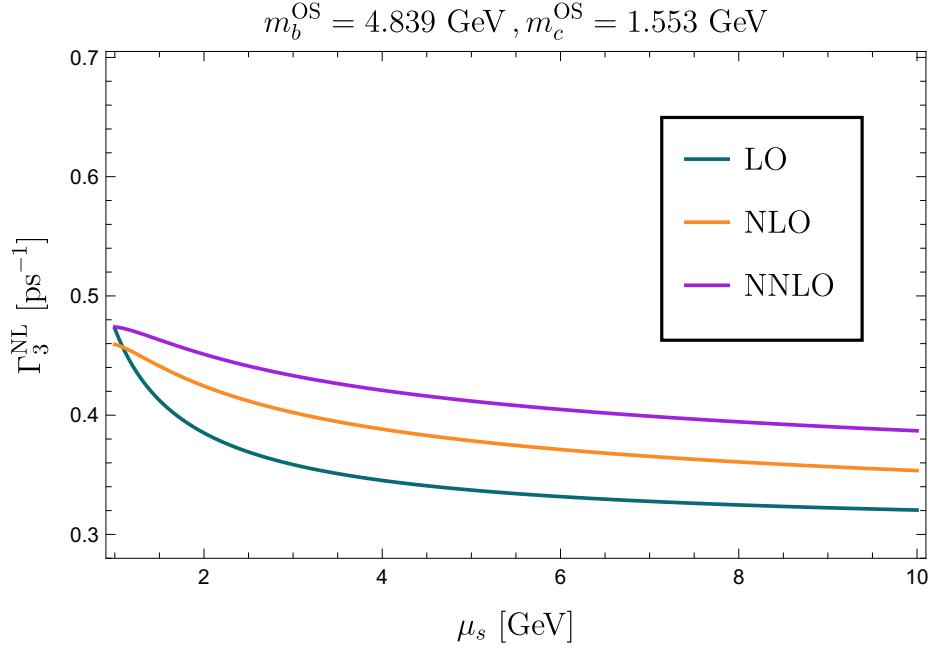$$

Figure 6.2.: The decay width for all nonleptonic decay channels combined in the on-shell mass scheme for both quark masses. The numerical values given in Equation (6.5) are used as input parameters for the masses.

$$= \left[0.33827 + 0.60982 \frac{\alpha_s^{(4)}}{\pi} + 7.13744 \left(\frac{\alpha_s^{(4)}}{\pi} \right)^2 \right] \mathrm{ps}^{-1}, \tag{6.31}$$

where the contributions of the different decay channels are flagged separately. We observe that the CKM enhanced decay channels $b \to c\bar{u}d$ and $b \to c\bar{c}s$ contribute $\sim 65\%$ and $\sim 29\%$ to the total decay width. The remaining contributions come from the CKM suppressed channels. Variation of the input parameters yield the theoretical uncertainties

$$\Gamma_3^{\mathrm{NL}} \Big|_{m_c^{\mathrm{OS, 2loop}}, m_b^{\mathrm{OS, 2loop}}} = 0.41313^{+0.18815}_{-0.15213}(m_c)^{+0.21878}_{-0.15517}(m_b)^{+0.00176}_{-0.00171}(\alpha_s)^{+0.02895}_{-0.02505}(\mu_s) \, \mathrm{ps}^{-1}. \tag{6.32}$$

The uncertainty induced by the renormalization scale is obtained by the variation of μ_s between $m_b/2 < \mu_s < 2m_b$ and is of the order of 7% of the total result. The dependence on the renormalization scale is shown in Figure 6.2. The uncertainty induced by the variation of the strong coupling constant α_s is below the per cent level.

For the variation of the masses, we obtain rather large uncertainties. We vary both quark masses by $\pm 0.3 \, \mathrm{GeV}$ to account for the bad convergence of the perturbative series relating the on-shell and the $\overline{\mathrm{MS}}$ mass. Considering the set of on-shell masses calculated with two and four loop relations in Equation (6.5) and (6.6), $0.3 \, \mathrm{GeV}$ is a small variation. The on-shell mass of the charm quarks differs by $\sim 0.5 \, \mathrm{GeV}$ between Equation (6.5) and (6.6). Nevertheless, the theoretical uncertainties induced by the variation of $0.3 \, \mathrm{GeV}$ is of the order of 40% to even 50% of the central value and assuming a variation of $0.5 \, \mathrm{GeV}$ would introduce an even larger uncertainty.

The strong dependence of our result on the quark masses combined with the large uncertainties of their numerical values makes the on-shell inadequate for a phenomenological analysis of B meson decays.

$\overline{\text{MS}}$ scheme for bottom and charm quark

In this scenario, both quark masses are transformed to the $\overline{\text{MS}}$ mass scheme. For the bottom quark mass, the value given in Equation (6.4) is used. The charm quark mass is evaluated with `RunDec` at the scale $\mu_c = 3\,\text{GeV}$. The decay width at the scale $\mu_s = \overline{m}_b(\overline{m}_b)$ as the sum of the different decay channels reads

$$
\begin{aligned}
\Gamma_3^{\text{NL}}\bigg|_{\overline{m}_c(3\text{GeV}),\overline{m}_b(\overline{m}_b)} =& \left[\left(0.18301 + 1.07443\frac{\alpha_s^{(4)}}{\pi} + 8.34064\left(\frac{\alpha_s^{(4)}}{\pi}\right)^2\right)\bigg|_{b\to c\bar{u}x}\right.\\
&+\left(0.10943 + 0.56524\frac{\alpha_s^{(4)}}{\pi} + 3.88935\left(\frac{\alpha_s^{(4)}}{\pi}\right)^2\right)\bigg|_{b\to c\bar{c}x}\\
&+\left(0.00144 + 0.00998\frac{\alpha_s^{(4)}}{\pi} + 0.08257\left(\frac{\alpha_s^{(4)}}{\pi}\right)^2\right)\bigg|_{b\to u\bar{c}x}\\
&\left.+\left(0.00216 + 0.01502\frac{\alpha_s^{(4)}}{\pi} + 0.12696\left(\frac{\alpha_s^{(4)}}{\pi}\right)^2\right)\bigg|_{b\to u\bar{u}x}\right]\text{ps}^{-1}\\
=& \left[0.29604 + \left(0.50257 + 2.45923\delta_{m_b} - 1.29712\delta_{m_c}\right)\frac{\alpha_s^{(4)}}{\pi}\right.\\
&+\left(4.37949 + 28.81244\delta_{m_b} - 13.40144\delta_{m_c}\right.\\
&\left.\left.-7.35096\delta_{m_b}\delta_{m_c}\right)\left(\frac{\alpha_s^{(4)}}{\pi}\right)^2\right]\text{ps}^{-1}\\
=& \ \Gamma_0\left[0.29604 + 1.66467\frac{\alpha_s^{(4)}}{\pi} + 12.43953\left(\frac{\alpha_s^{(4)}}{\pi}\right)^2\right]\text{ps}^{-1}. \qquad (6.33)
\end{aligned}
$$

As outlined in the first part of this chapter, the mass scheme transformation yields additional NLO and NNLO corrections to the decay width. These contributions are marked by the labels δ_{m_b} and δ_{m_c}. The sum of the additional terms is positive and even is the dominates the NLO and NNLO corrections.

The LO, NLO and NNLO curves as functions of the renormalization scale are shown in Figure 6.3. We observe that both the NLO and the NNLO corrections are relatively large compared to the LO contribution due to the large corrections induced by the mass scheme change. This does not only hold for $\mu_s = \overline{m}_b(\overline{m}_b)$, where they contribute with roughly $\sim 30\%$ (NLO) and $\sim 20\%$ (NNLO), see Equation (6.33), but also in the whole physically interesting region of μ_s.
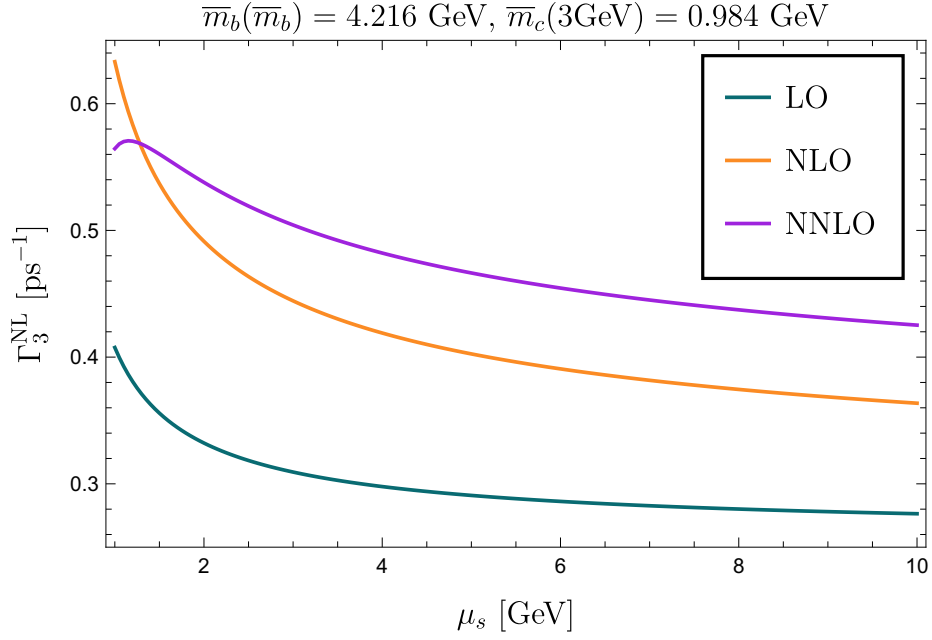
Figure 6.3.: The decay width for all nonleptonic channels combined and both quark masses renormalized in the $\overline{\text{MS}}$ scheme. The scales of the masses are fixed at $\mu_b = \overline{m}_b = 4.216\,\text{GeV}$ and $\mu_c = 3\,\text{GeV}$.

The uncertainties induced by the different input parameters are calculated as follows: For the renormalization scale μ_s, the variation between $\overline{m}_b(\overline{m}_b)/2 < \mu_s < 2\overline{m}_b(\overline{m}_b)$ is considered. For the renormalization scale of the charm quark mass μ_c, we consider the variation in the interval $2\,\text{GeV} \leq \mu_c \leq 6\,\text{GeV}$. Furthermore we take into account the parameter variation of the charm quark mass given by the uncertainty in Equation (6.3). For the bottom quark mass, we vary its numerical value in $\overline{\text{MS}}$ scheme according to the uncertainty given in Equation (6.4) . The strong coupling constant is varied according to its uncertainty given in Table 6.1. We obtain for the nonleptonic decay width

$$\Gamma_3^{\text{NL}}\bigg|_{\overline{m}_c(3\text{GeV}),\overline{m}_b(\overline{m}_b)} = 0.47831^{+0.02468}_{-0.0109}(\mu_c)^{+0.00591}_{-0.00593}(m_c)^{+0.00072}_{-0.00071}(m_b)^{+0.00421}_{-0.00410}(\alpha_s)^{+0.05354}_{-0.04373}(\mu_s)\,\text{ps}^{-1}.$$

$$(6.34)$$

The uncertainty induced by the renormalization scale μ_s is about $\sim 13\%$ at NLO and $\sim 10\%$ at NNLO which can be seen in Figure 6.3. Comparing the NNLO curve to the other scenarios shown for example in Figure 6.2 or 6.5. A much larger μ_s dependence is observed here.

Because of the large QCD corrections and strong dependence on the renormalization scale compared to other mass scheme choices, the scenario with both quark masses in the $\overline{\text{MS}}$ scheme turns out to be not a suitable choice for applications like the *B* meson decays.

$\overline{\text{MS}}$ scheme for bottom and charm quark with $\mu_c = \mu_s$

In the following, we consider a special case of the analysis in the $\overline{\text{MS}}$ mass scheme. In contrast to the previous subsection, we identify the scale of the charm quark mass μ_c with

the scale of the strong coupling constant, $\mu_c = \mu_s$. For the decay width at the central scale $\mu_s = \overline{m}_b(\overline{m}_b)$, we obtain slightly different numbers. The difference is due to the fact that the numerical value of the charm quark mass changes from $\overline{m}_c(\mu_c = 3\,\text{GeV}) = 0.984\,\text{GeV}$ to $\overline{m}_c(\mu_c = \overline{m}_b\,\text{GeV}) = 0.918\,\text{GeV}$, see also Equation (6.3). We refrain from showing the explicit expressions for the NLO and NNLO corrections of the different decay modes and only give the sum of all nonleptonic channels:

$$\Gamma_3^{\text{NL}}\bigg|_{\overline{m}_c(\mu_s),\overline{m}_b(\overline{m}_b)} = \Gamma_0 \left[0.32074 + 1.60764 \frac{\alpha_s^{(4)}}{\pi} + 11.01604 \left(\frac{\alpha_s^{(4)}}{\pi} \right)^2 \right] \text{ps}^{-1} \tag{6.35}$$

As for the previous scenario, the corrections at NLO an NNLO that arise from the mass scheme change are relatively large.

To estimate the theoretical uncertainties, we perform the same parameter variation as before. However, since we identified the scales of the strong coupling constant and the charm quark mass here, there are only four different sources of uncertainties. We obtain

$$\Gamma_3^{\text{NL}}\bigg|_{\overline{m}_c(\mu_s),\overline{m}_b(\overline{m}_b)} = 0.49168^{+0.00591}_{-0.00588}(m_c)^{+0.00064}_{-0.00065}(m_b)^{+0.00389}_{-0.00379}(\alpha_s)^{+0.02789}_{-0.02034}(\mu_s)\, \text{ps}^{-1}. \tag{6.36}$$

The uncertainties induced by the bottom quark mass and the strong coupling constant variation are again below the per cent level. For the parameter variation of the charm mass at the scale $\mu_c = \overline{m}_b(\overline{m}_b)$, we find uncertainties of the order of $\sim 1\%$.

It is interesting to observe that the uncertainty induced by the renormalization scale is of the order of $\sim 5\%$, which is roughly only half as big as in the previous scenario with fixed charm quark mass scale.

$\overline{\text{MS}}$ scheme for charm quark, kinetic mass scheme for bottom quark

In this scheme, the bottom quark mass is transformed to the kinetic mass scheme according to Equation (6.25) while the charm quark is transformed to the $\overline{\text{MS}}$ mass scheme again. The scale of the charm quark mass is fixed at $\mu_c = 3\,\text{GeV}$. For the bottom quark, the numerical value given in Equation (6.2) for $\mu_{\text{kin}} = 1\,\text{GeV}$ is used. As already explained in Section 6.3, when going to the kinetic mass scheme, Γ_3 gets additional corrections from the higher order operators ρ_D and μ_π. These corrections are also included in the following. The decay width obtained with this ansatz at the central scale $\mu_s = m_b^{\text{kin}}$ is given by

$$\begin{aligned}
\Gamma_3^{\text{NL}}\bigg|_{\overline{m}_c(3\text{GeV}),\, m_b^{\text{kin}}} = &\left[\left(0.28881 + 0.28415 \frac{\alpha_s^{(4)}}{\pi} + 3.21301 \left(\frac{\alpha_s^{(4)}}{\pi} \right)^2 \right) \right]\bigg|_{b \to c\bar{u}x} \\
&+ \left(0.18894 - 0.02645 \frac{\alpha_s^{(4)}}{\pi} + 0.19220 \left(\frac{\alpha_s^{(4)}}{\pi} \right)^2 \right)\bigg|_{b \to c\bar{c}x} \\
&+ \left(0.00228 + 0.00399 \frac{\alpha_s^{(4)}}{\pi} + 0.03764 \left(\frac{\alpha_s^{(4)}}{\pi} \right)^2 \right)\bigg|_{b \to u\bar{c}x}
\end{aligned}$$

$$\overline{m}_b(\overline{m}_b) = 4.216 \text{ GeV}, \ \overline{m}_c(\mu_s)$$
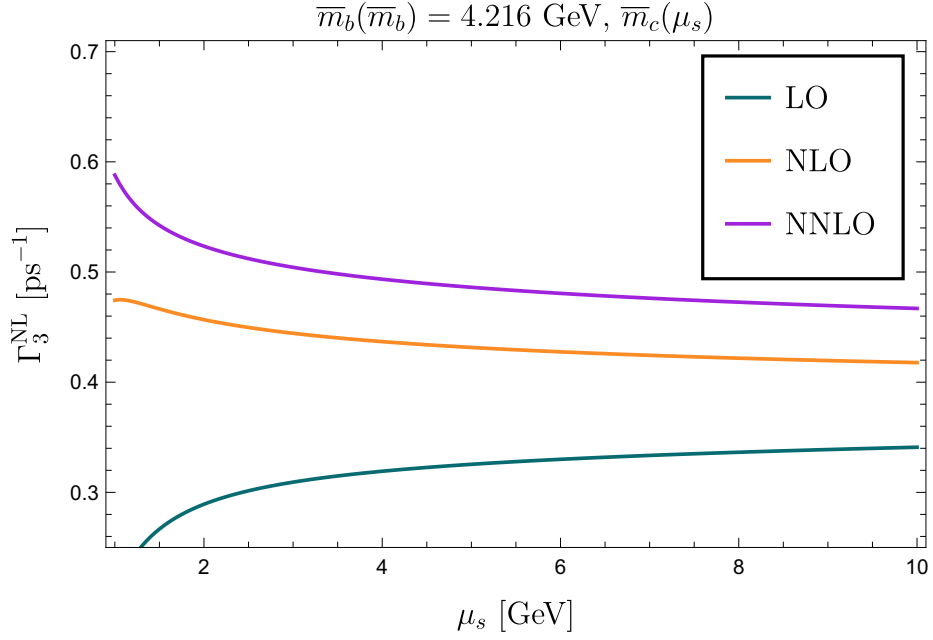

Figure 6.4.: The decay width for all nonleptonic channels combined and both quark masses in the $\overline{\text{MS}}$ scheme. The scales of the bottom mass is fixed at $\mu_b = \overline{m}_b = 4.216 \text{ GeV}$ while the scale of the charm mass is identified with the renormalization scale $\mu_s = \mu_c$.

$$
\begin{aligned}
&+ \left. \left(0.00321 + 0.00727\frac{\alpha_s^{(4)}}{\pi} + 0.07013\left(\frac{\alpha_s^{(4)}}{\pi}\right)^2\right)\right|_{b\to u\bar{u}x} \Bigg] \text{ps}^{-1} \\[2ex]
&= \Bigg[0.48324 + \left(0.73419 + 1.22916\delta_{m_b} - 1.80195\delta_{m_c}\right)\frac{\alpha_s^{(4)}}{\pi} \\[2ex]
&\quad + \left(5.93979 + 18.9694\delta_{m_b} - 19.1282\delta_{m_c} - 3.07714\delta_{m_b}\delta_{m_c}\right)\left(\frac{\alpha_s^{(4)}}{\pi}\right)^2 \\[2ex]
&\quad + 0.01541\delta_{\mu_\pi}\frac{\alpha_s^{(4)}}{\pi} + \left(0.19709 + 0.02622\delta_{m_b} - 0.05744\delta_{m_c}\right)\delta_{\mu_\pi}\left(\frac{\alpha_s^{(4)}}{\pi}\right)^2 \\[2ex]
&\quad + 0.09214\delta_{\rho_D}\frac{\alpha_s^{(4)}}{\pi} \\[2ex]
&\quad + \left(0.96978 + 0.13445\delta_{m_b} - 0.45656\delta_{m_c}\right)\delta_{\rho_D}\left(\frac{\alpha_s^{(4)}}{\pi}\right)^2 \Bigg] \text{ps}^{-1} \\[2ex]
&= \left[0.48324 + 0.26895\frac{\alpha_s^{(4)}}{\pi} + 3.51297\left(\frac{\alpha_s^{(4)}}{\pi}\right)^2 \right]\text{ps}^{-1},
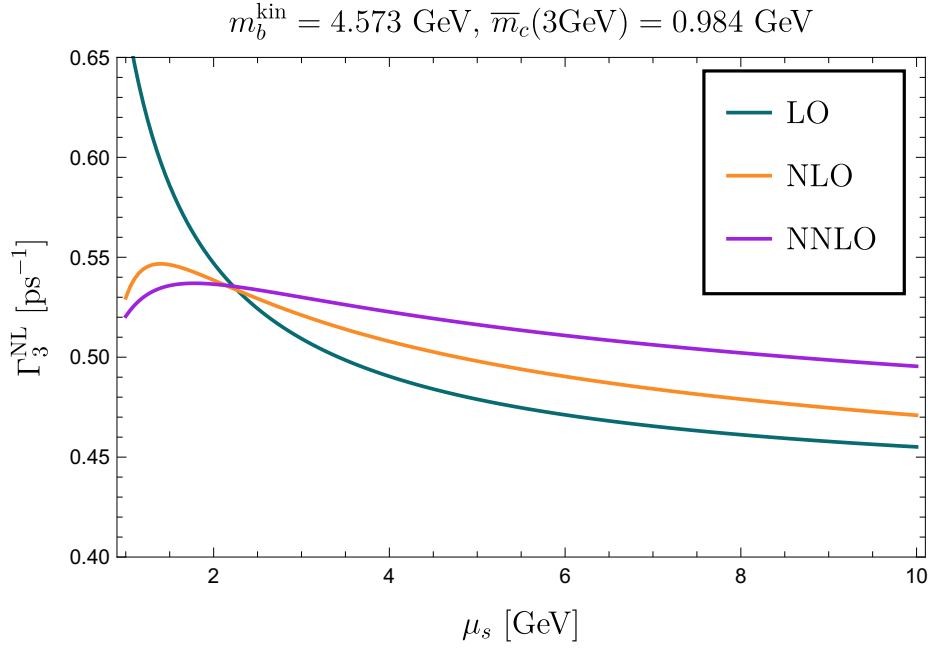\end{aligned}
\tag{6.37}
$$

Figure 6.5.: The decay width for all channels combined with the bottom mass in the kinetic mass scheme and the charm mass in the $\overline{\text{MS}}$ scheme. The scale of the $\overline{\text{MS}}$ mass is set to $\mu_c = 3\,\text{GeV}$.

where the contributions of the different decay channels are labelled separately. Also in this mass scheme, the CKM favoured decay channels with one-charm final states $b \to c\bar{u}d$ and $b \to c\bar{c}s$ contribute the most to the total decay width; they amount up to $\sim 59\%$ and $\sim 35\%$ of the total result. We observe that the relative contribution of $b \to c\bar{c}s$ is larger than for the pole scheme analysis. This can be explained by the numerical smaller value of the mass ratio $\overline{m}_c(3\text{GeV})/m_b^{\text{kin}} = 0.215 < m_c^{\text{OS}}/m_b^{\text{OS}} = 0.321$, which allows for a larger phase space for the decay channels with two charm quarks in the final state.

It is also interesting to split the higher order corrections into terms from purely NLO and NNLO diagrams, the additional terms induced by the mass scheme changes and the contributions from higher order operators: In contrast to the $\overline{\text{MS}}$ mass scheme for the bottom quarks, we observe large cancellations of the contributions introduced by the mass scheme changes. Their sum is negative at NLO and NNLO and reduces the size of the perturbative corrections.

The theoretical uncertainties induced by the renormalization scale and the strong coupling constant are obtained in the same way as described in the previous scenarios. For the quark mass uncertainties, the scale $\mu_c = 3\,\text{GeV}$ is varied in the range $2\,\text{GeV} < \mu_c < 6\,\text{GeV}$. The parameter variation of the charm quark mass is done according to Equation (6.3). For the bottom quark mass, we vary the central value according to Equation (6.18). As an additional input parameter that appears in the kinetic mass scheme, we vary the Wilsonian cutoff in the range $0.7\,\text{GeV} \le \mu_{\text{kin}} \le 1.3\,\text{GeV}$. We obtain

$$\left. \Gamma_3^{\mathrm{NL}} \right|_{\overline{m}_c(3\,\mathrm{GeV}),m_b^{\mathrm{kin}}}$$
$$= 0.51890^{+0.05015}_{-0.04011}(\mu_{\mathrm{kin}})^{+0.01919}_{-0.02191}(\mu_c)^{+0.00639}_{-0.00636}(m_c)^{+0.00142}_{-0.00142}(m_b)^{+0.00087}_{-0.00085}(\alpha_s)^{+0.01611}_{-0.02062}(\mu_s)\,\mathrm{ps}^{-1}\,. \tag{6.38}$$

In Figure 6.5, the decay width is shown as a function of the renormalization scale μ_s. The uncertainty on the decay width induced by the renormalization scale is of the order of $\sim 5\%$. The NNLO corrections are sizeable; however, they are not as big as for the scenario with both masses in the $\overline{\mathrm{MS}}$ scheme. At $\mu_s = m_b$, they are of the order of $\sim 3.5\%$ of the LO contribution whereas the NLO corrections are $\sim 4\%$. At $\mu_s \sim 2.5\,\mathrm{GeV}$, the NLO and NNLO corrections vanish completely.

We observe that the uncertainty on our result in Equation (6.38) is dominated by the uncertainty induced by the Wilsonian cutoff μ_{kin}. This is due to the fact that the perturbative contributions $\mu_\pi^2|_{\mathrm{pert}}$ and $\rho_D^3|_{\mathrm{pert}}$ are included in the definition of Γ_3 when going to the kinetic mass scheme. The μ_{kin}-dependence partially cancels for the total decay width where also μ_π^2 and ρ_D^3 contributions are taken into account. As a consequence, the uncertainty on the total decay width induced by μ_{kin} is significantly smaller than the uncertainty on Γ_3^{NL}, for more details, see Ref. [109].

For further analysis in Chapter 7, we also want to consider the uncertainties for Γ_3^{NL} at NLO in this scenario. With the same parameter and scale variation as outlined above, we find

$$\left. \Gamma_3^{\mathrm{NL,\,NLO}} \right|_{\overline{m}_c(3\,\mathrm{GeV}),m_b^{\mathrm{kin}}}$$
$$= 0.50194^{+0.02821}_{-0.01919}(\mu_{\mathrm{kin}})^{+0.03720}_{-0.03543}(\mu_c)^{+0.00581}_{-0.00579}(m_c)^{+0.00143}_{-0.00144}(m_b)^{+0.00031}_{-0.00030}(\alpha_s)^{+0.03099}_{-0.02763}(\mu_s)\,\mathrm{ps}^{-1}\,. \tag{6.39}$$

$\overline{\mathrm{MS}}$ scheme for charm quark with $\mu_c = \mu_s$, kinetic mass scheme for bottom quark

In the previous subsection, the kinetic scheme for the bottom quark mass was considered in combination with the $\overline{\mathrm{MS}}$ scheme for the charm quark mass where the scale of $\overline{m}_c$ was fixed at $\mu_c = 3\,\mathrm{GeV}$. Similar to the discussion of the bottom and charm quark mass in the $\overline{\mathrm{MS}}$ scheme, we also consider the special case where we identify the two renormalization scales $\mu_s = \mu_c$. The decay width at the scale $\mu_s = m_b^{\mathrm{kin}}$ is then obtained with

$$\left. \Gamma_3^{\mathrm{NL}} \right|_{\overline{m}_c(\mu_s),m_b^{\mathrm{kin}}} = \left[0.52441 + 0.03672\frac{\alpha_s^{(4)}}{\pi} + 1.11034\left(\frac{\alpha_s^{(4)}}{\pi}\right)^2 \right]\mathrm{ps}^{-1}\,, \tag{6.40}$$

We again observe a large cancellation of the terms introduced by the mass scheme change. The remaining contributions are negative and reduce the seize of the NLO and NNLO corrections significantly, which can be observed in Figure 6.6, where the decay width as a function of μ_s is shown. For the theoretical uncertainties, we obtain

$$\left. \Gamma_3^{\mathrm{NL}} \right|_{\overline{m}_c(\mu_s),m_b^{\mathrm{kin}}} = 0.53232^{+0.05315}_{-0.0427}(\mu_{\mathrm{kin}})^{+0.00643}_{-0.00641}(m_c)^{+0.00137}_{-0.00138}(m_b)^{+0.00022}_{-0.00021}(\alpha_s)^{+0.00730}_{-0.00303}(\mu_s)\,\mathrm{ps}^{-1}\,,$$
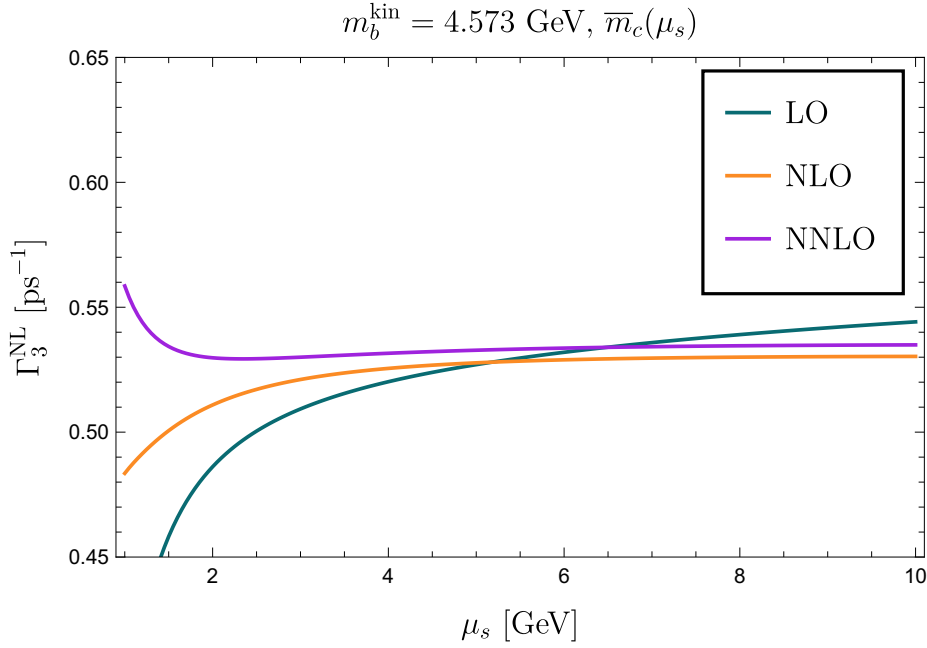$$\tag{6.41}$$

Figure 6.6.: The decay width for all channels combined with the bottom mass in the kinetic mass scheme and the charm mass in the $\overline{\text{MS}}$ scheme. The scale of the $\overline{\text{MS}}$ mass is identified with the scale of the strong coupling constant $\mu_c = \mu_s$.

where the parameter and scale variations are done in the same way as in the previous subsection. The uncertainty induced by the renormalization scale is relatively small, of the order of $\sim 1\%$. As it was also observed in the previous scenario, the dependence on the bottom quark mass is rather small, which can be explained by the small uncertainty on the value of m_b^{kin}. The theoretical uncertainty is dominated by the variation of Wilsonian cutoff μ_{kin}. As discussed in the previous section, this large uncertainty will reduce when considering the total decay width including contributions from μ_π^2 and ρ_D^3.

It is interesting to note that the total theoretical uncertainty of the decay width is reduced when the charm mass in the $\overline{\text{MS}}$ scheme is identified with the scale of the strong coupling constant $\mu_c = \mu_s$ instead of a fixed μ_c. This leads to a sizeable reduction of the renormalization scale induced uncertainty, both in the scenario with the bottom quark mass in the kinetic as well as in the $\overline{\text{MS}}$ scheme.

Conclusion

Considering the findings above, we can exclude several mass schemes for further phenomenological analysis of the decay rate. As already mentioned, the scheme where both masses are renormalized on-shell should not be considered for phenomenological predictions even if its renormalization scale dependence is small. The fact that the perturbative series of the on-shell mass shows a bad convergence behaviour results in large uncertainties of the decay width.

The analysis of the results applying the $\overline{\text{MS}}$ scheme, which is usually used for high energy processes, for both quark masses leads to large corrections at NLO and NNLO and a

bad convergence of the perturbative series of the decay width. For this reason it is not considered for the phenomenological application.

The scheme that shows the best behaviour is the kinetic mass scheme for the bottom quark mass and the $\overline{\text{MS}}$ mass scheme. In this scheme, the μ_s dependence of the NNLO decay width is significantly reduced, especially in the case where we identify $\mu_c = \mu_s = \mu_b$. We observe that the scheme conversion leads to large cancellations of higher order corrections which results in a good convergence of the perturbative series. In total the perturbative corrections are of the order of per cent for the schemes with the kinetic bottom mass.

Because of the good behaviour of Γ_3^{NL} in this scheme and also because many other quantities that enter the decay rate of the B mesons, as, e.g., the parameters μ_π^2, μ_G^2 and ρ_D^3, have been extracted in this scheme [55], we will use the the kinetic mass for the bottom quark and the $\overline{\text{MS}}$ mass as the default mass scheme for further analysis.

7. Decay width of B mesons

In this chapter, the NNLO corrections for the nonleptonic b-quark decay Γ_3^{NL} that are calculated in this thesis and published in Ref. [34] are included in the analysis of the full decay width of B mesons. The explicit calculations in this Chapter are done in collaboration with Matteo Fael, Alexander Lenz, Maria Laura Psicopo, Aleksey Rusov, Kay Schönwald and Matthias Steinhauser. The results discussed in this Chapter can also be found in Ref. [109].

7.1. Decay width of B_s, B_d and B^+

In this section, we use the NNLO results for Γ_3 to update the theoretical predictions of B meson decay widths. The decay width of B mesons in the HQE as an operator expansion in $\Lambda_{\mathrm{QCD}}/m_b$ is given in Equation (2.43).

For the input parameters, the numerical values and corresponding uncertainties given in Section 6.1 are used. For the mass renormalization scheme of this calculation, we choose the $\overline{\mathrm{MS}}$ mass scheme for the charm quark and the kinetic mass scheme for the bottom quark. For this scheme choice, we observe a good behaviour of Γ_3, as outlined in Chapter 6. Furthermore, the same scheme has been used also in previous publications, see for example Ref. [15], and the values of many parameters in the HQE i.e. m_b, μ_π^2 and ρ_D^3 are extracted in this scheme [55].

In the following analysis, we fix the scale of the charm mass at $\mu_c = m_b^{\mathrm{kin}}$ and vary it between $m_b^{\mathrm{kin}}/2 \leq \mu_c \leq 2m_b^{\mathrm{kin}}$. For the renormalization scale of the strong coupling constant μ_s we choose the same central scale $\mu_s = m_b^{\mathrm{kin}}$ and vary it independently of μ_c in the range $m_b^{\mathrm{kin}}/2 \leq \mu_s \leq 2m_b^{\mathrm{kin}}$. For the renormalization scale of the $\Delta B = 0$ operators, μ_0, we choose the same central value and the same variation range as for μ_s and μ_c. The kinetic mass of the bottom quark is given in Equation (6.2) as a function of the Wilsonian cutoff $\mu_{\mathrm{kin}} = 1\,\mathrm{GeV}$. We vary this cutoff scale, similar to the analysis in the previous chapter, in the interval $0.7\,\mathrm{GeV} \leq \mu_{\mathrm{kin}} \leq 1.3\,\mathrm{GeV}$.

The parameter and scale variation is done similar to Chapter 6. After variation of the individual parameters and scales, all uncertainties are added in quadrature.

The total decay width of B mesons includes both semileptonic and nonleptonic decay channels. For consistency, we use the same order of accuracy for all contributions of the semileptonic and nonleptonic decays. This means for example that we consider Γ_3^{SL} as well as Γ_3^{NL} up to order α_s^2 and do not include the N³LO correction to the semileptonic decay channel. The same holds for the NLO corrections to the $1/m_b^2$ and $1/m_b^3$ suppressed operators that are known for the semileptonic decay but not for the nonleptonic channels.

For the B^+ meson, the following values for the decay width are obtained at different

orders in perturbation theory:

$$\Gamma(B^+)\Big|_{\text{HQE}} = 0.666^{+0.108}_{-0.124}\ \text{ps}^{-1}\Big|_{\text{LO}}$$

$$= 0.593^{+0.047}_{-0.061}\ \text{ps}^{-1}\Big|_{\text{NLO}}$$

$$= 0.587^{+0.025}_{-0.035}\ \text{ps}^{-1}\Big|_{\text{NNLO}}, \tag{7.1}$$

whereas the experimental value is given by [16]

$$\Gamma(B^+)\Big|_{\text{exp}} = 0.6105 \pm 0.0015\ \text{ps}^{-1}. \tag{7.2}$$

The same analysis for the B_d meson yields

$$\Gamma(B_d)\Big|_{\text{HQE}} = 0.688^{+0.118}_{-0.128}\ \text{ps}^{-1}\Big|_{\text{LO}}$$

$$= 0.642^{+0.049}_{-0.064}\ \text{ps}^{-1}\Big|_{\text{NLO}}$$

$$= 0.636^{+0.028}_{-0.037}\ \text{ps}^{-1}\Big|_{\text{NNLO}}, \tag{7.3}$$

which should be compared to the experimental value [16]

$$\Gamma(B_d)\Big|_{\text{exp}} = 0.6592 \pm 0.0017\ \text{ps}^{-1}. \tag{7.4}$$

For the remaining meson B_s, we find

$$\Gamma(B_s)\Big|_{\text{HQE}} = 0.680^{+0.116}_{-0.127}\ \text{ps}^{-1}\Big|_{\text{LO}}$$

$$= 0.633^{+0.048}_{-0.063}\ \text{ps}^{-1}\Big|_{\text{NLO}}$$

$$= 0.628^{+0.027}_{-0.035}\ \text{ps}^{-1}\Big|_{\text{NNLO}}, \tag{7.5}$$

where the experimental value reads [16]

$$\Gamma(B_s)\Big|_{\text{exp}} = 0.6579 \pm 0.0022\ \text{ps}^{-1}. \tag{7.6}$$

The central value and its theoretical uncertainty at LO, NLO and NNLO for all three B mesons is shown in Figure 7.1. For comparison we also plot the experimental values and their uncertainties. Going from LO to NLO and NNLO, we observe a significant reduction of the uncertainty bands. This is due to the expected effect of the decreasing renormalization scale dependence when including higher orders in perturbation theory. From NLO to NNLO, the uncertainty reduction is roughly of the order of $\sim 50\%$ for the total decay width. This uncertainty reduction is mainly due to the NNLO contributions of Γ_3, which can be seen by considering the uncertainty estimates at NLO and NNLO
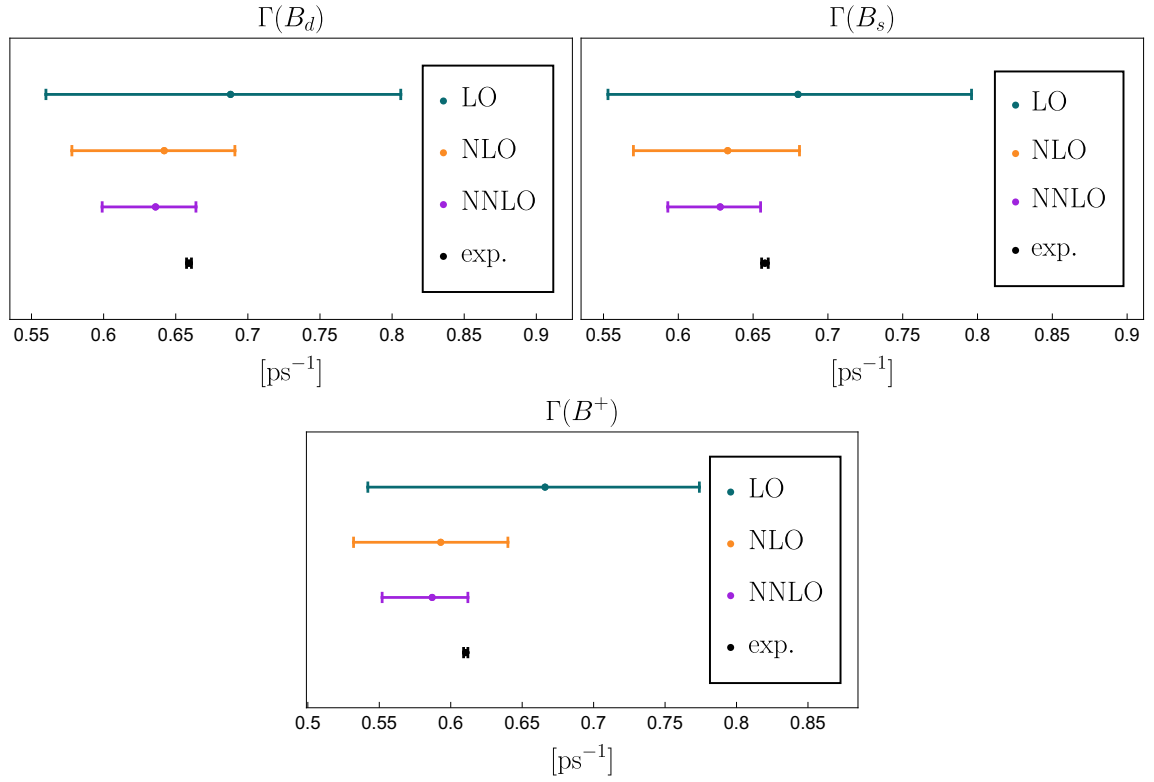
Figure 7.1.: The decay width of the mesons B^+, B_d and B_s at LO, NLO and NNLO accuracy compared to the experimental value. The error bars include the uncertainties induced by the renormalization scale μ_s, the scale of the charm quark mass, the Wilsonian cut-off μ^{kin} and μ_0 as well as the parameter variation of masses and CKM matrix elements.

for Γ_3^{NL} given in Equations (6.39) and (6.38). Adding the uncertainties in quadrature and comparing NLO and NNLO results, we find

$$\Gamma_3^{\mathrm{NL,\,NLO}}\Big|_{\overline{m}_c(3\mathrm{GeV}),m_b^{\mathrm{kin}}} = 0.50194^{+0.04878}_{-0.04532}\,\mathrm{ps}^{-1}\,,$$

$$\Gamma_3^{\mathrm{NL,\,NNLO}}\Big|_{\overline{m}_c(3\mathrm{GeV}),m_b^{\mathrm{kin}}} = 0.51890^{+0.02591}_{-0.03079}\,\mathrm{ps}^{-1}\,, \tag{7.7}$$

which is an uncertainty reduction of similar size as in Equations (7.1), (7.3) and (7.5). Note that we neglected the uncertainty contribution induced by the scale μ_{kin} in Equation (7.7) since the dependence on this scale drops out nearly completely when including higher order $1/m_b$-suppressed operators, see Ref. [109].

Comparing experiment and theory, we observe that the central value of the theoretical predictions underestimates the experimental values for all three mesons. However, theory and experiment are compatible within the 1σ range. The remaining uncertainty of the theoretical decay rate prediction is dominated by the uncertainty on the value of the bottom quark mass, which enters the prefactor Γ_0 with m_b^5, and the renormalization scale variation, although the latter is significantly reduced.

As mentioned before, the numbers presented for the theoretical predictions do not include all available contributions. For example the third order QCD corrections to Γ_3^{SL}, the QED contributions to Γ_3^{SL} and the NLO corrections to μ_G^2 of the $b \to c\bar{u}d$ are not taken into account in order to treat semileptonic and nonleptonic decay channels consistently. Including these contributions would lead to a shift of $\sim +0.7\%$ [109] of the total decay which would further reduce the discrepancy between experiment and theoretical prediction.

On top of that, there are corrections that are not known yet but might yield a sizeable correction to the total decay width. For example, the QED effects to the semileptonic decays $b \to c l \bar{\nu}_l$ with $l \in \{e, \mu\}$ is of the order of $\sim +2\%$ of the LO QCD contribution. It is possible that the corresponding contributions to $b \to c\tau\bar{\nu}_\tau$ and the nonleptonic decay channels are of the same size and could lead to an additional shift of the total decay width of the order of $\sim 1 - 2\%$.

Furthermore, the NLO corrections to the dimension-five operators of the decay channel $b \to c\bar{c}s$ might be of the order of the corresponding $b \to c\bar{u}d$ which is of the order of $\sim 0.5\%$ of the total result. Including the total NLO contributions may therefore yield a shift of $+1\%$ of the total result which would move the theoretical prediction further towards the experimental value.

7.2. Lifetime ratios

In addition to the total decay width, it is also interesting to consider the lifetime ratios of B mesons. They have the advantage that the leading contribution of the bottom quark decay cancels out. The lifetime ratios are therefore independent of the relative large uncertainties induced by Γ_3 and the prefactor containing m_b^5. Writing schematically the decay width of B mesons as

$$\Gamma(B_q) = \Gamma_3 + \delta\Gamma_{B_q}\,, \tag{7.8}$$

with the decay width of the bottom quark Γ_3 and higher order $1/m_b$ suppressed corrections $\delta\Gamma_{B_q}$, we find for the lifetime ratio of two B mesons B_q and $B_{q'}$

$$\frac{\tau(B_q)}{\tau(B_{q'})} = \frac{\Gamma_3 + \delta\Gamma_{B_{q'}}}{\Gamma_3 + \delta\Gamma_{B_q}} = \frac{\Gamma(B_q) - \delta\Gamma_{B_q} + \delta\Gamma_{B_{q'}}}{\Gamma_3 + \delta\Gamma_{B_q}} = 1 + \left(\delta\Gamma_{B_{q'}} - \delta\Gamma_{B_q}\right)\tau(B_q). \tag{7.9}$$

This expression can be used to make predictions for lifetime ratios that are independent of Γ_3 by using the theoretical results of the $1/m_b$ suppressed contributions $\delta\Gamma_{B_{q'}}$ and $\delta\Gamma_{B_q}$ together with the experimental value of $\Gamma(B_q)$. For the two lifetime ratios $\tau(B^+)/\tau(B_d)$ and $\tau(B_s)/\tau(B_d)$ the contributions of two-quark and four-quark operators read

$$\frac{\tau(B^+)}{\tau(B_d)}\bigg|_{\text{HQE}} = 1 + 16\pi^2\left[\left.\left(\tilde{\Gamma}_6\frac{\langle\tilde{O}_6\rangle}{m_b^3} + \tilde{\Gamma}_7\frac{\langle\tilde{O}_7\rangle}{m_b^4}\right)\right|_{B_d} - \left.\left(\tilde{\Gamma}_6\frac{\langle\tilde{O}_6\rangle}{m_b^3} + \tilde{\Gamma}_7\frac{\langle\tilde{O}_7\rangle}{m_b^4}\right)\right|_{B^+} + O\left(\frac{1}{m_b^5}\right)\right]\tau(B^+),$$

$$\frac{\tau(B_s)}{\tau(B_d)}\bigg|_{\text{HQE}} = 1 + \left(\left[\left.\left(\Gamma_5\frac{\langle O_5\rangle}{m_b^2} + \Gamma_6\frac{\langle O_6\rangle}{m_b^3}\right)\right|_{B_d} - \left.\left(\Gamma_5\frac{\langle O_5\rangle}{m_b^2} + \Gamma_6\frac{\langle O_6\rangle}{m_b^3}\right)\right|_{B_s} + O\left(\frac{1}{m_b^4}\right)\right]\right.$$

$$\left.+ 16\pi^2\left[\left.\left(\tilde{\Gamma}_6\frac{\langle\tilde{O}_6\rangle}{m_b^3} + \tilde{\Gamma}_7\frac{\langle\tilde{O}_7\rangle}{m_b^4}\right)\right|_{B_d} - \left.\left(\tilde{\Gamma}_6\frac{\langle\tilde{O}_6\rangle}{m_b^3} + \tilde{\Gamma}_7\frac{\langle\tilde{O}_7\rangle}{m_b^4}\right)\right|_{B^+} + O\left(\frac{1}{m_b^5}\right)\right]\right)\tau(B_s).$$

$$\tag{7.10}$$

Note that for the ratio between B^+ and B_d, the contributions of two-quark operators vanish due to the isospin symmetry of the matrix elements $\langle O_i\rangle|_{B_d} = \langle O_i\rangle|_{B^+}$. This is not the case for the ratio of B_s and B_d.

With these equations, we obtain for the lifetime ratios $\tau(B^+)/\tau(B_d)$ and $\tau(B_s)/\tau(B_d)$ the following theoretical predictions:

$$\frac{\tau(B^+)}{\tau(B_d)}\bigg|_{\text{HQE}} = 1.036^{+0.036}_{-0.027}\bigg|_{\text{LO}}$$

$$= 1.081^{+0.014}_{-0.016}\bigg|_{\text{NLO}}, \tag{7.11}$$

$$\frac{\tau(B_s)}{\tau(B_d)}\bigg|_{\text{HQE}} = 1.0132^{+0.0070}_{-0.0072}\bigg|_{\text{LO}}$$

$$= 1.0131^{+0.0073}_{-0.0074}\bigg|_{\text{NLO}}. \tag{7.12}$$

Note that only partial results can be obtained at NLO for $\tau(B_s)/\tau(B_d)$ since the complete order α_s^1 corrections to the two-quark operator contributions are not known. These missing contributions are expected to yield a dominating effect on the lifetime ratio.

To obtain the numbers that are given in Equation (7.11) and (7.12), we use the experimental results for the decay width of B^+ and B_s given in Equations (7.2) and (7.6). The experimental measurements of these ratios are very precise and reach per mille accuracy [16]:

$$\frac{\tau(B^+)}{\tau(B_d)}\bigg|_{\text{exp}} = 1.076 \pm 0.004,$$

$$\frac{\tau(B_s)}{\tau(B_d)}\bigg|_{\text{exp}} = 1.0032 \pm 0.0032. \tag{7.13}$$
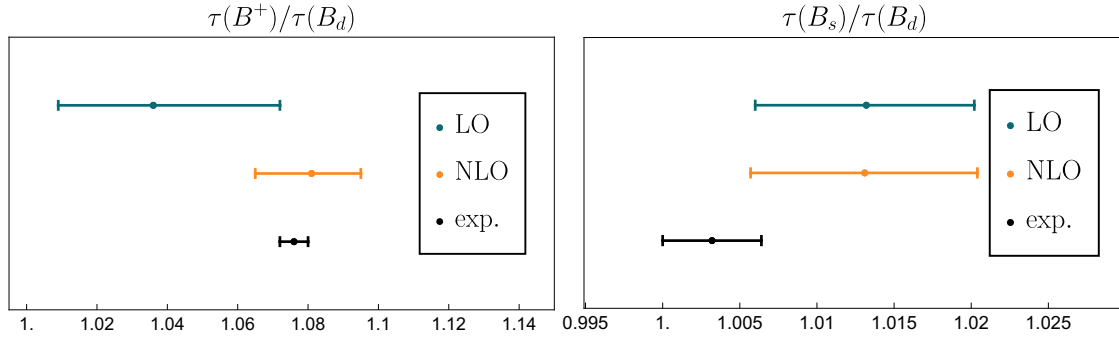
Figure 7.2.: LO and NLO predictions for the lifetime ratios of B mesons compared to the experimental value. For $\tau(B_s)/\tau(B_d)$ only partial NLO results are available.

We observe for $\tau(B^+)/\tau(B_d)$ that the NLO QCD corrections yield a positive shift of the central value. The theoretical prediction is in very good agreement with the experimental value. For $\tau(B_s)/\tau(B_d)$, we observe only minor changes when including the partially known NLO corrections. This might be due to more significant unknown contributions. As shown in Equation (7.10), not only the four-quark but also the two-quark operators enter this ratio. Since the NLO contributions to these two-quark operator coefficients are known $b \rightarrow c\bar{u}d$ but not for $b \rightarrow c\bar{c}s$, we can only obtain a partial NLO prediction for this lifetime ratio.

For both lifetime ratios, the theoretical predictions and the experimental results are in agreement within their uncertainties.

7.3. The semileptonic branching fraction purely from theory

In addition to the total decay width of B mesons, another interesting observable is the semileptonic branching fraction that gives that is defined by the ratio of the semileptonic decay width into electron-neutrino or muon-neutrino pair and the total decay width

$$\mathcal{B}^{\text{SL}}(B_q) = \frac{\Gamma^{\text{SL}}}{\Gamma^{\text{tot}}} = \frac{\Gamma^{\text{SL}}}{2\Gamma^{\text{SL}} + \Gamma^{\text{SL}}(\tau) + \Gamma^{\text{NL}}} = \frac{1}{2 + \frac{\Gamma^{\text{SL}}(\tau)}{\Gamma^{\text{SL}}} + \frac{\Gamma^{\text{NL}}}{\Gamma^{\text{SL}}}}, \tag{7.14}$$

where $\Gamma^{\text{SL}} = \Gamma(B_q \rightarrow X_c e\bar{\nu}_e) = \Gamma(B_q \rightarrow X_c\mu\bar{\nu}_\mu)$ denotes the semileptonic decay width. For the total decay width, we use the NNLO predictions obtained in Section 7.1. for the semileptonic decay width we use the implementation of the package kolya [120] that includes also the terms that were neglected in the calculation of the total decay width before.

We obtain for the three B mesons

$$\mathcal{B}^{\text{SL}}(B^+) = (11.46^{+0.47}_{-0.32})\%,$$
$$\mathcal{B}^{\text{SL}}(B_d) = (10.57^{+0.47}_{-0.27})\%,$$
$$\mathcal{B}^{\text{SL}}(B_s) = (10.52^{+0.50}_{-0.29})\%. \tag{7.15}$$

To compare these predictions with experiment, we consider the experimental average

$$\mathcal{B}_{\rm sl}(B^{\pm}/B^0 \text{ averaged}) = (10.48 \pm 0.13)\% \tag{7.16}$$

given in Ref. [121]. This value is obtained by an extrapolation to the full phase space of the branching ratio measurements of CLEO [122], Babar [123, 124] and Belle [125]. Furthermore, the semileptonic branching ratio can be extrapolated from the global fit in Ref. [55] which yields

$$\mathcal{B}_{\rm sl}(B^{\pm}/B^0 \text{ averaged}) = (10.63 \pm 0.15)\% . \tag{7.17}$$

In Ref. [125] the branching ratio is also given for the mesons B^+ and B_d separately, however only for electron energies greater than $E_{\rm cut} = 0.4\,\text{GeV}$. Extrapolating these measurements to the full phase space

$$\mathcal{B}_{\rm sl}^{\rm Belle}(B^+) = (10.95 \pm 0.37)\%, \tag{7.18}$$

$$\mathcal{B}_{\rm sl}^{\rm Belle}(B_d) = (10.23 \pm 0.38)\%. \tag{7.19}$$

The theoretical predictions are in agreement with the experimental results within the uncertainties. Remarkably, the accuracy of both the theoretical and experimental numbers are of the same order for this observable.

7.4. Discussion of results

In the analysis above, we find that the central values obtained for the decay widths of the B mesons are roughly $\sim 4\%$ smaller than the experimental determinations. The theoretical uncertainties are significantly reduced when NNLO corrections to Γ_3 are included compared to previous analyses. The obtained theoretical central value is in agreement with experiment within the theoretical 1σ uncertainties.

Similar results are found for the semileptonic branching fractions of B^+ and B_d, where also the central value of our calculation and the experimental value differ by roughly $\sim 4\%$ and are in agreement within the 1σ uncertainties. Considering the semileptonic branching fraction instead of the total decay width has the advantage that the decay width prefactor Γ_0 including the CKM matrix element V_{cb} and m_b^5 cancel out and therefore the result is not effected by possible uncertainties induced by these parameters.

We find also very good agreement between experimental data and theoretical predictions for the lifetime ratios in Equation (7.12) and (7.13). In the lifetime ratios, the contributions of the free b-quark decay drop out since they contribute equally to all B mesons. The ratios are therefore determined by $1/m_b$ suppressed operator contributions and in the case of $\tau(B^+)/\tau(B_d)$ only by the four-quark operator contributions.

Missing contributions that are needed to achieve a higher precision for the B meson decay widths are:

- Missing penguin operator contributions to $\Gamma_3^{\rm NL}$ up to NNLO. This includes diagrams with double insertions of penguin operators as well as mixed contributions of penguin and current-current operators at NLO and NNLO. However, the calculation

of these contribution will be very challenging and the effect on the nonleptonic NNLO contribution will be subleading. Furthermore the NNLO contributions of current-current operators in penguin-like topologies are not known up to now.

- QED corrections to the nonleptonic b-quark decays and the decay channel $b \rightarrow c\tau\bar{\nu}_\tau$.

- Complete NLO QCD corrections for O_5 and O_6 for all nonleptonic decay channels.

For further improvement of the lifetime ratio predictions, the calculation of the nonleptonic decay modes to the $\tilde{O}_7$ contribution would be a logical next step since this correction is only known for the semileptonic decay.

To conclude this analysis: We find very good agreement between experiment and theory for the total decay width of B mesons as well as for the lifetime ratios and the semileptonic branching fraction. Including the nonleptonic NNLO corrections to Γ_3 leads to a significant reduction of the theoretical uncertainties.

8. Conclusion

We revisited the semileptonic bottom-quark decays and obtained for the first time exact analytic results for the leading one-charm final state contribution. This result allows us to extract the subleading three-charm contribution from previous calculations in the limit $m_c \to 0$. Our analytic results are confirmed by a further calculation using the `expand and match` method which includes both contributions. The NNLO results for the semileptonic decay channel are published in Ref. [104] and can be obtained in computer readable form from Ref. [96].

The main achievement of this thesis is the calculation of the NNLO QCD corrections to the nonleptonic bottom-quark decay, which includes all four relevant partonic channels $b \to c\bar{u}d$, $b \to c\bar{c}s$, $b \to u\bar{c}s$ and $b \to u\bar{u}d$.

For practical purposes it is necessary to apply Fierz identities in this calculation, which requires that the current-current operators are accompanied with appropriate evanescent operators. This allows us to work with anti-commuting γ_5. Our results contain the full charm quark mass dependence. To achieve this, we use the `expand and match` method for the calculation of loop integrals which yields piecewise defined analytic expansions with numeric coefficients that allow us to cross several physical thresholds correctly. The results of the nonleptonic decay width calculation up to NNLO for all four partonic decay channels are published in Ref. [34] and can be obtained in computer readable form from Ref. [126].

The calculation of the NNLO nonleptonic contribution is conveniently carried out in the on-shell mass scheme which is not a suitable scheme for phenomenological analysis. To translate our results into reliable theoretical predictions, we transform the final expressions to different mass renormalization schemes. We find a choice of schemes, where the bottom and charm quark masses are transformed to the kinetic mass and the $\overline{\text{MS}}$ mass scheme respectively, in which the dependence on the renormalization scale is small and the perturbative series shows a good convergence behaviour. This scheme choice, which is also standard for similar phenomenological analysis in the literature, should be the preferred one when working with B meson decays.

Finally, the new NNLO nonleptonic results are used to improve the theoretical predictions for the B meson decay width. The phenomenological discussion is outlined in Chapter 7 and also published in Ref. [109]. We observe that the uncertainty of theoretical predictions for the B meson observables decreases significantly when including the NNLO contributions calculated in this thesis. For the total decay width, this reduction is of the order of up to $\sim 50\%$ compared to the NLO prediction uncertainty. We find that the theoretical predictions of the decay widths are systematically below the experimental values for all three B mesons but in agreement with the experimental data within their uncertainties. The remaining theoretical uncertainty is mainly dominated by the uncertainty on the values of the bottom quark mass m_b and the CKM matrix element V_{cb}, that both enter the overall prefactor

Γ_0 of the decay width, and the renormalization scale uncertainty, however the latter is significantly reduced by including NNLO corrections.

We furthermore consider the lifetime ratios of the B meson decays where good agreement between experimental measurements and theoretical prediction is found. This analysis is not directly improved by including the NNLO corrections calculated in this work, however it serves as a strong cross check of the validity of the application of the HQE in the analysis of B meson decays.

To summarize, the results obtained in this thesis provide an important contribution to the theoretical description of *B* meson decays. With the NNLO corrections to the leading term Γ_3 at hand, the focus for further improvement should be on the perturbative corrections of higher order operators in Λ/m_b.

A. Calculation setup

The process of generating Feynman diagrams up to the point of bare amplitudes expressed in terms of master integrals is highly automated. In the following section, the used programs and some occurring subtleties are outlined.

A.1. QGRAF

The first step is the generation of all contributing diagrams, which is done with the program QGRAF [127]. QGRAF needs as input the information about all particles and all possible interaction terms in the considered theory. In order to produce the diagrams needed for the optical theorem, we define one ingoing bottom and one ingoing anti-bottom quark. In our setup used for the calculations with effective four fermion operators, for every operator a separate W particle is introduced that connects two vertices with two fermions each. This is done for all operators and their fierzed counterparts separately. QGRAF offers the option to restrict the number of propagators of several particles. By restricting the numbers of propagators of these W particles, we are able to control the insertion of operators. Let us consider for example a diagram for the decay $b \to c\bar{u}d$ with the insertion of two operators, one as defined in the effective Hamiltonian and one fierzed counterpart of O_1. In this minimal example, the `.lag` file reads

```
* propagator

[W1mO1,W1pO1,+]
[W2mO1,W2pO1,+]
[fU,fu,-]
[fD,fd,-]
[fC,fc,-]
[fB,fb,-]

* vertices

[fC,fb,W1pO1]
[fD,fu,W1mO1]
[fU,fc,W2pO1]
[fB,fd,W2mO1]
```

where the particle in the first propagator denotes the operator O_1 and the particle in

the second propagator its fierzed version. In an analogue way, all other effective operators, physical and evanescent, are implemented with additional *W* particles. For the generation of the diagrams, the combination of one fierzed and one unfierzed operator is requested. In our minimal example, this would correspond to

```
true = iprop[W1mO1,1,1];
true = iprop[W2mO1,1,1];
```

in the `qgraf.dat`. Furthermore we use the `QGRAF` option

```
options = onshell;
```

that excludes all possible diagrams with self-energy corrections on the external legs. In addition to this, the options `nosnail` and `notadpole` are used. The *W* particles that are used here for the construction of the four fermion operators are not physical and should be treated as point interactions in the following. However, implemented in the way showed above, `QGRAF` interprets them as a standard particles and also assigns momenta to them. This issue can be solved in the next step of the calculation when the diagrams generated by `QGRAF` are processed using `tapir`.

A.2. Tapir and exp

To proceed the output of qgraf, the program `tapir` [128] is used. Tapir translates the files produced by `QGRAF` to `FORM` [129] code including all Feynman rules specified before. In addition to this, `tapir` generates all scalar integral families that are needed to map all Feynman diagrams. This set of families is however not minimal. Thus it is advisable to use a program like exp [130, 131] to map the diagrams to integral families and find additional symmetries.
`tapir` comes with a lot of functions that are helpful in our calculations regarding the four fermion operators. They are briefly outlined in the following:

- In the config file of `tapir`, there is the option do define particles as so-called `sigma particles`. This means, that these particles still get assigned a momentum but are not treated as physical particles and never appear in the list of propagators in the definition of integral families nor the final expression for the diagram. We use this option to model the four fermion vertices that appear in the effective theory with *W* particles as already described above. The *W* particles are then defined as `sigma particles` in `tapir`. Let us again consider the example of the decay $b \to c\bar{u}d$ with double insertion of the effective operator O_1, one time fierzed and one time unfierzed. In the `tapir.conf`, we add

  ```
  * tapir.sigma_particles W1mO1,W2mO1
  ```

  while in the `.vrtx` file the interactions of the *W*-particles are defined as

```
{fC,fb,W1pO1:*fvertO(<lorentz_index_particle_3>,
<spinor_index_particle_1>,<spinor_index_particle_2>) |...||}
```

```
{fD,fu,W1mO1:*fvertO(<lorentz_index_particle_3>,
<spinor_index_particle_1>,<spinor_index_particle_2>) |...||}
```

```
{fU,fc,W2pO1:*fvertO(<lorentz_index_particle_3>,
<spinor_index_particle_1>,<spinor_index_particle_2>) |...||}
```

```
{fB,fd,W2mO1:*fvertO(<lorentz_index_particle_3>,
<spinor_index_particle_1>,<spinor_index_particle_2>) |...||}
```

In the `.prop` file, we define the propagators of W particles as delta functions that contract the colour and Lorentz indices of the three particle vertices in the correct order:
```
{W1mO1,W1pO1:*d_(<lorentz_index_vertex_1>,<lorentz_index_vertex_2>)|...||}
```

```
{W2mO1,W2pO1:*d_(<lorentz_index_vertex_1>,<lorentz_index_vertex_2>)|...||}
```

Combining all these rules for the vertices and propagators, the Feynman rules for the operator O_1 and its fierzed counterpart are obtained.

- `tapir` offers the possibility to filter the Feynman diagrams provided by `QGRAF` for specific cuts. In our calculation setup, this is not necessary at LO and NLO, however starting from NNLO, diagrams are generated that do not have the structure that has to be considered for the nonleptonic decays. They can be excluded using the `tapir` command

  ```
  tapir.filter cuts :  true :  q1 :  fb :  0,0
  ```

  which means that only diagrams that have exactly zero cuts through bottom quark lines are considered, where q1 is the external momentum. This means that diagrams in which the physical cut includes bottom quarks are excluded.

- For the calculation of the decay channel $b \rightarrow u\bar{c}s$, the family definitions and topology files that are generated in the $b \rightarrow c\bar{u}d$ calculation can be used since both decay channels develop the same diagramatic structure. The mapping of the $b \rightarrow u\bar{c}s$ diagrams to the $b \rightarrow c\bar{u}d$ topsel file is however only possible if the sigma particles are explicitly excluded not only from the `.topsel` and `.dia` but also from the `.edia` file that is generated by `tapir`. This can be done by including the relatively new option

  ```
  * tapir.edia_no_sigma
  ```

  in the `tapir.conf` file.

- Since the IBP reduction of the integral families at NNLO can be quite challenging as described in the next Section, it is helpful to reduce the number of integral families to a minimal number. `tapir` offers two useful options to modify the `.topsel` file that includes the information about the integral families:

  * `tapir.ordertopsel`
  * `tapir.topo_allow_absent_massive_lines`

  Including `tapir.ordertopsel`, the integral families are listed by complexity in the `.topsel` file, starting with the most complicated ones on top. Since the mapping process tries to map diagrams to topologies starting from the top of the `.topsel` file, the more complex families are preferred over easy families. This means that integrals of a simple family A that lives in a subsector of a more complex family B are mapped to B instead of A, reducing the number of families that have to be considered.
  The option `tapir.topo_allow_absent_massive_lines` includes all mass combinations where one or more massive lines are absent in the generation of the `.topsel` file. This allows for mappings of simpler families to more complex families that would otherwise differ by the number of massive propagators.

After defining all needed topologies with `tapir` and generating the corresponding `.topsel` file, we us `exp` to map the amplitudes for the diagrams to the list of integral families. Since `tapir` does not find a minimal set of families, this step reduces the number of families again, which in general saves a lot of CPU time deriving the IBP reduction to master integrals.
The output of `exp` and the `tapir` topology files are processable `FORM` [129] code that is embedded in the following manipulation of the amplitudes.

A.3. Integral reduction

After the procedures outlined above, we obtain the physical amplitude in terms of scalar loop integrals that can be parametrized as

$$I(\vec{n}) = \int \frac{\prod_{i=1}^{L} \mathrm{d}^d k_i}{D_1^{n_1} D_2^{n_2} \dots D_N^{n_N}}, \tag{A.1}$$

where $D_j = m_j^2 - p_j^2$, $j = 1, \dots, N$ are N propagators with mass m_j and momentum p_j. The p_j are linear combinations of the L loop momenta k_i and external momenta q_k. The n_j are the powers of the propagators, also called indices.
Each integral we can assign a sector

$$S = \sum_{i=1}^{N} 2^{i-1} \Theta(n_i - 1/2), \tag{A.2}$$

where $\Theta(n_i - 1/2)$ is the Heaviside function. We call an sector S subsector of sector S' if $S < S'$ and all indices $n_i \leq n_i'$ for $i = 1, \dots, N$. The sector that is not subsector of any other

sector is the top-level sector of a family.

For the generation of the IBP reduction table, it is furthermore useful to define the sum of all positive indices

$$r = \sum_{i=1}^{N} n_i \Theta(n_i - 1/2) \,, \tag{A.3}$$

and negative indices

$$s = \sum_{i=1}^{N} (-n_i) \Theta(1/2 - n_i) \,. \tag{A.4}$$

These two quantities are measures for the complexity of integrals and the r and s values of the occurring integrals are needed as input parameters for the following IBP reduction procedure.

The reduction of the integrals appearing in the physical amplitude to a minimal set of master integrals is done with the program `kira` [87, 88]. `kira` relies on the usage of Integration-by-parts relations, which are discussed in Section B.1.

The reduction at LO and NLO are computationally relatively cheap and can be run on a normal desktop computer within minutes. However this does not hold for the NNLO families which have top-level sectors of 9 propagators and are more challenging. In order to save time and resources, it is therefore advisable to split the IBP reduction process into several steps, which are outlined in the following.

1. After running `exp`, every amplitude in the problem is mapped to a specific integral family. The first step of the IBP reduction is to find a good basis of master integrals for each individual family. A good basis in this context means, that there is a factorization of the $d = 4 - 2\epsilon$ and $\rho = m_c/m_b$ dependence in all IBP entries [68, 132]. An algorithm that tries to find such a good basis is implemented in the `Mathematica` package `ImproveMasters` [68]. As an input, `ImproveMasters` requires a test reduction that covers all relevant sectors of the integral family. Using the linear equations of integrals in this table, the program tries to find a set of basis integrals that do not develop bad denominators as described above.

2. As a second step, this table is fed to `ImproveMasters`. If a good basis can be found or not depends on the size of the input table and the complexity of the integral family. Increasing the set of linear equations by choosing larger values of r, s and d includes more linear relations with more master integral candidates and therefore increases the possibility of finding a good basis. However, increasing the size reduction table means that the reduction itself becomes more complicated and therefore increases the computing time.

3. After step 2, a set of good master integrals is found for every integral family separately. At this stage, it is possible that master integrals of different families are linearly dependent. Therefore, the set containing all good master integrals of all families can be overdetermined and is therefore not necessarily a basis. To eliminate

the linear dependent integrals, an IBP reduction including all integral families is performed to reduce all good master integrals to in minimal set of masters. To save time in this calculation step, the reduction is performed only over the list of good master integrals of step 2, and does not cover all top level sectors of all families necessarily.

4. In parallel to all the steps outlined before, the reduction of the integrals appearing in the physical amplitude are computed. The master integrals in this IBP reduction are the same that are found in step 1. The difference compared to the reduction in step 1 are the values of r, s and d. When calculating the input table for `ImproveMasters`, this values are set to be as small as possible, while here they are fixed by the integrals appearing in the amplitude which can produce high values of s and d that make the reduction more expensive. Therefore this step may take a lot of time and resources for complicated families.

After these steps, all relations to express the amplitude in terms of master integrals are known. In a first step the reduction tables obtained in step 4 are applied which reduces all integrals to the master integrals of the respective family. Afterwards we use the reduction table from step 3 to map the master integrals to a minimal set of master integrals. As a result, the amplitude is expressed in terms only containing linear independent integrals of the good basis that then have to be computed. This is described in the next section.

B. Mathematical tools

B.1. Integration by parts relations

The calculation of Feynman diagrams at higher loop order strongly depends on the usage of Integration by parts relations, short IBPs. They were introduced in Ref. [133] and relate loop integrals with different propagator powers via linear equations. The IBP relations are used to reduce the loop integrals appearing in the calculation of a Feynman diagram to a minimal set of independent integrals, so-called master integrals, see also Appendix A.3. Furthermore, they can be used to establish a differential equation for these master integrals that is used for the calculations outlined in Chapter 3.

The IBP relations rely on the fact that the integral over a total derivative vanishes in dimensional regularization. This means that

$$\int \frac{\mathrm{d}^d k_1}{(2\pi)^d} \cdots \int \frac{\mathrm{d}^d k_n}{(2\pi)^d} \frac{\partial}{\partial k_{j,\mu}} q_\mu f\left(k_i, p_i, m_i\right) = 0\,, \tag{B.1}$$

where the k_i denote the n loop momenta and p_i and m_i the external momenta and masses of the physical problem. The momentum q can be both loop or external momentum. Evaluating Equation (B.1) for different $q \in \{p_i, k_i\}$, we obtain linear equations of integrals with different powers of propagators that add up to zero.

Let us consider the one loop integral family

$$I(n_1, n_2) = \int \frac{\mathrm{d}^d k_1}{(2\pi)^d} \frac{1}{\left(-k_1^2\right)^{n_1} \left(m^2 - (k_1 - q)^2\right)^{n_1}}\,, \tag{B.2}$$

with one loop momentum k_1 and one external momentum q. We find two IBP relations

$$0 = \int \frac{\mathrm{d}^d k_1}{(2\pi)^d} \frac{\partial}{\partial k_{1\mu}} q_\mu \frac{1}{\left(-k_1^2\right)^{n_1} \left(m^2 - (k_1 - q)^2\right)^{n_1}}\,,$$

$$0 = \int \frac{\mathrm{d}^d k_1}{(2\pi)^d} \frac{\partial}{\partial k_{1\mu}} k_{1\mu} \frac{1}{\left(-k_1^2\right)^{n_1} \left(m^2 - (k_1 - q)^2\right)^{n_1}}\,, \tag{B.3}$$

that yield the relations

$$I(n_1, n_2) = \frac{n_2}{d - 2n_1 - n_2} I(n_1 - 1, n_2 - 1)\,,$$

$$I(n_1, n_2 + 1) = \frac{2(n_1 - n_2)}{n_2 q^2} I(n_1, n_2) - \frac{2n_1}{n_2 q^2} I(n1 + 1, n2 - 1) + \frac{2}{q^2} I(n_1 - 1, n_2 + 1)\,. \tag{B.4}$$

Applying the relations given in Equation (B.4) iteratively and using the on-shell relation $q^2 = m^2$, we can express every integral $I(n_1, n_2)$ with arbitrary n_1 and n_2 with the corresponding master integral $I(0, 1)$.

One algorithm that performs the reduction to master integrals using IBP relations is Laporta's algorithm [134]. This algorithm became standard for modern IBP reduction programs. In the calculations performed in this work, we use the program `kira` [87, 88] to find the IBP relations. The general procedure is outlined in Appendix A.3.

B.2. Differential equations in ϵ-form

In Chapter 3, two methods to calculate the master integrals with differential equations are described. In the analytic approach in Section 3.1, the differential equation of the master integrals is transformed to ϵ-form in which the analytic solution can be obtained in a simple way. In this Appendix, we give an example for this procedure for the LO master integrals with two massless and one charm quark in the final state. The corresponding integral family

$$\text{d2l1}(\vec{n}) = \int \frac{\mathrm{d}k_1\, \mathrm{d}k_2}{\left(-k_1^2\right)^{n_1} \left(-k_2^2\right)^{n_2} \left(-(k_2 - k_1 + q)^2\right)^{n_3} \left(-(k_1 - k_2)^2\right)^{n_4} \left(-(k_2 + q)^2\right)^{n_5}}, \quad \text{(B.5)}$$

has two master integrals: $\text{d2l1}(1, 1, 1, 0, 0)$ and $\text{d2l1}(1, 1, 2, 0, 0)$. In a first step, we set up the differential equation for the two master integrals in the form of Equation (3.2). Using IBP relations we obtain:

$$\frac{\mathrm{d}}{\mathrm{d}\rho} \begin{pmatrix} \text{d2l1}(1, 1, 1, 0, 0) \\ \text{d2l1}(1, 1, 2, 0, 0) \end{pmatrix} = \begin{pmatrix} 0 & 2\rho \\ \frac{2(2 - 7\epsilon + 6\epsilon^2)}{\rho(1 - \rho^2)} & \frac{2(\epsilon + 2\rho^2 - 5\epsilon\rho^2)}{\rho(\rho^2 - 1)} \end{pmatrix} \cdot \begin{pmatrix} \text{d2l1}(1, 1, 1, 0, 0) \\ \text{d2l1}(1, 1, 2, 0, 0) \end{pmatrix}$$
$$= A(\rho, \epsilon) \cdot \vec{I}. \quad \text{(B.6)}$$

in a next step, we want to transform this differential equation to ϵ-form, see Equation (3.4). The corresponding transformation matrix T that transforms the integrals according to

$$\vec{I} = \begin{pmatrix} \text{d2l1}(1, 1, 1, 0, 0) \\ \text{d2l1}(1, 1, 2, 0, 0) \end{pmatrix},$$
$$= T\vec{J}, \quad \text{(B.7)}$$

can be found using the `Mathematica` package `Canonica` [73]. We obtain

$$T = \begin{pmatrix} \epsilon\left(\rho^4 - 1\right) & \rho^2 - \frac{\epsilon\left(1 + 7\rho^2\right)}{2} \\ (3\epsilon - 2)\,\epsilon\left(1 - \rho^2\right) & 1 - \frac{11}{2}\epsilon + 6\epsilon^2 \end{pmatrix}. \quad \text{(B.8)}$$

The matrix T consists of polynomials in ρ and ϵ. To obtain the differential equation in the transformed integral basis, we insert Equation (B.7) into Equation (B.6) and obtain

$$\frac{\mathrm{d}}{\mathrm{d}\rho}\vec{J} = \left(T^{-1}AT - T^{-1}\frac{\mathrm{d}}{\mathrm{d}\rho}A\right) \cdot \vec{J}$$

$$= \begin{pmatrix} \frac{2\epsilon\left(1+2\rho^2-3\epsilon\left(1+3\rho^2\right)\right)}{(3\epsilon-1)\rho(\rho^2-1)} & \frac{2\rho^2-15\epsilon\rho^2-6\epsilon^3\left(\rho^2-1\right)+\epsilon^2\left(-2+30\rho^2\right)}{\epsilon(-1+3\epsilon)\rho(-1+\rho^2)^2} \\ -\frac{4\epsilon\left(-1+3\epsilon+\rho^2\right)}{\rho(-1+3\epsilon)} & -\frac{2\left(2\rho^2+\epsilon\left(2-9\rho^2\right)+6\epsilon^2\left(-1+\rho^2\right)\right)}{(-1+3\epsilon)\rho(-1+\rho^2)} \end{pmatrix} \cdot \vec{J}$$

$$- \begin{pmatrix} -\frac{2\epsilon\rho}{(-1+3\epsilon)(-1+\rho^2)} & \frac{(-1+4\epsilon)\rho(-2+7\epsilon)}{\epsilon(-1+3\epsilon)(-1+\rho^2)^2} \\ \frac{4\epsilon\rho}{1-3\epsilon} & \frac{2\rho(-2+7\epsilon)}{(-1+3\epsilon)(-1+\rho^2)} \end{pmatrix} \cdot \vec{J}$$

$$= \epsilon \begin{pmatrix} \frac{2\left(1+3\rho^2\right)}{\rho(1-\rho^2)} & \frac{2}{\rho(1-\rho^2)} \\ -\frac{4}{\rho} & -\frac{4}{\rho} \end{pmatrix} \cdot \vec{J} = \epsilon \tilde{A}(\rho) \cdot \vec{J}. \tag{B.9}$$

We observe that the differential equation for the integrals $\vec{J}$ is in ϵ-form and we can now solve for the integrals as outlined in Section 3.1. We can rewrite the matrix $\tilde{A}$ in the following way

$$\frac{\mathrm{d}}{\mathrm{d}\rho}\vec{J} = \epsilon\left[\frac{1}{1+\rho}\begin{pmatrix} -4 & -1 \\ 0 & 0 \end{pmatrix} + \frac{1}{\rho}\begin{pmatrix} 2 & 2 \\ -4 & -4 \end{pmatrix} + \frac{1}{1-\rho}\begin{pmatrix} 4 & 1 \\ 0 & 0 \end{pmatrix}\right] \cdot \vec{J}, \tag{B.10}$$

where we observe that the alphabet of the differential equation consists of the letters $\{1/(1+\rho), 1/\rho, 1/(1-\rho)\}$, the letters of the Harmonic Polylogarithms. We choose the ansatz

$$\vec{J} = \frac{\vec{j}_{-2}}{\epsilon^2} + \frac{\vec{j}_{-1}}{\epsilon} + \vec{j}_0 + \vec{j}_1\epsilon + \vec{j}_2\epsilon^2 + O\left(\epsilon^3\right), \tag{B.11}$$

where $\vec{j}_i$ are functions of ρ. We insert this ansatz into Equation (B.10) and consider each ϵ order:

$$\frac{\mathrm{d}\vec{j}_{-2}}{\mathrm{d}\rho} = 0,$$

$$\frac{\mathrm{d}\vec{j}_{-1}}{\mathrm{d}\rho} = \tilde{A}(\rho) \cdot \vec{j}_{-2},$$

$$\frac{\mathrm{d}\vec{j}_0}{\mathrm{d}\rho} = \tilde{A}(\rho) \cdot \vec{j}_{-1},$$

$$\dots \tag{B.12}$$

The first equation is solved trivially by a constant $\vec{j}_{-2} = \vec{c}_{-2}$. Integrating over the second line in Equation (B.12) yields

$$\vec{j}_{-1} = \int^\rho \frac{\mathrm{d}\rho'}{1+\rho'}\begin{pmatrix} -4 & -1 \\ 0 & 0 \end{pmatrix} \cdot \vec{c}_{-2} + \int^\rho \frac{\mathrm{d}\rho'}{\rho'}\begin{pmatrix} 2 & 2 \\ -4 & -4 \end{pmatrix} \cdot \vec{c}_{-2}$$

$$+ \int^\rho \frac{\mathrm{d}\rho'}{1-\rho'}\begin{pmatrix} 4 & 1 \\ 0 & 0 \end{pmatrix} \cdot \vec{c}_{-2} + \vec{c}_{-1}. \tag{B.13}$$

Using the definition in Section B.4.1 and writing $\vec{c}_i = (c_{i,1}, c_{i,2})^\mathrm{T}$, we can express the occurring integrals in terms of Harmonic Polylogarithms:

$$\vec{j}_{-1} = \begin{pmatrix} -\left(4c_{-2,1} + c_{-2,2}\right)H_{-1}(\rho) + 2\left(c_{-2,1} + c_{-2,2}\right)H_0(\rho) + \left(4c_{-2,1} + c_{-2,2}\right)H_1(\rho) + c_{-1,1} \\ -42\left(c_{-2,1} + c_{-2,2}\right)H_0(\rho) + c_{-1,2} \end{pmatrix}.$$

$$\tag{B.14}$$

In the same way, we can find the solutions for $\vec{j}_0$ and all other $\vec{j}_i$ recursively. With every order in ϵ, the weight of the iterated integrals appearing in the solutions increase by one. In the calculation of the semileptonic decay rate, we calculate asymptotic expansions of the master integrals $\vec{I}$ around $\rho = 1$ as boundary conditions, see Section 3.2. We then expand the analytic solution of $\vec{I}$ obtained by transforming the solution of $\vec{J}$ in Equation (B.11) with Equation (B.7) around $\rho = 1$ using `HarmonicSums` [78] and fix the undetermined $\vec{c}_i$ by comparison of coefficients.

Algorithm to obtain a canonical form

In the following, a brief description of the algorithm to obtain the transformation to canonical or ϵ-form given in [71] is outlined. Similar Algorithms are described in Refs. [69, 70].

In the following, N master integrals depending on ϵ and a set of invariants $\{x_i\}$ are considered. The master integrals are given by the vector $\vec{I}$ and fulfil the differential equation

$$\mathrm{d}\vec{I} = A\left(\epsilon, \{x_i\}\right) \cdot \vec{I}. \tag{B.15}$$

Here the matrix $A\left(\epsilon, \{x_i\}\right)$ is required to be rational in ϵ and the invariants $\{x_i\}$. If this is not the case, it is not possible to find a transformation to ϵ-form. However, in some applications, it is possible to perform a variable transformation that rationalizes the matrix A. Whether or not such a transformation can be found strongly depends on the physical problem and the structure of the differential equation. In cases where it is not possible to rationalize the differential equation, one has to consider other approaches, for example the `expand and match` approach outlined in detail in Section 3.3

Assuming the differential equation was rationalized successfully, it can be brought to ϵ-form by performing the transformation

$$\vec{I} = T \cdot \vec{J}, \tag{B.16}$$

which yields

$$\mathrm{d}\vec{J} = \epsilon \tilde{A}\left(\{x_i\}\right) \cdot \vec{J}. \tag{B.17}$$

The matrix $\tilde{A}$ is then given by

$$\epsilon \tilde{A} = T^{-1}AT - T^{-1}\mathrm{d}T, \tag{B.18}$$

and can be written in the form

$$\epsilon \tilde{A}\left(\{x_i\}\right) = \epsilon \sum_{l=1}^{N} \tilde{A}_l \, \mathrm{d}\log\left(L_l\left(\{x_i\}\right)\right). \tag{B.19}$$

Here the $\tilde{A}_l$ are $N \times N$ matrices with constant entries. The $L_l\left(\{x_i\}\right)$ are functions of the invariants $\{x_i\}$, called letters and correspond to the set of irreducible denominator factors

of the matrix A. This shape of the differential equation simplifies the calculation of the master integrals a lot, see Section 3.1, so the main goal is to find this transformation T. The starting point is given in Equation (B.18). Multiplying this equation by T from the left yields

$$\epsilon T\tilde{A} - AT + \mathrm{d}T = 0 \, . \tag{B.20}$$

This equation can now be expanded in ϵ. First, the matrix A is considered. Since A is rational in ϵ and $\{x_i\}$, it is possible to find a Taylor series in ϵ such that

$$Ah = \sum_{m=0}^{m_{\max}} (Ah)^{(m)} \epsilon^m \, , \tag{B.21}$$

where $h\left(\epsilon, \{x_i\}\right)$ is a polynomial of ϵ and $\{x_i\}$. The polynomial h can also be expanded in ϵ:

$$h\left(\epsilon, \{x_i\}\right) = \sum_{l=l_{\min}}^{l_{\max}} \epsilon^l h^{(l)}\left(\{x_i\}\right) \, . \tag{B.22}$$

In a next step, Equation (B.18) is rewritten in terms of $\hat{T} = (Th)$ which yields

$$\epsilon\hat{T}\tilde{A} - A\hat{T} + h\mathrm{d}\hat{T} - \hat{T}\mathrm{d}h = \epsilon Th\tilde{A} - ATh + h\mathrm{d}(Th) - Th\mathrm{d}h = 0 \, . \tag{B.23}$$

Following Ref. [71], this equation can be solved by expanding $\hat{T}$ as a finite series in ϵ, if Equation (B.19) can be solved by T composed of rational functions. Therefore, the following ansatz is made:

$$\hat{T} = \sum_{n=l_{\min}}^{n_{\max}} \epsilon^n \hat{T}^{(n)} \, , \tag{B.24}$$

where now all $\hat{T}^{(n)}$ have to be determined. This is done by inserting this ansatz into Equation (B.23) and solving for each order in ϵ separately. The only unknown quantity except for the $\hat{T}^{(n)}$ in this equation is $\tilde{A}$, for which the ansatz

$$\tilde{A} = \sum_{l=1}^{N} \tilde{A}_l \mathrm{d}\log\left(L_l\left(\{x_i\}\right)\right) \, , \tag{B.25}$$

is made, where $L_l\left(\{x_i\}\right)$ are the letters of the considered system and $\tilde{A}_l$ are unknown constant matrices. For the $\hat{T}^{(n)}$, the ansatz

$$\hat{T}^{(n)} = \sum_{k=1}^{k_{\max}} \tau_k^{(n)} r_k(\{x_i\}) \tag{B.26}$$

is chosen. Here the $\{r_1(\{x_i\}), \ldots, r_{k_{\max}}(\{x_i\})\}$ are rational functions in the invariants $\{x_i\}$. The $\tau_k^{(n)}$ are constant matrices which have to be determined. Inserting all these expansions into Equation (B.23), the equations necessary to determine all free parameters are obtained.

B.3. Decoupling differential equations

In this section, we give an example for the solution of differential equations by decoupling using the `Mathematica` package `OreSys` [76] that relies on `Sigma.m` [77]. We again consider the LO differential equation given in Equation (B.6). In a first step, similar to the approach shown before, we expand the integrals in ϵ:

$$\vec{I} = \begin{pmatrix} \frac{I_{1,-2}}{\epsilon^2} + \frac{I_{1,-1}}{\epsilon} + I_{1,0} + I_{1,1}\epsilon + I_{1,2}\epsilon^2 + \mathcal{O}(\epsilon^3) \\ \frac{I_{2,-2}}{\epsilon^2} + \frac{I_{2,-1}}{\epsilon} + I_{2,0} + I_{2,1}\epsilon + I_{2,2}\epsilon^2 + \mathcal{O}(\epsilon^3) \end{pmatrix}. \tag{B.27}$$

We insert this expansion into Equation (B.6) and consider the highest pole in ϵ on both sides of the differential equation, which is in this case ϵ^{-2}. The differential equation at this ϵ order gives two coupled differential equations in ρ for the functions $I_{1,-2}(\rho)$ and $I_{2,-2}(\rho)$ and reads:

$$\frac{\mathrm{d}}{\mathrm{d}\rho} \begin{pmatrix} I_{1,-2}(\rho) \\ I_{2,-2}(\rho) \end{pmatrix} = \begin{pmatrix} 0 & 2\rho \\ \frac{4}{\rho(1-\rho^2)} & \frac{4\rho}{(-1+\rho^2)} \end{pmatrix} \cdot \begin{pmatrix} I_{1,-2}(\rho) \\ I_{2,-2}(\rho) \end{pmatrix}. \tag{B.28}$$

We now use the `OreSys` function `UncoupleDifferentialSystem`. This function finds a transformation that transforms the functions $I_{1,-2}(\rho)$ and $I_{2,-2}(\rho)$ thereby decouples the differential equations in (B.28). In the example shown here, this transformation is given by

$$\begin{pmatrix} I_{1,-2}(\rho) \\ I_{2,-2}(\rho) \end{pmatrix} = \begin{pmatrix} 1 & 0 \\ 0 & \frac{1}{2\rho} \end{pmatrix} \cdot \begin{pmatrix} J_{1,-2}(\rho) \\ J_{2,-2}(\rho) \end{pmatrix}. \tag{B.29}$$

Using the new set of functions, $J_{1,-2}(\rho)$ and $J_{2,-2}(\rho)$, `OreSys` finds one differential equation of second order for $J_{1,-2}(\rho)$

$$\frac{\mathrm{d}^2}{\mathrm{d}\rho^2}J_{1,-2}(\rho) = \frac{5\rho^2 - 1}{\rho(\rho^2 - 1)}\frac{\mathrm{d}}{\mathrm{d}\rho}J_{1,-2}(\rho) - \frac{8}{-1+\rho^2}J_{1,-2}(\rho), \tag{B.30}$$

and the relation

$$J_{2,-2}(\rho) = \frac{\mathrm{d}}{\mathrm{d}\rho}J_{1,-2}(\rho). \tag{B.31}$$

The differential equation for $J_{1,-2}(\rho)$ can be solved in terms of iterated integrals using the function `SolveDE` which is implemented in the `Mathematica` package `HarmonicSums` [78]. The solution of the second order DEQ reads

$$J_{1,-2}(\rho) = -c_1\rho^2 + c_2\frac{1}{2}\left(1 - \rho^4 + 4\rho^2 H_0(\rho)\right), \tag{B.32}$$

which yields

$$J_{2,-2}(\rho) = -2c_1\rho + c_2\frac{1}{2}\left(4\rho - 4\rho^3 + 8\rho H_0(\rho)\right). \tag{B.33}$$

Now that the functions $J_{1,-2}(\rho)$ and $J_{2,-2}(\rho)$ are determined, we can find the expressions for $I_{1,-2}(\rho)$ and $I_{2,-2}(\rho)$ via Equation (B.29) as functions of ρ and the undetermined coefficients

c_1 and c_2. These coefficients can now be calculated by comparing the obtained solutions with boundary conditions of the master integrals, similar to the procedure outlined before. After we found the solution for the differential equation at order ϵ^{-2}, we consider the differential equation in (B.28) at the order ϵ^{-1}, which not only depends on $I_{1,-1}(\rho)$ and $I_{2,-1}(\rho)$ but also on $I_{1,-2}(\rho)$ and $I_{2,-2}(\rho)$. We insert the solution for $I_{1,-2}(\rho)$ and $I_{2,-2}(\rho)$ that we found before and repeat the steps outlined above. This procedure is repeated iteratively up to the needed ϵ order.

The final result obtained with this approach is identical to the result obtained in Section B.2.

B.4. Iterated integrals

In the caclulation of the semileptonic decays up to NNLO and the nonleptonic decays up to NLO, analytic expressions for the master integrals are obtained via differential equations. These analytic expressions consist of iterated integrals which can be expressed as Harmonic Polylogarithms and Cyclotomic Harmonic Polylogarithms. In this appendix, the definition of these functions is briefly outlined.

B.4.1. Harmonic Polylogarithms

The Harmonic Polylogarithms (HPL) [95] are defined by their argument and w indices $\{i_1, \ldots, i_w\}$, where w denotes the weight of the HPL and the indices can take the values $\{-1, 0, 1\}$. The notation used in this work is

$$H_{i_w,\ldots,i_1}(x)\,, \tag{B.34}$$

where x is the argument of the HPL. Starting at weight $w = 1$, the HPLs are defined by

$$H_{-1}(x) = \int_0^x \frac{1}{1+x'}\,\mathrm{d}x' = -\log(1-x)\,,$$

$$H_0(x) = \log(x)\,,$$

$$H_1(x) = \int_0^x \frac{1}{1-x'}\,\mathrm{d}x' = \log(1+x)\,. \tag{B.35}$$

For higher weights $w > 1$, the definition is given iteratively. For this definition, we first have to specify the three letters

$$f_{-1}(x) = \frac{1}{1+x}\,, \qquad f_0(x) = \frac{1}{x}\,, \qquad f_1(x) = \frac{1}{1-x}\,, \tag{B.36}$$

of the HPLs. Starting from the functions given above for weight one, these letters can be used to obtain the HPLs at weight two by

$$H_{-1,i_1}(x) = \int_0^x f_{-1}(x')H_{i_1}(x')\,\mathrm{d}x' = \int_0^x \frac{1}{1+x'}H_{i_1}(x')\,\mathrm{d}x'\,,$$

$$H_{0,i_1}(x) = \begin{cases} \frac{1}{2}\log^2(x) & \text{if } i_1 = 0 \\ \int_0^x f_0(x')H_{i_1}(x')\,\mathrm{d}x' = \int_0^x \frac{1}{x'}H_{i_1}(x')\,\mathrm{d}x' & \text{if } i_1 \neq 0 \end{cases},$$

$$H_{1,i_1}(x) = \int_0^x f_1(x')H_{i_1}(x')\,\mathrm{d}x' = \int_0^x \frac{1}{1-x'}H_{i_1}(x')\,\mathrm{d}x'\,. \tag{B.37}$$

With exception of the case of all indices being zero, the Harmonic Polylogarithm of weight w with the indices $\{i_1,\dots,i_w\}$ and argument x is defined via the Harmonic Polylogarithm of weight $w-1$ with the indices $\{i_1,\dots,i_{w-1}\}$ by

$$H_{i_w,\dots,i_1}(x) = \int_0^x f_{i_w}(x')H_{i_{w-1},\dots,i_1}(x')\,\mathrm{d}x'\,. \tag{B.38}$$

The definition of the HPL with weight w where all indices are zero is given by

$$H_{0,\dots,0}(x) = \frac{1}{w!}\log^w(x)\,. \tag{B.39}$$

With the definition of the Harmonic Polylogarithms via the iterated integrals given in Equation (B.38), the derivative of the HPLs is obtained trivially by

$$\frac{\mathrm{d}H_{i_w,\dots,i_1}(x)}{\mathrm{d}x} = f_{i_w}(x)H_{i_{w-1},\dots,i_1}(x)\,. \tag{B.40}$$

B.4.2. Cyclotomic Harmonic Polylogarithms

For the LO and NLO calculation, the function class of the HPLs is sufficient to describe the solution of all master integrals. However, at for the calculation of the NNLO semileptonic decay rate, see Chapter 4, the alphabet of letters that appear in the solution of the differential equation have to be extended to

$$\left\{\frac{1}{1+t},\frac{1}{t},\frac{1}{1-t},\frac{t}{1+t^2},\frac{t^3}{1+t^4}\right\}\,, \tag{B.41}$$

including two new letters. Therefore, the solution exceeds the function class of the HPLs. The two additional letters produce iterated integrals that can be expressed by Cyclotomic Harmonic Polylogarithms. In this class of functions the alphabet of letters is extended by the cyclotomic polynomials [105]. The nth cyclotomic polynomial is the irreducible polynomial that is a divisor of $t^n - 1$ and is not a divisor of $t^d - 1$, where d and n are positive integer numbers and $d < n$ [135]:

$$\phi_n(t) = \frac{t^n - 1}{\prod_{d|n,d<n}\phi_d(t)}\,. \tag{B.42}$$

The roots of the cyclotomic polynomial $\phi_n(t)$ are all the nth roots of unity $\exp(2\pi id/n)$, with d running over all positive integers coprime to n and $d < n$ [135]. The first eight cyclotomic polynomials are given by

$$\phi_1(t) = t - 1\,, \qquad\qquad \phi_2(t) = t + 1\,,$$
$$\phi_3(t) = t^2 + t + 1\,, \qquad\qquad \phi_4(t) = t^2 + 1\,,$$
$$\phi_5(t) = t^4 + t^3 + t^2 + t + 1\,, \qquad\qquad \phi_6(t) = t^2 - t + 1\,,$$

$$\phi_7(t) = t^6 + t^5 + t^4 + t^3 + t^2 + t + 1 \,, \qquad\qquad \phi_8(t) = t^4 + 1 \,, \qquad \text{(B.43)}$$

The letters of the Cyclotomic Harmonic Polylogarithms are then constructed by

$$f_{k,l}(x) = \frac{x^l}{\phi_k(x)} \,. \qquad\qquad \text{(B.44)}$$

Considering for example the Harmonic Polylogarithms discussed in section B.4.1, their alphabet can be written as $\{\frac{1}{x}, -f_{1,0}(x), f_{2,0}(x)\}$.
In the case of the semileptonic NNLO master integrals discussed in chapter 4, the two additional letter in the alphabet can be identified as

$$f_{4,1}(t) = \frac{t}{1 + t^2} \,, \qquad\qquad f_{8,3}(t) = \frac{t^3}{1 + t^4} \,. \qquad \text{(B.45)}$$

The definition of the Cyclotomic Harmonic Polylogarithms via iterated integrals is, analogous to the Harmonic Polylogarithms, given iteratively via

$$H_{\{k_1,l_1\}}(x) = \int_0^x f_{k_1,l_1}(x') \, \mathrm{d}x' \,,$$

$$H_{\{k_w,l_w\},\dots,\{k_1,l_1\}}(x) = \int_0^x f_{k_w,l_w}(x') H_{\{k_{w-1},l_{w-1}\},\dots,\{k_1,l_1\}}(x') \, \mathrm{d}x' \,. \qquad \text{(B.46)}$$

In the special case, when all pair of indices $\{k_w, l_w\}, \dots, \{k_1, l_1\}$ are $\{0, 0\}$, one obtains

$$H_{\{0,0\},\dots,\{0,0\}}(x) = \frac{1}{w!} \log^w(x) \,. \qquad\qquad \text{(B.47)}$$

B.5. Feynman parameters

The calculation of Feynman diagrams includes integrals over loop momenta. The integrand of such integrals typically consists of a product of propagators depending on momenta and masses. One way to calculate such Feynman integrals is to use Feynman parameters, which is outlined in the following. Feynamn parameters can be used to rewrite terms like [26]

$$\frac{1}{A \cdot B} = \int_0^1 \mathrm{d}x_1 \int_0^1 \mathrm{d}x_2 \frac{\delta(x_1 + x_2 - 1)}{(x_1 A + x_2 B)^2} \,, \qquad \text{(B.48)}$$

or in a more generalized form

$$\frac{1}{A_1^{m_1} \dots A_n^{m_n}} = \int_0^1 \mathrm{d}x_1 \cdots \int_0^1 \mathrm{d}x_n \frac{\delta(\sum_i x_i - 1) \prod_i x_i^{m_i - 1}}{(\sum_i x_i A_i)^{\sum_i m_i}} \frac{\Gamma(\sum_i m_i)}{\prod_i \Gamma(m_i)} \,, \qquad \text{(B.49)}$$

where the x_i are the Feynman parameters. This relation allows for the following strategy when calculating loop integrals: The starting point is a integral over a loop momentum with an integrand consisting of propagators to arbitrary powers. In a first step, the integrand is

rewritten in the form of Equation (B.49). After that, a substitution of the loop momentum is performed in order to obtain an integral of the form [26]

$$
\int \frac{\mathrm{d}^d p}{(p^2 - \Delta)^n} = (-1)^n \, i\pi^{d/2} \frac{\Gamma\left(n - \frac{d}{2}\right)}{\Gamma(n)} \left(\frac{1}{\Delta}\right)^{n - d/2} .
\tag{B.50}
$$

After the integration of the loop momentum, the integration over the Feynman parameters remain. In some cases, these integrals can be identified as Beta functions, which are defined by

$$
B(\alpha, \beta) = \int_0^1 \mathrm{d}x \, x^{\alpha-1} (1-x)^{\beta-1} = \frac{\Gamma(\alpha)\,\Gamma(\beta)}{\Gamma(\alpha+\beta)} ,
\tag{B.51}
$$

and can therefore be rewritten in terms of Γ functions. If this is not the case, it is often useful to use Mellin-Barnes representation, which is outlined in the next section B.6.
As an example for the application of Feynman parameters, the calculation of a simple loop integral with one massive and one massless propagator is outlined in detail:

$$
I = \int \frac{\mathrm{d}^d k_1}{\left(-k_1^2\right)^{n_1} \left(m_1^2 - (k_1 - q)^2\right)^{n_2}} .
\tag{B.52}
$$

We denote the external momentum with q and the finite mass with m_1, Furthermore, we apply the on-shell condition $q^2 = m_1^2$. In a first step, Equation (B.49) is applied and the Feynman parameters a and b are introduced:

$$
\begin{aligned}
I &= \int \frac{\mathrm{d}^d k_1}{\left(-k_1^2\right)^{n_1} \left(m_1^2 - (k_1 - q)^2\right)^{n_2}} \\
&= \int \mathrm{d}^d k_1 \int_0^1 \mathrm{d}a \int_0^1 \mathrm{d}b \, \frac{\delta(a + b - 1)\, a^{n_2-1} b^{n_1-1} \Gamma(n_1 + n_2)}{\left(am_1^2 - a(k_1 - q)^2 - bk_1^2\right)^{n_1+n_2} \Gamma(n_1)\,\Gamma(n_2)}
\end{aligned}
\tag{B.53}
$$

In a next step, we exchange the order of integration and substitute $p = k_1 - aq$, which yields

$$
I = \int_0^1 \mathrm{d}a \int_0^1 \mathrm{d}b \, \frac{\delta(a + b - 1)\, a^{n_2-1} b^{n_1-1} \Gamma(n_1 + n_2)}{\Gamma(n_1)\,\Gamma(n_2)} \int \frac{\mathrm{d}^d p}{\left(-(p^2 - a^2 m_1^2)\right)^{n_1+n_2}} .
\tag{B.54}
$$

Now the integral over the loop momentum can be evaluated using Equation (B.50). In a last step, the integrals over the Feynman parameters are calculated by first using the delta function to eliminate the Feynman parameter a and then identifying the remaining b-integral with Equation (B.51):

$$
\begin{aligned}
I &= \int_0^1 \mathrm{d}a \int_0^1 \mathrm{d}b \, \frac{\delta(a + b - 1)\, a^{n_2-1} b^{n_1-1} \Gamma(n_1 + n_2)}{\Gamma(n_1)\,\Gamma(n_2)} i\pi^{d/2} \frac{\Gamma\left(n_1 + n_2 - \frac{d}{2}\right)}{\Gamma(n_1 + n_2)} \left(\frac{1}{a^2 m_1^2}\right)^{n_1+n_2-d/2} \\
&= i\pi^{d/2} \left(\frac{1}{m_1^2}\right)^{n_1+n_2-d/2} \frac{\Gamma\left(n_1 + n_2 - \frac{d}{2}\right)}{\Gamma(n_1)\,\Gamma(n_2)} \int_0^1 \mathrm{d}b \, b^{n_1-1} (1 - b)^{-n_2-2n_1-1+d}
\end{aligned}
$$

$$= i\pi^{d/2} \left(\frac{1}{m_1^2} \right)^{n_1 + n_2 - d/2} \frac{\Gamma\left(n_1 + n_2 - \frac{d}{2} \right) \Gamma(-n_2 - 2n_1 + d)}{\Gamma(n_2) \, \Gamma(-n_1 - n_2 + d)}. \tag{B.55}$$

The result obtained in Equation (B.55) gives the expression of the loop integral in terms of Gamma functions depending on the indices n_1, n_2 and the dimension $d = 4 - 2\epsilon$.

B.6. Mellin-Barnes representation

In the previous section, the calculation of loop integrals by using Feynman parameters is outlined. In this procedure, the integral over the Feynman parameter is evaluated using the relation for the Beta-function given in Equation (B.51). However, this is not possible for all integrals. As an example, consider the integral

$$\int_0^1 da \, \frac{1}{\left(m_1^2 + a(a-1)p^2\right)^n} \, , \tag{B.56}$$

with the Feynman parameter a, arbitrary propagator power n and a linear combination of momenta p. This integral can not be brought to the form of the Beta-function. One possibility to solve this integral is the Mellin-Barnes representation [136, 137], where the relation

$$\frac{1}{(X+Y)^\lambda} = \frac{1}{2\pi i \Gamma(\lambda)} \int_{-i\infty}^{+i\infty} dz \, \Gamma(\lambda + z) \, \Gamma(-z) \, \frac{Y^z}{X^{\lambda+z}} \tag{B.57}$$

is applied to rewrite integrands of the form given in Equation (B.56). The integration contour along the complex axis is chosen in a way that the poles of the $\Gamma(\cdots + z)$ and the poles of the $\Gamma(\cdots - z)$ are separated. The complex integral can then be evaluated in some cases by Barnes Lemma [138]

$$\frac{1}{2\pi i} \int_{-i\infty}^{+i\infty} dz \, \Gamma(\alpha_1 - z) \, \Gamma(\alpha_2 - z) \, \Gamma(\beta_1 + z) \, \Gamma(\beta_2 + z)$$
$$= \frac{\Gamma(\alpha_1 + \beta_1) \, \Gamma(\alpha_1 + \beta_2) \, \Gamma(\alpha_2 + \beta_1) \, \Gamma(\alpha_2 + \beta_2)}{\Gamma(\alpha_1 + \beta_1 + \alpha_2 + \beta_2)} \tag{B.58}$$

or by closing the contour in the complex plane at $+\infty$ or $-\infty$ and summing up the enclosed poles according to the residue theorem.

To demonstrate this procedure, we consider the massive sunset integral that is needed for the analytic boundary conditions for the NNLO semileptonic master integrals. Its result is given in Equation (3.21). We will outline the explicit calculation of this integral in the following. We start with

$$I_4 = I_4(1, 1, 1) = \int \frac{d^d k_1 \, d^d k_2}{\left(m_b^2 - (k_1 + k_2)^2\right) \left(m_b^2 - k_1^2\right) \left(m_b^2 - (k_2 + q)^2\right)} \, , \tag{B.59}$$

with $m_b^2 = q^2$. Performing the integration over k_1 by introducing Feynman parameters, we obtain

$$I_4 = \int \frac{d^d k_2}{\left(m_b^2 - (k_2 + q)^2\right)} \int \frac{d^d k_1}{\left(m_b^2 - (k_1 + k_2)^2\right) \left(m_b^2 - k_1^2\right)}$$
$$= \int \frac{d^d k_2}{\left(m_b^2 - (k_2 + q)^2\right)} \frac{i}{(4\pi)^{d/2}} \Gamma(\epsilon) \int_0^1 db \, \frac{1}{\left(m_b^2 + b(b-1) k_2^2\right)^\epsilon} \, . \tag{B.60}$$

At this point, the application of Equation (B.57) is useful to get rid of the m_b^2 term in the denominator. We find

$$
\begin{aligned}
I_4 &= \int \frac{\mathrm{d}^d k_2}{\left(m_b^2 - (k_2 + q)^2\right)} \left(i\pi^{d/2}\right) \Gamma(\epsilon) \int_0^1 \mathrm{d}b \, \frac{1}{\left(m_b^2 + b(b-1)k_2^2\right)^\epsilon} \\
&= \int \frac{\mathrm{d}^d k_2}{\left(m_b^2 - (k_2 + q)^2\right)} \left(i\pi^{d/2}\right) \Gamma(\epsilon) \int_0^1 \mathrm{d}b \, \frac{1}{2\pi i \Gamma(\epsilon)} \int_{-i\infty}^{+i\infty} \mathrm{d}z \, \frac{\Gamma(\epsilon+z)\Gamma(-z) m_b^{2z}}{\left(b(b-1)k_2^2\right)^{\epsilon+z}} \, .
\end{aligned}
$$

$$(B.61)$$

After the Mellin-Barnes representation is applied, the integral over the Feynman parameter can be evaluated by using Equation (B.51) and the result of the k_1 integration can be written as

$$
\begin{aligned}
I_4 &= \int \frac{\mathrm{d}^d k_2}{\left(m_b^2 - (k_2 + q)^2\right)} \left(i\pi^{d/2}\right) \Gamma(\epsilon) \int_0^1 \mathrm{d}b \, \frac{1}{2\pi i \Gamma(\epsilon)} \int_{-i\infty}^{+i\infty} \mathrm{d}z \, \frac{\Gamma(\epsilon+z)\Gamma(-z) m_b^{2z}}{\left(b(b-1)k_2^2\right)^{\epsilon+z}} \\
&= \int \frac{\mathrm{d}^d k_2}{\left(m_b^2 - (k_2 + q)^2\right)} \frac{\left(i\pi^{d/2}\right)}{2\pi i} \int_{-i\infty}^{+i\infty} \mathrm{d}z \frac{m_b^{2z}}{\left(-(k_2)^2\right)^{\epsilon+z}} \frac{\Gamma(\epsilon+z)\Gamma(-z)\Gamma^2(1-\epsilon-z)}{\Gamma(2-2\epsilon-2z)} \, ,
\end{aligned}
$$

$$(B.62)$$

including a massless propagator with the momentum k_2 and the non-integer power $\epsilon + z$. The remaining k_2 integral can be written after exchanging the integration order

$$
\int \frac{\mathrm{d}^d k_2}{\left(m_b^2 - (k_2 + q)^2\right)\left(-k_2^2\right)^{\epsilon+z}} \, .
$$

$$(B.63)$$

We can evaluate this expression without any further problems using Feynman parameters:

$$
\begin{aligned}
&\int \frac{\mathrm{d}^d k_2}{\left(m_b^2 - (k_2 + q)^2\right)\left(-k_2^2\right)^{\epsilon+z}} \\
&= \left(i\pi^{d/2}\right) \frac{\Gamma(-1+2\epsilon+z)\Gamma(\epsilon+z)\Gamma(3-4\epsilon-2z)\left(m_b^2\right)^{1-z-2\epsilon}}{\Gamma(\epsilon+z)\Gamma(3-3\epsilon-z)} \, .
\end{aligned}
$$

$$(B.64)$$

As a result, for the integral I_4 we obtain a complex integral over z that is given by

$$
\begin{aligned}
I_4 = &\left(i\pi^{d/2}\right)^2 m_1^2 \left(\frac{\mu^2}{m_1^2}\right)^{2\epsilon} \\
&\frac{1}{2\pi i} \int_{-i\infty}^{+i\infty} \mathrm{d}z \frac{\Gamma(\epsilon+z)\Gamma^2(1-\epsilon-z)\Gamma(-z)\Gamma(-1+2\epsilon+z)\Gamma(3-4\epsilon-2z)}{\Gamma(2-2\epsilon-2z)\Gamma(3-3\epsilon-z)} \, .
\end{aligned} \quad (B.65)
$$

The evaluation of this integral is now done by closing the integration contour in the complex plane. The value of the integral is then evaluated by summing all residues of the

enclosed poles. The only functions in the integrand that develop poles are the Gamma functions. The poles of the general Gamma function $\Gamma(x)$ are located at $x = -n$, where $n \in \{0, 1, 2, \dots\}$. We set the integration contour along the complex axis such that the poles of Gamma functions of the form $\Gamma(\cdots + z)$ are located to the left while the poles of $\Gamma(\cdots - z)$ are to the right of the contour. The next step is to close the contour and evaluate the integral with the residue theorem. In the particular case of Equation (B.65), closing the contour at $\mathrm{Re}(z) \to -\infty$ is a suitable choice, since in this case only the poles of $\Gamma(-1 + 2\epsilon + z)$ are enclosed. The poles of the integrand given in Equation (B.65) are therefore located at $z = 1 - 2\epsilon - n$, with $n \in \{0, 1, 2, \dots\}$. The residue of the Gamma function $\Gamma(x)$ at $x = -n$ is given by $(-1)^n/(n!)$, so summing up all residues starting from $n = 0$, we obtain

$$\sum_{n=0}^{\infty} \frac{4^n}{n!} \frac{\Gamma(1 - \epsilon)\,\Gamma(1 + n)\,(\Gamma(\epsilon + n))^2\,\Gamma(-1 + 2\epsilon + n)}{\Gamma(2 - \epsilon + n)\,\Gamma(2\epsilon + 2n)}\,. \tag{B.66}$$

The sum over the Gamma functions can now be expressed in terms of generalized hypergeometric functions which are defined by

$$_pF_q\left(a_1, \dots, a_p; b_1, \dots b_q; z\right) = \sum_{n=0}^{\infty} \prod_{i=1}^{p} \frac{\Gamma(n + a_i)}{\Gamma(a_i)} \prod_{j=1}^{q} \frac{\Gamma(b_j)}{\Gamma(n + b_j)} \frac{z^n}{n!}\,. \tag{B.67}$$

In order to identify this pattern in Equation (B.66), the Gamma function $\Gamma(2\epsilon + 2n)$ is replaced using the relation

$$2^{1-2z}\sqrt{\pi}\,\Gamma(2z) = \Gamma(z)\,\Gamma\left(z + \frac{1}{2}\right)\,. \tag{B.68}$$

We finally obtain the result for I_4 expressed in terms of hypergeometric functions by

$$
\begin{aligned}
I_4 &= \left(i\pi^{d/2}\right)^2 m_1^2 \left(\frac{\mu^2}{m_1^2}\right)^{2\epsilon} \sum_{n=0}^{\infty} \frac{\sqrt{\pi}2^{1-2\epsilon}}{n!} \frac{\Gamma(1 - \epsilon)\,\Gamma(1 + n)\,\Gamma(\epsilon + n)\,\Gamma(-1 + 2\epsilon + n)}{\Gamma(2 - \epsilon + n)\,\Gamma\left(\epsilon + n + \frac{1}{2}\right)} \\
&= \left(i\pi^{d/2}\right)^2 m_1^2 \left(\frac{\mu^2}{m_1^2}\right)^{2\epsilon} \frac{2\sqrt{\pi}}{4^\epsilon} \frac{\Gamma(1 - \epsilon)\,\Gamma(\epsilon)\,\Gamma(2\epsilon - 1)}{\Gamma(2 - \epsilon)\,\Gamma\left(\epsilon + \frac{1}{2}\right)} \,_3F_2\left(1, \epsilon, 2\epsilon - 1; 2 - \epsilon, \frac{1}{2} + \epsilon; 1\right)\,.
\end{aligned}
$$
$$\tag{B.69}$$

In order to express this result as a series in ϵ, this hypergeometric function has to be expanded around $\epsilon = 0$. This can be done with the `Mathematica` package `HypExp` [139, 140]. The final result as expansion in ϵ is given in Equation (3.22).

B.7. Fierz identities

In this section we consider general Fierz transformation and show how they can be derived. This procedure can be found in most quantum field theory textbooks, for example in Ref. [26].
We write the general Fierz identity in the form

$$\left(\overline{u}_1 \Gamma^A u_2\right)\left(\overline{u}_3 \Gamma^B u_4\right) = -\sum_{C,D} c[A, B, C, D]\left(\overline{u}_3 \Gamma^C u_2\right)\left(\overline{u}_1 \Gamma^D u_4\right), \tag{B.70}$$

with unknown coefficients $c[A, B, C, D]$ and Γ^j the elements of the basis

$$\{\mathbb{1}, \gamma^\mu, \sigma^{\mu\nu}, \gamma^\mu \gamma_5, \gamma_5\} . \tag{B.71}$$

The minus sign in Equation (B.70) accounts for the Grassmann nature of the fermion fields u_i. To prove this relation, Equation (B.70) is multiplied from the left by $(\overline{u}_2 \Gamma^F u_3)(\overline{u}_4 \Gamma^E u_1)$ which leads to the left hand side

$$\left(\overline{u}_2 \Gamma^F u_3\right)\left(\overline{u}_4 \Gamma^E u_1\right)\left(\overline{u}_1 \Gamma^A u_2\right)\left(\overline{u}_3 \Gamma^B u_4\right) = \left(\overline{u}_4 \Gamma^E u_1\right)\left(\overline{u}_1 \Gamma^A u_2\right)\left(\overline{u}_2 \Gamma^F u_3\right)\left(\overline{u}_3 \Gamma^B u_4\right)$$
$$= \text{Tr}\left[\Gamma^E \Gamma^A \Gamma^F \Gamma^B\right], \tag{B.72}$$

while the right hand side can be written as

$$\sum_{C,D} c[A, B, C, D]\left(\overline{u}_2 \Gamma^F u_3\right)\left(\overline{u}_4 \Gamma^E u_1\right)\left(\overline{u}_3 \Gamma^C u_2\right)\left(\overline{u}_1 \Gamma^D u_4\right)$$
$$= \sum_{C,D} c[A, B, C, D]\left(\overline{u}_2 \Gamma^F u_3\right)\left(\overline{u}_4 \Gamma^E u_1\right)\left(\overline{u}_1 \Gamma^C u_4\right)\left(\overline{u}_3 \Gamma^D u_2\right)$$
$$= \sum_{C,D} c[A, B, C, D]\left(\overline{u}_4 \Gamma^E u_1\right)\left(\overline{u}_1 \Gamma^C u_4\right)\left(\overline{u}_2 \Gamma^F u_3\right)\left(\overline{u}_3 \Gamma^D u_2\right)$$
$$= \sum_{C,D} c[A, B, C, D]\text{Tr}\left[\Gamma^E \Gamma^C\right]\text{Tr}\left[\Gamma^F \Gamma^D\right]. \tag{B.73}$$

Using the relation

$$\text{Tr}\left[\Gamma^A \Gamma^B\right] = 4\delta^{AB}, \tag{B.74}$$

we then obtain for the coefficients $c[A, B, C, D]$ in Equation (B.70) the relation

$$c[A, B, C, D] = -\frac{\text{Tr}\left[\Gamma^C \Gamma^A \Gamma^D \Gamma^B\right]}{16} . \tag{B.75}$$

Let us now consider the Fierz identity for the quantity

$$\left(\overline{u}_1 \gamma^\mu (1 - \gamma_5) u_2\right)\left(\overline{u}_3 \gamma^\mu (1 - \gamma_5) u_4\right), \tag{B.76}$$

where all traces

$$\text{Tr}\left[\Gamma^C \gamma^\mu (1 - \gamma_5) \Gamma^D \gamma_\mu (1 - \gamma_5)\right] \tag{B.77}$$

for all possible Γ^C and Γ^D have to be computed. All terms with $\Gamma^D \in \{\mathbb{1}, \sigma^{\mu\nu}, \gamma_5\}$ evaluates to zero since in these cases

$$
\begin{aligned}
\Gamma^C \gamma^\mu (1 - \gamma_5) \Gamma^D \gamma_\mu (1 - \gamma_5) &= \Gamma^C \gamma^\mu (1 - \gamma_5) \gamma_\mu (1 - \gamma_5) \Gamma^D \\
&= \Gamma^D \gamma^\mu (1 - \gamma_5)(1 + \gamma_5) \gamma_\mu \Gamma^D \\
&= 0 \,,
\end{aligned}
\tag{B.78}
$$

where $\{\gamma^\mu, \gamma_5\} = 0$ and $\gamma_5 \gamma_5 = \mathbb{1}$ is used. The same argument holds for $\Gamma^C \in \{\mathbb{1}, \sigma^{\mu\nu}, \gamma_5\}$ because of the cyclicity of the trace. The traces over the remaining combinations of basis elements can be evaluated to

$$
\begin{aligned}
\mathrm{Tr}[\gamma^\nu \gamma^\mu (1 - \gamma_5) \gamma_\nu \gamma_\mu (1 - \gamma_5)] &= -64 \,, \\
\mathrm{Tr}[\gamma^\nu \gamma_5 \gamma^\mu (1 - \gamma_5) \gamma_\nu \gamma_\mu (1 - \gamma_5)] &= -64 \,, \\
\mathrm{Tr}[\gamma^\nu \gamma^\mu (1 - \gamma_5) \gamma_\nu \gamma_5 \gamma_\mu (1 - \gamma_5)] &= -64 \,, \\
\mathrm{Tr}[\gamma^\nu \gamma_5 \gamma^\mu (1 - \gamma_5) \gamma_\nu \gamma_5 \gamma_\mu (1 - \gamma_5)] &= -64 \,.
\end{aligned}
\tag{B.79}
$$

This leads to $c[A, B, C, D] = 4$ for $\Gamma^A = \Gamma^B = \gamma^\mu (1 - \gamma_5)$ and $\Gamma^C, \Gamma^D \in \{\gamma^\mu, \gamma^\mu \gamma_5\}$ while we obtain
$c[A, B, C, D] = 0$ for $\Gamma^A = \Gamma^B = \gamma^\mu (1 - \gamma_5)$ and $\Gamma^C, \Gamma^D \in \{\mathbb{1}, \sigma^{\mu\nu}, \gamma_5\}$. Finally, we obtain

$$
(\overline{u}_1 \gamma^\mu P_L u_2)(\overline{u}_3 \gamma_\mu P_L u_4) = (\overline{u}_3 \gamma^\mu P_L u_2)(\overline{u}_1 \gamma_\mu P_L u_4) \,,
\tag{B.80}
$$

with the left-handed projector $P_L = (1 - \gamma_5)/2$. This relation corresponds to the Fierz identity that is introduced in Chapter 5.1 in order to rewrite the $\Delta B = 1$ operators.

C. Renormalization constants

As described in Chapter 5.1, the usage of Fierz identities leads to a redefinitions of the evanescent operators, which mix via renormalization into the physical operators. This chapter describes the procedure to obtain the corresponding renormalization constants. For the NNLO calculations performed in this thesis, the renormalization constants for the current-current operators and their corresponding evanescent operators are needed up to order α_s^2 in the historical basis. The renormalization constants for the current-current operators are known in the literature [27, 101, 24, 141], however, they are only available for fixed number of colours $n_c = 3$. To obtain expressions for general n_c, we decided to repeat the calculation which also serves as a cross check on the implementation of the four-quark operators. The calculation procedure to obtain these constants is outlined in Section C.1. In addition to the historical basis, we also perform the explicit calculation in the CMM basis as a cross check of our setup.

As introduced in Section 2.2.3, the operators of both bases can be transformed into each other via linear relations and so can be the renormalization constants. In Section C.2, we discuss the basis transformation of the renormalization constants in detail. The relations between the renormalization constants in both bases serve as a strong cross-check of our results. Furthermore, we use the this ansatz to obtain the renormalization constants in the historical basis including the penguin operators.

C.1. Calculation of renormalization constants

The calculation setup is the following: We consider diagrams with four external quarks and the insertion of one effective operator as shown in Figure C.1. Since we are only interested in the ultraviolet divergences we can assign the same mass m_q to all quark lines and can set all external momenta to zero. The gluons can be kept massless since this does not introduce any infrared divergences.

In amplitudes like this we have to renormalize the wave function, the masses and the coupling constants, and in addition, the effective four-quark operator O_i. The operators can mix under renormalization into another four fermion operator O_j and we therefore consider renormalized expressions like

$$A_{\text{eff}} = C_j(\mu) Z_{ji} \langle Z(O_i) \rangle_R, \tag{C.1}$$

where C_j is a Wilson coefficient and $\langle Z(O_i) \rangle_R$ describes the expectation value of the operator O_i, where wave function, masses and coupling constants are all renormalized. At higher orders in α_s, $\langle Z(O_i) \rangle_R$ still contains UV poles that must be cancelled by the renormalization constant Z_{ij}. The Wilson coefficients therefore behave under renormalization according to

$$C_{i,B}(\mu) = C_j(\mu) Z_{ji}. \tag{C.2}$$
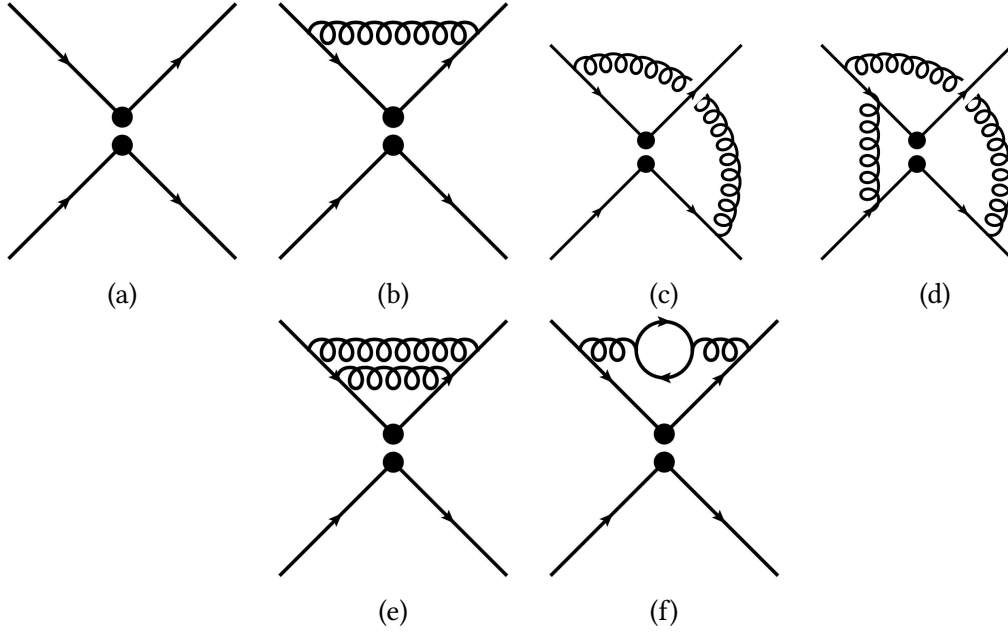
Figure C.1.: Sample diagrams for the calculation of the operator renormalization constants. The two dots denote the insertion of a four-quark operator. All quark lines are massive and have the mass m_q and all external momenta are zero.

The quantities we have to calculate are the renormalization constants Z_{ij} which we decompose in the following way:

$$Z_{ij} = \delta_{ij} + \sum_{k=1}^{\infty} \left(\frac{\alpha_s}{4\pi} \right)^k Z_{ij}^{(k)}, \tag{C.3}$$

where

$$Z_{ij}^{(k)} = \sum_{l=0}^{k} \frac{Z_{ij}^{(k,l)}}{\epsilon^l}. \tag{C.4}$$

We work in the $\overline{\text{MS}}$ renormalization scheme, which implies $l > 0$. This is however not the case if i is the coefficient of an evanescent operator, while j corresponds to a physical one. In these cases, the renormalization constant includes ϵ-finite terms that ensure that the matrix elements of evanescent operators vanish in four dimensions. In this setup for the calculation of the renormalization constants, we consider all the quarks to be massive and having the same mass m_q. For the renormalization of this mass we introduce counterterms in the propagator of all the quarks. The external momenta of the quarks are set to zero from the beginning. Let us give a few remarks about the implementation of the calculation:

- As mentioned above, the momenta of the external quarks are set to zero. This can be done easily be using the `tapir` [128] option

```
* tapir.external_momentum q1:0
```

- The quark masses are all set to $m_q \neq 0$. The renormalization of this mass is done by introducing mass counterterms in the quark propagator in the same way as described in Chapter 4 and 5.2.

- The loop integrals occurring in the calculation of the NLO and NNLO diagrams can be reduced to massive tadpole integrals, which are implemented in the program MATAD [142]. In our case, we can map to the topologies tad1l and tad2lt. This simplifies our calculation significantly.

- The numerators of the loop integrals contain terms with powers of slashed loop momenta. The topology files of MATAD can deal with tensor integrals containing strings of gamma matrices in the numerator. Therefore, we replace all the slashed momenta with replacement rules like

```
id once g_(1,p`k´) = g_(1,rho`j´`k´ )*p`k´(sig`j´`k´);
```

where the indices rho`j´`k´ and sig`j´`k´ are independent at this step of the calculation. The momentum is therefore stripped off the integral and only gamma matrices remain. After the integration routine successfully calculated the integral, we contract rho`j´`k´ and sig`j´`k´ again and obtain our final result for the integral.

- After the calculation of the loop integrals, the result contains effective operators with up to nine gamma matrices and different colour structures. To map these structures of Dirac matrices to physical and evanescent operators, one does not only need the definition of the ones appearing in the calculation of the physical process that are introduced in Chapter 2 for the historical and the CMM basis, but also the evanescent operators at third and fourth order, which then introduce structures with seven and nine gamma matrices. In the historical basis, they read

$$
\begin{aligned}
E_1^{(3)\,q_1q_2q_3} &= (\overline{q}_1^\alpha \gamma^{\mu_1...\mu_7} P_L b^\beta)(\overline{q}_2^\alpha \gamma_{\mu_1...\mu_7} P_L q_3^\beta) - (4096 - 7680\epsilon) O_1^{q_1q_2q_3}, \\
E_2^{(3)\,q_1q_2q_3} &= (\overline{q}_1^\alpha \gamma^{\mu_1...\mu_7} P_L b^\alpha)(\overline{q}_2^\beta \gamma_{\mu_1...\mu_7} P_L q_3^\beta) - (4096 - 7680\epsilon) O_2^{q_1q_2q_3}, \\
E_1^{(4)\,q_1q_2q_3} &= (\overline{q}_1^\alpha \gamma^{\mu_1...\mu_9} P_L b^\beta)(\overline{q}_2^\alpha \gamma_{\mu_1...\mu_9} P_L q_3^\beta) - (65536 - 176128\epsilon) O_1^{q_1q_2q_3}, \\
E_2^{(4)\,q_1q_2q_3} &= (\overline{q}_1^\alpha \gamma^{\mu_1...\mu_9} P_L b^\alpha)(\overline{q}_2^\beta \gamma_{\mu_1...\mu_9} P_L q_3^\beta) - (65536 - 176128\epsilon) O_2^{q_1q_2q_3}.
\end{aligned}
\tag{C.5}
$$

For the CMM basis, they are given by

$$
\begin{aligned}
E_1'^{(3)\,q_1q_2q_3} &= (\overline{q}_1 \gamma^{\mu_1...\mu_7} T^a P_L b)(\overline{q}_2 \gamma_{\mu_1...\mu_7} T^a P_L q_3) - 4096 O_1'^{q_1q_2q_3} - 336 E_1'^{(1)\,q_1q_2q_3}, \\
E_2'^{(3)\,q_1q_2q_3} &= (\overline{q}_1 \gamma^{\mu_1...\mu_7} P_L b)(\overline{q}_2 \gamma_{\mu_1...\mu_7} P_L q_3) - 4096 O_2'^{q_1q_2q_3} - 336 E_2'^{(1)\,q_1q_2q_3}, \\
E_1'^{(4)\,q_1q_2q_3} &= (\overline{q}_1 \gamma^{\mu_1...\mu_9} T^a P_L b)(\overline{q}_2 \gamma_{\mu_1...\mu_9} T^a P_L q_3) - 65536 O_1'^{q_1q_2q_3} - 5440 E_1'^{(1)\,q_1q_2q_3}, \\
E_2'^{(4)\,q_1q_2q_3} &= (\overline{q}_1 \gamma^{\mu_1...\mu_9} P_L b)(\overline{q}_2 \gamma_{\mu_1...\mu_9} P_L q_3) - 65536 O_2'^{q_1q_2q_3} - 5440 E_2'^{(1)\,q_1q_2q_3}.
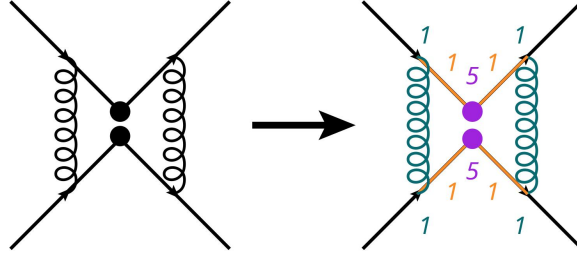\end{aligned}
\tag{C.6}
$$

Figure C.2.: Sample diagram for the calculation of the renormalization constant of an evanescent operator $E_1^{(2)}$. The evanescent operator introduces five gamma matrices on every fermion line. The number of gamma matrices is on each spin line are visualized by the coloured numbers.

As mentioned before, for our calculation, the evanescent operators only up to the second order are relevant, meaning we are only interested in the coefficients of $\{O_1, O_2, E_1^{(1)}, E_2^{(1)}, E_1^{(2)}, E_2^{(2)}\}$. However, since we calculate α_s^2 corrections also to the evanescent operators, we produce structures of at most nine gamma matrices, which can be seen in Figure C.2. There we consider the insertion of a second order evanescent operator $E_i^{(2)}$ which introduces five gamma matrices per fermion line, see Equation (2.19) for its definition. In addition to these five gamma matrices, one additional gamma matrix is introduced for every quark propagator and every quark-gluon coupling. Therefore we add up to at most nine gamma matrices per fermion line. Using Equation (C.5) to map this structure to an fourth order evanescent operator $E_i^{(4)}$, we also obtain a contribution with an physical operator O_i.

- The mapping of the terms in our result to the set of effective operators could in principle be done by constructing projectors for Lorentz and colour structures. However, in this special case, the identification of the operators in the result is quite simple and straightforward so we do not use projectors here, but just identify the operators directly.

Let us have a look at the explicit calculation of the renormalization matrix in more detail. As an example we consider calculation of the one loop renormalization constant of operator O_i. For this renormalization constant, have to calculate the one loop correction to the four point function with insertion of O_i, see for example Figure C.1 (b). At NLO, there are six six diagrams of this form. We consider Equation (C.1) up to order α_s^1 and obtain

$$
\begin{aligned}
A_{\text{eff}} &= C_j(\mu)\left(Z_{ji}^{(0)} + \frac{\alpha_s}{4\pi}Z_{ji}^{(1)}\right)\left(\langle Z(O_i)\rangle_R^{(0)} + \frac{\alpha_s}{4\pi}\langle Z(O_i)\rangle_R^{(1)}\right) + O\left(\alpha_s^2\right) \\
&= C_j(\mu)\langle Z(O_j)\rangle_R^{(0)} + \frac{\alpha_s}{4\pi}C_j(\mu)\left(Z_{ji}^{(1)}\langle Z(O_i)\rangle_R^{(0)} + \langle Z(O_i)\rangle_R^{(1)}\right) + O\left(\alpha_s^2\right).
\end{aligned} \tag{C.7}
$$

Since A_{eff} must have no UV poles at any order in α_s, we find that

$$
Z_{ji}^{(1)}\langle Z(O_i)\rangle_R^{(0)} = -\langle Z(O_i)\rangle_R^{(1)} + O(\epsilon^0), \tag{C.8}
$$

at any order of ϵ^k with $k < 0$. Let us recall that $\langle Z(O_i)\rangle_R^{(n)}$ denotes the matrix element of operator O_i with renormalized quark wave function, masses and strong coupling constant

at order n. We rewrite Equation (C.8) and obtain

$$Z_{ij}^{(1)}\langle O_j\rangle_B^{(0)} = -\langle O_i\rangle_B^{(1)} - Z^{(1)}\langle O_i\rangle_B^{(0)} + O(\epsilon^0), \tag{C.9}$$

where $\langle O_i\rangle_B^{(0)}$ denotes the bare LO matrix element of operator O_i, $\langle O_i\rangle_B^{(1)}$ the bare NLO matrix element. The term $Z^{(1)}\langle O_i\rangle_B^{(0)}$ denotes the contributions obtained from LO matrix elements with one loop renormalization of quark wave function, quark mass and strong coupling constant. In the case of Equation (C.9), only the quark wave function contributes to this term since there are no diagrams with mass counterterms and no factor of α_s in the LO diagram. Requiring Equation (C.9) for every $i \in \{1, \ldots, 6\}$ and $j \in \{1, \ldots, 6\}$ for all poles in ϵ, we can determine $Z_{ij}^{(1)}$ and obtain for the $\overline{\text{MS}}$ renormalization constant

$$Z^{(1,1)} = \begin{pmatrix} -1 & 3 & \frac{7}{12} & \frac{1}{4} & 0 & 0 \\ 3 & -1 & \frac{1}{2} & -\frac{1}{6} & 0 & 0 \\ 0 & 0 & -\frac{59}{3} & -5 & \frac{7}{12} & \frac{1}{4} \\ 0 & 0 & -13 & \frac{13}{3} & \frac{1}{2} & -\frac{1}{6} \\ 0 & 0 & -\frac{1888}{3} & 96 & \frac{41}{3} & -9 \\ 0 & 0 & -288 & \frac{1568}{3} & 3 & -\frac{67}{3} \end{pmatrix}, \tag{C.10}$$

where we have set $n_c = 3$. For the complete result of the renormalization constant expressed in general n_c, see Section C.3.

At NNLO the procedure is similar. The equation analogous to (C.9) at two loop order reads

$$Z_{ij}^{(2)}\langle O_j\rangle_B^{(0)} = -\langle O_i\rangle_B^{(2)} - Z^{(2)}\langle O_i\rangle_B^{(0)} - Z^{(1)}\langle O_i\rangle_B^{(1)} - Z^{(1)}Z_{ij}^{(1)}\langle O_j\rangle_B^{(0)} - Z_{ij}^{(1)}\langle O_j\rangle_B^{(1)} + O(\epsilon^0), \tag{C.11}$$

where we now find contributions from terms up to order α_s^2 in the renormalization constants. The last two terms contain the NLO operator renormalization matrix $Z_{ij}^{(1)}$ which was calculated already using Equation (C.9). These terms now also introduce matrix elements of the operator O_j with $j \neq i$.

For the NNLO poles, there are several cross checks which show that the obtained result is reasonable. One of them is to check that all of the $\log(\mu^2/m_q^2)$ factors that are introduced by the NLO and NNLO matrix elements cancel in the ϵ-pole terms on the right hand side of equation (C.11). Furthermore we can predict the $1/\epsilon^2$ poles of the NNLO renormalization constant from the $1/\epsilon$ pole of the NLO renormalization constant [143]:

$$Z^{(2,2)} = \frac{1}{2}\left(Z^{(1,1)}\right)^2 - \frac{1}{2}\beta_0 Z^{(1,1)}. \tag{C.12}$$

The explicit results for the renormalization constants of the current-current operators in the historical basis and the CMM basis are given explicitly in Section C.3 and C.5.

C.2. Basis transformation for renormalization constants

The operator bases introduced in Section 2.2.1 and 2.2.2 are related by linear transformations as described in Section 2.2.3. The physical and evanescent operators of CMM basis

are related to its counterparts in the historical basis via the relations

$$\vec{O} = R\left(\vec{O}' + W\vec{E}'\right),$$

$$\vec{E} = M\left(\left(\epsilon U + \epsilon^2 V\right)\vec{O}' + \left(1 + \epsilon UW + \epsilon^2 VW\right)\vec{E}'\right), \tag{C.13}$$

with the transformation matrices R, M, W, U and V. Defining the transformation matrices

$$A = \begin{pmatrix} R & 0 \\ 0 & M \end{pmatrix} \qquad B = \begin{pmatrix} \mathbb{1} & 0 \\ \epsilon U + \epsilon^2 V & \mathbb{1} \end{pmatrix}, \qquad C = \begin{pmatrix} \mathbb{1} & W \\ 0 & \mathbb{1} \end{pmatrix} \tag{C.14}$$

we can rewrite Equation (C.13) as

$$\begin{pmatrix} \vec{O} \\ \vec{E} \end{pmatrix} = ABC \begin{pmatrix} \vec{O}' \\ \vec{E}' \end{pmatrix}. \tag{C.15}$$

Using these transformation matrices it is also possible to transform the renormalization constants of the different bases. Requiring that the renormalized quantities of the form of Equation (C.1) stays the same under the basis transformation, we obtain [1]

$$Z = (ABC)Z'(C^{-1}B^{-1}A^{-1}), \tag{C.16}$$

where Z and Z' denote the renormalization matrix for the operators in the historical and in the CMM basis respectively. Note that these matrices are given in the space of $\{\vec{O}, \vec{E}\}$. For the transformation matrices A, B and C, we obtain

$$(ABC) = \begin{pmatrix} R & 0 \\ 0 & M \end{pmatrix} \cdot \begin{pmatrix} \mathbb{1} & 0 \\ \epsilon U + \epsilon^2 V & \mathbb{1} \end{pmatrix} \cdot \begin{pmatrix} \mathbb{1} & W \\ 0 & \mathbb{1} \end{pmatrix}$$

$$= \begin{pmatrix} R & RW \\ \epsilon MU + \epsilon^2 MV & M + \epsilon MUW + \epsilon^2 MUW \end{pmatrix}, \tag{C.17}$$

and

$$(C^{-1}B^{-1}A^{-1}) = \begin{pmatrix} \mathbb{1} & W \\ 0 & \mathbb{1} \end{pmatrix}^{-1} \cdot \begin{pmatrix} \mathbb{1} & 0 \\ \epsilon U + \epsilon^2 V & \mathbb{1} \end{pmatrix}^{-1} \cdot \begin{pmatrix} R & 0 \\ 0 & M \end{pmatrix}^{-1}$$

$$= \begin{pmatrix} \mathbb{1} & -W \\ 0 & \mathbb{1} \end{pmatrix} \cdot \begin{pmatrix} \mathbb{1} & 0 \\ -\epsilon U - \epsilon^2 V & \mathbb{1} \end{pmatrix} \cdot \begin{pmatrix} R^{-1} & 0 \\ 0 & M^{-1} \end{pmatrix}$$

$$= \begin{pmatrix} R^{-1} + \epsilon WUR^{-1} + \epsilon^2 WVR^{-1} & -WM^{-1} \\ -\epsilon UR^{-1} - \epsilon^2 VR^{-1} & M^{-1} \end{pmatrix}, \tag{C.18}$$

We devide the renormalization matrices into subblocks for physical and evanescent operators:

$$Z = \begin{pmatrix} Z_{QQ} & Z_{QE} \\ Z_{EQ} & Z_{EE} \end{pmatrix}. \tag{C.19}$$

---

[1] Note that Equation (C.16) leads to ϵ-finite terms in renormalization constants which have to be subtracted in order to obtain $\overline{\text{MS}}$ renormalization constants, see also Ref. [27, 28]. The contributions that are needed to subtract the ϵ-finite parts are discussed in Equation (C.26).

Inserting this ansatz into Equation (C.16) yields

$$
\begin{pmatrix} Z_{QQ} & Z_{QE} \\ Z_{EQ} & Z_{EE} \end{pmatrix} = (ABC) \cdot \begin{pmatrix} Z'_{QQ} & Z'_{QE} \\ Z'_{EQ} & Z'_{EE} \end{pmatrix} \cdot (C^{-1}B^{-1}A^{-1}), \tag{C.20}
$$

which allows us to extract the most general expressions in terms of the transformation matrices:

$$
\begin{aligned}
Z_{QQ} &= RZ'_{QQ}R^{-1} + RZ'_{QQ}W(\epsilon U + \epsilon^2 V)R^{-1} - RZ'_{QE}(\epsilon U + \epsilon^2 V)R^{-1} + RWZ'_{EQ}R^{-1} \\
&\quad + RWZ'_{EQ}W(\epsilon U + \epsilon^2 V)R^{-1} - RWZ'_{EE}(\epsilon U + \epsilon^2 V)R^{-1}, \\
Z_{QE} &= -RZ'_{QQ}WM^{-1} + RZ'_{QE}M^{-1} - RWZ'_{EQ}WM^{-1} + RWZ'_{EE}M^{-1}, \\
Z_{EQ} &= M(\epsilon U + \epsilon^2 V)Z'_{QQ}R^{-1} + M(\epsilon U + \epsilon^2 V)Z'_{QQ}W(\epsilon U + \epsilon^2 V)R^{-1} + MZ'_{EQ}R^{-1} \\
&\quad - M(\epsilon U + \epsilon^2 V)Z'_{QE}(\epsilon U + \epsilon^2 V)R^{-1} + M(\epsilon U + \epsilon^2 V)WZ'_{EQ}R^{-1} \\
&\quad - M(\epsilon U + \epsilon^2 V)Z'_{QE}(\epsilon U + \epsilon^2 V)R^{-1} + M(\epsilon U + \epsilon^2 V)WZ'_{EQ}W(\epsilon U + \epsilon^2 V)R^{-1} \\
&\quad + MZ'_{EQ}W(\epsilon U + \epsilon^2 V)R^{-1} - M(\epsilon U + \epsilon^2 V)WZ'_{EE}(\epsilon U + \epsilon^2 V)R^{-1} \\
&\quad - MZ'_{EE}(\epsilon U + \epsilon^2 V)R^{-1}, \\
Z_{EE} &= M(\epsilon U + \epsilon^2 V)Z'_{QQ}WM^{-1} + M(\epsilon U + \epsilon^2 V)Z'_{QE}M^{-1} - M(\epsilon U + \epsilon^2 V)WZ'_{EQ}WM^{-1} \\
&\quad + M(\epsilon U + \epsilon^2 V)WZ'_{EE}M^{-1} - MZ'_{EQ}WM^{-1} + MZ'_{EE}M^{-1}, \tag{C.21}
\end{aligned}
$$

Let us again consider the calculation including the current-current operators and their first, second and third order evanescent operators. In this case, the transformation matrices can be found in Equations (2.37), (5.36) and (5.42). We repeat them here for convenience:

$$
R = \begin{pmatrix} 2 & \frac{1}{3} \\ 0 & 1 \end{pmatrix}, \qquad M = \begin{pmatrix} 2 & \frac{1}{3} & 0 & 0 & 0 & 0 \\ 0 & 1 & 0 & 0 & 0 & 0 \\ 40 & \frac{20}{3} & 2 & \frac{1}{3} & 0 & 0 \\ 0 & 20 & 0 & 1 & 0 & 0 \\ 672 & 112 & 0 & 0 & 2 & \frac{1}{3} \\ 0 & 336 & 0 & 0 & 0 & 1 \end{pmatrix},
$$

$$
U = \begin{pmatrix} 4 & 0 \\ 0 & 4 \\ 144 & 0 \\ 0 & 144 \\ 6336 & 0 \\ 0 & 6336 \end{pmatrix}, \qquad V = \begin{pmatrix} 4 & 0 \\ 0 & 4 \\ \frac{36736}{115} & -\frac{2304}{23} \\ 0 & \frac{105856}{115} \\ -1344 & 0 \\ 0 & -1344 \end{pmatrix} \tag{C.22}
$$

Note that for this set of operators, all entries of the matrix W are zero. Rewriting the renormalization constants using the convention

$$
Z_{ij} = \sum_n \sum_m \left(\frac{\alpha_s}{4\pi}\right)^n \frac{1}{\epsilon^m} Z_{ij}^{(n,m)}, \tag{C.23}
$$

this means for the order α_s contributions:

$$
Z_{QQ}^{(1,1)} = RZ'^{(1,1)}_{QQ}R^{-1},
$$

$$Z_{QE}^{(1,1)} = R Z_{QE}^{'(1,1)} M^{-1} \, ,$$

$$Z_{EE}^{(1,1)} = M Z_{EE}^{'(1,1)} M^{-1} \, ,$$

$$Z_{QQ}^{(1,0)} = -R Z_{QE}^{'(1,1)} U R^{-1} \, ,$$

$$Z_{EQ}^{(1,0)} = M \left[Z_{EQ}^{'(1,0)} + U Z_{QQ}^{'(1,1)} - Z_{EE}^{'(1,1)} U \right] R^{-1} \, . \tag{C.24}$$

At order α_s^2 we obtain

$$Z_{QQ}^{(2,2)} = R Z_{QQ}^{'(2,2)} R^{-1} \, ,$$

$$Z_{QE}^{(2,2)} = R Z_{QE}^{'(2,2)} M^{-1} \, ,$$

$$Z_{EE}^{(2,2)} = M Z_{EE}^{'(2,2)} M^{-1} \, ,$$

$$Z_{QQ}^{(2,1)} = R \left[Z_{QQ}^{'(2,1)} - Z_{QE}^{'(2,2)} U \right] R^{-1} \, ,$$

$$Z_{QE}^{(2,1)} = R Z_{QE}^{'(2,1)} M^{-1} \, ,$$

$$Z_{EE}^{(2,1)} = R \left[Z_{EE}^{'(2,1)} - U Z_{QE}^{'(2,2)} \right] M^{-1} \, ,$$

$$Z_{EQ}^{(2,1)} = M \left[Z_{EQ}^{'(2,1)} + U Z_{QQ}^{'(2,2)} - Z_{EE}^{'(2,2)} U \right] R^{-1} \, ,$$

$$Z_{QQ}^{(2,0)} = R \left[- Z_{QE}^{'(2,1)} U - Z_{QE}^{'(2,2)} V + Z_{QE}^{'(1,1)} V Z_{QQ}^{'(1,1)} \right] R^{-1} \, ,$$

$$Z_{EQ}^{(2,0)} = M \left[Z_{EQ}^{'(2,0)} + U Z_{QQ}^{'(2,1)} + V Z_{QQ}^{'(2,2)} - Z_{EE}^{'(2,1)} U - Z_{EE}^{'(2,2)} V - U Z_{QE}^{'(2,2)} U \right] R^{-1} \, . \tag{C.25}$$

For simplicity, we refrain from giving the corresponding relations for non-zero W. They can be obtained straight forward from Equation (C.21).

After rotating the CMM basis into the historical basis, the ϵ finite elements $Z_{QQ}^{(1,0)}$ and $Z_{QQ}^{(2,0)}$ are different from zero and therefore the obtained renormalization constants do not correspond to $\overline{\text{MS}}$ renormalization constants. Such finite contributions must be removed by a suitable change of scheme. For the renormalization constants this corresponds to the transformation

$$Z_{\overline{\text{MS}}} = \left[1 - \frac{\alpha_s}{4\pi} r_1 - \left(\frac{\alpha_s}{4\pi} \right)^2 (r_2 - r_1^2) \right] Z \, , \tag{C.26}$$

where for the sub block including only the physical current-current operators we obtain

$$(r_1)_{QQ} = Z_{QQ}^{(1,0)} = \begin{pmatrix} -\frac{7}{3} & -1 \\ -2 & \frac{2}{3} \end{pmatrix} \, ,$$

$$(r_2)_{QQ} = Z_{QQ}^{(2,0)} = \begin{pmatrix} -\frac{153257}{2070} - \frac{35}{54} n_f & -\frac{1763}{138} - \frac{5}{18} n_f \\ -\frac{6493}{276} - \frac{5}{9} n_f & -\frac{239239}{4140} + \frac{5}{27} n_f \end{pmatrix} \, , \tag{C.27}$$

from Equation (C.24) and Equation (C.25). Note that the two loop constant depends on the choice of the evanescent operators. Keeping the ϵ^2 coefficients general, we obtain

$$(r_2)_{QQ} = Z_{QQ}^{(2,0)} = \begin{pmatrix} -\frac{200}{9} + \frac{45}{8} V_{11} - \frac{9}{2} V_{12} - \frac{67}{288} V_{31} & \frac{68}{3} + \frac{25}{8} V_{11} - \frac{33}{4} V_{12} - \frac{5}{96} V_{31} + \frac{5}{16} V_{32} \\ -\frac{7}{4} + \frac{23}{8} V_{11} + 3 - \frac{5}{48} V_{31} & \frac{397}{36} + \frac{3}{8} V_{11} + \frac{27}{4} V_{12} - \frac{11}{144} V_{31} + \frac{11}{24} V_{32} \end{pmatrix}$$

$$+ n_f \begin{pmatrix} \frac{7}{54} - \frac{7}{36}V_{11} & \frac{1}{18} - \frac{1}{12}V_{11} + \frac{1}{2}V_{12} \\ \frac{1}{9} - \frac{1}{6}V_{11} & -\frac{1}{27} + \frac{1}{18}V_{11} - \frac{1}{3}V_{12} \end{pmatrix}, \tag{C.28}$$

where V_{ij} denote the entries of the matrix V as discussed in Section 5.1. The matrix elements of V are related to the ϵ^2 terms in the definition of the evanescent operators via Equation (5.41).

The transformation rule for the Wilson coefficients is obtained by the rotation matrix R of the physical operators and the finite renormalization matrices $Z_{QQ}^{(i,0)}$:

$$\vec{C}(\mu_b) = \vec{C}'(\mu_b)R^{-1}\left[1 + \frac{\alpha_s}{4\pi}Z_{QQ}^{(1,0)} + \left(\frac{\alpha_s}{4\pi}\right)^2 Z_{QQ}^{(2,0)}\right], \tag{C.29}$$

while the ADMs transform in the following way [28]

$$\begin{aligned}
\gamma^{(0)} &= R\gamma'^{(0)}R^{-1}, \\
\gamma^{(1)} &= R\gamma'^{(1)}R^{-1} - \left[Z_{QQ}^{(1,0)}, \gamma^{(0)}\right] - 2\beta_0 Z^{(1,0)}, \\
\gamma^{(2)} &= R\gamma'^{(2)}R^{-1} - \left[Z_{QQ}^{(2,0)}, \gamma^{(0)}\right] - \left[Z_{QQ}^{(1,0)}, \gamma^{(1)}\right] + \left[Z_{QQ}^{(1,0)}, \gamma^{(0)}\right]Z_{QQ}^{(1,0)} \\
&\quad - 4\beta_0 Z_{QQ}^{(2,0)} - 2\beta_1 Z_{QQ}^{(1,0)} + 2\beta_0 \left(Z_{QQ}^{(1,0)}\right)^2.
\end{aligned} \tag{C.30}$$

The transformation of the ADM is needed in Chapter 5.1 where the higher order ϵ coefficients of the evanescent operators of the historical basis are determined.

C.3. Historical basis

The following renormalization matrices are given as 6×6 matrices for the set of operators $\{O_1, O_2, E_1^{(1)}, E_2^{(1)}, E_1^{(2)}, E_2^{(2)}\}$ where the physical operators O_1 and O_2 are defined in the usual way in the historical basis as given in Equation (2.16). The evanescent operators of first and second order are given in Equation (5.35) with the coefficients A_2, B_1 and B_2 of Equation (5.41). For convenience we provide results both for generic number of colours n_c and for $n_c = 3$. The corresponding renormalization constants read at one loop level:

$$Z^{(1,1)} = \begin{pmatrix}
-\frac{3}{n_c} & 3 & -\frac{1}{2n_c} + \frac{n_c}{4} & \frac{1}{4} & 0 & 0 \\
3 & -\frac{3}{n_c} & \frac{1}{2} & -\frac{1}{2n_c} & 0 & 0 \\
0 & 0 & \frac{13}{n_c} - 8n_c & -5 & -\frac{1}{2n_c} + \frac{n_c}{4} & \frac{1}{4} \\
0 & 0 & -13 & \frac{13}{n_c} & \frac{1}{2} & -\frac{1}{2n_c} \\
0 & 0 & \frac{128}{n_c} - 224n_c & 96 & \frac{5}{n_c} + 4n_c & -9 \\
0 & 0 & -288 & \frac{128}{n_c} + 160n_c & 3 & \frac{5}{n_c} - 8n_c
\end{pmatrix}$$

$$
= \begin{pmatrix}
-1 & 3 & \frac{7}{12} & \frac{1}{4} & 0 & 0 \\
3 & -1 & \frac{1}{2} & -\frac{1}{6} & 0 & 0 \\
0 & 0 & -\frac{59}{3} & -5 & \frac{7}{12} & \frac{1}{4} \\
0 & 0 & -13 & \frac{13}{3} & \frac{1}{2} & -\frac{1}{6} \\
0 & 0 & -\frac{1888}{3} & 96 & \frac{41}{3} & -9 \\
0 & 0 & -288 & \frac{1568}{3} & 3 & -\frac{67}{3}
\end{pmatrix},
\tag{C.31}
$$

$$
Z^{(1,0)} = \begin{pmatrix}
0 & 0 & 0 & 0 & 0 & 0 \\
0 & 0 & 0 & 0 & 0 & 0 \\
\frac{48}{n_c} & -48 & 0 & 0 & 0 & 0 \\
-24 & \frac{48}{n_c} - 24n_c & 0 & 0 & 0 & 0 \\
\frac{1536}{n_c} & -1536 & 0 & 0 & 0 & 0 \\
-768 & \frac{1536}{n_c} - 768n_c & 0 & 0 & 0 & 0
\end{pmatrix}
$$

$$
= \begin{pmatrix}
0 & 0 & 0 & 0 & 0 & 0 \\
0 & 0 & 0 & 0 & 0 & 0 \\
16 & -48 & 0 & 0 & 0 & 0 \\
-24 & -56 & 0 & 0 & 0 & 0 \\
512 & -1536 & 0 & 0 & 0 & 0 \\
-768 & -1792 & 0 & 0 & 0 & 0
\end{pmatrix}.
\tag{C.32}
$$

At two loop level we obtain:

$$
Z^{(2,2)} = \begin{pmatrix}
10 + \frac{9}{2n_c^2} & -\frac{9}{n_c} - \frac{11n_c}{2} & 79/24 - \frac{5}{2n_c^2} - \frac{35n_c^2}{24} & \frac{7}{4n_c} - \frac{13n_c}{12} & -\frac{1}{16} + \frac{1}{8n_c^2} + \frac{n_c^2}{32} & -\frac{1}{8n_c} + \frac{n_c}{32} \\
-\frac{9}{n_c} - \frac{11n_c}{2} & 10 + \frac{9}{2n_c^2} & \frac{5}{n_c} - \frac{61n_c}{24} & \frac{1}{24} - \frac{5}{2n_c^2} & -\frac{1}{4n_c} + \frac{n_c}{16} & \frac{1}{16} + \frac{1}{8n_c^2} \\
0 & 0 & -\frac{178}{3} + \frac{105}{2n_c^2} + \frac{56n_c^2}{3} & -\frac{73}{n_c} + \frac{367n_c}{6} & \frac{79}{24} - \frac{9}{2n_c^2} - \frac{23n_c^2}{24} & \frac{23}{4n_c} - \frac{43n_c}{12} \\
0 & 0 & -\frac{65}{n_c} + \frac{119n_c}{6} & -\frac{22}{3} + \frac{105}{2n_c^2} & \frac{7}{n_c} - \frac{37n_c}{24} & -\frac{23}{24} - \frac{9}{2n_c^2} \\
0 & 0 & -\frac{3392}{3} + \frac{640}{n_c^2} + \frac{848n_c^2}{3} & -\frac{416}{n_c} + 624n_c & \frac{364}{3} - \frac{39}{2n_c^2} - \frac{166n_c^2}{3} & -\frac{109}{n_c} + \frac{125n_c}{2} \\
0 & 0 & -\frac{1312}{n_c} + 304n_c & \frac{3904}{3} + \frac{640}{n_c^2} - \frac{2800n_c^2}{3} & \frac{175}{n_c} - \frac{127n_c}{2} & -\frac{416}{3} - \frac{39}{2n_c^2} + \frac{140n_c^2}{3}
\end{pmatrix}
$$

$$+ n_f \begin{pmatrix} -\frac{1}{n_c} & 1 & -\frac{1}{6n_c} + \frac{n_c}{12} & \frac{1}{12} & 0 & 0 \\ 1 & -\frac{1}{n_c} & \frac{1}{6} & -\frac{1}{6n_c} & 0 & 0 \\ 0 & 0 & \frac{13}{3n_c} - \frac{8n_c}{3} & -\frac{5}{3} & -\frac{1}{6n_c} + \frac{n_c}{12} & \frac{1}{12} \\ 0 & 0 & -\frac{13}{3} & \frac{13}{3n_c} & \frac{1}{6} & -\frac{1}{6n_c} \\ 0 & 0 & \frac{128}{3n_c} - \frac{224n_c}{3} & 32 & \frac{5}{3n_c} + \frac{4n_c}{3} & -3 \\ 0 & 0 & -96 & \frac{128}{3n_c} + \frac{160n_c}{3} & 1 & \frac{5}{3n_c} - \frac{8n_c}{3} \end{pmatrix}$$

$$= \begin{pmatrix} \frac{21}{2} & -\frac{39}{2} & -\frac{91}{9} & -\frac{8}{3} & \frac{67}{288} & \frac{5}{96} \\ -\frac{39}{2} & \frac{21}{2} & -\frac{143}{24} & -\frac{17}{72} & \frac{5}{48} & \frac{11}{144} \\ 0 & 0 & \frac{229}{2} & \frac{955}{6} & -\frac{35}{6} & -\frac{53}{6} \\ 0 & 0 & \frac{227}{6} & -\frac{3}{2} & -\frac{55}{24} & -\frac{35}{24} \\ 0 & 0 & \frac{13360}{9} & \frac{5200}{3} & -\frac{2273}{6} & \frac{907}{6} \\ 0 & 0 & \frac{1424}{3} & -\frac{63248}{9} & -\frac{793}{6} & \frac{1675}{6} \end{pmatrix}$$

$$+ n_f \begin{pmatrix} -\frac{1}{3} & 1 & \frac{7}{36} & \frac{1}{12} & 0 & 0 \\ 1 & -\frac{1}{3} & \frac{1}{6} & -\frac{1}{18} & 0 & 0 \\ 0 & 0 & -\frac{59}{9} & -\frac{5}{3} & \frac{7}{36} & \frac{1}{12} \\ 0 & 0 & -\frac{13}{3} & \frac{13}{9} & \frac{1}{6} & -\frac{1}{18} \\ 0 & 0 & -\frac{1888}{9} & 32 & \frac{41}{9} & -3 \\ 0 & 0 & -96 & \frac{1568}{9} & 1 & -\frac{67}{9} \end{pmatrix} . \tag{C.33}$$

$$Z^{(2,1)} = \left(\begin{array}{cccc} \frac{7}{6} - \frac{153}{8n_c^2} & \frac{111}{4n_c} - \frac{235n_c}{24} & -\frac{439}{144} + \frac{39}{16n_c^2} + \frac{47n_c^2}{36} & -\frac{1}{n_c} + \frac{11n_c}{36} \\ \frac{111}{4n_c} - \frac{19n_c}{24} & -\frac{47}{6} - \frac{153}{8n_c^2} & -\frac{53}{8n_c} + \frac{103n_c}{36} & \frac{191}{144} + \frac{39}{16n_c^2} \\ -196 - \frac{144}{n_c^2} & \frac{288}{n_c} + 52n_c & -\frac{197}{18} + \frac{47}{8n_c^2} - \frac{43n_c^2}{9} & \frac{175}{4n_c} - \frac{2441n_c}{72} \\ \frac{216}{n_c} + 8n_c & -124 - \frac{144}{n_c^2} + 44n_c^2 & -\frac{153}{4n_c} - \frac{1657n_c}{72} & \frac{865}{18} + \frac{47}{8n_c^2} + \frac{22n_c^2}{3} \\ -3968 & 3968n_c & -\frac{14564}{9} + \frac{1296}{n_c^2} + \frac{5084n_c^2}{9} & -\frac{912}{n_c} + \frac{2008n_c}{3} \\ \frac{2304}{n_c} + 1408n_c & -6272 + 2560n_c^2 & -\frac{2128}{n_c} - 1180n_c & \frac{7828}{9} + \frac{1296}{n_c^2} + \frac{10280n_c^2}{9} \end{array} \right.$$

$$\left. \begin{array}{cc} \frac{7}{128} - \frac{7}{64n_c^2} - \frac{n_c^2}{128} & \frac{7}{64n_c} - \frac{3n_c}{64} \\ \frac{7}{32n_c} - \frac{7n_c}{128} & -\frac{7}{128} - \frac{7}{64n_c^2} \\ -\frac{205}{144} + \frac{31}{16n_c^2} + \frac{29n_c^2}{36} & -\frac{9}{4n_c} + \frac{67n_c}{72} \\ -\frac{37}{8n_c} + \frac{215n_c}{72} & -\frac{43}{144} + \frac{31}{16n_c^2} \\ -\frac{1430}{9} + \frac{79}{8n_c^2} + \frac{1087n_c^2\{18}{} & \frac{927}{4n_c} - \frac{1145n_c}{8} \\ -\frac{985}{4n_c} + \frac{995n_c}{8} & \frac{1036}{9} + \frac{79}{8n_c^2} - \frac{28n_c^2}{9} \end{array} \right)$$

$$
+ n_f \begin{pmatrix}
-\frac{1}{6n_c} & \frac{1}{6} & \frac{1}{36n_c} - \frac{n_c}{72} & -\frac{1}{72} & 0 & 0 \\
\frac{1}{6} & -\frac{1}{6n_c} & -\frac{1}{36} & \frac{1}{36n_c} & 0 & 0 \\
\frac{16}{n_c} & -16 & -\frac{43}{18n_c} + \frac{22n_c}{9} & -\frac{1}{18} & \frac{1}{36n_c} - \frac{n_c}{72} & -\frac{1}{72} \\
-8 & \frac{16}{n_c} - 8n_c & \frac{67}{18} & -\frac{43}{18n_c} - \frac{4n_c}{3} & -\frac{1}{36} & \frac{1}{36n_c} \\
\frac{512}{n_c} & -512 & -\frac{400}{9n_c} + \frac{520n_c}{9} & -\frac{40}{3} & -\frac{23}{18n_c} + \frac{25n_c}{9} & -\frac{3}{2} \\
-256 & \frac{512}{n_c} - 256n_c & 80 & -\frac{400}{9n_c} - \frac{320n_c}{9} & \frac{7}{2} & -\frac{23}{18n_c} - \frac{20n_c}{9}
\end{pmatrix}
$$

$$
= \begin{pmatrix}
-\frac{23}{24} & -\frac{161}{8} & \frac{323}{36} & \frac{7}{12} & -\frac{1}{36} & -\frac{5}{48} \\
\frac{55}{8} & -\frac{239}{24} & \frac{51}{8} & \frac{115}{72} & -\frac{35}{384} & -\frac{77}{1152} \\
-212 & 252 & -\frac{1279}{24} & -\frac{697}{8} & \frac{145}{24} & \frac{49}{24} \\
96 & 256 & -\frac{1963}{24} & \frac{2753}{24} & \frac{89}{12} & -\frac{1}{12} \\
-3968 & 11904 & \frac{32488}{9} & 1704 & \frac{9257}{24} & -\frac{2817}{8} \\
4992 & 16768 & -\frac{12748}{3} & \frac{101644}{9} & \frac{6985}{24} & \frac{2117}{24}
\end{pmatrix}
$$

$$
+ n_f \begin{pmatrix}
-\frac{1}{18} & \frac{1}{6} & -\frac{7}{216} & -\frac{1}{72} & 0 & 0 \\
\frac{1}{6} & -\frac{1}{18} & -\frac{1}{36} & \frac{1}{108} & 0 & 0 \\
\frac{16}{3} & -16 & \frac{353}{54} & -\frac{1}{18} & -\frac{7}{216} & -\frac{1}{72} \\
-8 & -\frac{56}{3} & \frac{67}{18} & -\frac{259}{54} & -\frac{1}{36} & \frac{1}{108} \\
\frac{512}{3} & -512 & \frac{4280}{27} & -\frac{40}{3} & \frac{427}{54} & -\frac{3}{2} \\
-256 & -\frac{1792}{3} & 80 & -\frac{3280}{27} & \frac{7}{2} & -\frac{383}{54}
\end{pmatrix} ,
\tag{C.34}
$$

$$
Z^{(2,0)} = \begin{pmatrix}
0 & 0 & 0 & 0 & 0 & 0 \\
0 & 0 & 0 & 0 & 0 & 0 \\
-\frac{201038}{345} + \frac{259746}{115n_c^2} + \frac{1164n_c^2}{5} & -\frac{804348}{115n_c} + \frac{1305248n_c}{345} & 0 & 0 & 0 & 0 \\
-\frac{4560}{n_c} + \frac{134944n_c}{345} & \frac{568318}{345} + \frac{674466}{115n_c^2} - \frac{188n_c^2}{3} & 0 & 0 & 0 & 0 \\
-\frac{24124528}{345} + \frac{896}{n_c^2} + \frac{942832n_c^2}{115} & \frac{2878976}{23n_c} - \frac{12555488n_c}{345} & 0 & 0 & 0 & 0 \\
-\frac{706880}{23n_c} - \frac{10386928n_c}{345} & \frac{61042928}{345} + \frac{896}{n_c^2} - \frac{3448256n_c^2}{69} & 0 & 0 & 0 & 0
\end{pmatrix}
$$

$$
+ n_f \begin{pmatrix}
0 & 0 & 0 & 0 & 0 & 0 \\
0 & 0 & 0 & 0 & 0 & 0 \\
\frac{15608}{345n_c} - \frac{2448n_c}{115} & -\frac{25544}{345} & 0 & 0 & 0 & 0 \\
-\frac{15148}{345} & \frac{50168}{345n_c} - \frac{4n_c}{3} & 0 & 0 & 0 & 0 \\
-\frac{404288}{345n_c} - \frac{42848n_c}{115} & \frac{1154912}{345} & 0 & 0 & 0 & 0 \\
\frac{56192}{69} & -\frac{957248}{345n_c} + \frac{883648n_c}{345} & 0 & 0 & 0 & 0
\end{pmatrix}
$$

$$
= \begin{pmatrix}
0 & 0 & 0 & 0 & 0 & 0 \\
0 & 0 & 0 & 0 & 0 & 0 \\
\frac{202796}{115} - \frac{50488 n_f}{1035} & \frac{1037132}{115} - \frac{25544 n_f}{345} & 0 & 0 & 0 & 0 \\
-\frac{15148 n_f}{345} - \frac{39856}{115} & \frac{46028 n_f}{1035} + \frac{39904}{23} & 0 & 0 & 0 & 0 \\
\frac{4098848}{1035} - \frac{1561184 n_f}{1035} & \frac{1154912 n_f}{345} - \frac{1011808}{15} & 0 & 0 & 0 & 0 \\
\frac{56192 n_f}{69} - \frac{34695184}{345} & \frac{6995584 n_f}{1035} - \frac{282282736}{1035} & 0 & 0 & 0 & 0
\end{pmatrix} .
\tag{C.35}
$$

For $n_c = 3$ the corresponding anomalous dimension matrix reads

$$
\gamma^{(0)} = \begin{pmatrix} -2 & 6 \\ 6 & -2 \end{pmatrix} ,
$$

$$
\gamma^{(1)} = \begin{pmatrix} -\frac{21}{2} & \frac{7}{2} \\ \frac{7}{2} & -\frac{21}{2} \end{pmatrix} + n_f \begin{pmatrix} -\frac{2}{9} & \frac{2}{3} \\ \frac{2}{3} & -\frac{2}{9} \end{pmatrix} ,
$$

$$
\gamma^{(2)} = \begin{pmatrix} \frac{1340209}{460} & \frac{401635}{276} - 672\zeta_3 \\ \frac{401635}{276} - 672\zeta_3 & \frac{1340209}{460} \end{pmatrix} + n_f \begin{pmatrix} -\frac{1190291}{6210} + \frac{80\zeta_3}{3} & -\frac{16657}{414} - 80\zeta_3 \\ -\frac{16657}{414} - 80\zeta_3 & -\frac{1190291}{6210} \frac{80\zeta_3}{3} \end{pmatrix}
$$

$$
+ n_f^2 \begin{pmatrix} \frac{130}{81} & -\frac{130}{27} \\ -\frac{130}{27} & \frac{130}{81} \end{pmatrix} .
\tag{C.36}
$$

C.4. Historical basis with penguin operators

In the calculation of the penguin like topology contributions to the decay channels $b \to c\bar{c}s$ and $b \to u\bar{u}d$, also the renormalization constants including penguin operators and their evanescent operators in the historical basis are needed. We obtain the needed renormalization constants by transforming their counterparts in the CMM basis to the historical basis with an appropriate choice of transformation constants as introduced in Section 2.2.3.

It turns out, that for the transformation including the penguin operators, we have to introduce four additional evanescent operators in the CMM basis at one-loop level [28]

$$
E_5'^{(1)} = (\bar{q}_1 \gamma^{\mu_1} P_L b) \sum_q (\bar{q} \gamma_{\mu_1} \gamma_5 q) - \frac{5}{3} O_3' + \frac{1}{6} O_5' ,
$$

$$
E_6'^{(1)} = (\bar{q}_1 \gamma^{\mu_1} T^a P_L b) \sum_q (\bar{q} \gamma_{\mu_1} T^a \gamma_5 q) - \frac{5}{3} O_4' + \frac{1}{6} O_6' ,
$$

$$
E_7'^{(1)} = (\bar{q}_1 \gamma^{\mu_1 \mu_2 \mu_3} P_L b) \sum_q (\bar{q} \gamma_{\mu_1 \mu_2 \mu_3} \gamma_5 q) - \frac{32}{3} O_3' + \frac{5}{3} O_5' ,
$$

$$
E_8'^{(1)} = (\bar{q}_1 \gamma^{\mu_1 \mu_2 \mu_3} T^a P_L b) \sum_q (\bar{q} \gamma_{\mu_1 \mu_2 \mu_3} T^a \gamma_5 q) - \frac{32}{3} O_4' + \frac{5}{3} O_6' ,
\tag{C.37}
$$

and two-loop level:

$$
E_5'^{(2)} = (\bar{q}_1 \gamma^{\mu_1 \cdots \mu_5} P_L b) \sum_q (\bar{q} \gamma_{\mu_1 \cdots \mu_5} \gamma_5 q) - \frac{320}{3} O_3' + \frac{68}{3} O_5' ,
$$

$$E_6'^{(2)} = (\bar{q}_1 \gamma^{\mu_1 \dots \mu_5} T^a P_L b) \sum_q (\bar{q} \gamma_{\mu_1 \dots \mu_5} T^a \gamma_5 q) - \frac{320}{3} O_4' + \frac{68}{3} O_6' \,,$$

$$E_7'^{(2)} = (\bar{q}_1 \gamma^{\mu_1 \dots \mu_7} P_L b) \sum_q (\bar{q} \gamma_{\mu_1 \dots \mu_7} \gamma_5 q) - \frac{4352}{3} O_3' + \frac{1040}{3} O_5' \,,$$

$$E_8'^{(2)} = (\bar{q}_1 \gamma^{\mu_1 \dots \mu_7} T^a P_L b) \sum_q (\bar{q} \gamma_{\mu_1 \dots \mu_7} T^a \gamma_5 q) - \frac{4352}{3} O_4' + \frac{1040}{3} O_6' \,, \tag{C.38}$$

These additional evanescent operators are not needed as counterterms in the basis of operators defined in Section 2.2.2. However, linear combinations of them will be part of the physical and evanescent operators in the historical basis after the transformation. The operator basis in the CMM basis then reads

$$\vec{Q}' = \{ O_1', O_2', O_3', O_4', O_5', O_6' \} \,,$$
$$\vec{E}' = \{ E_1'^{(1)}, \dots, E_8'^{(1)}, E_1'^{(2)}, \dots, E_8'^{(2)} \} \,. \tag{C.39}$$

In the historical basis we have the the set of operators [28]

$$\vec{Q} = \{ O_1, O_2, O_3, O_4, O_5, O_6 \} \,,$$
$$\vec{E}' = \{ E_1^{(1)}, \dots, E_6^{(1)}, E_1^{(2)}, \dots, E_6^{(2)}, E_3'^{(2)}, E_4'^{(2)}, E_7'^{(2)}, E_8'^{(2)} \} \,, \tag{C.40}$$

with the un-primed operators defined in Equations (2.16), (2.17), (2.19) and (2.20). The operators $\{ E_3'^{(2)}, E_4'^{(2)}, E_7'^{(2)}, E_8'^{(2)} \}$ are in principle not necessary in the historical basis but kept here for completeness.

The transformation matrices that transform the operators of the CMM basis given in Equation (C.39) to the operators in the historical basis given in Equation (C.40) are extracted from Ref. [28] and read

$$R = \begin{pmatrix} 2 & \frac{1}{3} & 0 & 0 & 0 & 0 \\ 0 & 1 & 0 & 0 & 0 & 0 \\ 0 & 0 & -\frac{1}{3} & 0 & \frac{1}{12} & 0 \\ 0 & 0 & -\frac{1}{9} & -\frac{2}{3} & \frac{1}{36} & \frac{1}{6} \\ 0 & 0 & \frac{4}{3} & 0 & -\frac{1}{12} & 0 \\ 0 & 0 & \frac{4}{9} & \frac{8}{3} & -\frac{1}{36} & -\frac{1}{6} \end{pmatrix} \,,$$

$$M = \begin{pmatrix}
2 & \frac{1}{3} & 0 & 0 & 0 & 0 & 0 & 0 & 0 & 0 & 0 & 0 & 0 & 0 & 0 & 0 \\
0 & 1 & 0 & 0 & 0 & 0 & 0 & 0 & 0 & 0 & 0 & 0 & 0 & 0 & 0 & 0 \\
0 & 0 & 0 & 0 & 8 & 0 & -\frac{1}{2} & 0 & 0 & 0 & 0 & 0 & 0 & 0 & 0 & 0 \\
0 & 0 & 0 & 0 & \frac{8}{3} & 16 & -\frac{1}{6} & -1 & 0 & 0 & 0 & 0 & 0 & 0 & 0 & 0 \\
0 & 0 & 0 & 0 & -2 & 0 & \frac{1}{2} & 0 & 0 & 0 & 0 & 0 & 0 & 0 & 0 & 0 \\
0 & 0 & 0 & 0 & -\frac{2}{3} & -4 & \frac{1}{6} & 1 & 0 & 0 & 0 & 0 & 0 & 0 & 0 & 0 \\
40 & \frac{20}{3} & 0 & 0 & 0 & 0 & 0 & 0 & 2 & \frac{1}{3} & 0 & 0 & 0 & 0 & 0 & 0 \\
0 & 20 & 0 & 0 & 0 & 0 & 0 & 0 & 0 & 1 & 0 & 0 & 0 & 0 & 0 & 0 \\
0 & 0 & \frac{1}{2} & 0 & 128 & 0 & 0 & 0 & 0 & 0 & 0 & 0 & -\frac{1}{2} & 0 & 0 & 0 \\
0 & 0 & \frac{1}{6} & 1 & \frac{128}{3} & 256 & 0 & 0 & 0 & 0 & 0 & 0 & -\frac{1}{6} & -1 & 0 & 0 \\
0 & 0 & \frac{1}{2} & 0 & -8 & 0 & 0 & 0 & 0 & 0 & 0 & 0 & \frac{1}{2} & 0 & 0 & 0 \\
0 & 0 & \frac{1}{6} & 1 & -\frac{8}{3} & -16 & 0 & 0 & 0 & 0 & 0 & 0 & \frac{1}{6} & 1 & 0 & 0 \\
0 & 0 & 0 & 0 & 0 & 0 & 0 & 0 & 0 & 0 & 1 & 0 & 0 & 0 & 0 & 0 \\
0 & 0 & 0 & 0 & 0 & 0 & 0 & 0 & 0 & 0 & 0 & 1 & 0 & 0 & 0 & 0 \\
0 & 0 & 0 & 0 & 0 & 0 & 0 & 0 & 0 & 0 & 0 & 0 & 0 & 0 & 1 & 0 \\
0 & 0 & 0 & 0 & 0 & 0 & 0 & 0 & 0 & 0 & 0 & 0 & 0 & 0 & 0 & 1
\end{pmatrix},$$

$$U = \begin{pmatrix}
4 & 0 & 0 & 0 & 0 & 0 \\
0 & 4 & 0 & 0 & 0 & 0 \\
0 & 0 & -112 & 0 & 16 & 0 \\
0 & 0 & 0 & -112 & 0 & 16 \\
0 & 0 & -\frac{10}{9} & 0 & \frac{1}{9} & 0 \\
0 & 0 & 0 & -\frac{10}{9} & 0 & \frac{1}{9} \\
0 & 0 & -\frac{136}{9} & 0 & \frac{10}{9} & 0 \\
0 & 0 & 0 & -\frac{136}{9} & 0 & \frac{10}{9} \\
144 & 0 & 0 & 0 & 0 & 0 \\
0 & 144 & 0 & 0 & 0 & 0 \\
0 & 0 & 0 & 0 & 0 & 0 \\
0 & 0 & 0 & 0 & 0 & 0 \\
0 & 0 & -\frac{2224}{9} & 0 & \frac{64}{9} & 0 \\
0 & 0 & 0 & -\frac{2224}{9} & 0 & \frac{64}{9} \\
0 & 0 & 0 & 0 & 0 & 0 \\
0 & 0 & 0 & 0 & 0 & 0
\end{pmatrix},$$

$$W = \begin{pmatrix}
0 & 0 & 0 & 0 & 0 & 0 & 0 & 0 & 0 & 0 & 0 & 0 & 0 & 0 & 0 & 0 \\
0 & 0 & 0 & 0 & 0 & 0 & 0 & 0 & 0 & 0 & 0 & 0 & 0 & 0 & 0 & 0 \\
0 & 0 & 0 & 0 & 0 & 0 & 0 & 0 & 0 & 0 & 0 & 0 & 0 & 0 & 0 & 0 \\
0 & 0 & 0 & 0 & 0 & 0 & 0 & 0 & 0 & 0 & 0 & 0 & 0 & 0 & 0 & 0 \\
0 & 0 & 0 & 0 & -6 & 0 & 0 & 0 & 0 & 0 & 0 & 0 & 0 & 0 & 0 & 0 \\
0 & 0 & 0 & 0 & 0 & -6 & 0 & 0 & 0 & 0 & 0 & 0 & 0 & 0 & 0 & 0
\end{pmatrix}, \tag{C.41}$$

With these transformation matrices we can now transform the renormalization constants given in the CMM basis, taken from Ref. [28], to the historical basis according to Equation (C.21). Note that at NNLO we only want to consider current-current operators. In order to renormalize such diagrams, we need the renormalization constants that mix penguin and evanescent operators to current-current operators to two-loop order. This corresponds to the first two lines of $Z_{QQ}^{(2,n)}$ and $Z_{QE}^{(2,n)}$.

The mixing matrix for physical operators read (for $n_c = 3$)

$$
Z_{QQ}^{(1,1)} = \begin{pmatrix}
-1 & 3 & 0 & 0 & 0 & 0 \\
3 & -1 & -\frac{1}{9} & \frac{1}{3} & -\frac{1}{9} & \frac{1}{3} \\
0 & 0 & -\frac{11}{9} & \frac{11}{3} & -\frac{2}{9} & \frac{2}{3} \\
0 & 0 & 3 - \frac{n_f}{9} & -1 + \frac{n_f}{3} & -\frac{n_f}{9} & \frac{n_f}{3} \\
0 & 0 & 0 & 0 & 1 & -3 \\
0 & 0 & -\frac{n_f}{9} & \frac{n_f}{3} & -\frac{n_f}{9} & -8 + \frac{n_f}{3}
\end{pmatrix},
\tag{C.42}
$$

$$
Z_{QQ}^{(2,2)} = \begin{pmatrix}
\frac{21}{2} - \frac{n_f}{3} & -\frac{39}{2} + n_f & \frac{-1}{6} & \frac{1}{2} & -\frac{1}{6} & \frac{1}{2} \\
-\frac{39}{2} + n_f & \frac{21}{2} - \frac{n_f}{3} & \frac{100}{81} - \frac{2n_f}{27} & -\frac{64}{27} + \frac{2n_f}{9} & \frac{101}{162} - \frac{2n_f}{27} & -\frac{173}{54} + \frac{2n_f}{9} \\
* & * & * & * & * & * \\
* & * & * & * & * & * \\
* & * & * & * & * & * \\
* & * & * & * & * & *
\end{pmatrix},
\tag{C.43}
$$

$$
Z_{QQ}^{(2,1)} = \begin{pmatrix}
-\frac{13}{8} - \frac{n_f}{18} & -\frac{209}{8} + \frac{n_f}{6} & \frac{83}{36} & -\frac{11}{12} & -\frac{61}{36} & -\frac{11}{12} \\
\frac{87}{8} + \frac{n_f}{6} & -\frac{133}{8} - \frac{n_f}{18} & -\frac{137}{486} & \frac{713}{162} & -\frac{316}{243} & \frac{244}{81} \\
* & * & * & * & * & * \\
* & * & * & * & * & * \\
* & * & * & * & * & * \\
* & * & * & * & * & *
\end{pmatrix},
\tag{C.44}
$$

In addition we need the renormalization constants that mix evanescent operators and physical operators which are given by

$$
Z_{QE}^{(1,1)} = \begin{pmatrix}
\frac{7}{12} & \frac{1}{4} & 0 & 0 & 0 & 0 & 0 & 0 & 0 & 0 & 0 & 0 & 0 & 0 & 0 & 0 \\
\frac{1}{2} & -\frac{1}{6} & 0 & 0 & 0 & 0 & 0 & 0 & 0 & 0 & 0 & 0 & 0 & 0 & 0 & 0 \\
0 & 0 & -\frac{1}{6} & \frac{1}{2} & 0 & 0 & 0 & 0 & 0 & 0 & 0 & 0 & 0 & 0 & 0 & 0 \\
0 & 0 & \frac{1}{4} & \frac{7}{12} & 0 & 0 & 0 & 0 & 0 & 0 & 0 & 0 & 0 & 0 & 0 & 0 \\
0 & 0 & 0 & 0 & -\frac{1}{6} & \frac{1}{2} & 0 & 0 & 0 & 0 & 0 & 0 & 0 & 0 & 0 & 0 \\
0 & 0 & 0 & 0 & \frac{1}{4} & \frac{7}{12} & 0 & 0 & 0 & 0 & 0 & 0 & 0 & 0 & 0 & 0
\end{pmatrix},
\tag{C.45}
$$

$$Z_{QE}^{(2,2)} = \begin{pmatrix} -\frac{91}{9} + \frac{7n_f}{36} & -\frac{8}{3} + \frac{n_f}{12} & 0 & 0 & 0 & 0 & \frac{67}{288} & \frac{5}{96} & 0 & 0 & 0 & 0 & 0 & 0 & 0 & 0 \\ -\frac{143}{24} + \frac{n_f}{6} & -\frac{17}{72} - \frac{n_f}{18} & \frac{11}{216} & \frac{5}{72} & \frac{11}{216} & \frac{5}{72} & \frac{5}{48} & \frac{11}{144} & 0 & 0 & 0 & 0 & 0 & 0 & 0 & 0 \\ * & * & * & * & * & * & * & * & * & * & * & * & * & * & * & * \\ * & * & * & * & * & * & * & * & * & * & * & * & * & * & * & * \\ * & * & * & * & * & * & * & * & * & * & * & * & * & * & * & * \\ * & * & * & * & * & * & * & * & * & * & * & * & * & * & * & * \end{pmatrix},$$

$$\tag{C.46}$$

$$Z_{QE}^{(2,1)} = \begin{pmatrix} \frac{64}{9} - \frac{7n_f}{216} & \frac{1}{6} - \frac{n_f}{72} & \frac{1}{3} & 0 & \frac{1}{3} & 0 & -\frac{1}{36} & -\frac{5}{48} & 0 & 0 & 0 & 0 & 0 & 0 & 0 & 0 \\ \frac{133}{24} - \frac{n_f}{36} & \frac{71}{72} + \frac{n_f}{108} & \frac{77}{648} & \frac{35}{216} & \frac{77}{648} & \frac{35}{216} & -\frac{35}{384} & -\frac{77}{1152} & 0 & 0 & 0 & 0 & 0 & 0 & 0 & 0 \\ * & * & * & * & * & * & * & * & * & * & * & * & * & * & * & * \\ * & * & * & * & * & * & * & * & * & * & * & * & * & * & * & * \\ * & * & * & * & * & * & * & * & * & * & * & * & * & * & * & * \\ * & * & * & * & * & * & * & * & * & * & * & * & * & * & * & * \end{pmatrix}.$$

$$\tag{C.47}$$

The quantity $(r_1)_{QQ}$ (see Equation (C.26)) is given by

$$(r_1)_{QQ} = Z_{QQ}^{(1,0)} = \begin{pmatrix} -\frac{7}{3} & -1 & 0 & 0 & 0 & 0 \\ -2 & -\frac{2}{3} & 0 & 0 & 0 & 0 \\ 0 & 0 & \frac{178}{27} & -\frac{34}{9} & -\frac{164}{27} & \frac{20}{9} \\ 0 & 0 & 1 - \frac{n_f}{9} & -\frac{25}{3} + \frac{n_f}{3} & -2 - \frac{n_f}{9} & 6 + \frac{n_f}{3} \\ 0 & 0 & -\frac{160}{27} & \frac{16}{9} & \frac{146}{27} & -\frac{2}{9} \\ 0 & 0 & -2 + \frac{n_f}{9} & 6 - \frac{n_f}{3} & 3 + \frac{n_f}{9} & -\frac{11}{3} - \frac{n_f}{3} \end{pmatrix}, \tag{C.48}$$

Since we also need counterterms introduced by diagrams of the order α_s^1 with one insertion of the operator O_8, the first order renormalization constant for the physical operators including O_8 is also required. We obtain for the set of operators $\{O_1, O_2, O_3, O_4, O_5, O_6, O_8\}$:

$$Z_{QQ}^{(1,1)} = \begin{pmatrix} -1 & 3 & 0 & 0 & 0 & 0 & \frac{3}{4} \\ 3 & -1 & -\frac{1}{9} & \frac{1}{3} & -\frac{1}{9} & \frac{1}{3} & \frac{19}{27} \\ 0 & 0 & -\frac{11}{9} & \frac{11}{3} & -\frac{2}{9} & \frac{2}{3} & \frac{152}{27} + \frac{3n_f}{4} \\ 0 & 0 & 3 - \frac{n_f}{9} & -1 + \frac{n_f}{3} & -\frac{n_f}{9} & \frac{n_f}{3} & -\frac{7}{6} + \frac{19n_f}{27} \\ 0 & 0 & 0 & 0 & 1 & -3 & -\frac{20}{9} - \frac{3n_f}{4} \\ 0 & 0 & -\frac{n_f}{9} & \frac{n_f}{3} & -\frac{n_f}{9} & -8 + \frac{n_f}{3} & -\frac{1}{3} - \frac{113n_f}{108} \\ 0 & 0 & 0 & 0 & 0 & 0 & -\frac{19}{3} + \frac{2n_f}{3} \end{pmatrix}. \tag{C.49}$$

C.5. CMM basis

For completeness, we also provide the renormalization constants for the current-current operators and their first and second order evanescent operators $\{O_1', O_2', E_1'^{(1)}, E_2'^{(1)}, E_1'^{(2)}, E_2'^{(2)}\}$.

For $n_c = 3$ the one- and two-loop results are given by

$$
Z'^{(1,1)} = \begin{pmatrix}
-\frac{6}{n_c} & \frac{3}{2} - \frac{3}{2n_c^2} & -\frac{1}{n_c} + \frac{n_c}{4} & \frac{1}{4} - \frac{1}{4n_c^2} & 0 & 0 \\
6 & 0 & 1 & 0 & 0 & 0 \\
0 & 0 & \frac{6}{n_c} - 3n_c & -\frac{3}{2} + \frac{3}{2n_c^2} & -\frac{1}{n_c} + \frac{n_c}{4} & \frac{1}{4} - \frac{1}{4n_c^2} \\
0 & 0 & -6 & 0 & 1 & 0 \\
0 & 0 & 0 & 0 & \frac{22}{n_c} - n_c & -\frac{7}{2} + \frac{7}{2n_c^2} \\
0 & 0 & 0 & 0 & -14 & \frac{8}{n_c} - 8n_c
\end{pmatrix}
$$

$$
= \begin{pmatrix}
-2 & \frac{4}{3} & \frac{5}{12} & \frac{2}{9} & 0 & 0 \\
6 & 0 & 1 & 0 & 0 & 0 \\
0 & 0 & -7 & -\frac{4}{3} & \frac{5}{12} & \frac{2}{9} \\
0 & 0 & -6 & 0 & 1 & 0 \\
0 & 0 & 0 & 0 & \frac{13}{3} & -\frac{28}{9} \\
0 & 0 & 0 & 0 & -14 & -\frac{64}{3}
\end{pmatrix}, \tag{C.50}
$$

$$
Z'^{(1,0)} = \begin{pmatrix}
0 & 0 & 0 & 0 & 0 & 0 \\
0 & 0 & 0 & 0 & 0 & 0 \\
-\frac{24}{n_c} + 24n_c & 12 - \frac{12}{n_c^2} & 0 & 0 & 0 & 0 \\
48 & \frac{24}{n_c} - 24n_c & 0 & 0 & 0 & 0 \\
-\frac{1440}{n_c} + 1440n_c & 720 - \frac{720}{n_c^2} & 0 & 0 & 0 & 0 \\
2880 & \frac{1440}{n_c} - 1440n_c & 0 & 0 & 0 & 0
\end{pmatrix}
$$

$$
= \begin{pmatrix}
0 & 0 & 0 & 0 & 0 & 0 \\
0 & 0 & 0 & 0 & 0 & 0 \\
64 & \frac{32}{3} & 0 & 0 & 0 & 0 \\
48 & -64 & 0 & 0 & 0 & 0 \\
3840 & 640 & 0 & 0 & 0 & 0 \\
2880 & -3840 & 0 & 0 & 0 & 0
\end{pmatrix}, \tag{C.51}
$$

$$
Z'^{(2,2)} = \begin{pmatrix}
\frac{31}{2} + \frac{27}{2n_c^2} & \frac{9}{2n_c^3} - \frac{7}{4n_c} - \frac{11n_c}{4} & \frac{10}{3} - \frac{5n_c^2}{6} & \frac{31}{48n_c} - \frac{31n_c}{48} \\
-\frac{18}{n_c} - 11n_c & \frac{9}{2} - \frac{9}{2n_c^2} & \frac{-31n_c}{12} & 0 \\
0 & 0 & -\frac{49}{2} + \frac{27}{2n_c^2} + 10n_c^2 & \frac{9}{2n_c^3} - \frac{19}{2n_c} + 5n_c \\
0 & 0 & -\frac{18}{n_c} + 20n_c & \frac{9}{2} - \frac{9}{2n_c^2} \\
0 & 0 & 0 & 0 \\
0 & 0 & 0 & 0
\end{pmatrix}
$$

$$
\begin{pmatrix}
-\frac{1}{8}+\frac{3}{8n_c^2}+\frac{n_c^2}{32} & \frac{1}{8n_c^3}-\frac{5}{32n_c}+\frac{n_c}{32} \\
-\frac{1}{2n_c}+\frac{n_c}{8} & \frac{1}{8}-\frac{1}{8n_c^2} \\
\frac{29}{6}-\frac{23}{2n_c^2}-\frac{23n_c^2}{24} & -\frac{7}{2n_c^3}+\frac{277}{48n_c}-\frac{109n_c}{48} \\
\frac{14}{n_c}-\frac{37n_c}{12} & -\frac{5}{2}+\frac{5}{2n_c^2} \\
\frac{529}{6}+\frac{71}{2n_c^2}-\frac{217n_c^2}{6} & -\frac{35}{2n_c^3}-\frac{49}{6n_c}+\frac{77n_c}{3} \\
\frac{70}{n_c}-\frac{196n_c}{3} & -\frac{913}{6}+\frac{211}{2n_c^2}+\frac{140n_c^2}{3}
\end{pmatrix}
$$

$$
+n_f
\begin{pmatrix}
-\frac{2}{n_c} & \frac{1}{2}-\frac{1}{2n_c^2} & -\frac{1}{3n_c}+\frac{n_c}{12} & \frac{1}{12}-\frac{1}{12n_c^2} & 0 & 0 \\
2 & 0 & \frac{1}{3} & 0 & 0 & 0 \\
0 & 0 & \frac{2}{n_c}-n_c & -\frac{1}{2}+\frac{1}{2n_c^2} & -\frac{1}{3n_c}+\frac{n_c}{12} & \frac{1}{12}-\frac{1}{12n_c^2} \\
0 & 0 & -2 & 0 & \frac{1}{3} & 0 \\
0 & 0 & 0 & 0 & \frac{22}{3n_c}-\frac{n_c}{3} & -\frac{7}{6}+\frac{7}{6n_c^2} \\
0 & 0 & 0 & 0 & -\frac{14}{3} & \frac{8}{3n_c}-\frac{8n_c}{3}
\end{pmatrix}
$$

$$
=
\begin{pmatrix}
17 & -\frac{26}{3} & -\frac{25}{6} & -\frac{31}{18} & \frac{19}{96} & \frac{5}{108} \\
-39 & 4 & \frac{-31}{4} & 0 & \frac{5}{24} & \frac{1}{9} \\
0 & 0 & 67 & 12 & -\frac{365}{72} & -\frac{271}{54} \\
0 & 0 & 54 & 4 & -\frac{55}{12} & -\frac{20}{9} \\
0 & 0 & 0 & 0 & -\frac{4201}{18} & \frac{1988}{27} \\
0 & 0 & 0 & 0 & -\frac{518}{3} & \frac{2516}{9}
\end{pmatrix}
$$

$$
+n_f
\begin{pmatrix}
-\frac{2}{3} & \frac{4}{9} & \frac{5}{36} & \frac{2}{27} & 0 & 0 \\
2 & 0 & \frac{1}{3} & 0 & 0 & 0 \\
0 & 0 & -\frac{7}{3} & -\frac{4}{9} & \frac{5}{36} & \frac{2}{27} \\
0 & 0 & -2 & 0 & \frac{1}{3} & 0 \\
0 & 0 & 0 & 0 & \frac{13}{9} & -\frac{28}{27} \\
0 & 0 & 0 & 0 & -\frac{14}{3} & -\frac{64}{9}
\end{pmatrix},
\tag{C.52}
$$

$$
Z'^{(2,1)}=
\begin{pmatrix}
\frac{79}{12} & -\frac{205}{18} & \frac{1531}{288} & -\frac{1}{72} & \frac{1}{384} & -\frac{35}{864} \\
\frac{83}{4} & 3 & \frac{119}{16} & \frac{8}{9} & -\frac{35}{192} & -\frac{7}{72} \\
480 & -304 & \frac{3305}{72} & -\frac{1171}{27} & \frac{157}{36} & \frac{49}{27} \\
1224 & 672 & \frac{449}{6} & \frac{875}{9} & \frac{47}{3} & \frac{17}{6} \\
74880 & -18240 & \frac{94400}{9} & -\frac{37040}{27} & \frac{8849}{36} & -\frac{9103}{54} \\
73440 & 86400 & \frac{20360}{3} & \frac{87040}{9} & \frac{3785}{12} & \frac{1381}{9}
\end{pmatrix}
$$

$$
+ n_f \begin{pmatrix}
\frac{4}{9} & \frac{10}{27} & \frac{5}{216} & -\frac{1}{81} & 0 & 0 \\
\frac{5}{3} & 0 & \frac{1}{18} & 0 & 0 & 0 \\
\frac{64}{3} & \frac{32}{9} & \frac{77}{18} & \frac{10}{9} & -\frac{5}{216} & -\frac{1}{81} \\
16 & -\frac{64}{3} & 5 & -\frac{32}{9} & -\frac{1}{18} & 0 \\
1280 & \frac{640}{3} & \frac{1280}{9} & +\frac{640}{27} & \frac{389}{54} & \frac{146}{81} \\
960 & -1280 & \frac{320}{3} & -\frac{1280}{9} & \frac{7}{9} & -\frac{160}{27}
\end{pmatrix} ,
\tag{C.53}
$$

$$
Z'^{(2,0)} = \begin{pmatrix}
0 & 0 & 0 & 0 & 0 & 0 \\
0 & 0 & 0 & 0 & 0 & 0 \\
\frac{1036}{3} + \frac{160n_f}{9} & \frac{752}{9} + \frac{80n_f}{27} & 0 & 0 & 0 & 0 \\
520 + \frac{40n_f}{3} & -\frac{928}{3} - \frac{160n_f}{9} & 0 & 0 & 0 & 0 \\
12080 + \frac{3200n_f}{3} & \frac{24640}{3} + \frac{1600n_f}{9} & 0 & 0 & 0 & 0 \\
45600 + 800n_f & -22400 - \frac{3200n_f}{3} & 0 & 0 & 0 & 0
\end{pmatrix} .
\tag{C.54}
$$

D. $1/m_b$-suppressed operators

In this Appendix, we list the functions $G_{G,ij}^{(0)}$ and $G_{D,ij}^{(0)}$ for the $1/m_b$-suppressed operators introduced in Equation (6.29). The following expressions are taken from Ref. [47]. The LO coefficients of the chromo-magnetic operator μ_G read

$$G_{G,11}^{(0),\,cud} = -\frac{1}{2}\left(3 - 8\rho^2 + 24\rho^4 \log\rho + 24\rho^4 - 24\rho^6 + 5\rho^8\right),$$

$$G_{G,22}^{(0),\,cud} = G_{G,11}^{(0),\,cud},$$

$$G_{G,12}^{(0),\,cud} = -\frac{1}{2}\left(19 - 56\rho^2 + 24\rho^4 \log\rho + 72\rho^4 - 40\rho^6 + 5\rho^8\right),$$

$$G_{G,11}^{(0),\,ccs} = -\frac{1}{2}\left[\sqrt{1 - 4\rho^2}\left(3 - 10\rho^2 + 10\rho^4 + 60\rho^6\right)\right.$$

$$\left. -24\rho^4\left(1 - 5\rho^4\right)\log\left(\frac{1 + \sqrt{1 - 4\rho^2}}{1 - \sqrt{1 - 4\rho^2}}\right)\right],$$

$$G_{G,22}^{(0),\,ccs} = G_{G,11}^{(0),\,ccs},$$

$$G_{G,12}^{(0),\,ccs} = -\frac{1}{2}\left[\sqrt{1 - 4\rho^2}\left(19 - 2\rho^2 + 58\rho^4 + 60\rho^6\right)\right.$$

$$\left. -24\rho^4\left(2 + \rho^2 - 4\rho^4 - 5\rho^6\right)\log\left(\frac{1 + \sqrt{1 - 4\rho^2}}{1 - \sqrt{1 - 4\rho^2}}\right)\right],$$

$$G_{G,11}^{(0),\,ucs} = -\frac{1}{2}\left(3 - 8\rho^2 + 24\rho^4 \log\rho + 24\rho^4 - 24\rho^6 + 5\rho^8\right),$$

$$G_{G,22}^{(0),\,ucs} = G_{G,11}^{(0),\,ucs},$$

$$G_{G,12}^{(0),\,ucs} = -\frac{1}{2}\left(19 + 16\rho^2 + 24\rho^2\left(\rho^2 + 4\right)\log\rho - 24\rho^4 - 16\rho^6 + 5\rho^8\right),$$

$$G_{G,11}^{(0),\,uud} = -\frac{3}{2},$$

$$G_{G,22}^{(0),\,uud} = G_{G,11}^{(0),\,uud},$$

$$G_{G,12}^{(0),\,uud} = -\frac{19}{2}. \tag{D.1}$$

For the Darwin operator, they are given by

$$G_{D,22}^{(0),\,cud} = \frac{2}{3}\left(17 + 24\log\rho - 16\rho^2 - 12\rho^4 + 16\rho^6 - 5\rho^8\right),$$

$$G_{D,12}^{(0),\,cud} = \frac{2}{3}\left(-9 + 24\left(1 - 3\rho^4 + \rho^6\right)\log\rho + 24\left(1 - \rho^2\right)^3\log\left(1 - \rho^2\right) + 50\rho^2\right.$$

$$\left. -90\rho^4 + 54\rho^6 - 5\rho^8\right)$$

$$- 8 \left(1 - \rho^2\right)^3 \log\left(\frac{\mu_0^2}{m_b^2}\right),$$

$$G_{D,11}^{(0),\,cud} = \frac{2}{3} \left(1 - \rho^2\right) \left(9 + 11\rho^2 - 24\rho^4 \log\rho - 24\left(1 - \rho^4\right) \log\left(1 - \rho^2\right) - 25\rho^4 + 5\rho^6\right)$$

$$+ 8 \left(1 - \rho^2\right)^2 \left(1 + \rho^2\right) \log\left(\frac{\mu_0^2}{m_b^2}\right),$$

$$G_{D,22}^{(0),\,ccs} = \frac{2}{3} \left[\sqrt{1 - 4\rho^2} \left(17 + 8\rho^2 - 22\rho^4 - 60\rho^6\right) \right.$$

$$\left. -12 \left(1 - \rho^2 - 2\rho^4 + 2\rho^6 + 10\rho^8\right) \log\left(\frac{1 + \sqrt{1 - 4\rho^2}}{\sqrt{1 - \sqrt{1 - 4\rho^2}}}\right) \right],$$

$$G_{D,11}^{(0),\,ccs} = \frac{2}{3} \left[\sqrt{1 - 4\rho^2} \left(-3 + 22\rho^2 - 34\rho^4 - 60\rho^6\right) \right.$$

$$\left. -24\rho^2 \left(1 + \rho^2 + 2\rho^4 + 5\rho^6\right) \log\left(\frac{1 + \sqrt{1 - 4\rho^2}}{1 - \sqrt{1 - 4\rho^2}}\right) \right]$$

$$+ 8\sqrt{1 - 4\rho^2} \log\left(\frac{\mu_0^2}{m_b^2}\right) + 8\left(\mathcal{M}_{112}(\rho,\eta) - \sqrt{1 - 4\rho^2}\log\eta\right)\Big|_{\eta \to 0},$$

$$G_{D,12}^{(0),\,ccs} = \frac{2}{3} \left[\sqrt{1 - 4\rho^2} \left(-45 + 46\rho^2 - 106\rho^4 - 60\rho^6\right) \right.$$

$$\left. +12 \left(1 + 4\rho^4 - 16\rho^6 - 10\rho^8\right) \log\left(\frac{1 + \sqrt{1 - 4\rho^2}}{1 - \sqrt{1 - 4\rho^2}}\right) \right]$$

$$+ 8\sqrt{1 - 4\rho^2} \log\left(\frac{\mu^2}{m_b^2}\right) + 8\left(\mathcal{M}_{112}(\rho,\eta) - \sqrt{1 - 4\rho^2}\log\eta\right)\Big|_{\eta \to 0},$$

$$G_{D,11}^{(0),\,ucs} = \frac{2}{3} \left[-9 + 24 \left(1 - 3\rho^4 + \rho^6\right) \log\rho + 24\left(1 - \rho^2\right)^3 \log\left(1 - \rho^2\right) + 50\rho^2 - 90\rho^4 \right.$$

$$\left. +54\rho^6 - 5\rho^8\right] - 8 \left(1 - \rho^2\right)^3 \log\left(\frac{\mu_0^2}{m_b^2}\right),$$

$$G_{D,22}^{(0),\,ucs} = G_{D,11}^{(0),\,ucs},$$

$$G_{D,12}^{(0),\,ucs} = \frac{2}{3} \left[-41 - 24 \left(2 + 5\rho^2 + 2\rho^4 - 2\rho^6\right) \log\rho - 48 \left(1 - \rho^2\right)^2 \left(1 + \rho^2\right) \log\left(1 - \rho^2\right) \right.$$

$$\left. +26\rho^2 - 18\rho^4 + 38\rho^6 - 5\rho^8\right] + 16 \left(1 - \rho^2\right)^2 \left(1 + \rho^2\right) \log\left(\frac{\mu_0^2}{m_b^2}\right),$$

$$G_{D,11}^{(0),\,uud} = 6 + 8 \log\left(\frac{\mu_0^2}{m_b^2}\right),$$

$$G_{D,22}^{(0),\,uud} = G_{D,11}^{(0),\,uud},$$

$$G_{D,12}^{(0),\,uud} = -\frac{34}{3}. \tag{D.2}$$

with

$$\mathcal{M}_{112}(\rho, \eta) = - \int_{(\sqrt{\rho}+\sqrt{\eta})^2}^{(1-\sqrt{\rho})^2} \frac{\left(t^2 - 2t\,(1+\rho) + (1-\rho)^2\right)(t - \eta + \rho)}{t\sqrt{\left(t^2 - 2t\,(1+\rho) + (1-\rho)^2\right)\left(t^2 - 2t\,(\eta+\rho) + (\eta-\rho)^2\right)}} \mathrm{d}t\ .$$

(D.3)

In Ref. [48] the relation

$$\left[\mathcal{M}_{112}(\rho, \eta) - \sqrt{1 - 4\rho^2}\,\log\eta\right]\bigg|_{\eta\to 0} = 2\left(1 - \rho^2\right)\log\left(\frac{1 + \sqrt{1 - 4\rho^2}}{1 - \sqrt{1 - 4\rho^2}}\right)$$

$$+ \sqrt{1 - 4\rho^2}\left(1 + 4\log\rho - 4\log\sqrt{1 - 4\rho^2}\right),\quad \text{(D.4)}$$

is given, which is used for the implementation of $\mathcal{M}_{112}(\rho, \eta)$.

Bibliography

[1] S. Navas et al. "Review of particle physics". In: *Phys. Rev. D* 110.3 (2024), p. 030001. DOI: 10.1103/PhysRevD.110.030001.

[2] Yosef Nir. "The Mass Ratio m(c) / m(b) in Semileptonic B Decays". In: *Phys. Lett. B* 221 (1989), pp. 184–190. DOI: 10.1016/0370-2693(89)91495-0.

[3] Alexey Pak and Andrzej Czarnecki. "Mass Effects in Muon and Semileptonic $b \rightarrow c$ Decays". In: *Physical Review Letters* 100.24 (June 2008). DOI: 10.1103/physrevlett.100.241807. URL: https://doi.org/10.1103%2Fphysrevlett.100.241807.

[4] Alexey Pak and Andrzej Czarnecki. "Heavy-to-heavy quark decays at next-to-next-to-leading order". In: *Physical Review D* 78.11 (Dec. 2008). ISSN: 1550-2368. DOI: 10.1103/physrevd.78.114015. URL: http://dx.doi.org/10.1103/PhysRevD.78.114015.

[5] Matthew Dowling, Jan H. Piclum, and Andrzej Czarnecki. "Semileptonic decays in the limit of a heavy daughter quark". In: *Physical Review D* 78.7 (Oct. 2008). DOI: 10.1103/physrevd.78.074024. URL: https://doi.org/10.1103%2Fphysrevd.78.074024.

[6] Matteo Fael, Kay Schönwald, and Matthias Steinhauser. "Third order corrections to the semileptonic $b \rightarrow c$ and the muon decays". In: *Phys. Rev. D* 104 (1 July 2021), p. 016003. DOI: 10.1103/PhysRevD.104.016003. URL: https://link.aps.org/doi/10.1103/PhysRevD.104.016003.

[7] Matteo Fael, Kay Schönwald, and Matthias Steinhauser. "A first glance to the kinematic moments of $B \rightarrow Xcl\nu$ at third order". In: *Journal of High Energy Physics* 2022.8 (Aug. 2022). ISSN: 1029-8479. DOI: 10.1007/jhep08(2022)039. URL: http://dx.doi.org/10.1007/JHEP08(2022)039.

[8] Michał Czakon, Andrzej Czarnecki, and Matthew Dowling. "Three-loop corrections to the muon and heavy quark decay rates". In: *Physical Review D* 103.11 (June 2021). DOI: 10.1103/physrevd.103.l111301. URL: https://doi.org/10.1103%2Fphysrevd.103.l111301.

[9] Guido Altarelli and S. Petrarca. "Inclusive beauty decays and the spectator model". In: *Phys. Lett. B* 261 (1991), pp. 303–310. DOI: 10.1016/0370-2693(91)90332-K.

[10] Gerhard Buchalla. "O (alpha-s) QCD corrections to charm quark decay in dimensional regularization with nonanticommuting gamma-5". In: *Nucl. Phys. B* 391 (1993), pp. 501–514. DOI: 10.1016/0550-3213(93)90081-Y.

[11] Emilio Bagan, Patricia Ball, Vladimir M. Braun, and P. Gosdzinsky. "Charm quark mass dependence of QCD corrections to nonleptonic inclusive B decays". In: *Nucl. Phys. B* 432 (1994), pp. 3–38. DOI: `10.1016/0550-3213(94)90591-6`. arXiv: `hep-ph/9408306`.

[12] E. Bagan, Patricia Ball, B. Fiol, and P. Gosdzinsky. "Next-to-leading order radiative corrections to the decay b —> c c s". In: *Phys. Lett. B* 351 (1995), pp. 546–554. DOI: `10.1016/0370-2693(95)00437-P`. arXiv: `hep-ph/9502338`.

[13] Fabian Krinner, Alexander Lenz, and Thomas Rauh. "The inclusive decay $b \to c\bar{c}s$ revisited". In: *Nuclear Physics B* 876.1 (Nov. 2013), pp. 31–54. ISSN: 0550-3213. DOI: `10.1016/j.nuclphysb.2013.07.028`. URL: `http://dx.doi.org/10.1016/j.nuclphysb.2013.07.028`.

[14] Andrzej Czarnecki, Maciej Slusarczyk, and Fyodor V. Tkachov. "Enhancement of the hadronic b quark decays". In: *Phys. Rev. Lett.* 96 (2006), p. 171803. DOI: `10.1103/PhysRevLett.96.171803`. arXiv: `hep-ph/0511004`.

[15] Alexander Lenz, Maria Laura Piscopo, and Aleksey V. Rusov. "Disintegration of beauty: a precision study". In: *Journal of High Energy Physics* 2023.1 (Jan. 2023). ISSN: 1029-8479. DOI: `10.1007/jhep01(2023)004`. URL: `http://dx.doi.org/10.1007/JHEP01(2023)004`.

[16] Yasmine Sara Amhis et al. "Averages of b-hadron, c-hadron, and τ-lepton properties as of 2021". In: *Phys. Rev. D* 107.5 (2023), p. 052008. DOI: `10.1103/PhysRevD.107.052008`. arXiv: `2206.07501 [hep-ex]`.

[17] Johannes Albrecht, Florian Bernlochner, Alexander Lenz, and Aleksey Rusov. "Lifetimes of b-hadrons and mixing of neutral B-mesons: theoretical and experimental status". In: *Eur. Phys. J. ST* 233.2 (2024), pp. 359–390. DOI: `10.1140/epjs/s11734-024-01124-3`. arXiv: `2402.04224 [hep-ph]`.

[18] Kenneth G. Wilson. "Non-Lagrangian Models of Current Algebra". In: *Phys. Rev.* 179 (5 Mar. 1969), pp. 1499–1512. DOI: `10.1103/PhysRev.179.1499`. URL: `https://link.aps.org/doi/10.1103/PhysRev.179.1499`.

[19] K. G. Wilson and W. Zimmermann. "Operator product expansions and composite field operators in the general framework of quantum field theory". In: *Commun. Math. Phys.* 24 (1972), pp. 87–106. DOI: `10.1007/BF01878448`.

[20] Edward Witten. "Short Distance Analysis of Weak Interactions". In: *Nucl. Phys. B* 122 (1977), pp. 109–143. DOI: `10.1016/0550-3213(77)90428-X`.

[21] Wolfhart Zimmermann. "Normal products and the short distance expansion in the perturbation theory of renormalizable interactions". In: *Annals Phys.* 77 (1973), pp. 570–601. DOI: `10.1016/0003-4916(73)90430-2`.

[22] Andrzej J. Buras and Peter H. Weisz. "QCD Nonleading Corrections to Weak Decays in Dimensional Regularization and 't Hooft-Veltman Schemes". In: *Nucl. Phys. B* 333 (1990), pp. 66–99. DOI: `10.1016/0550-3213(90)90223-Z`.

[23] Gerhard Buchalla, Andrzej J. Buras, and Markus E. Lautenbacher. "Weak decays beyond leading logarithms". In: *Reviews of Modern Physics* 68.4 (Oct. 1996), pp. 1125–1244. ISSN: 1539-0756. DOI: `10.1103/revmodphys.68.1125`. URL: `http://dx.doi.org/10.1103/RevModPhys.68.1125`.

[24] Andrzej J. Buras, Matthias Jamin, Markus E. Lautenbacher, and Peter H. Weisz. "Two loop anomalous dimension matrix for $\Delta S = 1$ weak nonleptonic decays I: $O(\alpha_s^2)$". In: *Nucl. Phys. B* 400 (1993), pp. 37–74. DOI: `10.1016/0550-3213(93)90397-8`. arXiv: `hep-ph/9211304`.

[25] Frederick J. Gilman and Mark B. Wise. "Effective Hamiltonian for $\Delta S = 1$ weak nonleptonic decays in the six-quark model". In: *Phys. Rev. D* 20 (9 Nov. 1979), pp. 2392–2407. DOI: `10.1103/PhysRevD.20.2392`. URL: `https://link.aps.org/doi/10.1103/PhysRevD.20.2392`.

[26] Michael E. Peskin and Daniel V. Schroeder. *An Introduction to quantum field theory*. Reading, USA: Addison-Wesley, 1995. ISBN: 978-0-201-50397-5.

[27] Konstantin G. Chetyrkin, Mikolaj Misiak, and Manfred Munz. "$|\Delta F| = 1$ nonleptonic effective Hamiltonian in a simpler scheme". In: *Nucl. Phys. B* 520 (1998), pp. 279–297. DOI: `10.1016/S0550-3213(98)00131-X`. arXiv: `hep-ph/9711280`.

[28] Martin Gorbahn. "QCD and QED anomalous dimension matrix for weak decays at NNLO". Other thesis. Oct. 2003.

[29] Andrzej J. Buras, Martin Gorbahn, Ulrich Haisch, and Ulrich Nierste. "Charm quark contribution to K+ −> pi+ nu anti-nu at next-to-next-to-leading order". In: *JHEP* 11 (2006). [Erratum: JHEP 11, 167 (2012)], p. 002. DOI: `10.1007/JHEP11(2012)167`. arXiv: `hep-ph/0603079`.

[30] Alexander Lenz, Ulrich Nierste, and Gaby Ostermaier. "Penguin diagrams, charmless B decays and the missing charm puzzle". In: *Phys. Rev. D* 56 (1997), pp. 7228–7239. DOI: `10.1103/PhysRevD.56.7228`. arXiv: `hep-ph/9706501`.

[31] Alexander Lenz, Ulrich Nierste, and Gaby Ostermaier. "Determination of the CKM angle gamma and |V(ub) / V(cb)| from inclusive direct CP asymmetries and branching ratios in charmless B decays". In: *Phys. Rev. D* 59 (1999), p. 034008. DOI: `10.1103/PhysRevD.59.034008`. arXiv: `hep-ph/9802202`.

[32] Q. Ho-kim and Xuan-Yem Pham. "Exact One Gluon Corrections for Inclusive Weak Processes". In: *Annals Phys.* 155 (1984), p. 202. DOI: `10.1016/0003-4916(84)90258-6`.

[33] M. B. Voloshin. "QCD radiative enhancement of the decay b −> c anti-c s". In: *Phys. Rev. D* 51 (1995), pp. 3948–3951. DOI: `10.1103/PhysRevD.51.3948`. arXiv: `hep-ph/9409391`.

[34] Manuel Egner, Matteo Fael, Kay Schönwald, and Matthias Steinhauser. "Nonleptonic B-meson decays to next-to-next-to-leading order". In: *JHEP* 10 (2024), p. 144. DOI: `10.1007/JHEP10(2024)144`. arXiv: `2406.19456 [hep-ph]`.

[35] B. Blok and Mikhail A. Shifman. "The Rule of discarding 1/N(c) in inclusive weak decays. 1." In: *Nucl. Phys. B* 399 (1993), pp. 441–458. DOI: `10.1016/0550-3213(93)90504-I`. arXiv: `hep-ph/9207236`.

[36] B. Blok and Mikhail A. Shifman. "The Rule of discarding 1/N(c) in inclusive weak decays. 2." In: *Nucl. Phys. B* 399 (1993), pp. 459–476. DOI: `10.1016/0550-3213(93)90505-J`. arXiv: `hep-ph/9209289`.

[37] Ikaros I. Y. Bigi, B. Blok, Mikhail A. Shifman, N. G. Uraltsev, and Arkady I. Vainshtein. "A QCD 'manifesto' on inclusive decays of beauty and charm". In: *7th Meeting of the APS Division of Particles Fields*. Nov. 1992, pp. 610–613. arXiv: `hep-ph/9212227`.

[38] Thomas Mannel, Daniel Moreno, and Alexei A. Pivovarov. "QCD corrections at subleading power for inclusive nonleptonic $b \to c\bar{u}d$ decays". In: (Aug. 2024). arXiv: `2408.06767 [hep-ph]`.

[39] S. Balk, J. G. Korner, D. Pirjol, and K. Schilcher. "Inclusive semileptonic B decays in QCD including lepton mass effects". In: *Z. Phys. C* 64 (1994), pp. 37–44. DOI: `10.1007/BF01557233`. arXiv: `hep-ph/9312220`.

[40] L. Koyrakh. "Nonperturbative corrections to the heavy lepton energy distribution in the inclusive decays H(b) —> tau anti-neutrino X". In: *Phys. Rev. D* 49 (1994), pp. 3379–3384. DOI: `10.1103/PhysRevD.49.3379`. arXiv: `hep-ph/9311215`.

[41] Andrea Alberti, Paolo Gambino, and Soumitra Nandi. "Perturbative corrections to power suppressed effects in semileptonic B decays". In: *JHEP* 01 (2014), p. 147. DOI: `10.1007/JHEP01(2014)147`. arXiv: `1311.7381 [hep-ph]`.

[42] Thomas Mannel, Alexei A. Pivovarov, and Denis Rosenthal. "Inclusive semileptonic B decays from QCD with NLO accuracy for power suppressed terms". In: *Phys. Lett. B* 741 (2015), pp. 290–294. DOI: `10.1016/j.physletb.2014.12.058`. arXiv: `1405.5072 [hep-ph]`.

[43] Thomas Mannel, Alexei A. Pivovarov, and Denis Rosenthal. "Inclusive weak decays of heavy hadrons with power suppressed terms at NLO". In: *Phys. Rev. D* 92.5 (2015), p. 054025. DOI: `10.1103/PhysRevD.92.054025`. arXiv: `1506.08167 [hep-ph]`.

[44] Martin Gremm and Anton Kapustin. "Order 1/m(b)**3 corrections to B –> X(c) lepton anti-neutrino decay and their implication for the measurement of Lambda-bar and lambda(1)". In: *Phys. Rev. D* 55 (1997), pp. 6924–6932. DOI: `10.1103/PhysRevD.55.6924`. arXiv: `hep-ph/9603448`.

[45] Thomas Mannel and Alexei A. Pivovarov. "QCD corrections to inclusive heavy hadron weak decays at $\Lambda_{\mathrm{QCD}}^3/m_Q^3$". In: *Phys. Rev. D* 100.9 (2019), p. 093001. DOI: `10.1103/PhysRevD.100.093001`. arXiv: `1907.09187 [hep-ph]`.

[46] Daniel Moreno. "NLO QCD corrections to inclusive semitauonic weak decays of heavy hadrons up to 1/mb3". In: *Phys. Rev. D* 106.11 (2022), p. 114008. DOI: `10.1103/PhysRevD.106.114008`. arXiv: `2207.14245 [hep-ph]`.

[47] Alexander Lenz, Maria Laura Piscopo, and Aleksey V. Rusov. "Contribution of the Darwin operator to non-leptonic decays of heavy quarks". In: *JHEP* 12 (2020), p. 199. DOI: 10.1007/JHEP12(2020)199. arXiv: 2004.09527 [hep-ph].

[48] Thomas Mannel, Daniel Moreno, and Alexei Pivovarov. "Heavy quark expansion for heavy hadron lifetimes: completing the $1/m_b^3$ corrections". In: *JHEP* 08 (2020), p. 089. DOI: 10.1007/JHEP08(2020)089. arXiv: 2004.09485 [hep-ph].

[49] Daniel Moreno. "Completing $1/m_b^3$ corrections to non-leptonic bottom-to-up-quark decays". In: *JHEP* 01 (2021), p. 051. DOI: 10.1007/JHEP01(2021)051. arXiv: 2009.08756 [hep-ph].

[50] E. Franco, V. Lubicz, F. Mescia, and C. Tarantino. "Lifetime ratios of beauty hadrons at the next-to-leading order in QCD". In: *Nucl. Phys. B* 633 (2002), pp. 212–236. DOI: 10.1016/S0550-3213(02)00262-6. arXiv: hep-ph/0203089.

[51] Alexander Lenz and Thomas Rauh. "D-meson lifetimes within the heavy quark expansion". In: *Phys. Rev. D* 88 (2013), p. 034004. DOI: 10.1103/PhysRevD.88.034004. arXiv: 1305.3588 [hep-ph].

[52] Fabrizio Gabbiani, Andrei I. Onishchenko, and Alexey A. Petrov. "Spectator effects and lifetimes of heavy hadrons". In: *Phys. Rev. D* 70 (2004), p. 094031. DOI: 10.1103/PhysRevD.70.094031. arXiv: hep-ph/0407004.

[53] Fabrizio Gabbiani, Andrei I. Onishchenko, and Alexey A. Petrov. "Lambda(b) lifetime puzzle in heavy quark expansion". In: *Phys. Rev. D* 68 (2003), p. 114006. DOI: 10.1103/PhysRevD.68.114006. arXiv: hep-ph/0303235.

[54] Florian Bernlochner, Matteo Fael, Kevin Olschewsky, Eric Persson, Raynette van Tonder, K. Keri Vos, and Maximilian Welsch. "First extraction of inclusive V_{cb} from q^2 moments". In: *JHEP* 10 (2022), p. 068. DOI: 10.1007/JHEP10(2022)068. arXiv: 2205.10274 [hep-ph].

[55] Gael Finauri and Paolo Gambino. "The q^2 moments in inclusive semileptonic B decays". In: *JHEP* 02 (2024), p. 206. DOI: 10.1007/JHEP02(2024)206. arXiv: 2310.20324 [hep-ph].

[56] Joshua Lin, William Detmold, and Stefan Meinel. "Lattice Study of Spectator Effects in b-hadron Decays". In: *PoS* LATTICE2022 (2023), p. 417. DOI: 10.22323/1.430.0417. arXiv: 2212.09275 [hep-lat].

[57] Matthew Black, Robert Harlander, Fabian Lange, Antonio Rago, Andrea Shindler, and Oliver Witzel. "Using Gradient Flow to Renormalise Matrix Elements for Meson Mixing and Lifetimes". In: *PoS* LATTICE2023 (2024), p. 263. DOI: 10.22323/1.453.0263. arXiv: 2310.18059 [hep-lat].

[58] M. Kirk, A. Lenz, and T. Rauh. "Dimension-six matrix elements for meson mixing and lifetimes from sum rules". In: *JHEP* 12 (2017). [Erratum: JHEP 06, 162 (2020)], p. 068. DOI: 10.1007/JHEP12(2017)068. arXiv: 1711.02100 [hep-ph].

[59] Daniel King, Alexander Lenz, and Thomas Rauh. "SU(3) breaking effects in B and D meson lifetimes". In: *JHEP* 06 (2022), p. 134. DOI: 10.1007/JHEP06(2022)134. arXiv: 2112.03691 [hep-ph].

[60] Matthew Black, Martin Lang, Alexander Lenz, and Zachary Wüthrich. "HQET sum rules for matrix elements of dimension-six four-quark operators for meson lifetimes within and beyond the Standard Model". In: (Dec. 2024). arXiv: 2412.13270 [hep-ph].

[61] M. Neubert and C.T. Sachrajda. "Spectator effects in inclusive decays of beauty hadrons". In: *Nuclear Physics B* 483.1–2 (Jan. 1997), pp. 339–367. ISSN: 0550-3213. DOI: 10.1016/s0550-3213(96)00559-7. URL: http://dx.doi.org/10.1016/S0550-3213(96)00559-7.

[62] N.G Uraltsev. "On the problem of boosting non-leptonic b baryon decays". In: *Physics Letters B* 376.4 (May 1996), pp. 303–308. ISSN: 0370-2693. DOI: 10.1016/0370-2693(96)00305-x. URL: http://dx.doi.org/10.1016/0370-2693(96)00305-X.

[63] E. Franco, V. Lubicz, F. Mescia, and C. Tarantino. "Lifetime ratios of beauty hadrons at the next-to-leading order in QCD". In: *Nuclear Physics B* 633.1–2 (June 2002), pp. 212–236. ISSN: 0550-3213. DOI: 10.1016/s0550-3213(02)00262-6. URL: http://dx.doi.org/10.1016/S0550-3213(02)00262-6.

[64] Thomas Mannel, Sascha Turczyk, and Nikolai Uraltsev. "Higher Order Power Corrections in Inclusive B Decays". In: *JHEP* 11 (2010), p. 109. DOI: 10.1007/JHEP11(2010)109. arXiv: 1009.4622 [hep-ph].

[65] Matteo Fael, Fabian Lange, Kay Schönwald, and Matthias Steinhauser. "A semi-analytic method to compute Feynman integrals applied to four-loop corrections to the $\overline{\text{MS}}$-pole quark mass relation". In: *JHEP* 09 (2021), p. 152. DOI: 10.1007/JHEP09(2021)152. arXiv: 2106.05296 [hep-ph].

[66] Matteo Fael, Fabian Lange, Kay Schönwald, and Matthias Steinhauser. "Massive Vector Form Factors to Three Loops". In: *Phys. Rev. Lett.* 128.17 (2022), p. 172003. DOI: 10.1103/PhysRevLett.128.172003. arXiv: 2202.05276 [hep-ph].

[67] Matteo Fael, Fabian Lange, Kay Schönwald, and Matthias Steinhauser. "Singlet and nonsinglet three-loop massive form factors". In: *Phys. Rev. D* 106.3 (2022), p. 034029. DOI: 10.1103/PhysRevD.106.034029. arXiv: 2207.00027 [hep-ph].

[68] A.V. Smirnov and V.A. Smirnov. "How to choose master integrals". In: *Nuclear Physics B* 960 (Nov. 2020), p. 115213. ISSN: 0550-3213. DOI: 10.1016/j.nuclphysb.2020.115213. URL: http://dx.doi.org/10.1016/j.nuclphysb.2020.115213.

[69] J. M. Henn. "Multiloop Integrals in Dimensional Regularization Made Simple". In: *Physical Review Letters* 110.25 (June 2013). ISSN: 1079-7114. DOI: 10.1103/physrevlett.110.251601. URL: http://dx.doi.org/10.1103/PhysRevLett.110.251601.

[70] Roman N. Lee. "Reducing differential equations for multiloop master integrals". In: *Journal of High Energy Physics* 2015.4 (Apr. 2015). ISSN: 1029-8479. DOI: 10.1007/jhep04(2015)108. URL: http://dx.doi.org/10.1007/JHEP04(2015)108.

[71] C. Meyer. "Transforming differential equations of multi-loop Feynman integrals into canonical form". In: *Journal of High Energy Physics* 2017.4 (Apr. 2017). ISSN: 1029-8479. DOI: `10.1007/jhep04(2017)006`. URL: `http://dx.doi.org/10.1007/JHEP04(2017)006`.

[72] R. N. Lee. "Libra: A package for transformation of differential systems for multiloop integrals". In: *Comput. Phys. Commun.* 267 (2021), p. 108058. DOI: `10.1016/j.cpc.2021.108058`. arXiv: `2012.00279 [hep-ph]`.

[73] C. Meyer. "Algorithmic transformation of multi-loop master integrals to a canonical basis with CANONICA". In: *Computer Physics Communications* 222 (Jan. 2018), pp. 295–312. ISSN: 0010-4655. DOI: `10.1016/j.cpc.2017.09.014`. URL: `http://dx.doi.org/10.1016/j.cpc.2017.09.014`.

[74] D. Maître. "HPL, a Mathematica implementation of the harmonic polylogarithms". In: *Computer Physics Communications* 174.3 (Feb. 2006), pp. 222–240. ISSN: 0010-4655. DOI: `10.1016/j.cpc.2005.10.008`. URL: `http://dx.doi.org/10.1016/j.cpc.2005.10.008`.

[75] J. Ablinger, J. Blümlein, P. Marquard, N. Rana, and C. Schneider. "Automated solution of first order factorizable systems of differential equations in one variable". In: *Nuclear Physics B* 939 (Feb. 2019), pp. 253–291. ISSN: 0550-3213. DOI: `10.1016/j.nuclphysb.2018.12.010`. URL: `http://dx.doi.org/10.1016/j.nuclphysb.2018.12.010`.

[76] Stefan Gerhold. "Uncoupling Systems of Linear Ore Operator Equations". PhD thesis. J. Kepler University, Linz, February 2002.

[77] Carsten Schneider. *Simplifying Multiple Sums in Difference Fields*. 2013. arXiv: `1304.4134 [cs.SC]`. URL: `https://arxiv.org/abs/1304.4134`.

[78] J. Ablinger. *A Computer Algebra Toolbox for Harmonic Sums Related to Particle Physics*. 2010. arXiv: `1011.1176 [math-ph]`.

[79] M. Beneke and V.A. Smirnov. "Asymptotic expansion of Feynman integrals near threshold". In: *Nuclear Physics B* 522.1-2 (June 1998), pp. 321–344. ISSN: 0550-3213. DOI: `10.1016/s0550-3213(98)00138-2`. URL: `http://dx.doi.org/10.1016/S0550-3213(98)00138-2`.

[80] Vladimir A. Smirnov. *Analytic tools for Feynman integrals*. Vol. 250. 2012. DOI: `10.1007/978-3-642-34886-0`.

[81] A. Pak and A. Smirnov. "Geometric approach to asymptotic expansion of Feynman integrals". In: *The European Physical Journal C* 71.4 (Apr. 2011). DOI: `10.1140/epjc/s10052-011-1626-1`. URL: `https://doi.org/10.1140%2Fepjc%2Fs10052-011-1626-1`.

[82] Bernd Jantzen, Alexander V. Smirnov, and Vladimir A. Smirnov. "Expansion by regions: revealing potential and Glauber regions automatically". In: *The European Physical Journal C* 72.9 (Sept. 2012). DOI: `10.1140/epjc/s10052-012-2139-2`. URL: `https://doi.org/10.1140%2Fepjc%2Fs10052-012-2139-2`.

[83] Florian Herren. "Precision Calculations for Higgs Boson Physics at the LHC - Four-Loop Corrections to Gluon-Fusion Processes and Higgs Boson Pair-Production at NNLO". PhD thesis. KIT, Karlsruhe, 2020. DOI: 10.5445/IR/1000125521.

[84] R. N. Lee. *Presenting LiteRed: a tool for the Loop InTEgrals REDuction.* 2012. arXiv: 1212.2685 [hep-ph].

[85] R. N. Lee. "LiteRed 1.4: a powerful tool for reduction of multiloop integrals". In: *Journal of Physics: Conference Series* 523 (June 2014), p. 012059. ISSN: 1742-6596. DOI: 10.1088/1742-6596/523/1/012059. URL: http://dx.doi.org/10.1088/1742-6596/523/1/012059.

[86] A.I. Davydychev and V.A. Smirnov. "Threshold expansion of the sunset diagram". In: *Nuclear Physics B* 554.1–2 (Aug. 1999), pp. 391–414. ISSN: 0550-3213. DOI: 10.1016/s0550-3213(99)00269-2. URL: http://dx.doi.org/10.1016/S0550-3213(99)00269-2.

[87] P. Maierhöfer, J. Usovitsch, and P. Uwer. "Kira—A Feynman integral reduction program". In: *Computer Physics Communications* 230 (Sept. 2018), pp. 99–112. ISSN: 0010-4655. DOI: 10.1016/j.cpc.2018.04.012. URL: http://dx.doi.org/10.1016/j.cpc.2018.04.012.

[88] J. Klappert, F. Lange, P. Maierhöfer, and J. Usovitsch. "Integral reduction with Kira 2.0 and finite field methods". In: *Computer Physics Communications* 266 (Sept. 2021), p. 108024. ISSN: 0010-4655. DOI: 10.1016/j.cpc.2021.108024. URL: http://dx.doi.org/10.1016/j.cpc.2021.108024.

[89] Jonas Klappert and Fabian Lange. "Reconstructing rational functions with FireFly". In: *Computer Physics Communications* 247 (Feb. 2020), p. 106951. ISSN: 0010-4655. DOI: 10.1016/j.cpc.2019.106951. URL: http://dx.doi.org/10.1016/j.cpc.2019.106951.

[90] Jonas Klappert, Sven Yannick Klein, and Fabian Lange. "Interpolation of dense and sparse rational functions and other improvements in FireFly". In: *Computer Physics Communications* 264 (July 2021), p. 107968. ISSN: 0010-4655. DOI: 10.1016/j.cpc.2021.107968. URL: http://dx.doi.org/10.1016/j.cpc.2021.107968.

[91] Roman N. Lee, Alexander V. Smirnov, and Vladimir A. Smirnov. "Solving differential equations for Feynman integrals by expansions near singular points". In: *Journal of High Energy Physics* 2018.3 (Mar. 2018). ISSN: 1029-8479. DOI: 10.1007/jhep03(2018)008. URL: http://dx.doi.org/10.1007/JHEP03(2018)008.

[92] Xiao Liu and Yan-Qing Ma. "AMFlow: A Mathematica package for Feynman integrals computation via auxiliary mass flow". In: *Computer Physics Communications* 283 (Feb. 2023), p. 108565. DOI: 10.1016/j.cpc.2022.108565. URL: https://doi.org/10.1016%2Fj.cpc.2022.108565.

[93] M. Fael, K. Schönwald, and M. Steinhauser. "Exact results for Z_m^{OS} and Z_2^{OS} with two mass scales and up to three loops". In: *Journal of High Energy Physics* 2020.10 (Oct. 2020). ISSN: 1029-8479. DOI: 10.1007/jhep10(2020)087. URL: http://dx.doi.org/10.1007/JHEP10(2020)087.

[94] A. Sirlin. "Large m(W), m(Z) Behavior of the O(alpha) Corrections to Semileptonic Processes Mediated by W". In: *Nucl. Phys. B* 196 (1982), pp. 83–92. DOI: 10.1016/0550-3213(82)90303-0.

[95] E. Remiddi and J. A. M. Vermaseren. "HARMONIC POLYLOGARITHMS". In: *International Journal of Modern Physics A* 15.05 (Feb. 2000), pp. 725–754. ISSN: 1793-656X. DOI: 10.1142/s0217751x00000367. URL: http://dx.doi.org/10.1142/S0217751X00000367.

[96] https://www.ttp.kit.edu/preprints/2023/ttp23-030.

[97] Christian Bauer, Alexander Frink, and Richard Kreckel. *Introduction to the GiNaC Framework for Symbolic Computation within the C++ Programming Language.* 2001. arXiv: cs/0004015 [cs.SC]. URL: https://arxiv.org/abs/cs/0004015.

[98] Jens Vollinga and Stefan Weinzierl. "Numerical evaluation of multiple polylogarithms". In: *Computer Physics Communications* 167.3 (May 2005), pp. 177–194. ISSN: 0010-4655. DOI: 10.1016/j.cpc.2004.12.009. URL: http://dx.doi.org/10.1016/j.cpc.2004.12.009.

[99] Christoph Bobeth, Mikolaj Misiak, and Jorg Urban. "Photonic penguins at two loops and m_t dependence of $BR[B \to X_s l^+ l^-]$". In: *Nucl. Phys. B* 574 (2000), pp. 291–330. DOI: 10.1016/S0550-3213(00)00007-9. arXiv: hep-ph/9910220.

[100] Martin Gorbahn and Ulrich Haisch. "Effective Hamiltonian for non-leptonic $|\Delta F| = 1$ decays at NNLO in QCD". In: *Nucl. Phys. B* 713 (2005), pp. 291–332. DOI: 10.1016/j.nuclphysb.2005.01.047. arXiv: hep-ph/0411071.

[101] Andrzej J. Buras, Matthias Jamin, M. E. Lautenbacher, and Peter H. Weisz. "Effective Hamiltonians for $\Delta S = 1$ and $\Delta B = 1$ nonleptonic decays beyond the leading logarithmic approximation". In: *Nucl. Phys. B* 370 (1992). [Addendum: Nucl.Phys.B 375, 501 (1992)], pp. 69–104. DOI: 10.1016/0550-3213(92)90345-C.

[102] Mikolaj Misiak and Matthias Steinhauser. "NNLO QCD corrections to the anti-B —> X(s) gamma matrix elements using interpolation in m(c)". In: *Nucl. Phys. B* 764 (2007), pp. 62–82. DOI: 10.1016/j.nuclphysb.2006.11.027. arXiv: hep-ph/0609241.

[103] P. A. Baikov, K. G. Chetyrkin, and Johann H. Kuhn. "Perturbative QCD and tau-decays". In: *Nucl. Phys. B Proc. Suppl.* 144 (2005). Ed. by T. Ohshima and H. Hayashii, pp. 81–87. DOI: 10.1016/j.nuclphysbps.2005.02.011.

[104] Manuel Egner, Matteo Fael, Kay Schönwald, and Matthias Steinhauser. "Revisiting semileptonic B meson decays at next-to-next-to-leading order". In: *JHEP* 09 (2023), p. 112. DOI: 10.1007/JHEP09(2023)112. arXiv: 2308.01346 [hep-ph].

[105] J. Ablinger, J. Blümlein, and C. Schneider. "Harmonic sums and polylogarithms generated by cyclotomic polynomials". In: *Journal of Mathematical Physics* 52.10 (Oct. 2011), p. 102301. ISSN: 1089-7658. DOI: 10.1063/1.3629472. URL: http://dx.doi.org/10.1063/1.3629472.

[106] Michel Gourdin and Xuan-Yem Pham. "STUDY OF ELECTRON TYPE NEUTRAL HEAVY LEPTON IN ELECTRON - POSITRON REACTIONS. 2. LEPTONIC DECAY". In: *Nucl. Phys. B* 164 (1980), pp. 399–412. DOI: 10.1016/0550-3213(80)90518-0.

[107] E. Bagan, Patricia Ball, V.M. Braun, and P. Gosdzinsky. "Theoretical update of the semileptonic branching ratio of B mesons". In: *Physics Letters B* 342.1–4 (Jan. 1995), pp. 362–368. ISSN: 0370-2693. DOI: 10.1016/0370-2693(94)01410-e. URL: http://dx.doi.org/10.1016/0370-2693(94)01410-E.

[108] Vladimir A. Smirnov. "Evaluating Feynman integrals". In: *Springer Tracts Mod. Phys.* 211 (2004), pp. 1–244.

[109] Manuel Egner, Matteo Fael, Alexander Lenz, Maria Laura Piscopo, Aleksey V. Rusov, Kay Schönwald, and Matthias Steinhauser. "Total decay rates of B mesons at NNLO-QCD". In: (Dec. 2024). arXiv: 2412.14035 [hep-ph].

[110] K. G. Chetyrkin, J. H. Kuhn, A. Maier, P. Maierhofer, P. Marquard, M. Steinhauser, and C. Sturm. "Charm and Bottom Quark Masses: An Update". In: *Phys. Rev. D* 80 (2009), p. 074010. DOI: 10.1103/PhysRevD.80.074010. arXiv: 0907.2110 [hep-ph].

[111] Florian Herren and Matthias Steinhauser. "Version 3 of RunDec and CRunDec". In: *Comput. Phys. Commun.* 224 (2018), pp. 333–345. DOI: 10.1016/j.cpc.2017.11.014. arXiv: 1703.03751 [hep-ph].

[112] J. Charles, Andreas Hocker, H. Lacker, S. Laplace, F. R. Le Diberder, J. Malcles, J. Ocariz, M. Pivk, and L. Roos. "CP violation and the CKM matrix: Assessing the impact of the asymmetric B factories". In: *Eur. Phys. J. C* 41.1 (2005), pp. 1–131. DOI: 10.1140/epjc/s2005-02169-1. arXiv: hep-ph/0406184.

[113] Matteo Fael, Kay Schönwald, and Matthias Steinhauser. "Relation between the $\overline{\text{MS}}$ and the kinetic mass of heavy quarks". In: *Phys. Rev. D* 103.1 (2021), p. 014005. DOI: 10.1103/PhysRevD.103.014005. arXiv: 2011.11655 [hep-ph].

[114] S. Bekavac, A. Grozin, D. Seidel, and M. Steinhauser. "Light quark mass effects in the on-shell renormalization constants". In: *JHEP* 10 (2007), p. 006. DOI: 10.1088/1126-6708/2007/10/006. arXiv: 0708.1729 [hep-ph].

[115] Alexander Kurz, Matthias Steinhauser, and Nikolai Zerf. "Decoupling Constant for α_s and the Effective Gluon-Higgs Coupling to Three Loops in Supersymmetric QCD". In: *JHEP* 07 (2012), p. 138. DOI: 10.1007/JHEP07(2012)138. arXiv: 1206.6675 [hep-ph].

[116] K. G. Chetyrkin, Bernd A. Kniehl, and M. Steinhauser. "Decoupling relations to O (alpha-s**3) and their connection to low-energy theorems". In: *Nucl. Phys. B* 510 (1998), pp. 61–87. DOI: 10.1016/S0550-3213(97)00649-4. arXiv: hep-ph/9708255.

[117] Ikaros I. Y. Bigi, Mikhail A. Shifman, N. Uraltsev, and Arkady I. Vainshtein. "High power n of m(b) in beauty widths and n=5 —> infinity limit". In: *Phys. Rev. D* 56 (1997). Ed. by Ikaros I Bigi, Paolo Gambino, and Thomas Mannel, pp. 4017–4030. DOI: 10.1103/PhysRevD.56.4017. arXiv: hep-ph/9704245.

[118] I. Bigi, M. Shifman, N. G. Uraltsev, and A. Vainshtein. "Sum rules for heavy flavor transitions in the small velocity limit". In: *Physical Review D* 52.1 (July 1995), pp. 196–235. ISSN: 0556-2821. DOI: 10.1103/physrevd.52.196. URL: http://dx.doi.org/10.1103/PhysRevD.52.196.

[119] A. Czarnecki, K. Melnikov, and N. Uraltsev. "NonAbelian dipole radiation and the heavy quark expansion". In: *Phys. Rev. Lett.* 80 (1998), pp. 3189–3192. DOI: 10.1103/PhysRevLett.80.3189. arXiv: hep-ph/9708372.

[120] Matteo Fael, Ilija S. Milutin, and K. Keri Vos. "Kolya: an open-source package for inclusive semileptonic B decays". In: (Sept. 2024). arXiv: 2409.15007 [hep-ph].

[121] Florian Bernlochner, Matteo Fael, Kevin Olschewsky, Eric Persson, Raynette van Tonder, K. Keri Vos, and Maximilian Welsch. "First extraction of inclusive V_{cb} from q^2 moments". In: (May 2022). arXiv: 2205.10274 [hep-ph].

[122] A. H. Mahmood et al. "Measurement of the B-meson inclusive semileptonic branching fraction and electron energy moments". In: *Phys. Rev. D* 70 (2004), p. 032003. DOI: 10.1103/PhysRevD.70.032003. arXiv: hep-ex/0403053.

[123] Bernard Aubert et al. "Measurement and interpretation of moments in inclusive semileptonic decays anti-B −> X(c) l- anti-nu". In: *Phys. Rev. D* 81 (2010), p. 032003. DOI: 10.1103/PhysRevD.81.032003. arXiv: 0908.0415 [hep-ex].

[124] J. P. Lees et al. "Measurement of the inclusive electron spectrum from B meson decays and determination of |Vub|". In: *Phys. Rev. D* 95.7 (2017), p. 072001. DOI: 10.1103/PhysRevD.95.072001. arXiv: 1611.05624 [hep-ex].

[125] P. Urquijo et al. "Moments of the electron energy spectrum and partial branching fraction of B −> X(c) e nu decays at Belle". In: *Phys. Rev. D* 75 (2007), p. 032001. DOI: 10.1103/PhysRevD.75.032001. arXiv: hep-ex/0610012.

[126] https://www.ttp.kit.edu/preprints/2024/ttp24-020/.

[127] P. Nogueira. "Automatic Feynman Graph Generation". In: *Journal of Computational Physics* 105.2 (1993), pp. 279–289. ISSN: 0021-9991. DOI: https://doi.org/10.1006/jcph.1993.1074. URL: https://www.sciencedirect.com/science/article/pii/S0021999183710740.

[128] Marvin Gerlach, Florian Herren, and Martin Lang. "tapir: A tool for topologies, amplitudes, partial fraction decomposition and input for reductions". In: *Comput. Phys. Commun.* 282 (2023), p. 108544. DOI: 10.1016/j.cpc.2022.108544. arXiv: 2201.05618 [hep-ph].

[129] B. Ruijl, T. Ueda, and J. Vermaseren. *FORM version 4.2*. 2017. arXiv: 1707.06453 [hep-ph].

[130] T. Seidensticker. "Automatic application of successive asymptotic expansions of Feynman diagrams". In: *6th International Workshop on New Computing Techniques in Physics Research: Software Engineering, Artificial Intelligence Neural Nets, Genetic Algorithms, Symbolic Algebra, Automatic Calculation.* May 1999. arXiv: hep-ph/9905298.

[131] R. Harlander, T. Seidensticker, and M. Steinhauser. "Complete corrections of Order alpha alpha-s to the decay of the Z boson into bottom quarks". In: *Phys. Lett. B* 426 (1998), pp. 125–132. DOI: 10.1016/S0370-2693(98)00220-2. arXiv: hep-ph/9712228.

[132] Johann Usovitsch. "Factorization of denominators in integration-by-parts reductions". In: (Feb. 2020). arXiv: 2002.08173 [hep-ph].

[133] K. G. Chetyrkin and F. V. Tkachov. "Integration by Parts: The Algorithm to Calculate beta Functions in 4 Loops". In: *Nucl. Phys. B* 192 (1981), pp. 159–204. DOI: 10.1016/0550-3213(81)90199-1.

[134] S. Laporta. "High-precision calculation of multiloop Feynman integrals by difference equations". In: *Int. J. Mod. Phys. A* 15 (2000), pp. 5087–5159. DOI: 10.1142/S0217751X00002159. arXiv: hep-ph/0102033.

[135] S. Lang. *Algebra*. New York, NY: Springer, 2002. ISBN: 9781461300410 146130041X.

[136] N.I. Ussyukina and A.I. Davydychev. "An approach to the evaluation of three- and four-point ladder diagrams". In: *Physics Letters B* 298.3 (1993), pp. 363–370. ISSN: 0370-2693. DOI: https://doi.org/10.1016/0370-2693(93)91834-A. URL: https://www.sciencedirect.com/science/article/pii/037026939391834A.

[137] M C Bergere and Y M.P. Lam. "Asymptotic expansion of Feynman amplitudes. P. 1. The convergent case". In: *Commun. Math. Phys., v. 39, no. 1, pp. 1-32* (Nov. 1974). URL: https://www.osti.gov/biblio/4207212.

[138] E. W. Barnes. "A New Development of the Theory of the Hypergeometric Functions". In: *Proceedings of the London Mathematical Society* s2-6.1 (1908), pp. 141–177. DOI: https://doi.org/10.1112/plms/s2-6.1.141. eprint: https://londmathsoc.onlinelibrary.wiley.com/doi/pdf/10.1112/plms/s2-6.1.141. URL: https://londmathsoc.onlinelibrary.wiley.com/doi/abs/10.1112/plms/s2-6.1.141.

[139] T. Huber and D. Maître. "HypExp, a Mathematica package for expanding hypergeometric functions around integer-valued parameters". In: *Computer Physics Communications* 175.2 (July 2006), pp. 122–144. ISSN: 0010-4655. DOI: 10.1016/j.cpc.2006.01.007. URL: http://dx.doi.org/10.1016/j.cpc.2006.01.007.

[140] Tobias Huber and Daniel Maître. "HypExp 2, Expanding hypergeometric functions about half-integer parameters". In: *Computer Physics Communications* 178.10 (May 2008), pp. 755–776. ISSN: 0010-4655. DOI: 10.1016/j.cpc.2007.12.008. URL: http://dx.doi.org/10.1016/j.cpc.2007.12.008.

[141] Marco Ciuchini, E. Franco, G. Martinelli, and L. Reina. "The Delta S = 1 effective Hamiltonian including next-to-leading order QCD and QED corrections". In: *Nucl. Phys. B* 415 (1994), pp. 403–462. DOI: 10.1016/0550-3213(94)90118-X. arXiv: hep-ph/9304257.

[142] Matthias Steinhauser. "MATAD: a program package for the computation of MAssive TADpoles". In: *Computer Physics Communications* 134.3 (Mar. 2001), pp. 335–364. ISSN: 0010-4655. DOI: 10.1016/s0010-4655(00)00204-6. URL: http://dx.doi.org/10.1016/S0010-4655(00)00204-6.

[143]   Konstantin Chetyrkin, Mikoaj Misiak, and Manfred Münz. "Beta functions and anomalous dimensions up to three loops". In: *Nuclear Physics B* 518.1–2 (May 1998), pp. 473–494. ISSN: 0550-3213. DOI: 10.1016/s0550-3213(98)00122-9. URL: http://dx.doi.org/10.1016/S0550-3213(98)00122-9.

Acknowledgements

schränkte Unterstützung bei jeder meiner Lebensentscheidungen. Danke für Alles. Diese Arbeit ist für dich Mama, Ich glaube du würdest dich hierüber sehr freuen.